The Dissertation Committee for Luz Cristal Sanchez Glangchai Certifies that this is the approved version of the following dissertation:

Nanoimprint Lithography Based Fabrication of Size and Shape-Specific, Enzymatically-Triggered Nanoparticles for Drug Delivery Applications

Committee:

Krishnendu Roy, Supervisor

Li Shi, Co-Supervisor

Wolfgang Frey

John D. Hazle

Nicholas A. Peppas

Nanoimprint Lithography Based Fabrication of Size and Shape-Specific, Enzymatically-Triggered Nanoparticles for Drug Delivery Applications

by

Luz Cristal Sanchez Glangchai, B.A.; B.S.; M.S.

Dissertation

Presented to the Faculty of the Graduate School of

The University of Texas at Austin

in Partial Fulfillment

of the Requirements

for the Degree of

Doctor of Philosophy

The University of Texas at Austin

May 2008

Dedication

I dedicate this to my loving husband Saranyoo Golf Glangchai and my son Javier Silar Glangchai, as well as to my parents Elaine and Adolfo Sanchez, and my sisters Laura and Sara Sanchez.

Acknowledgements

I would like to thank Dr. Krishnendu Roy, my PhD advisor, for giving me the opportunity to perform research in his lab at UT over the past 5 years. After being laid off from 3M, and having little background in chemistry and biology, I still remember the excitement of coming to the Biomedical Engineering Department to work in Dr. Roy's lab. I would like to thank him for his advice, his guidance in research, and his patience in dealing with a new mom. He has been a great mentor throughout the many challenges of my doctoral studies and has allowed me to pursue my interests to the fullest.

My sincere thanks go to Dr. Li Shi, my co-advisor, for his advice and encouragement, and for giving me the opportunity to collaborate with him on a cross-disciplinary research subject. I appreciate all the help and guidance he has provided me on the AFM and fabrication related topics, as well as on the struggles of daily life. I would also like to thank my committee members, Drs. Wolfgang Frey, John D. Hazle, and Nicholas A. Peppas for their advice and knowledgeable input on the direction my PhD project.

Furthermore I would like to thank Dr. Steven P. Nichols for his guidance and support. His support provided me with the opportunity to continue performing my research and successfully finish my studies. I would also like to thank him for introducing me to the concept of technology commercialization, which has truly changed the way I view ideas, research and technology. Along the same lines, I would like to thank Dr. Rob Adams for his guidance and support as an advisor for NANOTaxi. His support also allowed me to continue my studies as well as enabled me to participate in

numerous business plan competitions. The experiences I have gained from these commercialization and business plan competitions will stay with me forever. I would also like to thank Dr. Scott Evans for introducing me to technology commercializing, for his advice during my final semesters, and for his sense of humor.

I would further like to thank Anastassios Mavrokefalos for his help in the cleanroom and with thermal imprinting. I would like to thank Mary Caldorera-Moore for her steadfast help with acrylation. Thanks go to Bilal Ghosn for his help with transfection and with almost anything I had a question about. I really appreciate all the help and advice. I would like to thank the undergraduate assistants, Cristina Garcia for her help with viscosity studies and swelling studies, and Nick Jew for his help with PLGA characterization, swelling studies and acrylation. I would like to thank the staff at the Microelectronic Research Center, Gabriel Glenn, Jesse James, Bill Ostler, Marylene Palard, and William Fordyce for all of the invaluable help in the cleanroom. I would also like to thank Dr. Yangming Sun for his help and advice on XPS and AFM, and Klaus Linse for his help with peptide fabrication. I further acknowledge Elsevier for permission to use my entire first author paper, J Control Release, 125, L. C. Glangchai, M. Caldorera-Moore, L. Shi, and K. Roy, 263 – 272, 2008, in this work.

Thanks goes out to everyone in the lab for being great and fun people to vent with about classes and the PhD process. I would like to thank Ted Gaubert and Scott Collins for some great discussions. I would like to thank Tania Betancourt for her advice and encouragement. Special thanks go out to Jon Nickels for all of his advice and support, and for his help with the AFM. I would like to thank Jon for being so helpful and always willing to do whatever at the drop of a hat.

I would like to thank team NANOTaxi: Abiola Ajetunmobi, Jakub Felkl, and Nick Rojeski. This group of amazing people really made an impression on me and taught

me a lot about friendship. I thank Abiola for his wonderful sense of humor. I thank Nick for teaching me how to behave in business and social settings, and I would like to thank Jakub for his great friendship and fun adventures.

Finally, my special thanks go out to my family. I thank my parents, Elaine and Adolfo Sanchez, for their constant support throughout my PhD studies. Special thanks go out to my mother-in-law, Sue Glangchai, for taking care of Javi every day. Without her help my achievements would not have been possible. Most importantly I would like to thank my husband, Golf, for his unwavering support and understanding throughout the hardest of times. At many times he has had to be like a single father because I was constantly at school doing research. I truly appreciate all of his help in taking care of Javi; without his help I could not have finished. Finally I would like to thank my son Javi. Although he will not remember this time period in his life, he motivated me to do the best that I could to, and he motivated me to finish so that I could provide him with a happy and stable environment.

Nanoimprint Lithography Based Fabrication of Size and Shape-Specific, Enzymatically-Triggered Nanoparticles for Drug Delivery Applications

Publication No._____

Luz Cristal Sanchez Glangchai, PhD

The University of Texas at Austin, 2008

Supervisors: Krishnendu Roy and Li Shi

Our ability to precisely manipulate size, shape, and composition of nanoscale carriers is essential for controlling their in-vivo transport, biodistribution, and drug release mechanism. Shape-specific, "smart" nanoparticles that deliver drugs or imaging agents to target tissues primarily in response to disease-specific or physiological signals could significantly improve therapeutic care of complex diseases. Current methods in nanoparticle synthesis do not allow such simultaneous control over particle size, shape, and environmentally-triggered drug release, especially at the sub-100 nm range. In this dissertation, we discuss the development of high-throughput nanofabrication techniques using synthetic and biological macromers (peptides) to produce highly monodisperse nanoparticles, as well as enzymatically-triggered nanoparticles, of precise sizes and shapes. We evaluated thermal nanoimprint lithography (ThNIL) and step and flash imprint lithography (SFIL) as two possible fabrication techniques. We successfully employed ThNIL and SFIL for fabricating nanoparticles and have extensively

characterized the SFIL fabrication process, as well as the properties of the imprinted biopolymers. Particles as small as 50 nm were fabricated on silicon wafers and harvested directly into aqueous buffer using a biocompatible, one-step release technique. These methods provide a novel way to fabricate biocompatible nanoparticles with precise size and geometry. Furthermore, we developed an enzyme-degradable material system and demonstrated successful encapsulation and enzyme-triggered release of antibodies and nucleic acids from these imprinted nanoparticles; thus providing a potential means for disease-controlled delivery of biomolecules. Finally, we evaluated the bioactivity of the encapsulated therapeutics in-vitro. The development of the SFIL method for fabrication of biocompatible nanocarriers has great potential in the drug delivery field for its ability to create monodisperse particles of pre-designed geometry and size, and to incorporate stimulus-responsive release mechanisms. This research provides the potential to broaden the study of how particle size and shape affect the biodistribution of drugs within the body.

Table of Contents

List of Tables

List of Figures

CHAPTER ONE

Introduction: Specific Aims and Overview

1.1 INTRODUCTION

Nanoparticle-based delivery of therapeutics has been extensively studied in a variety of diseases and is considered to be an ideal platform for targeted intravenous and intracellular delivery of bioactive agents. Current concepts in the synthesis of drug nanocarriers primarily involve the use of polymers or lipids to fabricate self-assembled or emulsion-based particles that are mostly spherical, polydisperse, and release drugs through diffusion or hydrolytic degradation. Although significant progress has been made in polymeric or liposomal drug delivery systems, there remain critical limitations in synthesizing nanocarriers with highly controllable architectures that can, at the same time, impart environmentally-triggered release mechanisms. Our ability to precisely manipulate size, shape, composition, and drug release mechanism of nanoparticles is essential for controlling their in-vivo transport, biodistribution, and therapeutic efficacy [1-3].

While particles below 500 nm in size can be injected intravenously, only those below 200 nm are efficiently internalized by somatic cells. Recent reports also suggest that delivery into the lymphatic circulation requires particles that are even smaller in size (< 50 nm) [4]. Besides size, mechanism of drug release from particle carriers is another important design parameter in nanomedicine. Stimuli-sensitive hydrogels have been

widely studied as micro or macroscale “smart” delivery systems to release drugs in response to specific environmental stimuli [5-8]. Similar nanoparticles that deliver their cargo to target cells primarily in response to disease-specific environmental signals could significantly improve therapeutic care of complex diseases. For example, most chemotherapeutic drugs that are toxic to normal cells would have significantly less morbidity and mortality if they could be released primarily in response to a tumor-specific, pathological signal. The design of carriers at the nanometer length scale that incorporate such triggered-release mechanisms has remained elusive because of the lack of flexible fabrication methods that can incorporate responsive bio-molecules within the nanoparticle matrix.

Size, material chemistry, and particle surface characteristics have so far been the primary variables used to fabricate nanocarriers. However, recent reports suggest that particle shape could play a significant role in the in-vivo performance of delivery vehicles [1, 9]. Specifically, shape and shape-related form factors, like aspect ratio or edges, affect particle transport characteristics, influence cell-particle interactions, and alter drug release kinetics [1, 3]. Furthermore, theoretical modeling has shown that size and shape can significantly affect how particles interact with tumor capillaries during transport [10, 11]. Until recently, particle shape has been an unexplored area of research in drug delivery due to our inability to reliably synthesize nano or microparticle carriers with precise and pre-designed geometry.

Nano-sized, injectable drug carriers having precise geometry and environmentally-responsive release mechanisms could provide targeted, disease-specific

delivery of molecules as well as tunable in-vivo release characteristics. In order to create such multi-functional, shape-specific drug delivery carriers, recent research has focused on top-down manufacturing approaches such as soft-lithography, micromolding and nanoimprinting to generate devices with more controllable properties [12-14]. Top-down fabrication of nanocarriers for drug delivery can allow for fabrication of highly monodisperse particles of precise size and shape, thus allowing for better control of transport, biodistribution and release kinetics.

We have previously reported that polyethylene glycol (PEG)-based materials can be used to create three dimensional, container-like nanostructures suitable for drug delivery using nanoimprint lithography [15]. Recently, DeSimone and colleagues elegantly demonstrated the ability to form nano-sized particles on silicon wafers using a top-down particle nanoreplication (PRINT) method [14, 16, 17]. Synthesis of shape-specific particles as small as 160 nm was demonstrated using this process. However, methods to generate particles with precise size and shape that also incorporate environmentally-triggered drug release are yet to be reported, especially at the sub-100 nm range. In addition, a major limitation in current nanofabricated delivery devices is the process of particle harvesting. For example, the PRINT particles are harvested from the wafer either using physical scraping with surgical blades [14] or by shear force using a glass slide, [17] both of which could damage the particles and may not be suitable for large scale manufacturing.

Recent advances in nanoscale fabrication methods could provide unique solutions to manufacture stimuli-sensitive nanocarriers for drug delivery in a high-throughput

manner. However, it is evident that successful translation of any top-down nanofabrication technologies to drug delivery applications would require development of techniques that are mild and compatible with a variety of biological molecules. Furthermore, any such technique must allow easy harvesting of nanoparticles and the ability to incorporate unique functionalities, such as disease-triggered drug release.

The research presented here provides a novel application of imprint lithography techniques to fabricate biocompatible, as well as stimuli-responsive, easily-harvestable, nanoparticles (as small as 50 nm) of precise sizes, shapes and compositions. This project provides a significant advance in the creation of monodisperse, injectable nanocarriers of specific geometry and can provide a characterized environment for the study of the effect of size and shape in in-vivo release properties of nanoparticles. The overall goal of this work is to develop nano-fabrication techniques to create monodisperse, biocompatible, nanocarriers as well as demonstrate triggered-release of therapeutics. Nano-sized, injectable drug carriers having precise geometry and environmentally-responsive release mechanisms could provide targeted, disease-specific delivery of molecules as well as tunable in-vivo release characteristics. The long term goal is to achieve site-specific, controlled, on-demand systemic drug delivery leading to lower side-effects, increased bioavailability, and improved therapeutic effectiveness, as well as simultaneous non-invasive monitoring of the therapeutics and the delivery device.

1.2 SPECIFIC AIMS

1.2.1 Aim 1: To synthesize a peptide-based material system for creating photo-crosslinked PEG-peptide hydrogels suitable for enzyme-triggered degradation and drug release.

We hypothesized that the use of a specific peptide sequence within acrylated polyethylene glycol polymers would allow the cross-linked hydrogel to dissolve and cause an enzyme-triggered release of drug in the presence of a tissue/cell-specific enzyme. Such a design would allow for incorporation of other degradable peptide sequences specific for other tissue targets, and could thus provide a platform technology for disease-controlled delivery of biomolecules. In this particular design we explored Gly-Phe-Leu-Gly-Lys (GFLGK), a Cathepsin sensitive peptide as the degradable component of the photo-crosslinkable hydrogel material system. Two photo-crosslinkable configurations were evaluated: acrylate-poly(ethylene glycol)-GFLGK-poly(ethylene glycol)-acrylate (ACRL-PEG-GFLGK-PEG-ACRL) and poly(ethylene glycol)-diacrylate-GFLGK-diacrylate (PEGDA-GFLGK-DA). ACRL-PEG-GFLGK-PEG-ACRL was successfully synthesized and imprinted. Release studies revealed an enzyme-triggered release of DNA in the presence of Cathepsin B as expected. To create a tighter network, PEGDA-GFLGK-DA and a lower molecular weight PEGDA were utilized. PEGDA-GFLGK-DA hydrogels were successfully synthesized and imprinted. In order to estimate the pore size of the cross-linked peptide-PEG hydrogels for future release studies, swelling studies were performed using PEGDA.

1.2.2 Aim 2: To develop a nanoimprint lithography technique with a gentle harvesting method to fabricate and release drug delivery nanoparticles of specific size and shape (< 500 nm).

We hypothesized that utilizing semiconductor nanoimprint lithography techniques to pattern biocompatible polymers would enable us to fabricate monodisperse, injectable drug nanocarriers (50 - 400 nm) of precise shape and size suitable for intracellular drug delivery applications. With the development of such a method, we believe there is broad applicability to aid in further study of how nanoparticle shape and size affect delivery of drugs to tissues and cells within the body. Two methods were evaluated and optimized for imprinting of biocompatible polymers: Thermal Nanoimprint Lithography (ThNIL) and Step and Flash Imprint Lithography (SFIL). We demonstrated the use of ThNIL and SFIL, coupled with biocompatible materials, to fabricate monodisperse nanoparticles of pre-designed sizes and geometries as small as 50 nm. Particles of varying shape (square, circular, pentagonal, and triangular), size (50 - 400 nm), and composition Poly(methyl methacrylate) (PMMA), Poly(lactide-co-glycolide) (PLGA), PEG) were fabricated using these techniques. Furthermore, we have demonstrated full wafer imprinting and successful isolation and release of the particles from the wafer using a mild harvesting method. The SFIL method, with its low temperature and force applications, as well as wafer-scale imprinting capability, was more suitable for large scale fabrication and was chosen for further optimization.

1.2.3 Aim 3: To demonstrate enzymatic degradation and in-vitro stimuli-responsive drug release of nanoimprinted nanocarriers fabricated by combining the material system in Aim 1 and the nanoimprinting technique developed in Aim 2.

We hypothesized that after nanoimprinting, the stimuli-responsive material developed in Aim 1 would retain its ability to: a) degrade in the presence of the tumor-specific enzyme Cathepsin B, and b) would show an enzyme-responsive release of model drug only upon addition of the tumor-specific enzyme Cathepsin B. Upon imprinting with the PEGDA-GFLGK-DA developed in Aim 1 and exposure to Cathepsin B, we demonstrated enzymatic degradation of the photo-crosslinked material system. In order to show release of both a nucleic acid and a protein, plasmid DNA and a fluorescently-labeled IgG were each encapsulated in PEGDA-GLFLG-DA and imprinted. The release studies demonstrated successful retention of the model drug in the absence of tumor-specific enzymes (with a small amount of leakage) and an enzyme-triggered release of model drug upon the addition of Cathepsin B. After performing swelling studies on macroscale PEGDA polymers in Aim 1, we further explored the change in morphology of imprinted PEGDA nanocarriers before and after swelling.

1.2.4 Aim 4: To demonstrate bioactivity of model drugs encapsulated in nanoimprinted nanocarriers fabricated by combining the material system in Aim 1 and the nanoimprinting technique developed in Aim 2.

Because the SFIL process utilizes low temperature, low pressure, and standard UV illumination, we hypothesized that encapsulated model drugs such as proteins and nucleic acids would remain bioactive after undergoing the imprinting process. We performed bioactivity studies using proteins (streptavidin, trypsin, and luciferase) and DNA with either PEGDA or stimuli-responsive PEGDA-GFLGK-DA material systems. The streptavidin bioactivity study successfully demonstrated qualitative evidence that the streptavidin remains bioactive after imprinting, as well as etching. Both the luciferase and trypsin bioactivity studies showed limited quantitative bioactivity. We hypothesize that the limited bioactivity is due to the fact that these particles are not able to diffuse from the nanocarriers due to the small pore size. The DNA transfection studies have been unsuccessful due to a limitation in the ability to concentrate the DNA sufficiently and separate it from Cathepsin B. Though qualitative and quantitative bioactivity has been demonstrated, we further suggest ways to more accurately measure the bioactivity of these proteins and nucleic acids after imprinting.

1.3 OVERVIEW

The following *Chapter Two* discusses the background and significance of the research study with references to the latest developments in nanoparticle synthesis,

nanoimprint lithography, top-down approaches to nanoparticle formation, and studies on the effect of size and shape of nanoparticles on drug delivery. *Chapter Three* describes the synthesis and characterization of photo-crosslinked, PEG-peptide material systems suitable for use as nanoimprinted, enzyme-responsive nanocarriers. *Chapter Four* discusses the development of nanoimprint lithography techniques for fabrication of nanoparticles of specific size and shape. ThNIL and SFIL are evaluated, and a discussion of the optimization of the SFIL process for biopolymer imprinting follows. This chapter demonstrates the ability of the SFIL technique to create nanoparticles of precise size and shape as small as 50 nm. *Chapter Five* illustrates in-vitro drug release of DNA and proteins from a nanoimprinted enzyme-responsive biomaterial, and demonstrates enzyme mediated degradation. *Chapter Six* describes in-vitro bioactivity studies of DNA and proteins encapsulated in nanoimprinted biomaterials. The biotin-streptavidin bioactivity assay demonstrates qualitative evidence of bioactivity. Finally, the implications of the research are explained in *Chapter Seven* with conclusions and recommendations for future studies.

1.4 REFERENCES

1. Champion JA, Katare YK, Mitragotri S. Particle shape: a new design parameter for micro- and nanoscale drug delivery carriers. J Control Release 2007;121(1-2):3-9.
2. Ferrari M. Cancer nanotechnology: opportunities and challenges. Nat Rev Cancer 2005;5(3):161-171.
3. Nishiyama N. Nanomedicine: Nanocarriers shape up for long life. Nature Nanotech 2007;2(4):203-204.
4. Reddy ST, Rehor A, Schmoekel HG, Hubbell JA, Swartz MA. In vivo targeting of dendritic cells in lymph nodes with poly(propylene sulfide) nanoparticles. J Control Release 2006;112(1):26-34.
5. Kamath KR, Park K. Biodegradable hydrogels in drug delivery. Adv Drug Deliv Rev 1993;11(1-2):59-84.
6. Kikuchi A, Okano T. Pulsatile drug release control using hydrogels. Adv Drug Deliv Rev 2002;54(1):53-77.
7. Miyata T, Uragami T, Nakamae K. Biomolecule-sensitive hydrogels. Adv Drug Deliv Rev 2002;54(1):79-98.
8. Qiu Y, Park K. Environment-sensitive hydrogels for drug delivery. Adv Drug Deliv Rev 2001;53(3):321-339.
9. Geng Y, Dalhaimer P, Cai S, Tsai R, Tewari M, Minko T, et al. Shape effects of filaments versus spherical particles in flow and drug delivery. Nature Nanotech 2007;2(4):249-255.

10. Decuzzi P, Causa F, Ferrari M, Netti PA. The effective dispersion of nanovectors within the tumor microvasculature. Ann Biomed Eng 2006;34(4):633-641.

11. Decuzzi P, Ferrari M. The adhesive strength of non-spherical particles mediated by specific interactions. Biomaterials 2006;27(30):5307-5314.

12. Guan J, Ferrell N, James Lee L, Hansford DJ. Fabrication of polymeric microparticles for drug delivery by soft lithography. Biomaterials 2006;27(21):4034-4041.

13. Tao SL, Lubeley MW, Desai TA. Bioadhesive poly(methyl methacrylate) microdevices for controlled drug delivery. J Control Release 2003;88(2):215-228.

14. Rolland JP, Maynor BW, Euliss LE, Exner AE, Denison GM, DeSimone JM. Direct fabrication and harvesting of monodisperse, shape-specific nanobiomaterials. J Am Chem Soc 2005;127(28):10096-10100.

15. Glangchai LC, Caldorera-Moore M, Shi L, Roy K. Nanoimprint lithography based fabrication of shape-specific, enzymatically-triggered smart nanoparticles. J Control Release 2008;125(3):263-272.

16. Euliss LE, Welch CM, Maynor BW, Rolland JP, Denison GM, Gratton SE, et al. Monodisperse nanocarriers: novel fabrication of polymeric nanoparticles for bio-nanotechnology. Proc SPIE 2006;6153:61534A.

17. Gratton SEA, Pohlhaus PD, Lee J, Guo J, Cho MJ, Desimone JM. Nanofabricated particles for engineered drug therapies: a preliminary biodistribution study of PRINT nanoparticles. J Control Release 2007;121(1-2):10-18.

CHAPTER TWO

Background and Significance

2.1 Overview of Drug Delivery in Cancer Therapy

The American Cancer Society estimates that 1.4 million new cancer cases are diagnosed and 550,000 Americans die every year from cancer. Chemotherapy has been the main modality of treatment for cancer patients; however, its success rate remains low, primarily due to the inability to target and release drugs only within tumor tissues and cells. The goal of cancer therapy is to selectively destroy cancer cells, while leaving normal tissues intact. Targeting of the diseased tissues is achieved through passive targeting, avoidance of the reticuloendothelial system (RES) and targeting through the enhanced permeability and retention (EPR) effect, as well as through active tumor-specific targeting of tumor tissues and vasculature, as seen in **Figure 2.1** [1-5]. The initial stage in cancer drug delivery design is to create a system that avoids uptake by the phagocytic cells of the RES, thus avoiding clearance from the body and providing for longer systemic circulation. Commonly this involves surface modification of the delivery system to provide stealth characteristics [1, 2, 4]. Furthermore, one must take into account how the system will interact with the biology of the disease.

Although cancer cells are similar to normal tissue cells in many aspects, there are certain structural and behavioral differences that can be utilized for tumor-specific drug delivery. Tumor cells tend proliferate rapidly and undergo angiogenesis to create new

vasculature that supplies nutrients to the cancerous tissues. This rapid replication leads to the creation of leaky vasculature. Furthermore, tumor tissue tends to have poor lymphatic drainage. The combination of these factors allows high molecular weight (MW) molecules and nanoparticles to passively accumulate at higher concentration than in normal tissues, a concept called the enhanced permeability and retention effect (EPR) [1-7]. Besides passive tumor targeting, systems have been developed to actively target cancerous tissue by targeting the tumor cell surface, vasculature, angiogenesis and extracellular space. Common tumor-specific targeting methods involve receptor-ligand based targeting [1, 3, 4]. Site-specific targeting has the potential to reduce systemic toxicity by allowing drugs to accumulate specifically at tumor tissues.

Successful drug delivery to tumor cells only solves half of the challenge. For many chemotherapeutic agents that cannot permeate the cell membrane, the drug must be delivered inside the cell through receptor mediated endocytosis. When a ligand binds to a receptor on the tumor cell surface it can trigger uptake of the ligand-drug conjugate, or ligand-carrier conjugate, into the endocytic pathway. The drug initiates in the early endosome (pH 5.5-6.5 as compared to physiological pH 7.4) and ends up in the lysosome (pH 3.0-5.0). Throughout the pathway the drug must be protected from degradation by the some 40 proteases present [8, 9]. Furthermore, the drug must have some means of escaping the endosome either by diffusion or pH triggered membrane-destabilization [10].

Currently, chemotherapy and other anti-cancer treatments are targeted to diseased cells and tissues in-vivo, however significant amount of toxic drugs diffuse to normal

tissues during transport resulting in unwanted side-effects and may cause a patient to cease treatment. If cytotoxic agents could be targeted and released in response to a disease-specific signal, the agent could be preferentially delivered to a particular diseased tissue or cell, which could provide a significant improvement in morbidity and mortality and potentially reduce systemic side-effects of toxic drugs.

2.2 CURRENT NANOPARTICLE SYSTEMS IN DRUG DELIVERY

Nanoparticle-based delivery of therapeutics has been extensively studied in a variety of diseases and is considered to be an ideal platform for targeted intravenous and intracellular delivery of bioactive agents [11]. The goals of nanoparticulate design are to: prevent drug degradation or interaction with the body's environment, enhance drug absorption into tissues, control the biodistribution profile and improve penetration into cells [4]. Current concepts in the synthesis of drug nanocarriers primarily involve the use of natural or synthetic polymers or lipids to fabricate self-assembled or emulsion-based particles that are mostly spherical, polydisperse, and release drugs through diffusion or hydrolytic degradation [4]. **Table 2.1** provides an extensive overview of current nanoparticulate delivery system architectures.

Although various nanoparticle carrier designs have significantly improved, several challenges still remain. In polymeric nanoparticle-based delivery systems, bottom-up synthesis processes produce a large polydisperse population of particles whose physico-chemcial characteristics, drug release profiles, degradation kinetics and material

properties are hard to evaluate and reproduce. Lipid-based carriers tend to be rapidly cleared by the RES and suffer from instability and burst release [4]. Liposomes and most emulsion or micelle-based particle type carriers have limited encapsulation efficacy and rapid leakage of drug leading to loss of expensive drugs; however solid lipid nanoparticles have recently shown promise in encapsulating both proteins and water-soluble drugs [12, 13]. These diffusion/degradation-based delivery systems have fundamental limitations of non-linearity, difficulty in predicting in-vivo release kinetics and a lack of stimuli responsive release mechanisms resulting in systemic side-effects.

2.3 Significance of Smart Nanoparticle Drug Delivery Systems

Disease-responsive release is a key issue in 'intelligent' nanocarrier design. Intravenously injectable nanocarriers, that can efficiently deliver drugs or contrast agents to target tissues only in response to cellular or disease-specific signals, could significantly improve therapeutic and diagnostic care of complex diseases [14, 15]. Despite current efforts to target drug nanoparticles and liposomal drug carriers to diseased cells in-vivo, significant amounts of toxic drugs diffuse to normal tissues during transport [16-19]. If the encapsulated cargo can be released preferentially at a particular diseased tissue or cell or inside a specific cellular compartment, it could provide significant improvement in patient compliance, especially for highly toxic chemotherapeutic drugs or for molecules with short half-life.

Stimuli-sensitive hydrogels have been developed in 'smart' drug delivery systems to sense environmental changes and induce a structural change on their own. PH-sensitive hydrogels, have been developed to swell in response to a change in pH from physiological conditions, and biomolecule-sensitive hydrogels have been used to deliver drugs when in contact with glucose or specific antigens [20-40]. There are also hydrogels that are sensitive to temperature, light, magnetic field and ultrasound [41-43].

Although stimuli-responsive release mechanisms are well established for macroscale devices and hydrogels [41-43], reports on nanocarriers incorporating environmental- or disease-triggered release of drugs are limited to only pH-responsive systems, which still reveal a large distribution in diameter [44-49]. Polymer-based pro-drugs combine multiple functionalities [50-57]; however, they do not allow for simultaneous delivery of multiple agents (drugs, contrast agents etc.). With current concepts, the inherent complexity of a bottom-up synthetic approach makes it difficult to achieve multiple functionalities such as targeting, loading multiple agents, and incorporating stimuli-sensitive properties in a single nanocarrier. Although significant progress has been made in polymeric or liposomal drug delivery systems, there remain critical limitations in synthesizing nanocarriers with highly controllable architecture that can, at the same time, impart environmentally-triggered release mechanisms.

2.4 Significance of Nanoparticle Size and Shape in Drug Delivery

Particle size has a large impact on the biodistribution, clearance and uptake of nanoparticles within the body and dictates the way in which particles can be administered [58]. While particles below 500 nm in size can be injected intravenously, only those below 200 nm are efficiently internalized by somatic cells. In fact, delivery efficiency of therapeutics inside cells as well as intravenous delivery to tissues and organs, especially tumors, increases with sub-100 nm particles [59-62]. Particles smaller than 100 nm are typically recognized less by the mononuclear phagocytic system (MPS) (synonymous with the RES), can circulate longer in the blood stream, and have efficient diffusion into the vasculature of diseased tissue [11]. Recent reports also suggest that delivery into the lymphatic circulation require particles that are even smaller in size (< 50 nm) [63].

As well as size, recent reports suggest that particle shape could play a significant role in the in-vivo performance of delivery vehicles [58, 64]. Specifically, shape and shape-related form factors, like aspect ratio or edges, affect particle transport characteristics, influence cell-particle interactions, and alter drug release kinetics [58, 65]. Ferrari and colleagues have shown through theoretical modeling that shape and size of nanovectors and spherical and spheroidal nanoparticles can significantly affect how particles interact with tumor capillaries during transport [66, 67]. Ferrari and colleagues concluded that there is a critical radius necessary for a larger number of nanovectors (hollow nanotubes) to reach tumor vessels, and that vectors of different diameters would need to be fabricated in order to specifically target drug nanocarriers to specific locations within the body [66]. Furthermore, spheroidal particles must circulate through small

capillaries, thus there is a limit to the aspect ratio of a spheroidal particle such that transport through the vasculature is not blocked and blood flow is not altered. Ferrari and colleagues further demonstrate, through mathematical modeling, that spheroidal particles can have larger volumes than spherical particles with the same probability of adhesion to a target tumor cell. They calculate that spheroidal particles with 2 to 1 aspect ratios could potentially be able to carry 50 times as much drug as 500 nm spherical particles with the same probability of adhesion (same adhesive strength); thus a higher dose of drug could be achieved at a target site. This is based on the derived formula:

$$V_{opt}(\gamma) = \alpha(\gamma)\left(\frac{m_r}{\mu S}\right)^{\beta}$$

where V_{opt} is the optimal volume, γ is the aspect ratio, m_r is the surface density of receptors, and μS is the shear stress at the capillary walls. The equation was shown to approximate independent experimental data by a separate group [67].

Discher and colleagues demonstrated that self-assembled, filamentous particles with very high aspect ratios (less than 100 nm diameter with several microns in length) have unique long-circulating properties compared to traditional spherical liposomes [64, 67]. In order to study the effect of shape on circulation time, filomecelles with varying lengths were injected into mice. Filomecelles with lengths greater than 8 μm circulated in-vivo for up to one week, while comparable PEGylated vesicles circulated for two days. To test the filomecelles as cancer drug delivery vehicles, they were loaded with paclitaxel and injected into mice. Discher and colleagues demonstrated that with an eightfold increase in length, they were able to achieve an equivalent increase in dose, and they

demonstrated a decrease in overall tumor size. This study verifies the model by Ferrari and colleagues by showing a larger dose capability with non-spherical particles [67].

Until recently, particle shape has been an unexplored area of research in drug delivery due to our inability to reliably synthesize nano or microparticle carriers with precise and pre-designed geometry. However, several groups have demonstrated the ability to create such particles using techniques varying from microfluidics, self-assembly and photopolymerization [58]. **Figure 2.2** provides a broad overview of the current capabilities to create micro and nanoparticles of specific shape. Whitesides and colleagues have demonstrated the ability to create monodisperse microparticles utilizing microfluidics techniques [68]. Monodisperse liquid droplets were formed using a microfluidic device and shaped in a microchannel. Subsequently the drops were solidified in situ by photopolymerization or other means to form non-spherical particles. **Figure 2.2D** demonstrates a micro-rod fabricated using these methods.

Dendukuri and colleagues have also demonstrated the ability to make particles of non-spherical particles using a similar technique, **Figure 2.2A** [69]. Subsequently the same group fabricated poly(ethylene glycol) diacrylate (PEGDA) particles combining microfluidics techniques with photolithography, **Figure 2.2E** [70]. Sozzani and colleagues have used a direct pattern transfer with a silica mold to create poly(styrene) (PS) and poly(methyl methacrylate) PMMA microparticles with gyroidal, tubular and hollow cylindrical shapes, as shown in **Figure 2.2C** [71]. Velev and colleagues have used self assembly to create poly(styrene) donuts, as shown in **Figure 2.2B** [72]. All of the before-mentioned groups, as well as more, are using new techniques to create

particles of various geometries [58,73]; however, the micron-sized dimensions of the particles created from these techniques are not suitable for intracellular delivery.

There are in fact only a few methods that have been developed to fabricate particles with varying shape, especially at the nanoscale. Recently, Mitragotri and colleagues reported unique solvent-based methods to generate poly(styrene) micro and nanoparticles of various shapes with feature sizes as low as 60 nm [74]. Spherical nanoparticles were suspended in an aqueous solution of PVA and cast into films. Subsequently, various shaped particles were created using a technique that involved: a) suspending liquefying spherical particles in heat (120-150^{o}C) or solvent, b) stretching the particles into a film, c) re-solidifying particles using solvent extraction or cooling and d) dissolving the film. It remains to be studied how these methods are translated to biopolymers and whether other features, like stimuli-responsiveness, can be incorporated. DeSimone and colleagues have recently demonstrated top-down nanofabrication to create nanoparticles of specific size and shape, as shown in **Figure 2.2D** [75].

2.5 TOP-DOWN MICROFABRICATION APPROACHES IN DRUG DELIVERY

In order to provide a unique approach to creating drug delivery particles with a pre-designed geometry and/or multiple functionalities, a new field of research has focused on top-down manufacturing approaches such as soft-lithography, micromolding and imprinting [76-80]. Several groups have successfully used top-down micro-fabrication techniques to create drug delivery microparticles, as shown in **Figure 2.3**.

Desai and colleagues initially reported bioadhesive microparticles fabricated using bulk micromachining and photolithography to create silicon and poly(methyl methacrylate) (PMMA) microcontainers, respectively. The silicon microcontainers were 50 μm with 25 μm reservoirs, and the PMMA microcontainers were 150 μm with 80 μm reservoirs. The PMMA devices underwent surface modification through avidin–biotin chemistry to attach targeting ligands (e.g. lectins) and thus targeted the GI tract for oral delivery [81-83].

Subsequently the same group demonstrated multi-layer fabrication of SU-8 epoxy, gelatin, and poly(lactide-co-glycolide) (PLGA) microparticles using a micromolding technique [84]. A poly(dimethyl siloxan) (PDMS) mold was used as a stamp to create microcontainers that were 150 μm in size with 70 - 80 μm reservoirs. Furthermore, a second layer of 10 μm posts were fabricated on top of the initial layer. **Figure 2.3A-B** demonstrates the stamped and released microcontainers fabricated from PMMA and SU-8. **Figure 2.3C** demonstrates the ability to create a tri-layered microparticle. The fabrication method for all polymers involved heating to at or above 65^{o}C, which could pose a problem for encapsulation of proteins.

Recently, Hansford and colleagues reported fabrication of PLGA and poly(ethylene glycol) dimethacrylates (PEGDMA) microparticles using soft lithography [85]. For the fabrication of PLGA microparticles, a PDMS stamp was dipped in PLGA/acetone solution and inverted onto a silicon wafer with poly(vinyl alcohol) PVA. The temperature was increased to 80^{o}C in order to mold the PLGA and the microparticles subsequently released in water. To fabricate PEGDMA microparticles, the

PEGDMA/water solution was brushed onto the PDMS stamp. The stamp was then exposed to UV light to crosslink the PEGDMA. Subsequently the stamp was inverted onto a silicon wafer with PVA and released in water. **Figure 2.3D-G** shows the microfabricated particles of varying size and shape before and after release. They report fabricating microparticles down to 6 μm; however there is little control over specific shape at that size with their current method.

Considerable innovation has gone into developing micro-fabrication approaches to drug delivery; however these systems are too large for systemic and intracellular applications and have not yet demonstrated stimuli-responsive mechanisms. Microfabricated particles can be used for delivery by ingestion, inhalation, and injection into tissue. To be released into circulation, microparticles must be smaller than 10 μm [86]. Although much research has been performed on micro-fabrication of microparticles, the field of nanofabricated devices capable of intracellular drug delivery and imaging is a nascent field.

2.6 NANOIMPRINT LITHOGRAPHY TECHNIQUES

Several recent advancements in nanomanufacturing methods could provide new approaches for top-down, high-throughput, large-scale fabrication of nanocarriers for drug delivery applications. One of the most promising nanoimprinting techniques is the step and flash imprint lithography (SFIL) method invented by Wilson and colleagues at UT Austin. The SFIL process [87-93], shown in **Figure 2.4**, is essentially a nanomolding

process in which the topography of a template defines the patterns created on a substrate. In brief, a transparent quartz template is treated with a release agent to facilitate substrate separation. Next, a low viscosity, UV curable, organosilicon monomer is dispensed onto a silicon substrate. The gap between the template and substrate is closed, using low pressure at room temperature. Following this, the quartz template is irradiated with UV light. The transparency of the quartz allows the UV light to pass through and photopolymerize the monomer beneath the template. When the template is separated from the substrate, the cured monomer on the substrate retains the desired 3D nanotopography. Further processing with oxygen plasma cleaning removes residual monomer for distinct features. Nanofeatures created using SFIL can be seen in **Figure 2.5**.

SFIL has several advantages over conventional lithography and micromolding processes. First, SFIL is only limited by the resolution of the imprint template created by e-beam lithography. Recent work has demonstrated 20 nm lines using the SFIL process **Figure 2.5B**. Traditional micromolding requires high pressures (> 10 MPa) and temperatures (> glass transition temperature of the polymer film), which may distort nanofeatures. SFIL uses a low-viscosity (~ 2-3 cps), photocurable, monomer that allows high resolution features to be imprinted at room temperature with minimal pressure (< 1 psi). Furthermore, the reusable transparent quartz template enables sub-10 nm alignment of nanofeatures, a task very difficult in other processes. Finally, 3D structures can accurately be replicated by the SFIL process, and patterns can be imprinted on top of existing topography by using an appropriate planarization material, as shown in **Figure**

2.5C-D. The ability for three-dimensional nanopatterning is particularly useful for biomedical applications [94], in particular for fabricating nanocontainers/particles for drug delivery [95].

Another nanoimprint method for fabricating nanoscale features is thermal nanoimprint lithography. First proposed in 1995 by SY Chou [96, 97], the process consists of imprinting with a reusable template and pattern transfer with RIE. However, in contrast to SFIL, thermal nanoimprint lithography requires heating a polymer above its glass transition temperature and applying considerably more pressure. Upon cooling, the polymer hardens into a desired 3D nanotopography. As with SFIL, this method is advantageous in that its resolution is limited only by the template fabrication process and it is capable of replicating precise 3D features.

2.7 Significance of Nanoimprint Fabrication in Drug Delivery

Nanofabrication techniques for biomedical applications have the potential to create well-defined and characterized drug delivery devices without the limitations of current methods. A top-down approach would ensure precise control of particle size, shape, and geometry, and would provide a monodisperse population of carriers, yielding better reproducibility and prediction of properties. Furthermore, this approach avoids high shear and mechanical forces typical for emulsion-based encapsulation, thus improving encapsulation efficiency and possibly improving drug stability. In addition, top-down manufacturing would allow for easy fabrication/incorporation of multiple

properties such as targeting and triggered release of drug in response to a stimulus. This approach could allow for the manufacturing of carriers that deliver toxic or unstable therapeutic compounds on demand to targeted organs in the body, while reducing systemic side-effects and providing for simultaneous monitoring of therapeutics and device.

Furthermore, the creation of size and shape-specific particles could allow for a controllable study of the affects that size and shape have on particle transport characteristics, influence cell-particle interactions, and alter drug release kinetics. Finally, top-down manufacturing provides a novel, high-throughput, and highly automated method for fabricating drug delivery devices. Since most of the top-down manufacturing processes are already well established and applicable in large industrial scales, the overall cost of development for such nanofabricated delivery devices could be significantly less than any novel bottom-up synthesis approach.

2.8 CURRENT TOP-DOWN NANOFABRICATION-BASED SYSTEMS IN DRUG DELIVERY

Recently, DeSimone and colleagues reported the ability to form nano-size PEG diacrylate (PEGDA) and poly(lactic acid) (PLA) particles using a particle nano-replication (PRINT) method, similar to nanoimprint lithography [75, 98]. Unlike many soft lithography or imprint lithography techniques, DeSimone and colleagues utilized a photocurable perfluoropolyether (PFPE) stamp that is non-wetting to both inorganic and organic materials. Thus, formation of particles without a residual film between them was

accomplished. To fabricate PLA particles, PLA was in-situ polymerized at 110^{o}C to mold the polymer solution. PEG particles were formed by imprinting and photopolymerization. **Figure 2.6A-D** demonstrates PEG particles fabricated in trapezoidal, conical, bar and arrow shapes with sizes ranging from 200 nm to 3 μm. Furthermore encapsulation of avidin-FITC and doxorubicin in PEG particles was demonstrated. **Figures 2.6G** shows fluorescence confocal images of encapsulated doxorubicin in 500 nm particles.

In any fabrication process involving therapeutics or biologics, harvesting of nanoparticles into a usable form is of considerable importance. A major limitation in the PRINT fabrication process is the mechanism of particle harvesting. Currently, the PRINT particles are harvested from the wafer either using physical scraping with surgical blades (as shown in **Figure 2.6E**) [75] or by shear force using a glass slide (as shown in **Figure 2.6F**) [99], both of which could damage the particles and may not be suitable for large scale manufacturing. Recently, DeSimone and colleagues have reported preliminary in-vitro and in-vivo studies using 200 nm PEG triacrylate particles [99]. The particles in the study were measured in their dry-state to have a width of 201 ± 10 nm and a height of 155 ± 10 nm. Using dynamic light-scattering the polydispersity of the particles remained at 234 ± 12 nm over the course of 6 hours at 37^{o}C. For in-vivo studies, PRINT particles were injected in a bolus dose into the tail of a healthy mouse. The particles were cleared rapidly from the blood, but otherwise appeared to be in agreement with liposomes in regards to biocompatibility and distribution.

Although nanoparticle synthesis was demonstrated using the PRINT method, stimuli-responsive nanoparticle fabrication has not been demonstrated. Top-down

nanofabrication methods to generate particles with precise size and shape that also incorporate environmentally-triggered drug release are yet to be reported, especially at the sub-100 nm range.

2.9 BIOCOMPATIBLE POLYMERS FOR TOP-DOWN FABRICATION

Currently only a few types of polymeric material have be used to make micro and nanofabricated drug delivery devices. The knowledge of the types of patternable polymers can allow us to choose from them the ones with properties (biocompatibility, biodegradability, and mechanical robustness) suitable for specific drug delivery applications.

2.9.1 Poly(methyl methacrylate) (PMMA)

PMMA has been previously used by Desai and co-workers to micro-fabricate oral drug delivery devices [81-83]. It is commonly used in such biomedical applications as bone cement and intraocular lenses [100, 101]. PMMA is biocompatible with a hydrophilic surface that can easily be modified for incorporation of targeting ligands and provides high resolution features in photolithography, e-beam lithography, and nanoimprint lithography techniques [96, 97]. Furthermore, it is a high strength material with good mechanical stability necessary to retain the shape and integrity of the nano-containers. Although PMMA is non-biodegradable it has been used to create nanospheres that have shown a prolonged half-life in circulation in mice [2, 102].

2.9.2 Poly(ethylene glycol) (PEG)

PEG is widely regarded as an extremely biocompatible polymer and has numerous uses in biomedical applications, including: drug delivery, tissue engineering, pro-drug design, tissue sealants, and nanoparticle surface modification. PEG has been shown to provide stealth characteristics, increase drug circulation time and to reduce nonspecific attachment or uptake by the RES (ie. less recognized by the macrophages of the mononuclear phagocyte system (MPS)) [11, 103-105]. PEG-based materials are also non-fouling and prevent protein adsorption to material or carrier surfaces [106-108]. In drug delivery, PEG-conjugation to nanoparticle surfaces (e.g. liposomes) has been shown to protect against particle clearance in blood, thus generating long-circulating carriers [109, 110]. Hansford and Colleagues and DeSimone and colleagues have both demonstrated successful imprinting and releasing of PEG-based microparticles using photopolymerization [75, 85].

2.9.3 Poly(lactide-co-glycolide) (PLGA)

PLGA is one of the most widely used biodegradable polymers in drug delivery, with other applications in tissue engineering and surgical sutures. Nanoimprinting-based fabrication would provide a novel method to synthesize PLGA-based carriers with precise size and shape for degradation controlled release. Desai and Hansford's groups have shown successful creation of PLGA microparticles using top-down approaches [84, 85]. Furthermore DeSimone and colleagues have successfully imprinted PLGA using the PRINT technique [75].

By synergizing the knowledge of top-down fabrication techniques with concepts from biomaterials and nanoparticle drug delivery systems surveyed from literature, this dissertation discusses development of nanoimprint lithography techniques to create monodisperse, injectable nanocarriers of specific sizes, shapes, and functionalities (i.e., stimulus responsiveness) with a gentle harvesting method.

Figure 2.1 Schematic of Passive and Active Targeting of Tumor Tissues and Cells. *Reprinted by permission from Macmillan Publishers Ltd: [Nature Nanotechnology] (4), copyright (2007).*

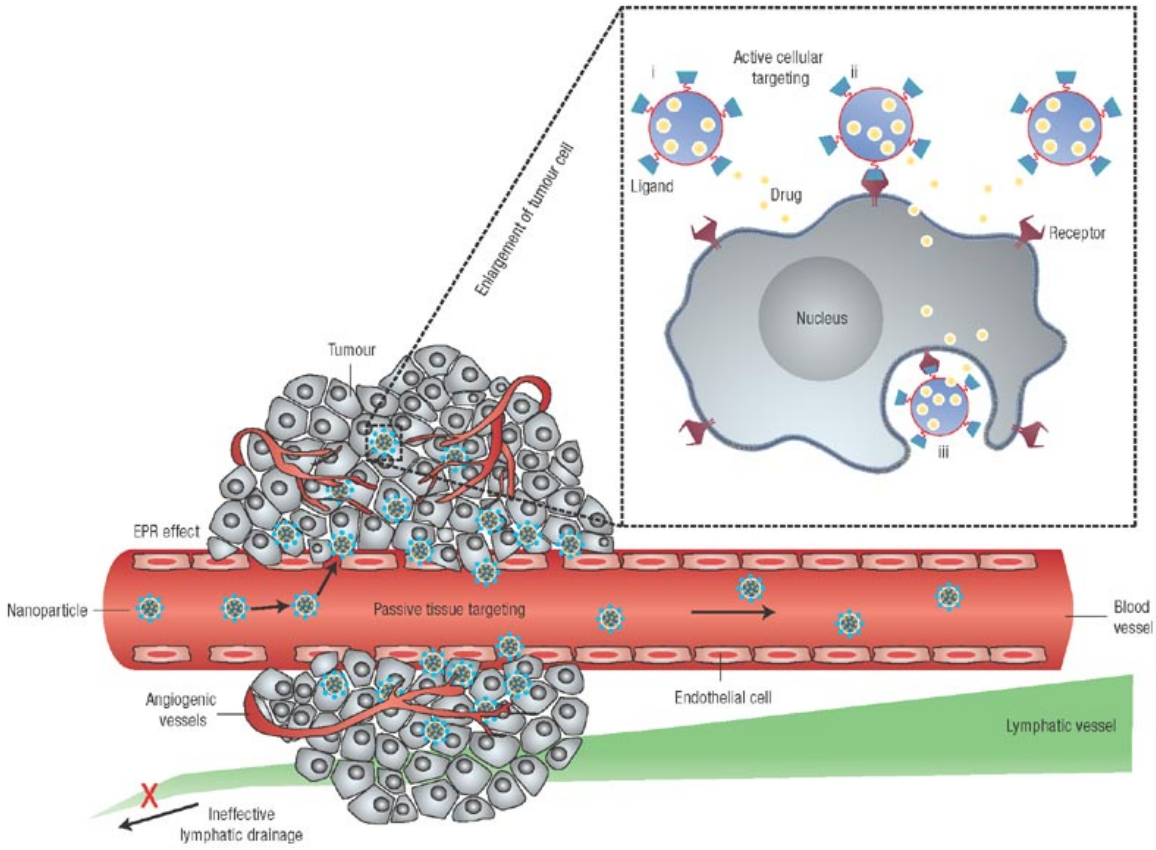

Table 2.1 Overview of Current Nanoparticulate Drug Carriers. *Table courtesy of Pharmaceutical Technology Europe magazine.*

Nanoparticulate drug carrier	Main component	Definition and comments[2,3]	Schematic representation and size range (diameter)
Solid lipid nanoparticles	Lipid	Particles formed with solid lipids.	160–220 nm
Lipid nanocapsules	Lipid	Reservoir-type particules containing an oil droplet.	50–200 nm
Polyplexe	Polycations* (PEI, Chitosan) + nucleic acids	Polyelectrolyte complex between polycation and nucleic acids, which are polyanions.	<80 nm 
Polymer micelles	Copolymers	Particles resulting from the self-assembling of polymer chains from copolymers composed of hydrophobic and hydrophilic moieties. These particles have a hydrophobic core and are stabilized by hydrophilic chains (mainly polyethylene glycol) surrounded by the hydrophobic core. The core of the micelle can be a polyplexe when one part of the copolymer is a polycation complexed with nucleic acids to form the micelle.	10–100 nm 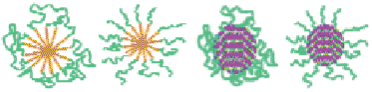
Nanoparticle	Polymers* (PACA, PCL, PLA, PLGA) or corresponding copolymers with PEG* or chitosan	Polymer particles with a diameter in the nanometer range. The whole volume of the particle is occupied by the polymer, which is generally insoluble in water.	80–300 nm 
Oil-containing nanocapsules	Polymers and oil	Reservoir-type particles encapsulating an oil droplet surrounded by a polymer envelope.	50–400 nm 
Water-containing nanocapsule	Polymer and water	Reservoir-type particles encapsulating a water droplet.	50–200 nm 
Nanogel	Polymer (chitosan, alginate) and water	Polymer network swollen by water-forming particles in the nanometer size range.	200–400 nm 
Stealth carrier	At present: mainly copolymers or lipids containing PEG*	Nanoparticulate drug carrier will reduce recognition by the immuno system and enhance circulation persistence after intravenous administration. It is possible to attach ligands to target specific cell types and obtain a drug-targeted system.	The size depends on the type of carrier 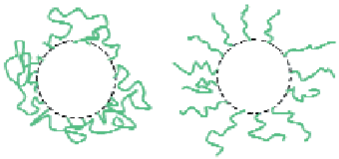 PEG* loops and trains PEG* or polysaccharides brush
Targeted carrier	Stealth carrier + pilot molecules: transferrin, antibody, folate, carbohydrates, aptamer	Mainly Stealth nanoparticulates drug carrier with a targeting ligand grafted on the surface.	The size depends on the type of carrier 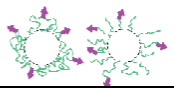

Figure 2.2 **Non-spherical Micro and Nanoparticles: (A) microparticles created using microfluidics [35][*1], (B) donut-shaped PS particles created using self-assembly [38][*2], (C) gyroidal particles created using a silica mold [37][*3], (D) micro-rods created using microfluidics [34][*4], (E) tear-drop shaped PEG microparticles created using microfluidics combined with photolithography [36][*5], (F) conical PEG particles created using the PRINT process [40].[*6]** *Overall figure reprinted from J Control Release, 121, J. A. Champion, Y. K. Katare, and S. Mitragotri, 3-9, 2007, with permission from Elsevier.*

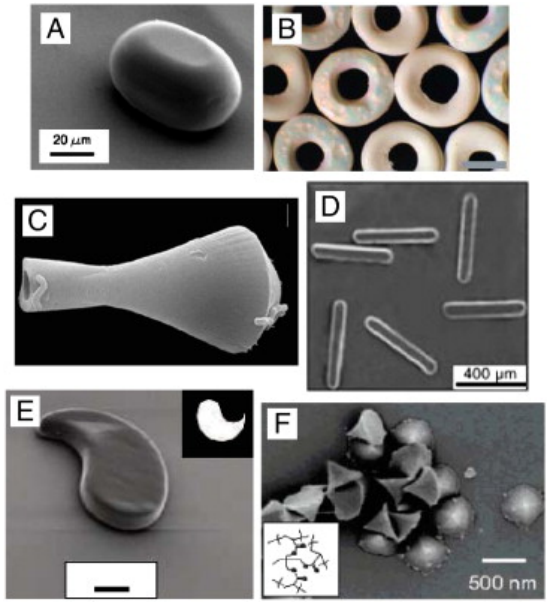

[*1] *Reprinted with permission from (35). Copyright (2005) American Chemical Society.*

[*2] *From [O. D. Velev, A. M. Lenhoff, and E. W. Kaler. A class of microstructured particles through colloidal crystallization. Science 287: 2240–2243(2000)]. Reprinted with permission from AAAS.*

[*3] *Reprinted by permission from Macmillan Publishers Ltd: [Nature Materials] (37), copyright (2006).*

[*4] *Reproduced with permission from S. Q. Xu, Z. H. Nie, M. Seo, P. Lewis, E. Kumacheva, H. A. Stone, P. Garstecki, D. B. Weibel, I. Gitlin, and G. M. Whitesides: Generation of monodisperse particles by using microfluidics: control over size, shape, and composition. 2005. 44. 724-728. Copyright Wiley-VCH Verlag GmbH & Co. KGaA.*

[*5] *Reprinted by permission from Macmillan Publishers Ltd: [Nature Materials] (36), copyright (2006).*

[*6] *Reprinted by permission from (40). Copyright (2005) American Chemical Society.*

Figure 2.3 Top-down Microfabricated Drug Delivery Microparticles: (A) PMMA microcontainers [44] [*1], (B) released SU-8 microcontainers [44] [*1], (C) profilometer side profile of tri-layered SU-8 microcontainers [44] [*1], (D) cross-shaped PEG microparticles [45] [*2], (E) released cross-shaped PEG particles [45] [*2], (F) square-shaped PLGA microparticles [45] [*2], and G) square-shaped PLGA microparticles [45].[*2]

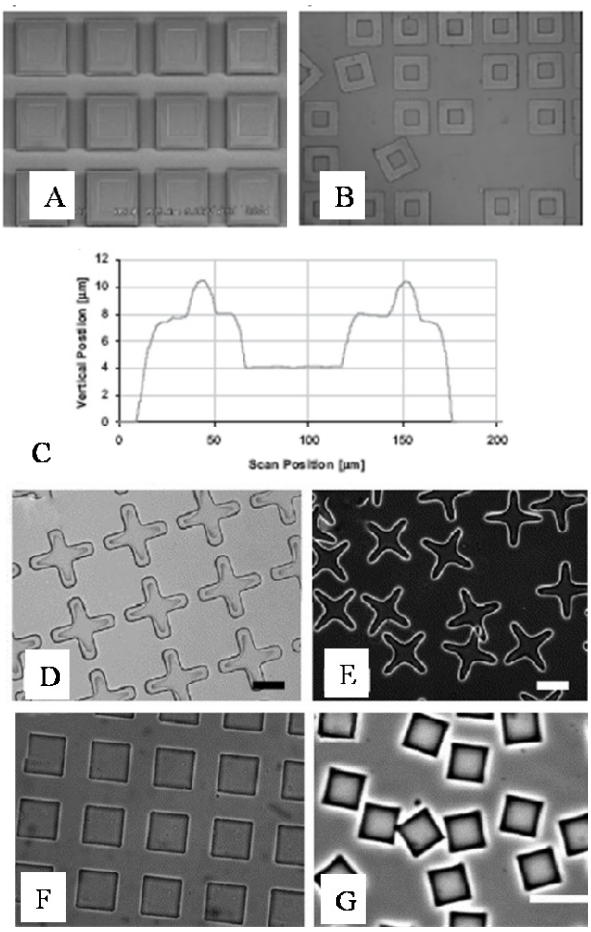

[*1] *Reproduced with permission from S. L. Tao and T. A. Desai: Microfabrication of multilayer, asymmetric, polymeric devices for drug delivery. 2005. 17. 1625-1630. Copyright Wiley-VCH Verlag GmbH & Co. KGaA.*

[*2] *Reprinted from Biomaterials, 27, J. Guan, N. Ferrell, L.J. Lee, and D.J. Hansford, 4034-4041, 2006, with permission from Elsevier.*

Figure 2.4 Schematic of Step and Flash Imprint Lithography (SFIL). *Reprinted from I. McMackin, P. Schumaker, D. Babbs, J. Choi, W. Collison, S. V. Sreenivasan, N. Schumaker, M. Watts, and R. Voisin, Design and Performance of a Step and Repeat Imprinting Machine Proc SPIE, Emerging Lithographic Technologies VII, 5037, 2003, with permission from SPIE and S. V. Sreenivasan.*

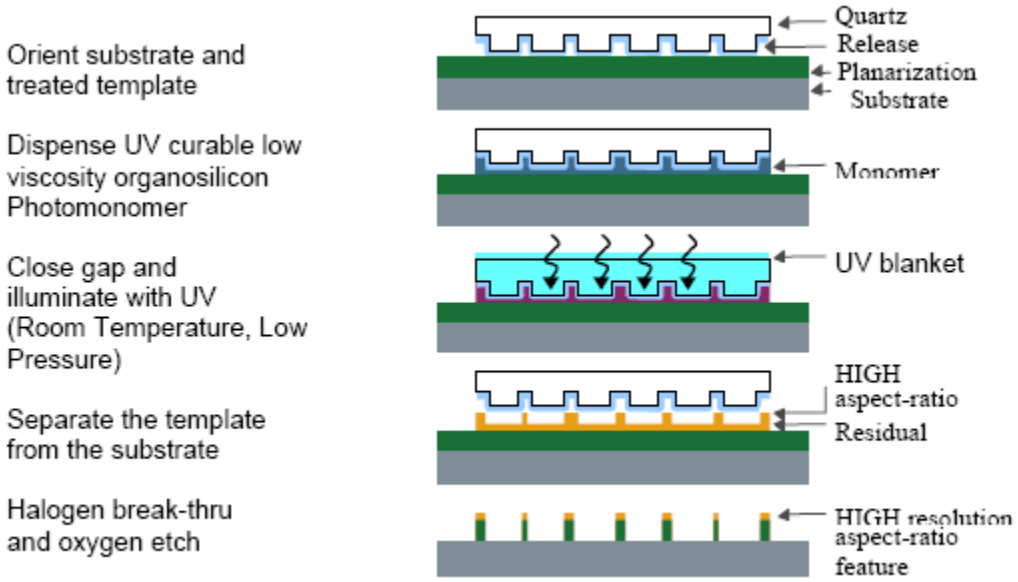

Figure 2.5 Three-dimensional Nano-topographies Created Using SFIL: (A) 50 nm dense lines [51][*1] (B) 20 nm spaced lines [51][*1], (C) 60 nm posts [51][*1], (D) multi-tiered structure (E) - (F) multi-tiered imprint profiles [52].[*2]

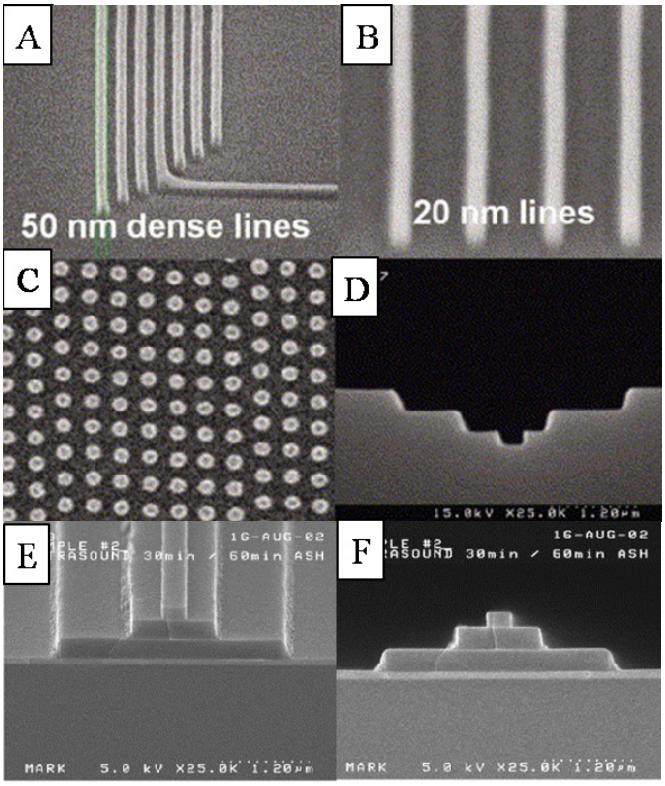

[*1] *Reproduced with permission from D. J. Resnick, S.V. Sreenivasan and C. G. Willson: Microfabrication Step & flash imprint lithography. 2005. 8. 34-42. Copyright Wiley-VCH Verlag GmbH & Co. KGaA.*

[*2] *Reproduced with permission from S. Johnson, D. J. Resnick, D. Mancini, K. Nordquist, W. J. Dauksher, K. Gehoski, J. H. Baker, L. Dues, A. Hooper, T. C. Bailey, S. V. Sreenivasan, J. G. Ekerdt and C. G. Willson: Fabrication of multi-tiered structures on step and flash imprint lithography templates. 2003. 67-68. 221-228. Copyright Wiley-VCH Verlag GmbH & Co. KGaA.*

Figure 2.6 **PRINT Particle Fabrication: (A) 200 nm trapezoidal PEG particles [40][*1], (B) 200 x 800 nm PEG bar particles [40][*1], (C) 500 nm conical PEG particles [40][*1], (D) 3 μm arrow PEG particles [40][*1], (E) isolated 200 nm trapezoidal triacrylate particles harvested mechanically with a doctor blade [40][*1], (F) 200 nm PEG particles released using a glass slide and acetone [57][*2] (G) fluorescent confocal micrograph of conical PEG particles containing doxorubicin [40].[*1].**

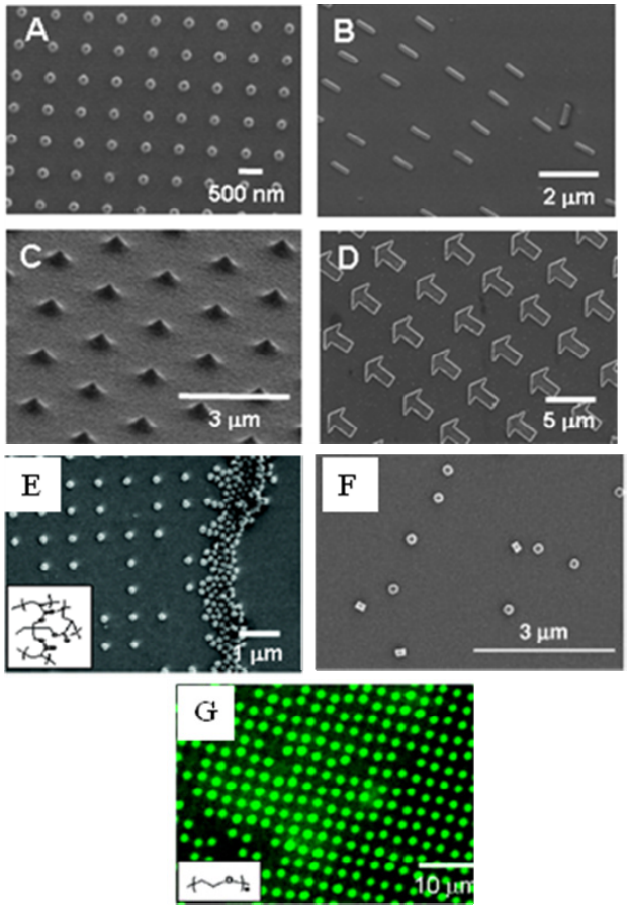

[*1] *Reprinted by permission from (40). Copyright (2005) American Chemical Society.*
[*2] *Reprinted from J Control Release, 121, S. E. Gratton, P. D. Pohlhaus, J. Lee, J. Guo, M. J. Cho, and J. M. DeSimone, 10-18, 2007, with permission from Elsevier.*

2.10 REFERENCES

1. Brannon-Peppas L, Blanchette JO. Nanoparticle and targeted systems for cancer therapy. Adv Drug Deliv Rev 2004;56(11):1649-1659.
2. Brigger I, Dubernet C, Couvreur P. Nanoparticles in cancer therapy and diagnosis. Adv Drug Deliv Rev 2002;54(5):631-651.
3. Page M, editor. Tumor targeting in cancer therapy. Totowa, NJ: Humana Press Inc., 2002.
4. Peer D, Karp JM, Hong S, Farokhzad OC, Margalit R, Langer R. Nanocarriers as an emerging platform for cancer therapy. Nature Nanotech 2007;2(12):751-760.
5. Vasir JK, Reddy MK, Labhasetwar VD. Nanosystems in drug targeting: opportunities and challenges. Curr Nanosci 2005;1:47-64.
6. Maeda H, Sawa T, Konno T. Mechanism of tumor-targeted delivery of macromolecular drugs, including the EPR effect in solid tumor and clinical overview of the prototype polymeric drug SMANCS. J Control Release 2001;74(1-3):47-61.
7. Maeda H, Wu J, Sawa T, Matsumura Y, Hori K. Tumor vascular permeability and the EPR effect in macromolecular therapeutics: a review. J Control Release 2000;65(1-2):271-284.
8. Asokan A, Cho MJ. Exploitation of intracellular pH gradients in the cellular delivery of macromolecules. J Pharm Sci 2002;91(4):903-913.

9. Hoffman AS, Stayton PS, Press O, Murthy N, Lackey CA, Cheung C, et al. Design of 'smart' polymers that can direct intracellular drug delivery. Polym Adv Technol 2002;13(10-12):992-999.

10. Murthy N, Campbell J, Fausto N, Hoffman AS, Stayton PS. Bioinspired pH-responsive polymers for the intracellular delivery of biomolecular drugs. Bioconjug Chem 2003;14(2):412-419.

11. Moghimi SM, Hunter AC, Murray JC. Nanomedicine: current status and future prospects. Faseb J 2005;19(3):311-330.

12. Wong HL, Bendayan R, Rauth AM, Li Y, Wu XY. Chemotherapy with anticancer drugs encapsulated in solid lipid nanoparticles. Adv Drug Deliv Rev 2007;59(6):491-504.

13. Almeida AJ, Souto E. Solid lipid nanoparticles as a drug delivery system for peptides and proteins. Adv Drug Deliv Rev 2007;59(6):478-490.

14. Ferrari M. Cancer nanotechnology: opportunities and challenges. Nat Rev Cancer 2005;5(3):161-171.

15. Farokhzad OC, Langer R. Nanomedicine: developing smarter therapeutic and diagnostic modalities. Adv Drug Deliv Rev 2006;58(14):1456-1459.

16. Noble CO, Kirpotin DB, Hayes ME, Mamot C, Hong K, Park JW, et al. Development of ligand-targeted liposomes for cancer therapy. Expert Opin Ther Targets 2004;8(4):335-353.

17. Park JW, Benz CC, Martin FJ. Future directions of liposome-and immunoliposome-based cancer therapeutics. Semin Oncol 2004;31(6):196-205.

18. Park JW, Hong K, Kirpotin DB, Papahadjopoulos D, Benz CC. Immunoliposomes for cancer treatment. Adv Pharmacol 1997;40:399-435.

19. Kreuter J. Influence of the surface properties on nanoparticle-mediated transport of drugs to the brain. J Nanosci Nanotechnol 2004;4(5):484-488.

20. Byrne ME, Hilt JZ, Peppas NA. Recognitive biomimetic networks with moiety imprinting for intelligent drug delivery. J Biomed Mater Res A 2008;84A(1):137-147.

21. Byrne ME, Park K, Peppas NA. Molecular imprinting within hydrogels. Adv Drug Deliv Rev 2002;54(1):149-161.

22. Bell CL, Peppas NA. Water, solute and protein diffusion in physiologically responsive hydrogels of poly(methacrylic acid-g-ethylene glycol). Biomaterials 1996;17(12):1203-1218.

23. Berger J, Reist M, Mayer JM, Felt O, Peppas NA, Gurny R. Structure and interactions in covalently and ionically crosslinked chitosan hydrogels for biomedical applications. Eur J Pharm Biopharm 2004;57(1):19-34.

24. Besheer A, Wood KM, Peppas NA, Mader K. Loading and mobility of spin-labeled insulin in physiologically responsive complexation hydrogels intended for oral administration. J Control Release 2006;111(1-2):73-80.

25. Brannon-Peppas L, Peppas NA. Dynamic and equilibrium swelling behaviour of pH-sensitive hydrogels containing 2-hydroxyethyl methacrylate. Biomaterials 1990;11(9):635-644.

26. Khare AR, Peppas NA. Release behavior of bioactive agents from pH-sensitive hydrogels. J Biomat Sci-Polym E 1993;4(3):275-289.

27. Kim B, Peppas NA. Synthesis and characterization of pH-sensitive glycopolymers for oral drug delivery systems. J Biomat Sci-Polym E 2002;13:1271-1281.

28. Kim B, Peppas NA. In vitro release behavior and stability of insulin in complexation hydrogels as oral drug delivery carriers. Int J Pharm 2003;266(1-2):29-37.

29. Lowman AM, Morishita M, Kajita M, Nagai T, Peppas NA. Oral delivery of insulin using pH-responsive complexation gels. J Pharm Sci 1999;88(9):933-937.

30. Lowman AM, Peppas NA. Solute transport analysis in pH-responsive, complexing hydrogels of poly(methacrylic acid-g-ethylene glycol). J Biomat Sci-Polym E 1999;10:999-1009.

31. Nakamura K, Maitani Y, Lowman AM, Takayama K, Peppas NA, Nagai T. Uptake and release of budesonide from mucoadhesive, pH-sensitive copolymers and their application to nasal delivery. J Control Release 1999;61(3):329-335.

32. Nakamura K, Murray RJ, Joseph JI, Peppas NA, Morishita M, Lowman AM. Oral insulin delivery using P(MAA-g-EG) hydrogels: effects of network morphology on insulin delivery characteristics. J Control Release 2004;95(3):589-599.

33. Oral E, Peppas NA. Responsive and recognitive hydrogels using star polymers. J Biomed Mater Res A 2004;68A(3):439-447.

34. Peppas NA. Devices based on intelligent biopolymers for oral protein delivery. Int J Pharm 2004;277(1-2):11-17.

35. Peppas NA, Huang Y. Polymers and Gels as Molecular Recognition Agents. Pharm Res 2002;19(5):578-587.

36. Peppas NA, Kavimandan NJ. Nanoscale analysis of protein and peptide absorption: Insulin absorption using complexation and pH-sensitive hydrogels as delivery vehicles. European J Pharm Sci 2006;29(3-4):183-197.

37. Podual K, Doyle FJ, Peppas NA. Glucose-sensitivity of glucose oxidase-containing cationic copolymer hydrogels having poly(ethylene glycol) grafts. J Control Release 2000;67(1):9-17.

38. Podual K, Doyle Iii FJ, Peppas NA. Dynamic behavior of glucose oxidase-containing microparticles of poly(ethylene glycol)-grafted cationic hydrogels in an environment of changing pH. Biomaterials 2000;21(14):1439-1450.

39. Serra L, Domenech J, Peppas NA. Drug transport mechanisms and release kinetics from molecularly designed poly(acrylic acid-g-ethylene glycol) hydrogels. Biomaterials 2006;27(31):5440-5451.

40. Vakkalanka SK, Brazel CS, Peppas NA. Temperature- and pH-sensitive terpolymers for modulated delivery of streptokinase. J Biomat Sci-Polym E 1997;8:119-129.

41. Miyata T, Uragami T, Nakamae K. Biomolecule-sensitive hydrogels. Adv Drug Deliv Rev 2002;54(1):79-98.

42. Qiu Y, Park K. Environment-sensitive hydrogels for drug delivery. Adv Drug Deliv Rev 2001;53(3):321-339.

43. Peppas NA, Bures P, Leobandung W, Ichikawa H. Hydrogels in pharmaceutical formulations. Eur J Pharm Biopharm 2000;50(1):27-46.

44. Blanchette J, Peppas NA. Oral chemotherapeutic delivery: design and cellular response. Ann Biomed Eng 2005;33(2):142-149.

45. Blanchette J, Peppas NA. Cellular evaluation of oral chemotherapy carriers. J Biomed Mater Res A 2005;72A(4):381-388.

46. Foss AC, Goto T, Morishita M, Peppas NA. Development of acrylic-based copolymers for oral insulin delivery. Eur J Pharm Biopharm 2004;57(2):163-169.

47. Torres-Lugo M, Garcia M, Record R, Peppas NA. pH-Sensitive hydrogels as gastrointestinal tract absorption enhancers: transport mechanisms of salmon calcitonin and other model molecules using the Caco-2 cell model. Biotechnol Prog 2002;18(3):612-616.

48. Shenoy D, Little S, Langer R, Amiji M. Poly(ethylene oxide)-modified poly(beta-amino ester) nanoparticles as a pH-sensitive system for tumor-targeted delivery of hydrophobic drugs: part 2. In vivo distribution and tumor localization studies. Pharm Res 2005;22(12):2107-2114.

49. Na K, Bae YH. Self-assembled hydrogel nanoparticles responsive to tumor extracellular pH from pullulan derivative/sulfonamide conjugate: characterization, aggregation, and adriamycin release in vitro. Pharm Res 2002;19(5):681-688.

50. Lu ZR, Shiah JG, Sakuma S, Kopeckova P, Kopecek J. Design of novel bioconjugates for targeted drug delivery. J Control Release 2002;78(1-3):165-173.

51. Peterson CM, Shiah JG, Sun Y, Kopeckova P, Minko T, Straight RC, et al. HPMA copolymer delivery of chemotherapy and photodynamic therapy in ovarian cancer. Adv Exp Med Biol 2003;519:101-123.

52. Kopecek J, Kopeckova P, Minko T, Lu Z. HPMA copolymer-anticancer drug conjugates: design, activity, and mechanism of action. Eur J Pharm Biopharm 2000;50(1):61-81.

53. Kovar M, Kovar L, Subr V, Etrych T, Ulbrich K, Mrkvan T, et al. HPMA copolymers containing doxorubicin bound by a proteolytically or hydrolytically cleavable bond: comparison of biological properties in vitro. J Control Release 2004;99(2):301-314.

54. Ulbrich K, Etrych T, Chytil P, Jelinkova M, Rihova B. HPMA copolymers with pH-controlled release of doxorubicin: in vitro cytotoxicity and in vivo antitumor activity. J Control Release 2003;87(1-3):33-47.

55. Ulbrich K, Subr V. Polymeric anticancer drugs with pH-controlled activation. Adv Drug Deliv Rev 2004;56(7):1023-1050.

56. Ulbrich K, Subr V, Strohalm J, Plocova D, Jelinkova M, Rihova B. Polymeric drugs based on conjugates of synthetic and natural macromolecules. I. Synthesis and physico-chemical characterisation. J Control Release 2000;64(1-3):63-79.

57. Rihova B, Jelinkova M, Strohalm J, Subr V, Plocova D, Hovorka O, et al. Polymeric drugs based on conjugates of synthetic and natural macromolecules. II. Anti-cancer activity of antibody or (Fab')(2)-targeted conjugates and combined therapy with immunomodulators. J Control Release 2000;64(1-3):241-261.

58. Champion JA, Katare YK, Mitragotri S. Particle shape: a new design parameter for micro- and nanoscale drug delivery carriers. J Control Release 2007;121(1-2):3-9.

59. Couvreur P, Vauthier C. Nanotechnology: intelligent design to treat complex disease. Pharm Res 2006;23(7):1417-1450.

60. Torchilin VP. Recent advances with liposomes as pharmaceutical carriers. Nat Rev Drug Discov 2005;4(2):145-160.

61. Hobbs SK, Monsky WL, Yuan F, Roberts WG, Griffith L, Torchilin VP, et al. Regulation of transport pathways in tumor vessels: role of tumor type and microenvironment. Proc Natl Acad Sci USA 1998;95(8):4607-4612.

62. Yuan F, Dellian M, Fukumura D, Leunig M, Berk DA, Torchilin VP, et al. Vascular permeability in a human tumor xenograft: molecular size dependence and cutoff size. Cancer Res 1995;55(17):3752-3756.

63. Reddy ST, Rehor A, Schmoekel HG, Hubbell JA, Swartz MA. In vivo targeting of dendritic cells in lymph nodes with poly(propylene sulfide) nanoparticles. J Control Release 2006;112(1):26-34.

64. Geng Y, Dalhaimer P, Cai S, Tsai R, Tewari M, Minko T, et al. Shape effects of filaments versus spherical particles in flow and drug delivery. Nature Nanotech 2007;2(4):249-255.

65. Nishiyama N. Nanomedicine: nanocarriers shape up for long life. Nature Nanotech 2007;2(4):203-204.

66. Decuzzi P, Causa F, Ferrari M, Netti PA. The effective dispersion of nanovectors within the tumor microvasculature. Ann Biomed Eng 2006;34(4):633-641.

67. Decuzzi P, Ferrari M. The adhesive strength of non-spherical particles mediated by specific interactions. Biomaterials 2006;27(30):5307-5314.

68. Xu S, Nie Z, Seo M, Lewis P, Kumacheva E, Stone HA, et al. Generation of monodisperse particles by using microfluidics: control over size, shape, and composition. Angew Chem Int Ed Engl 2005;44(5):724-728.

69. Dendukuri D, Tsoi K, Hatton TA, Doyle PS. Controlled synthesis of nonspherical microparticles using microfluidics. Langmuir 2005;21(6):2113-2116.

70. Dendukuri D, Pregibon DC, Collins J, Hatton TA, Doyle PS. Continuous-flow lithography for high-throughput microparticle synthesis. Nat Mater 2006;5(5):365-369.

71. Sozzani P, Bracco S, Comotti A, Simonutti R, Valsesia P, Sakamoto Y, et al. Complete shape retention in the transformation of silica to polymer micro-objects. Nat Mater 2006;5(7):545-551.

72. Velev OD, Lenhoff AM, Kaler EW. A class of microstructured particles through colloidal crystallization. Science 2000;287(5461):2240-2243.

73. Losi E, Bettini R, Santi P, Sonvico F, Colombo G, Lofthus K, et al. Assemblage of novel release modules for the development of adaptable drug delivery systems. J Control Release 2006;111(1-2):212-218.

74. Champion JA, Katare YK, Mitragotri S. Making polymeric micro- and nanoparticles of complex shapes. Proc Natl Acad Sci USA 2007;104(29):11901-11904.

75. Rolland JP, Maynor BW, Euliss LE, Exner AE, Denison GM, DeSimone JM. Direct fabrication and harvesting of monodisperse, shape-specific nanobiomaterials. J Am Chem Soc 2005;127(28):10096-10100.

76. Peppas NA, Huang Y. Nanoscale technology of mucoadhesive interactions. Adv Drug Deliv Rev 2004;56(11):1675-1687.

77. Peppas NA, Ward JH. Biomimetic materials and micropatterned structures using iniferters. Adv Drug Deliv Rev 2004;56(11):1587-1597.

78. Lu Y, Aguilar CA, Chen S. Shaping biodegradable polymers as nanostructures: Fabrication and applications. Drug Discov Today 2005;2(1):97-102.

79. Lu Y, Chen SC. Micro and nano-fabrication of biodegradable polymers for drug delivery. Adv Drug Deliv Rev 2004;56(11):1621-1633.

80. Betancourt T, Brannon-Peppas L. Micro-and nanofabrication methods in nanotechnological medical and pharmaceutical devices. Int J Nanomedicine 2006;1(4):483-495.

81. Ahmed A, Bonner C, Desai TA. Bioadhesive microdevices with multiple reservoirs: a new platform for oral drug delivery. J Control Release 2002;81(3):291-306.

82. Tao SL, Lubeley MW, Desai TA. Bioadhesive poly(methyl methacrylate) microdevices for controlled drug delivery. J Control Release 2003;88(2):215-228.

83. Tao SL, Lubeley MW, Desai TA. Synthesis of cytoadhesive poly(methylmethacrylate) for applications in targeted drug delivery. J Biomed Mater Res A 2003;67(2):369-375.

84. Tao SL, Desai TA. Microfabrication of multilayer, asymmetric, polymeric devices for drug delivery. Adv Mater 2005;17(13):1625-1630.

85. Guan J, Ferrell N, James Lee L, Hansford DJ. Fabrication of polymeric microparticles for drug delivery by soft lithography. Biomaterials 2006;27(21):4034-4041.

86. LaVan DA, McGuire T, Langer R. Small-scale systems for in vivo drug delivery. Nat Biotechnol 2003;21(10):1184-1191.

87. Resnick DJ, Dauksher WJ, Mancini D, Nordquist KJ, Bailey TC, Johnson S, et al. Imprint lithography for integrated circuit fabrication. J Vac Sci Technol B 2003;21(6):2624-2631.

88. Johnson SC, Bailey TC, Dickey MD, Smith BJ, Kim EK, Jamieson AT, et al. Advances in Step and Flash imprint lithography. Proc SPIE 2003;5037:197-202.

89. Johnson S, Resnick DJ, Mancini D, Nordquist K, Dauksher WJ, Gehoski K, et al. Fabrication of multi-tiered structures on step and flash imprint lithography templates. Microelectron Eng 2003;67-68:221-228.

90. Colburn M, Johnson SC, Stewart MD, Damle S, Bailey TC, Choi B, et al. Step and flash imprint lithography: a new approach to high-resolution patterning. Proc SPIE 1999;3676:379-389.

91. Choi BJ, Meissl MJ, Colburn M, Bailey TC, Ruchhoeft P, Sreenivasan SV, et al. Layer-to-layer alignment for step and flash imprint lithography. Proc SPIE 2001;4343:436-442.

92. McMackin I, Schumaker P, Babbs D, Choi J, Collison W, Sreenivasan SV, et al. Design and performance of a step and repeat imprinting machine. Proc SPIE 2003;5037:178-186.

93. Resnick DJ, Sreenivasan SV, Willson CG. Step & flash imprint lithography. Mater Today 2005;8(2):34-42.

94. Gaubert HE, Frey W. Highly parallel fabrication of nanopatterned surfaces with nanoscale orthogonal biofunctionalization imprint lithography. Nanotechnology 2007;18(13):135101.

95. Glangchai LC, Caldorera-Moore M, Shi L, Roy K. Nanoimprint lithography based fabrication of shape-specific, enzymatically-triggered smart nanoparticles. J Control Release 2008;125(3):263-272.

96. Chou SY, Krauss PR. Imprint lithography with sub-10 nm feature size and high throughput. Microelectron Eng 1997;35(1):237-240.

97. Chou SY, Krauss PR, Renstrom PJ. Imprint lithography with 25-nanometer resolution. Science 1996;272(5258):85-87.

98. Euliss LE, Welch CM, Maynor BW, Rolland JP, Denison GM, Gratton SE, et al. Monodisperse nanocarriers: novel fabrication of polymeric nanoparticles for bio-nanotechnology. Proc SPIE 2006;6153:61534A.

99. Gratton SEA, Pohlhaus PD, Lee J, Guo J, Cho MJ, Desimone JM. Nanofabricated particles for engineered drug therapies: a preliminary biodistribution study of PRINT nanoparticles. J Control Release 2007;121(1-2):10-18.

100. Johnston RC. Acrylic bone cement: clinical development and current status in North America. Orthop Clin North Am 2005;36(1):75-84.

101. Doan KT, Olson RJ, Mamalis N. Survey of intraocular lens material and design. Curr Opin Ophthalmol 2002;13(1):24-29.

102. Lode J, Fichtner I, Kreuter J, Berndt A, Diederichs JE, Reszka R. Influence of surface-modifying surfactants on the pharmacokinetic behavior of 14C-poly (methylmethacrylate) nanoparticles in experimental tumor models. Pharm Res 2001;18(11):1613-1619.

103. Owens Iii DE, Peppas NA. Opsonization, biodistribution, and pharmacokinetics of polymeric nanoparticles. Int J Pharm 2006;307(1):93-102.

104. Gref R, Luck M, Quellec P, Marchand M, Dellacherie E, Harnisch S, et al. 'Stealth' corona-core nanoparticles surface modified by polyethylene glycol (PEG): influences of the corona (PEG chain length and surface density) and of the core composition on phagocytic uptake and plasma protein adsorption. Colloid Surf B 2000;18(3-4):301-313.

105. Vonarbourg A, Passirani C, Saulnier P, Benoit JP. Parameters influencing the stealthiness of colloidal drug delivery systems. Biomaterials 2006;27(24):4356-4373.

106. Kishida A, Mishima K, Corretge E, Konishi H, Ikada Y. Interactions of poly(ethylene glycol)-grafted cellulose membranes with proteins and platelets. Biomaterials 1992;13(2):113-118.

107. Merrill EW, Salzman EW. Polyethylene oxide as a biomaterial. ASAIO J 1983;6(2):60-64.

108. Sharma S, Desai TA. Nanostructured antifouling poly(ethylene glycol) films for silicon-based microsystems. J Nanosci Nanotechnol 2005;5(2):235-243.

109. Awasthi VD, Garcia D, Goins BA, Phillips WT. Circulation and biodistribution profiles of long-circulating PEG-liposomes of various sizes in rabbits. Int J Pharm 2003;253(1-2):121-132.

110. Lian T, Ho RJ. Trends and developments in liposome drug delivery systems. J Pharm Sci 2001;90(6):667-680.

CHAPTER THREE

Photo-crosslinked, PEG-peptide Material Systems for use as Nanoimprinted, Enzyme-responsive Nanocarriers

3.1 INTRODUCTION

For the care of complex disorders, such as cancer, disease-responsive release is a key issue in the design of drug delivery carriers. The ability to efficiently deliver drugs or contrast agents to target tissues in response to a patient's therapeutic need could significantly improve therapeutic and diagnostic care of such diseases [1, 2]. Due to their biocompatibility and flexibility in design, hydrogels have been widely used in the biomedical field and in drug delivery. Hydrogels are three-dimensional crosslinked hydrophilic polymer networks that can imbibe large amounts of water. Hydrogels can protect drugs from the environment and control drug release [3]. Stimuli-sensitive hydrogels have been developed in 'smart' drug delivery systems to sense environmental changes and induce a structural change on their own [3-9]. For diseases that require a bolus dose of drug at a target location, such as for cancer therapy, enzymatically degradable hydrogel membranes could be advantageous. The use of enzyme-responsive membranes could allow degradation to be localized to tissues where the enzyme is present, while little or no diffusion of the drug would occur in the absence of the enzyme. The key issue would be to fabricate the membrane such that there is little or no diffusion of the drug through it in the absence of enzyme-triggered degradation.

A series of enzymatically degradable hydrogels have been extensively reported by West and coworkers and also by Hubbell and colleagues [10-12]. These hydrogels were developed to mimic the extracellular matrix and were specifically designed with a peptide linkage that dissolved in the presence of tissue-specific enzymes (e.g., collagenase, elastase or matrix metalloproteinases (MMPs)). Hubbell and colleagues reported highly specific enzyme-controlled release of recombinant human bone morphogenetic protein (rhBMP) from peptide-functionalized, enzymatically degradable poly(ethylene glycol) (PEG) hydrogels [11]. They demonstrated that PEG-peptide hydrogels (10% w/v) did not allow a significant release of entrapped rhBMP; however, with the addition of enzyme, a rapid burst release of rhBMP occurred (**Figure 3.1A**). West and coworkers demonstrated concentration dependent enzyme-controlled release using a PEG-peptide-PEG hydrogel (20% w/v) and various concentrations of peptide-specific enzymes (collagenase or elastase) [12]. They reported no hydrogel degradation in the absence of enzyme and were able to achieve rapid degradation upon optimization of enzyme concentration (**Figure 3.1B**). The key relevance of these studies is the possibility that similar peptide-functionalized, enzyme-degradable hydrogels could be used to control drug release from nano-fabricated devices.

The overall goal of this chapter is to develop a stimuli-responsive peptide-functionalized PEG material system that has: (a) little or no diffusion of the drug through it in the absence of enzyme-triggered degradation, and (b) the ability to be nanoimprinted. In this research we have developed an enzyme-responsive PEG hydrogel, using a Cathepsin sensitive peptide, Gly-Leu-Phe-Gly-Lys (GFLGK), as the degradable

component of a photo-crosslinkable material system. GFLG is a tetra-peptide sequence that has been widely used as a spacer in tumor-targeted polymer-drug conjugates [13-19]. This peptide cross linker can degrade in the presence of several lysosomal thiol proteases, especially cysteine proteases such as cathepsins B, H, L, and C [14, 18, 20-26]. Of the 11 cysteine cathepsins in the human genome, cathepsins B, L, and H are by far the most abundant [27-29]. GFLG is particularly sensitive to Cathepsin B [20, 22, 30], which is over-expressed in lung, ovarian and colorectal tumor cells and is present extracellularly in tumor tissues [26, 31-38]. Cathepsin B levels in tumor cells and tissues of patients with specific cancers are significantly elevated (2 to 50 times over-expression) and have been directly related to their prognosis [31, 32, 35, 39-44]. In addition, based on information from the ExPASy (**Ex**pert **P**rotein **A**nalysis **Sy**stem) proteomics server of the Swiss Institute of Bioinformatics (SIB), the other major human enzymes that can degrade GFLG include digestive enzymes such as chymotrypsin, trypsin, or pepsin. For intravenous, parenteral or intranasal delivery, those enzymes are not encountered and the sequence should be highly specific for cysteine cathepsins.

Because previous studies using GFLG as a spacer in drug-polymer conjugates have shown enzymatic degradability, we hypothesized that using GFLGK as an enzyme-degradable linker in a PEG-based material system would cause an enzyme-triggered release of drug in the presence of Cathepsin B. Two photo-crosslinkable configurations were evaluated: Acrylate-poly(ethylene glycol)-GFLGK-poly(ethylene glycol)-acrylate (ACRL-PEG-GFLGK-PEG-ACRL) and poly(ethylene glycol)-diacrylate-GFLGK-diacrylate (PEGDA-GFLGK-DA), as shown in **Figure 3.2A-B**. Both material systems

were successfully synthesized and imprinted. Release studies revealed an enzyme-triggered release of DNA in the presence of Cathepsin B as expected.

A primary design criterion of the material system is that it should allow drug release upon enzymatic degradation and that there should be minimal diffusion of drugs through the membrane beforehand. To create a tighter network, PEGDA-GFLGK-DA and a lower molecular weight PEG were utilized. In order to estimate the mesh size of the cross-linked peptide-PEG hydrogels for future release studies, swelling studies were performed on PEGDA.

3.2 MATERIALS AND METHODS

3.2.1 Polymers and Reagents

The peptide sequence Gly-Phe-Leu-Gly-Lys (GFLGK) (MW 527) was synthesized at ICMB Protein Facility at UT Austin and GFLGK (MW 520.6) was purchased from Bachem. Triethylamine, dimethylacetamide, acryloyl chloride, and n-heptane were purchased from Sigma-Aldrich. Acrylate-PEG-N-Hydroxy-succinamide (ACRL-PEG-NHS, MW 3400) and poly(ethylene glycol) diacrylate (PEGDA, MW 3400) were purchased from Nektar Therapeutics. Poly(ethylene glycol) diacrylate (PEGDA, MW 700) was purchased from Sigma Aldrich and poly(ethylene glycol) diacrylate (PEGDA, MW 1000) was purchased from Polysciences. Sodium bicarbonate and phosphate buffered saline (PBS, pH 7.4) were purchased from Sigma Aldrich. The ultraviolet (UV) photoinitiator, 2-hydroxy-1-[4-(hydroxyethoxy) phenyl]-2-methyl-1

propanone (I2959) was purchased from Ciba Geigy. Plasmid DNA, pgWiz β-galactosidase (8500 bps) was purchased from Aldevron. The Picogreen assay was purchased from Invitrogen. Cathepsin B from bovine spleen was purchased from Sigma Aldrich. Relmat (Molecular Imprints) was supplied by the NNIN and MRC at the University of Texas Pickle Research Center. Four inch p-type <100> silicon test wafers single-side polished were ordered from Silicon Quest International.

3.2.2 Conjugation of ACRL-PEG-NHS and GFLGK

The peptide sequence, GFLGK (MW 527), was reacted ACRL-PEG-NHS. The primary (alpha) amine of Glycine (G) and the primary amine of Lysine (K) at either end of the peptide molecule react with the N-Hydroxy-succinamide (NHS) groups of two hetero-bifunctional PEG chains, i.e. each peptide molecule cross-links two PEG molecules [45-46]. This creates a 2:1 molar reaction (ACRL-PEG-NHS:GFLGK) to form ACRL-PEG-GFLGK-PEG-ACRL (a homo-bifunctional PEG diacrylate), as illustrated in **Figure 3.3**. Specifically, the peptide was dissolved to a final concentration of 1 mg/mL in 50 m*M* sodium bicarbonate buffer, pH 8.2. Separately, the ACRL-PEG-NHS was also dissolved in 50 m*M* sodium bicarbonate buffer, pH 8.2. The PEG solution (300 μL) was then added one drop at a time into the peptide solution and reacted at room temperature for 2-3 hours [45-46]. Next the unconjugated ACRL-PEG-NHS and free peptides were removed by dialysis (Spectrum* Spectra/Por* 5000 MWCO dialysis tubing, Fischer Scientific) in deionized water. The solution was dialyzed for 4 hours at room temperature and then overnight at 4°C with periodic changing of buffer followed by lyophilization of

the sample. Matrix-assisted laser desorption/ionization time-of-flight (MALDI-TOF) mass spectrometry (Perspectives Biosystems Voyager) and H1 NMR were used to verify conjugation and removal of unconjugated material.

3.2.3 Photopolymerization of PEG-GFLGK-PEG and PEGDA

The lyophilized ACRY-PEG-GFLGK-PEG-ACRL was dissolved in dH_2O to form a (100% w/v) solution. PEGDA (MW 3400) was dissolved in dH_2O to form various weight percentages ranging from 25% to 100% (w/v). The ultraviolet (UV) photoinitiator, I2959, was first dissolved in dH_2O to a concentration of 0.7% (w/v) to ensure complete solubility. Subsequently the photoinitiator was added to the polymer solution at concentrations of 0.07 wt %, to generate free radicals to in order to induce chain polymerization. A thin film of the polymerized hydrogel was formed by dispensing specific volumes of the polymer solution onto substrates and placing them under a UV lamp (365 nm, intensity ~ 4 mW/cm^2, Blak-Ray Lamp, Ted Pella Inc.) for 10 to 20 minutes depending on the volume of solution dispensed. The photopolymerization process used is similar to that described by the Hubbell and Anseth groups [45-48].

3.2.4 Acrylation of GFLGK

3.2.4.1 Acrylation of GFLGK in Dimethylacetamide

The peptide sequence GFLGK was acrylated at the primary (alpha) amine of Glycine (G) and the primary amine of Lysine (K) at either end of the peptide sequence using acryloyl chloride as described previously by Hubbell, West, and Healy [49, 50].

Figure 3.4 shows a schematic of the reaction. 30 mg of peptide was dissolved in 1.2 mL of dimethylacetamide (DMAc) with equimolar triethylamine, and a 2-fold molar excess of acryloyl chloride was added drop wise while stirring. The reaction temperature was kept at 0-5°C. After adding all of the acryloyl chloride, the solution continued to stir for 4 h at 0-5°C and 20 h at room temperature. Subsequently the solution was rotovapped under vacuum in a water bath at 40ºC, and rotated at 103 rpm at a 45º angle, for 1-2 hours. The resulting concentrate was dialyzed (Spectrum* Spectra/Por* 500 MWCO Float-A-Lyzer dialysis tube, Spectrum Labs) for 48 hours in dH_2O and lyophilized over night. Acrylation of the free amine groups in the peptide sequence was analyzed with a 1H NMR spectrometer; and the spectra recorded in D_2O at room temperature.

3.2.4.2 Acrylation of GFLGK in dH_2O

Acrylation of the peptide sequence GFLGK was based on the previously described method using water as a solvent. 25 mg of GFLGK powder was dissolved into 2 mL of de-ionized water. A ten-fold molar excess of triethylamine and acryloyl chloride was added drop-wise to the dissolved peptide solution while stirring. The reaction was kept under nitrogen for 4 hours at 0-5^{o}C while stirring and then 20 hours at room temperature. Following this, the solution was filtered, dialyzed and lyophilized as previously described. Successful acrylation was analyzed using proton NMR.

3.2.5 Direct photopolymerization of PEGDA-GFLGK-DA

PEGDA and GFLGK-DA were dissolved in dH_2O in a 1:1 molar ratio to form varying concentration (% (w/v)) PEGDA-GFLGK-DA solutions. The ultraviolet (UV)

photoinitiator, I2959, was first dissolved in dH_2O to a concentration of 0.7% (w/v) to ensure complete solubility. Subsequently the photoinitiator was added to the polymer solution at concentrations of 0.05 wt % or 0.07 wt %, to generate free radicals in order to induce chain polymerization**.**

3.2.6 Evaluation of Enzyme-Responsive Release

3.2.6.1 Evaluation of PEG-GFLGK-PEG Release

The enzyme specific release kinetics of encapsulated plasmid DNA, pgWiz β-galactosidase (8500 bps), from a photo-crosslinked PEG-GFLGK-PEG homo-bifunctional network (100% w/v) was evaluated in vitro. The experiment was performed in duplicate with 40 μL hydrogels in 0.01 *M* PBS solution (pH 7.4) with 0.18% plasmid DNA (w/w of polymer). The DNA loaded hydrogels were rinsed, placed in 2mL tubes in PBS buffer (1 mL), and placed on a shaker in an incubator at 37^{o}C for the duration of the study. At various time intervals (2 hrs, 4 hrs, 6 hrs, 8 hrs, 12 hrs, 24 hrs, 48 hrs, 72 hrs), buffer samples were collected. At each time point 100 μL of buffer was removed and 100 μL of fresh buffer was replaced. At the 72 hour time point, the entire PBS buffer solution was removed from the samples. Then a 1 mL solution of Cathepsin B (10 U/mL in PBS pH 5) was added to each sample, in agreement with previous studies performed with Cathepsin B [51, 52]. The samples were returned to the incubator and at various time intervals buffer samples were collected. Each time 100 μL of enzyme solution was

removed, and 100 μL of fresh enzyme solution was replaced. The amount of plasmid DNA released into buffer was measured for each time point using the NanoDrop.

3.2.6.2 Evaluation of PEGDA-GFLGK-DA Release

The enzyme specific release kinetics of encapsulated plasmid DNA, pgWiz β-galactosidase (8500 bps), from a PEGDA-GFLGK-DA hydrogel (100% w/v) (PEGDA MW 1000) was evaluated in vitro. The experiment was performed in duplicate with 20 μL hydrogels in 0.01 *M* PBS solution (pH 7.4) with 0.18% plasmid DNA (w/w of polymer). The DNA loaded hydrogels were placed in 2 mL tubes in PBS buffer (1 mL), and were then placed on a shaker in an incubator at 37^{o}C for the duration of the study. At various time intervals (2 hrs, 4 hrs, 6 hrs, 8 hrs, 12 hrs, 24 hrs, 48 hrs, 72 hrs), buffer samples were collected. At each time point 100 μL of buffer was removed and 100 μL of fresh buffer was replaced. At the 72 hr time point, the entire PBS buffer solution was removed from the samples. Then a 1mL solution of Cathepsin B (10 U/mL in PBS pH 5) was added to each sample**.** The samples were returned to the incubator and at various time intervals buffer samples were collected. Each time 100 μL of enzyme solution was removed, and 100 μL of fresh enzyme solution was replaced. The amount of plasmid DNA released into the buffer was measured using a Picogreen Assay, an ultra-sensitive fluorescent nucleic acid stain used for quantification of double stranded DNA, and a fluorescence plate reader (DTX 880, Beckman Coulter).

3.2.7 PEGDA and PEGDA-GFLGK-DA Hydrogel Swelling Studies

3.2.7.1 PEGDA Hydrogel Swelling Experiment

PEGDA (MW 700) was dissolved in dH_2O to form various weight percentages ranging from 25%, 33%, 50%, 60% and 75% w/v. The ultraviolet (UV) photoinitiator, I2959, was first dissolved in dH_2O to a concentration of 0.7% (w/v) to ensure complete solubility. Subsequently, the photoinitiator was added to the polymer solution at concentrations of 0.05 wt %. The experiment was performed with n=8 for each PEGDA concentration. A volume of 100 μL polymer solution was pipetted into a mold (a cuvette cap) and exposed to 365 nm UV light (Blak-Ray, nominal intensity ~ 4 mW/cm^2) for 20 minutes. The relaxed state of the hydrogels immediately after cross-linking was measured in air ($W_{a,r}$) and in heptane ($W_{n,r}$). The hydrogels were then rinsed in 500 mL beakers of dH_2O to remove the unreacted polymer and then vacuum dried for 5 days. Following this, the weight of the hydrogels in the dried state was measured in air ($W_{a,d}$) followed by heptane ($W_{n,d}$). The hydrogels were then allowed to swell in 50 mL tubes for 48 hours in PBS at 37^{o}C. After swelling, the hydrogels in the swollen state were measured in air ($W_{a,s}$) and in heptane ($W_{n,s}$). For the heptane measurements, the hanging-basket method was used. Heptane was placed into a 250 mL beaker, with the hanging basket fully submerged in the heptane. Subsequently, each hydrogel was placed in the basket (submerged in the heptane) and a weight measurement was taken.

3.2.7.2 PEGDA-GFLGK-DA Hydrogel Swelling Experiment

PEGDA-GFLGK-DA (MW 700) was dissolved in dH_2O in a 1:1 molar ratio to 60% w/v. The ultraviolet (UV) photoinitiator, I2959, was first dissolved in dH_2O to a concentration of 0.7 wt% to ensure complete solubility. Subsequently the photoinitiator was added to the polymer solution at concentrations of 0.05 wt %. The experiment was performed in duplicate. A volume of 100 μL polymer solution was pipetted into a mold (a cuvette cap) and exposed to 365 nm UV light (Blak-Ray, nominal intensity ~ 4 mW/cm^2) for 20 minutes. The relaxed state of the hydrogels immediately after cross-linking was measured in air ($W_{a,r}$) and in heptane ($W_{n,r}$). Differing from the previous PEGDA swelling study, the hydrogels were then rinsed and lyophilized, following a protocol from Anseth [53]. The weight of the hydrogels in the dried state was measured in air ($W_{a,d}$) followed by heptane ($W_{n,d}$). The hydrogels were then allowed to swell in 50 mL tubes for 48 hours in PBS at 37°C. After swelling, the hydrogels in the swollen state were measured in air ($W_{a,s}$) and in heptane ($W_{n,s}$). For the heptane measurements, the hanging-basket method was used. Because we cannot use standard theory with the PEGDA-GFLGK polymer we simply measured the mass swelling ratio using equation below, to calculate the volumetric swelling ratio and compare it to the values obtained for PEGDA.

3.2.7.3 Calculation of PEGDA and PEGDA-GFLG-DA Hydrogel Properties

Average molecular weight between crosslinks (*Mc*), mesh size (ξ), as well as other PEG hydrogel properties were calculated using the Peppas and Merrill and Bar-Howell theories. The equation used to determine *Mc* is the Peppas and Merrill modified Flory-Rehner theory for molecular weight of the polymer chain between two adjacent crosslinks (*Mc*) of a neutral hydrogel prepared in the presence of water [3, 6, 7]:

$$\frac{1}{Mc} = \frac{2}{Mn} - \frac{\frac{v}{V_1}\left(\ln\left(1 - v_{2,s}\right) + v_{2,s} + \chi_1 v_{2,s}^2\right)}{v_{2,r}\left(\left(\frac{v_{2,s}}{v_{2,r}}\right)^{1/3} - \left(\frac{v_{2,s}}{2v_{2,r}}\right)\right)} \quad (1)$$

Where *Mn* is the number average molecular weight of the uncrosslinked polymer (ie – molecular weight of the macromer), V_1 is the molar volume of water (18 cm^3/mol), $v_{2,r}$ is the polymer volume fraction in the relaxed state, $v_{2,s}$ is the polymer volume fraction in the equilibrium swollen gel, ν is the specific volume of the polymer (0.893 cm^3/g), and χ is the polymer-solvent interaction parameter. A value of 0.426 was assumed for PEG [54].

The polymer volume fraction in the relaxed state is:

$$v_{2,r} = \frac{v_p}{v_{gel,r}} \quad (2)$$

where v_p is the volume of the polymer and $v_{gel,r}$ is the volume of the relaxed gel. The equations for v_p and $v_{gel,r}$ are as follows:

$$v_p = \frac{W_{a,d} - W_{n,d}}{\rho_n} \tag{3}$$

$$v_{gel,r} = \frac{W_{a,r} - W_{n,r}}{\rho_n} \tag{4}$$

where $W_{a,r}$ is the sample weight in air after crosslinking and $W_{n,r}$ is the sample weight in heptane (nonsolvent) after crosslinking, ρ_n is the density of the nonsolvent (0.684 g/cm^3 for heptane), $W_{a,d}$ is the sample weight in air after vacuum drying and $W_{n,d}$ is the sample weight in heptane after vacuum drying. Using the two equations above, the polymer volume fraction in the relaxed state can be re-written as:

$$v_{2,r} = \frac{W_{a,d} - W_{n,d}}{W_{a,r} - W_{n,r}} \tag{5}$$

The polymer volume fraction in the swollen state is:

$$v_{2,s} = \frac{v_p}{v_{gel,s}} = \frac{1}{Q} \tag{6}$$

where $\nu_{gel,s}$ is the volume of the swollen gel and Q is the volume swelling ratio. The equation for $\nu_{gel,s}$ is as follows:

$$v_{gel,s} = \frac{W_{a,s} - W_{n,s}}{\rho_n} \tag{7}$$

where $W_{a,s}$ is the sample weight in air after swelling and $W_{n,s}$ is the sample weight in heptane (nonsolvent) after swelling. Using the equations (3) and (7), the polymer volume fraction in the swollen state can be re-written as:

$$v_{2,s} = \frac{W_{a,d} - W_{n,d}}{W_{a,s} - W_{n,s}} \tag{8}$$

The mesh size was determined as described by Canal and Peppas [55]. To calculate mesh size in Angstroms of the swollen polymer, the following equations were used:

$$\left(r_o^2\right)^{1/2} = lC_n^{1/2}N^{1/2} \tag{9}$$

$$\xi = v_{2,s}^{-1/3}\left(r_o^2\right)^{1/2} \tag{10}$$

where r_o is the root mean squared end-to-end distance of the polymer chain in the unperturbed state, l is the length of the bond along the polymer backbone, C_n is the Flory characteristic ratio, N is the number of links/chains between crosslinks and ξ is the mesh size. Typical values for l and C_n for PEG are (1.47 Å - 1.5 Å) and 4.0, respectively [54, 56, 57]. In this case 1.5 Å was used for the value of l, and was taken as the weighted average of one carbon-carbon bond and two carbon-oxygen bonds. Substituting equation (9) into equation (10) we get:

$$\xi = v_{2,s}^{-1/3}lC_n^{1/2}N^{1/2} \tag{11}$$

In order to simplify further, we estimate that:

$$N = \frac{2Mc}{Mr} \tag{12}$$

where Mr is the molecular weight of the repeating units from which the polymer chain is composed (ie – the monomer). The value of Mr for PEG is 44 g/mol. Substituting equation (12) into equation (11) we get:

$$\xi = v_{2,s}^{-1/3}\left(\frac{2C_n Mc}{Mr}\right)^{1/2} l \qquad (13)$$

Equation (13) was used to calculate the mesh size in Angstroms of the swollen PEGDA polymers for the varying concentrations. This will provide a basic estimate on what cross-linking densities must be used to fabricate membranes for a particular drug size and will provide the theoretical limitation of stimuli-responsive release from such a design. To calculate an estimate of parameters for the PEGDA-GFGLK-DA hydrogels, the mass swelling ratio (*Qm*) was calculated using the equation:

$$Qm = \frac{Ws}{Wd} \qquad (14)$$

where Ws is the swollen weight of the hydrogel and Wd is the dry weight of the gel. From here we can estimate the value of the volumetric swelling ratio using equation (15) [58-60]:

$$Qv = 1 + \frac{\rho_p}{\rho_s}(Qm - 1) \qquad (15)$$

where ρ_p is the density of the polymer and ρ_s is the density of the solvent (~ 1 g/mL for dH_2O). The volumetric swelling ratio the density of the polymer was calculated by estimating the molar volume for the PEGDA-GFLGK and dividing by the molecular weight of the segment [59]. A molar volume for PEGDA MW 700 (784 cm^3/mol) and a molar volume of a penta-peptide incorporating Tyr-Gly-Gly-Phe-Leu (409.3 cm^3/mol) were used [61]. The values from this study provide a basic estimate on what cross-linking

densities must be used to fabricate membranes for a particular drug size and will provide the theoretical limitation of stimuli-responsive release from such a design.

3.2.8 Evaluation of PEGDA, PEG-GFLGK-PEG and PEG-GFLGK-DA Imprintability

As described previously, the ACRL-PEG-GFLGK-PEG-ACRL was dissolved in dH_2O to form a (100% w/v) solution. PEGDA (MW 3400) was dissolved in dH_2O to form a 100% w/v concentration. The ultraviolet (UV) photoinitiator, I2959, was first dissolved in dH_2O to a concentration of 0.7% (w/v) to ensure complete solubility. Subsequently, the photoinitiator was added to the polymer solution at concentrations of 0.07 wt %, to generate free radicals in order to induce chain polymerization (ref). To verify the imprintability of the PEGDA solutions, the IMPRIO 100 SFIL system (Molecular Imprints) was used. Prior to imprinting, a Relmat release layer was applied to a quartz template with a 25 x 25 mm mesa containing nanoline patterns (supplied by NNIN and the MRC at the University of Texas Pickle Research Center). The Relmat was dispensed using a dropper. Two to three drops of Relmat were dropped onto the mesa of the quartz template and subsequently blown dry with Nitrogen. Subsequently, a silicon wafer was manually loaded into the IMPRIO 100. The automated dispensing unit was inactivated and a volume of 0.5 to 2.5 μL of ACRL-PEG-GFLGK-PEG-ACRL and PEGDA concentrations was manually pipetted onto to the silicon wafer, prior to each imprint. The solutions were imprinted with a force of 2 N, a 30 second exposure time, and a pre-delay of 120 seconds. After optimization of the imprinting process described in

the following chapter, both ACRL-PEG-GFLGK-PEG-ACRL and PEGDA-GFLGK-DA were imprinted.

3.3 RESULTS

3.3.1 Verification of ACRL-PEG-NHS and GFLGK Conjugation

As shown in **Figure 3.5A** (measured before dialyzing through the 5000 MWCO membrane), the presence of a ~ 7300 Da peak indicates successful conjugation of one peptide to two PEG molecules, representing a conjugated PEG-GFLGK-PEG. The peak at 3707 may represent either a not fully conjugated PEG-GFLGK or possibly a dimer of the PEG-GFLGK-PEG. H NMR spectroscopy further supported the conjugation. The NMR data, **Figure 3.5B-D**, shows spectra of ACRL-PEG-NHS, GFLGK, and the conjugated form, respectively. In **Figure 3.5D**, the acrylate groups are seen at 5.9 – 6.4 ppm and the aromatic phenyl group on Phe of the peptide is seen at 7.15 – 7.3 ppm. To determine the degree of conjugation, the ratio of protons was calculated by comparing the area under the aromatic phenyl group on Phe (5 protons) to the area under the acrylate group (3 protons). The results show a 1 to 1.5 molar ratio of GFLGK to PEG, suggesting that there is ACRL-PEG-GLFGK and ACRL-PEG-GLFGK-PEG-ACRL; however, the cleanliness of the overall NMR spectra suggests that there is mostly one species. After dialyzing and lyophilizing the yield was approximately 80%.

3.3.2 Verification of Acrylation of GFLGK

H NMR data for both methods of acrylating GFLGK using DMAc and dH_2O as solvent, show successful acrylation of the peptide sequence. **Figure 3.6A-D** shows the 1H NMR data of acryloyl chloride, triethylamine, GFLGK, and the acrylated peptide using the first acrylation method with DMAc as a solvent. Successful acrylation was achieved using this method as can be seen by the addition of the acrylate peaks at 5.7 - 6.2 ppm in **Figure 3.6D.** However, due to impurities within the sample, it was difficult to estimate the actual degree of acrylation. The yield for this method was approximately 20%. **Figure 3.7A-B** shows acrylated peptide using the second method with water as a solvent. Successful acrylation was achieved using both the acrylation methods as can be seen by the addition of the acrylate peaks at 5.7 - 6.2 ppm in **Figure 3.6D** and **Figure 3.7B**. To determine the degree of acrylation, the ratio of protons were calculated by comparing the area under the isopropyl group (6 protons) and the area under the acrylate curve (3 protons). The NMR spectra for the second acrylation method showed a 1 to 2 molar ratio of GFLGK to acrylate, demonstrating successful di-acrylation of the peptide. The yield for this process is approximately 89%[1].

3.3.3 Evaluation of PEGDA, PEG-GFLGK-PEG and PEGDA-GLFKG-DA Enzyme-Responsive Release

As shown in **Figure 3.8A**, there was an initial release of 10 to 20% of the DNA from PEG-GFLGK-PEG hydrogel, followed by saturation and then an enzyme-triggered

[1] NMR analysis for Figure 2.7 and yield value courtesy Mary Caldorera-Moore.

release of DNA upon addition of Cathepsin B; however, we believe this may be due to the hydrophilic nature of the DNA. It may have adsorbed to the surface of the hydrogel or not fully encapsulated within the gel. When Cathepsin B was introduced to the PEGDA-GFLGK-DA hydrogel, **Figure 3.8B**, we see a rapid release of DNA. The results for the PEGDA-GFLGK also show a smaller ratio of initial DNA release compared to overall release. As expected, the results demonstrate that specific enzyme-induced burst release does occur.

3.3.4 PEGDA and PEGDA-GFLGK swelling properties

Results of the mesh size (ξ), the molecular weight between crosslinks (Mc), the polymer volume fraction in the swollen state ($v_{2,s}$), and the mass swelling ratio can be found in **Table 3.1.** The results indicate that mesh size, molecular weight between crosslinks and the mass swelling ratio decrease as the PEGDA concentration decreases. **Table 3.1** shows that the Mc varies from 18.09 ± 1.59 Å (75% w/v) to 179.10 ± 13.53 Å (25% w/v) with mesh sizes of 2.86 ± 0.3 Å to 12.92 ± 1.56 Å, respectively. Polymer volume fraction in the swollen state increased with a decrease in PEGDA concentration. Because the volumetric swelling ratio is inversely proportional to $v_{2,s}$, the results indicate that that the volumetric swelling ratio increases as the PEGDA concentration decreases. The $v_{2,s}$ ranged from 0.86 ± 0.05 Å (75% w/v) to 0.29 ± 0.03 Å (25% w/v) with volumetric swelling ratios calculated as 1.16 ± 0.06 Å and 3.44 ± 0.32 Å, respectively. The mass swelling ratio of the PEGDA-GFLGK (60% w/v) was 3.59 ± 0.59 Å, with an estimated volumetric swelling ratio of 3.51 ± 0.58 Å.

3.3.5 Evaluation of PEGDA, PEG-GFLGK-PEG and PEGDA-GLFKG-DA Imprintability

Figure 3.9A-B demonstrates that PEGDA (MW 3400) was successfully able to create well-defined patterns and nano-lines (800 nm with 200 nm spacing) with the imprinting process. **Figure 3.9C-D** demonstrates successful imprinting of PEG-GFLGK-PEG. The imprinted nano-lines were 600 nm in width with 100 nm spacing (**Figure 3.9C**), and 300 nm in width with 50 nm spacing (**Figure 3.9D**). There were some issues with the PEG-GFLGK-PEG adhering to the template/not adhering to the wafer; therefore only two to three imprints could be performed at a time. PEG-GFLGK-DA was also successfully imprinted and had fewer issues with adhering to the template.

3.4 DISCUSSION

The overall goal of these experiments was to create a stimuli-responsive peptide-functionalized PEG material system that demonstrated: (a) minimal diffusion of the drug through it in the absence of enzyme-triggered degradation, and (b) the ability to be nanoimprinted. We developed two configurations. The first configuration involved a photo-crosslinkable, homo-bifunctional PEG diacrylate, ACRL-PEG-GFGLK-PEG-ACRL, polymer using a 2 to 1 molar ratio of PEGDA (MW 3400) to ACRL-PEG-NHS. The second configuration involved a photo-crosslinkable PEGDA-GFLGK-DA hydrogel using an equimolar mixture of PEGDA (MW 700) and a diacrylated, enzymatically degradable peptide, GFLGK-DA. Both configurations create a matrix crosslinked with a

degradable peptide spacer, GFLGK, designed for degradation by Cathepsin B, shown in **Figure 3.2**. The results from NMR and MALDI show successful incorporation of GFLGK with PEGDA and ACRL-PEG-NHS using previously established techniques for the conjugation [46, 48] and acrylation [49, 50], respectively. The second acrylation method using water has shown to be much easier to perform and provides a better acrylation efficiency and yield than the previous acrylation method.

A primary design criterion of the material system is that it should demonstrate drug release upon enzymatic degradation and that there should be minimal diffusion of drugs beforehand. The pore size (ξ) and molecular weight between crosslinks (Mc) of these hydrogels dictate whether a certain drug can be entrapped without significant diffusive leaching prior to an environmental trigger. For little to no diffusion to occur, the cross-linking density of the membrane must be such that the pore sizes are smaller than the drug molecule sizes; thus it is possible to a priori model which particular therapeutic or diagnostic agents are suitable for stimuli-responsive, triggered release from particles of a specific composition. Assuming a spherical configuration for protein or DNA molecules, the expected hydrodynamic size (Stokes diameter) of a typical drug can be calculated using the Stokes-Einstein equation:

$$D_A = \frac{k_B T}{6\pi\mu d} \tag{16}$$

where k is the Boltzman constant, T is the temperature in Kelvin, μ is the viscosity of the solution, DA is the diffusion coefficient of the peptide or model drug and d is the

hydrodynamic size. The diffusion coefficient can be calculated using the following equation:

$$D_A = \frac{9.4x10^{-15}T}{\mu M_W^{1/3}} \tag{17}$$

for proteins and the empirical equation:

$$D_A = \frac{0.116RT}{(1-V\rho)M_W^{0.675}} \tag{18}$$

for DNA.

Pore size measurements for bulk PEGDA (MW 3400) hydrogels of various concentrations have been reported by Bryant and Anseth [62]. Anseth et al. experimentally determined the pore size of photo-crosslinked PEGDA (MW 3400) polymers at 10%, 20%, 30% and 40% w/v concentrations [62]. Their results indicate that the average pore sizes are approximately 14, 6, 5 and 4 nm, respectively. Our lab has experimentally determined the pore size of PEGDA 100% (w/v) (MW 3400) to be 1.5 nm (data not shown). Experimentally obtained values show that the hydrodynamic diameter of the model protein BSA (MW 67 kDa) is ~ 4 nm [63], while that of circular plasmid DNA is approximately 100 nm [64]. This indicates that at concentrations of 40% (w/v) or higher, the pore sizes are less than the calculated hydrodynamic size of BSA; meanwhile for plasmid DNA delivery, polymer concentrations of 20% (w/v) or above will be suitable.

Therefore, the PEG-GFLGK-PEG design (using PEGDA MW 3400) should efficiently prevent diffusion of both protein and DNA drugs in the absence of Cathepsin B. Our release study results indicate that ~ 20% of DNA is initially released using the PEG-GFLGK-PEG polymer configuration, followed by saturation and then an enzyme-triggered release of DNA upon addition of Cathepsin B. We believe some of the initial release and saturation may be due to the hydrophilic nature of plasmid DNA. It may have adsorbed to the surface of the hydrogel and or not fully encapsulated within the gel. Unfortunately, the company that manufactured the NHS-PEG-ACRL stopped producing the product, so no further studies could proceed with using a smaller molecular weight PEGDA in efforts to create a tighter polymer network.

In order to potentially reduce the initial DNA release we created the PEGDA-GFLGK-DA hydrogels. To create a tighter polymer network, a photo-crosslinkable PEGDA-GFLGK-DA polymer using an equimolar mixture of PEGDA (MW 700) and a diacrylated, enzymatically degradable peptide, GFLGK-DA were evaluated. In order to estimate the pore size of the PEGDA-GFLGK-DA polymer membranes, hydrogel swelling studies were performed on PEGDA (MW 700) hydrogels. Specific assumptions were used in the calculations, specifically for the polymer-solvent interaction factor (χ). We assumed a value of 0.426, based on a study by Merrill, et al. This value was shown to be nearly independent of polymer volume fraction for values of 0.04 to 0.2 with swelling performed in water [54]. Since we are using PBS and have larger polymer volume fractions, this value of χ may not be valid and would need to be measured for a more

accurate study. Needless to say, this is the value commonly reported in literature and should provide a good estimate of Mc and mesh size [65, 66].

The results of the swelling study demonstrated mesh sizes that range from 2.86 to 12.92 Å, for a 25% (w/v) to 75% (w/v) PEGDA hydrogel, respectively. While the PEGDA concentration increases, this affects the number of crosslinks, and leads to an increased entanglement and thus a decreased swelling ratio. Furthermore, the estimated volumetric swelling ratio of the 60% (w/v) PEGDA-GFLGK-DA resembled that of the 25% (w/v) PEGDA hydrogel. This suggests that the PEGDA-GFLGK-DA polymer membrane may be less entangled and may display similar properties to a 25% (w/v) PEGDA hydrogel. Depending on the concentration of the PEGDA (MW 700), we hypothesize that protein and nucleic acid-based drugs with hydrodynamic radii larger than two nanometers should be successfully retained and slowly released from such particles, even with a 25% (w/v) concentration. Thus protein, peptide and nucleic acid-based drugs, hydrophobic drug particles as well as nanoparticle-based contrast agents could be successfully retained within such hydrogels and released primarily upon environmentally-triggered matrix degradation. Using the PEGDA-GLFGK-DA polymer configuration did result in a smaller ratio of initial DNA release compared to overall release (~ 8%) than was present in the first hydrogel design. We also demonstrate a steep burst release of DNA. This is comparable to the ~ 10% initial release of rhBMP from the enzyme-responsive hydrogel demonstrated by Hubbell and colleagues, as seen in **Figure 3.1B.**

In conclusion, the PEG-GFGLK-PEG and PEGDA-GFLGK-DA configurations demonstrated an enzyme-triggered release of DNA upon addition of Cathepsin B and were both successfully imprinted. Characterization of degradation and release kinetics would be required for future study; however, the goal of this research was to demonstrate enzyme-responsive release with minimal initial diffusion of drug from the hydrogel material system, as well as to show the potential for use with nanoimprinting. The key relevance of these studies is the possibility that these material designs, as well as other similar peptide-functionalized, enzyme-degradable hydrogels could be nanoimprinted, and used to control drug release from nanoimprinted carriers. The ability to create nano-sized, injectable drug carriers fabricated with precise geometry and environmentally-responsive release mechanisms could provide targeted, disease-specific delivery of molecules as well as tunable in-vivo release characteristics.

Figure 3.1 Enzymatically Degradable Hydrogel Release and Degradation: (A) Hubbell and colleagues demonstrated rapid burst release of BMP-2 upon addition of MMP-2 [11][*1], and (B) West and colleagues demonstrated enzyme-dependent degradation of PEG-peptide-PEG hydrogels upon addition of enzyme [12].[*2]

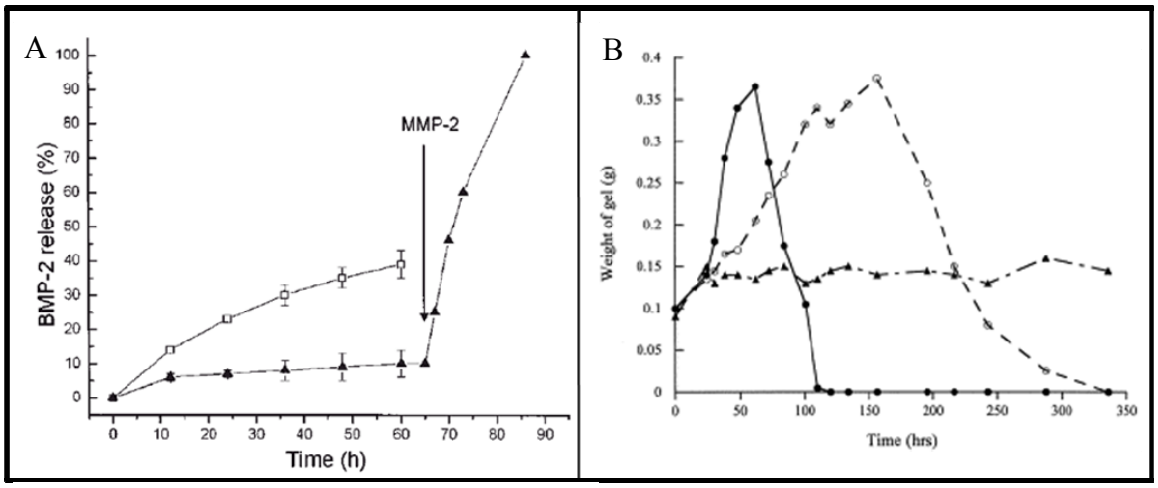

[*1] *Reproduced with permission from* M. P. Lutolf, F. E. Weber, H. G. Schmoekel, J. C. Schense, T. Kohler, R. Müller, and J. A. Hubbell*:* Repair of bone defects using synthetic mimetics of collagenous extracellular matrices*. 2003. 21. 513-518. Copyright Wiley-VCH Verlag GmbH & Co. KGaA.*

[*2] *Reproduced with permission from* B. K. Mann, A. S. Gobin, A.T. Tsai, R. H. Schmedlen, and J. L. West*:* Smooth muscle cell growth in photopolymerized hydrogels with cell adhesive and proteolytically degradable domains: synthetic ECM analogs for tissue engineering*. 2001. 22. 3045-3051. Copyright Wiley-VCH Verlag GmbH & Co. KGaA.*

Figure 3.2 **Enzyme-Responsive Polymer Chemistry, Photopolymerization and Degradation Mechanism: (A) Method 1: photo-crosslinked ACRL-PEG-GFLGK-PEG-ACRL polymer, and (B) Method 2: photo-crosslinked PEGDA-GFLGK-DA.**

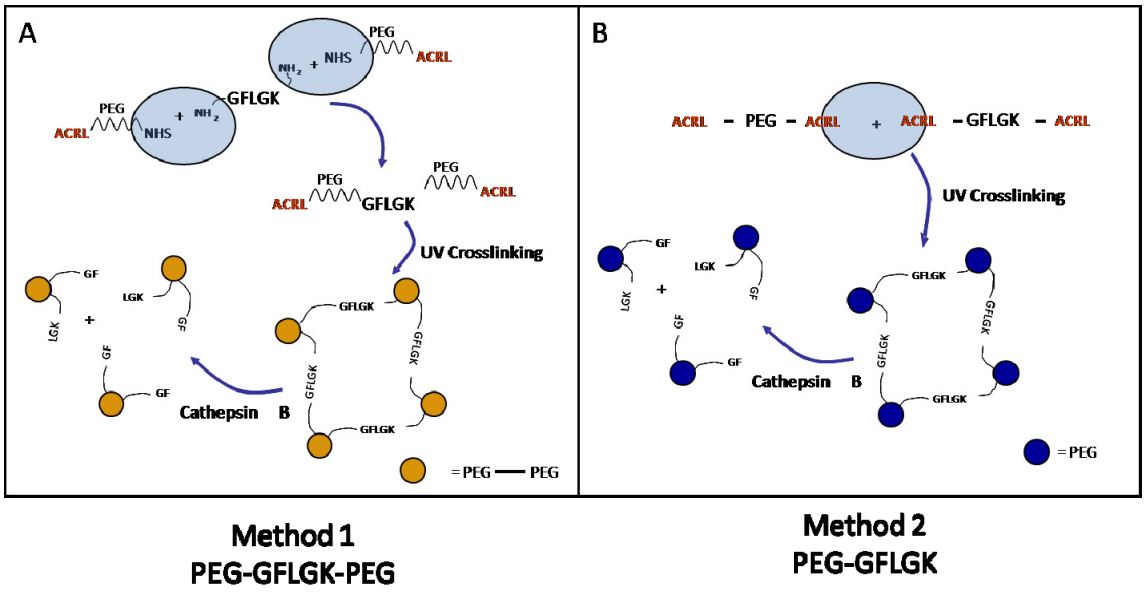

Figure 3.3 **Schematic of ACRL-PEG-NHS and GFLGK Conjugation.**

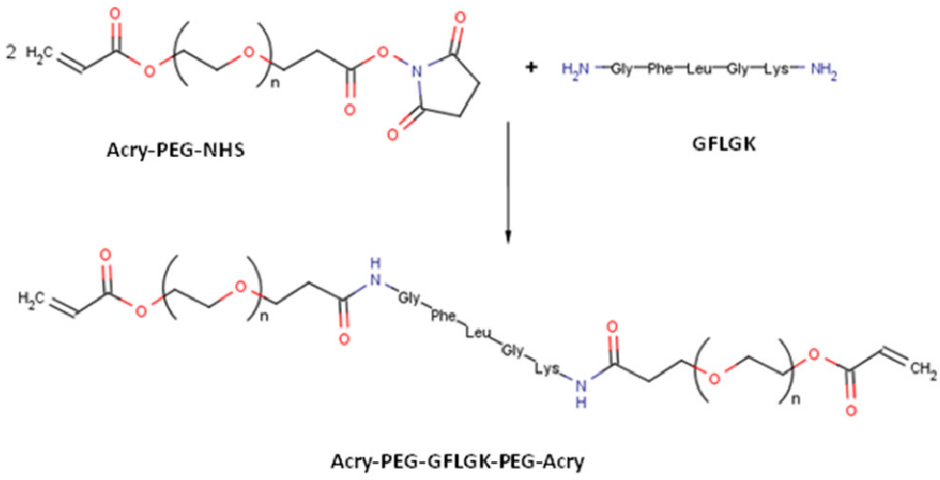

Figure 3.4 Schematic of GFLGK Acrylation.

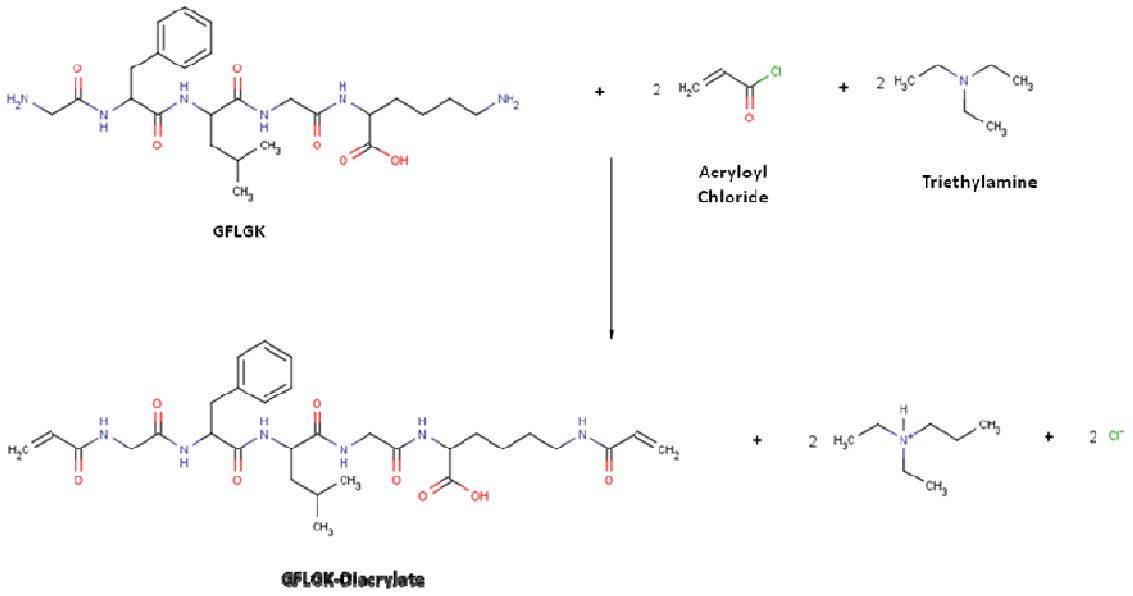

Figure 3.5 MALDI and NMR Images of Conjugated ACRL-PEG-GFLGK-PEG-ACRL: (A) MALDI image showing the conjugated ACRL-PEG-GFLGK-PEG-ACRL and a possible dimer or ACRL-PEG-GFLGK, (B) NMR image showing NHS-PEG-ACRL, (C) NMR image showing GFLGK, (D) NMR image showing conjugated ACRL-PEG-GFLGK-PEG-ACRL.

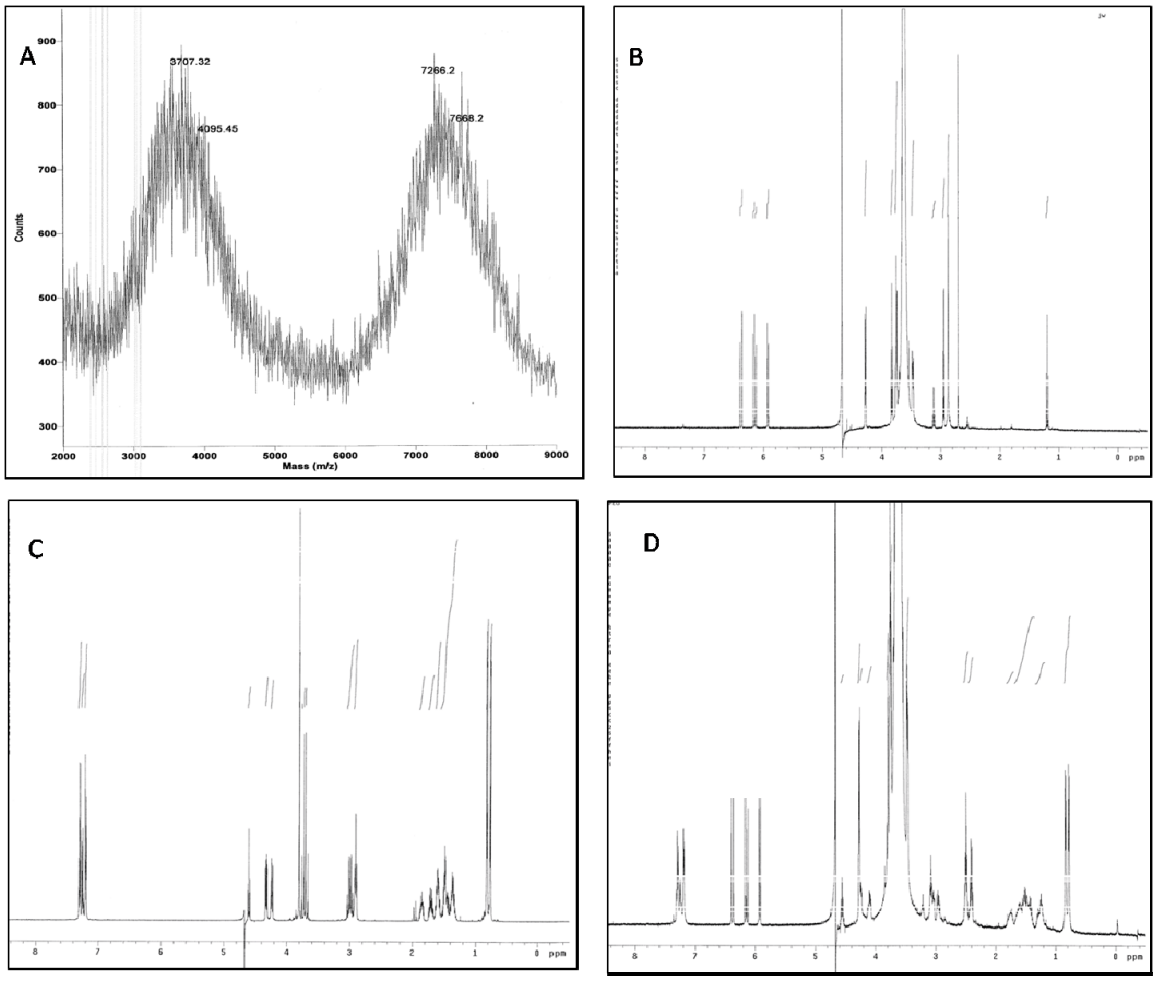

Figure 3.6 NMR images of Acrylated GFLGK using Dimethylacetamide as a solvent: (A) Acryloyl Chloride, (B) Triethylamine, (C) GFLGK, (D) acrylated GFLGK.

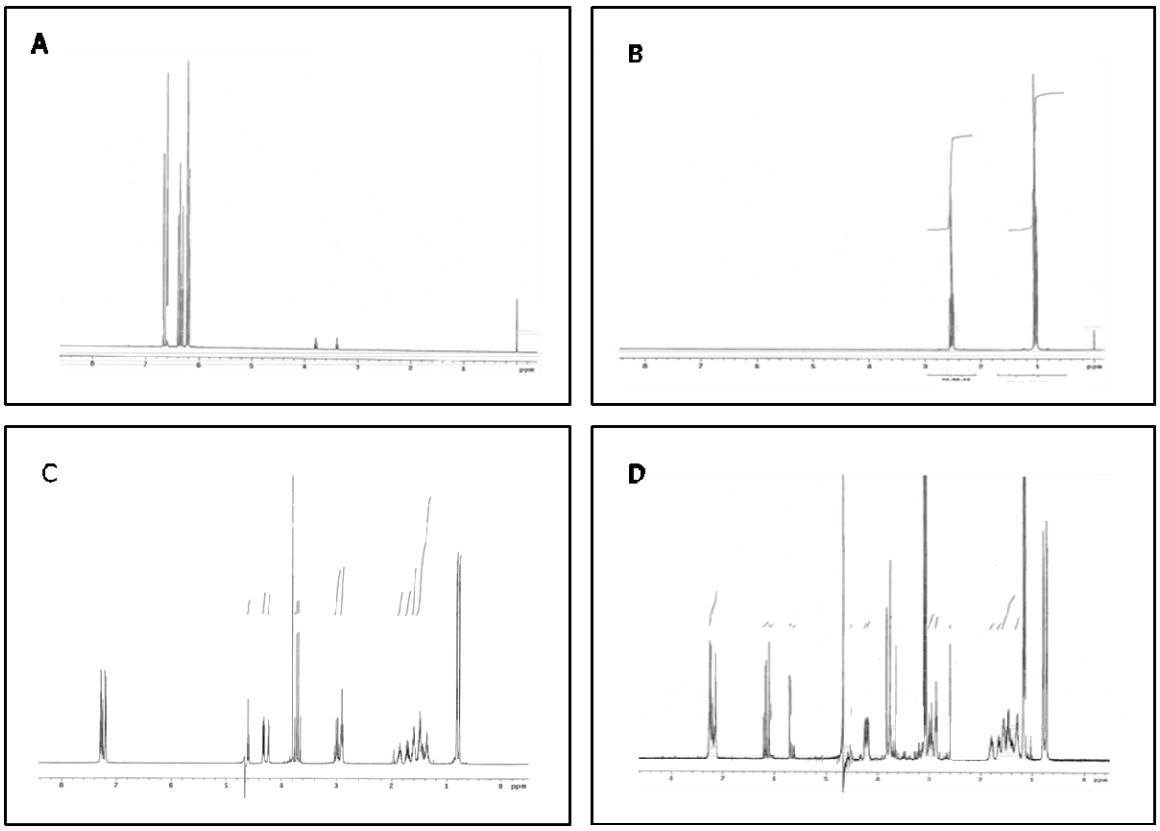

Figure 3.7 NMR images of Acrylated GFLGK using dH_2O as a solvent: (A) GFLGK and (B) successfully di-acrylated GFLGK. *Reprinted from J Control Release, 125, L. C. Glangchai, M. Caldorera-Moore, L. Shi, and K. Roy, 263 – 272, 2008, with permission from Elsevier.*

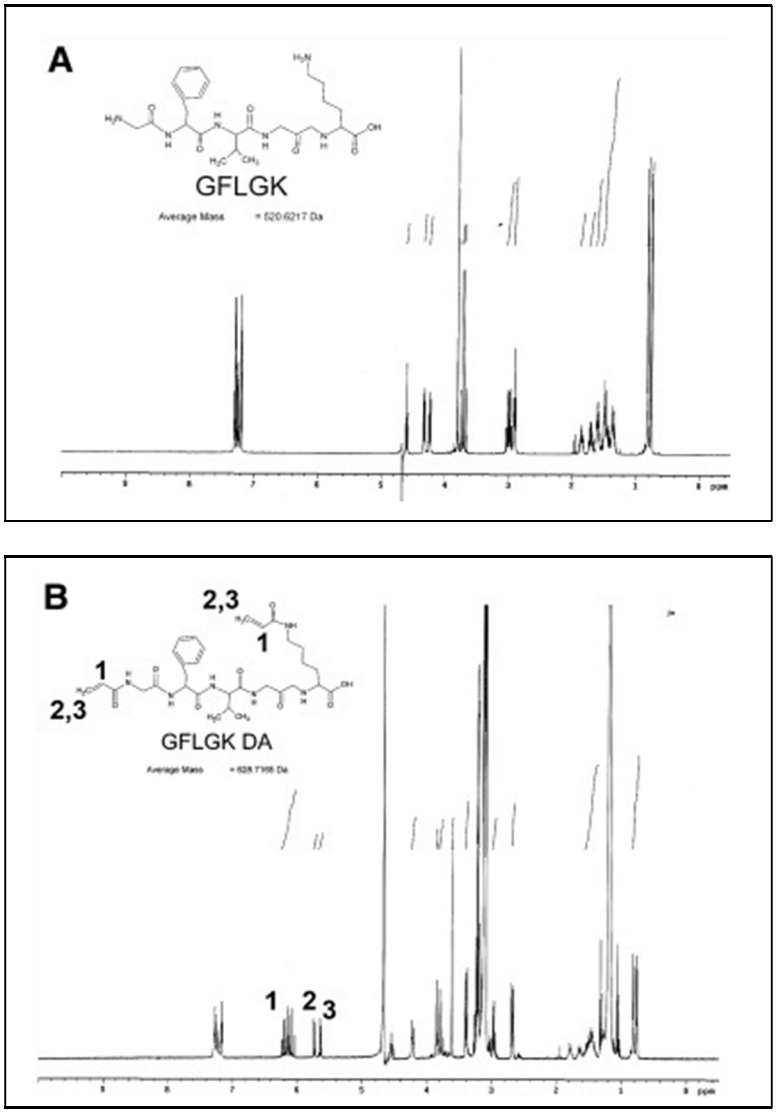

Figure 3.8 **Enzyme-Responsive Plasmid DNA Release from: (A) 100% (w/v) PEG-GFLGK-PEG hydrogel (PEGDA MW 3400), and (B) 100% (w/v) PEGDA-GFLGK-DA hydrogel (PEGDA MW 1000), showing enzyme-triggered release of DNA upon addition of Cathepsin B.**

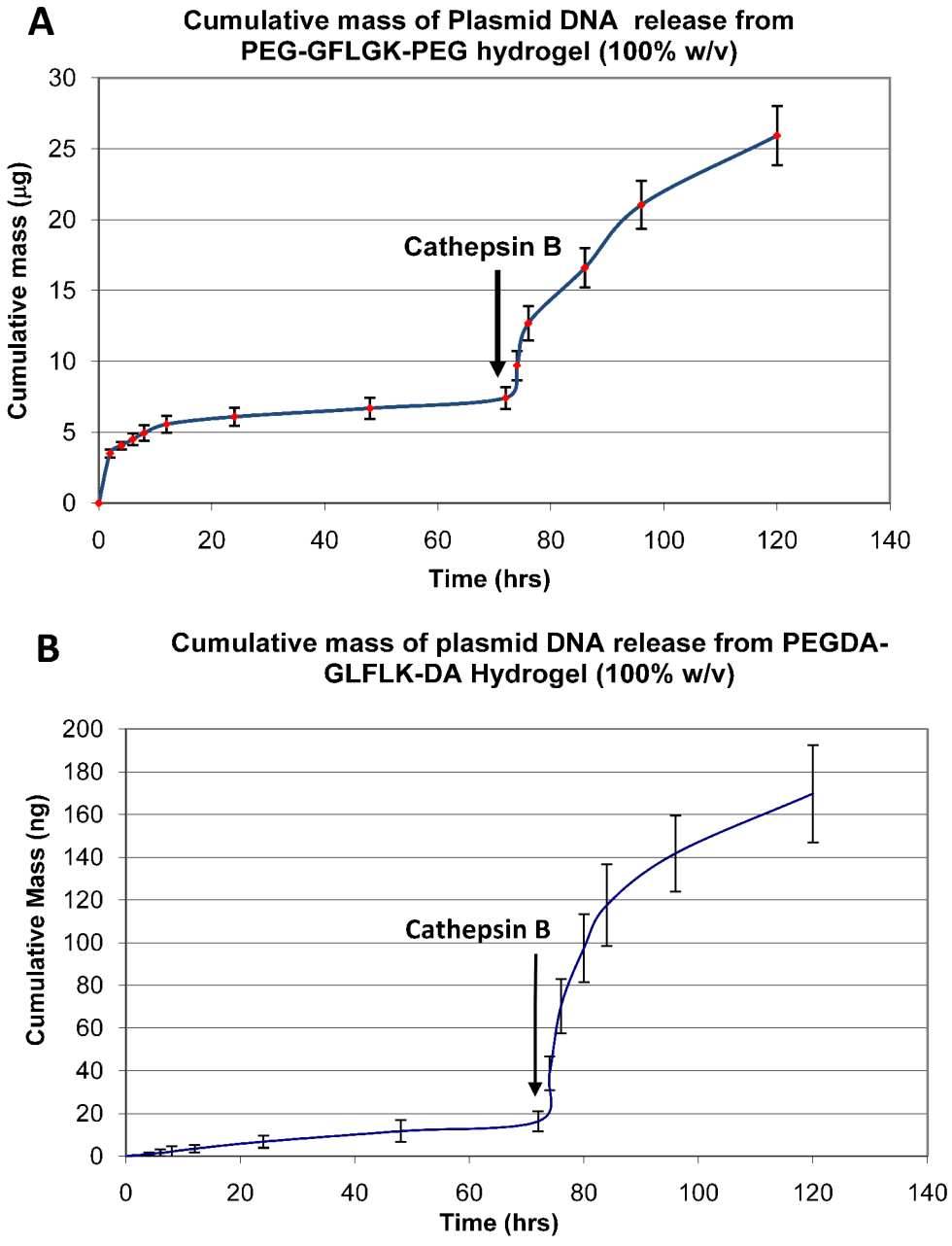

Table 3.1 Swelling Properties of PEGDA and PEGDA-GLFGK-DA: (A) PEGDA (MW 700) with concentrations varying from 75% to 25% (w/v) (n=8), and (B) mass swelling ratio of PEGDA-GFLGK-DA (60% w/v) (n=2).

A

% (w/v) PEGDA MW700	ζ (Angstrom)	(SD)	Mc	(SD)	v_{2s}	(SD)	Qv	(SD)
75	2.86	0.30	18.09	1.59	0.86	0.05	1.16	0.05
60	3.15	0.48	21.47	2.69	0.84	0.07	1.19	0.07
50	5.07	0.55	47.23	3.90	0.65	0.05	1.53	0.05
33	8.75	1.36	106.42	11.30	0.43	0.05	2.34	0.05
25	12.92	1.56	179.10	13.53	0.29	0.03	3.44	0.03

B

%(w/v) PEGDA-GFLGKDA (MW700)	Qm	(SD)	Qv	(SD)
60	3.59	0.59	3.36	0.56

Figure 3.9 SFIL Imprinted PEGDA and PEG-GFLGK-PEG: (A) Nanofeatures in 100% (w/v) PEGDA (MW 3400) *(scale bar = 4μm)*, **(B) 800 nm nanolines with 200 nm spacing in 100% (w/v) PEGDA (MW 3400)** *(scale bar = 400nm)*, **(C) 600 nm lines in 100% (w/v) PEG-GFLGK-PEG with 100 nm spacing** *(scale bar = 400nm)*, **(D) 300 nm nanolines with 50 nm spacing in 100% (w/v) PEG-GFLGK-PEG** *(scale bar = 200nm)*.

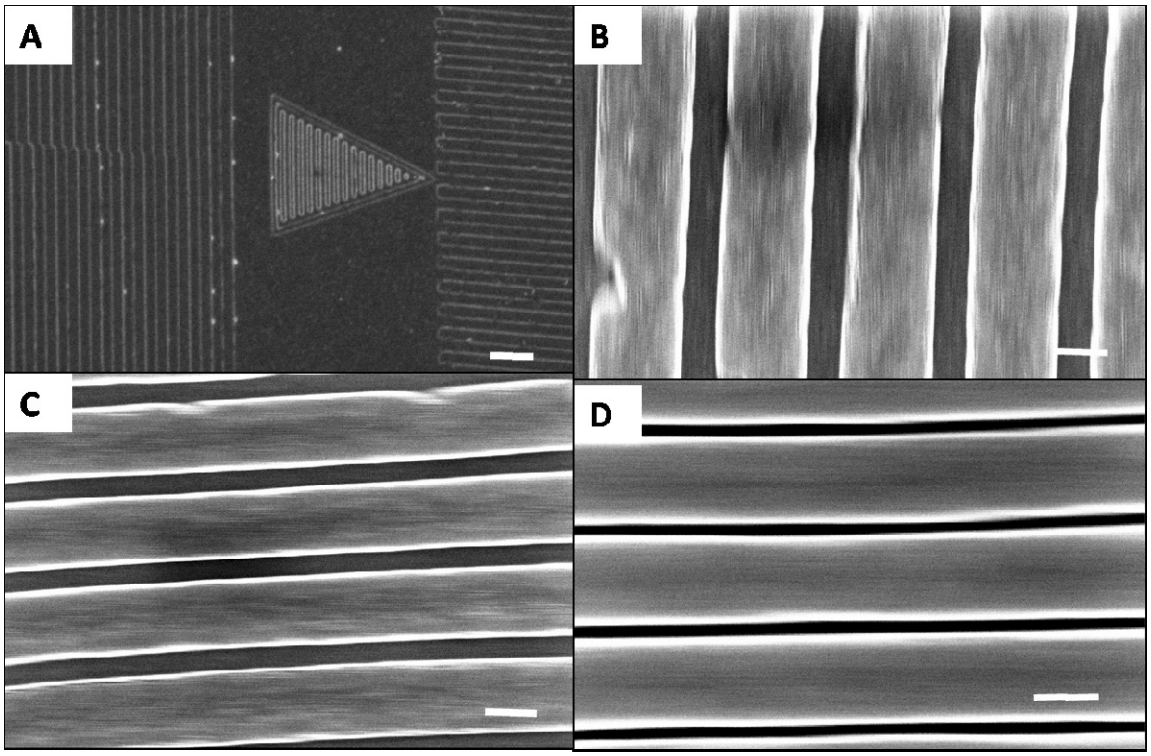

3.5 REFERENCES

1. Farokhzad OC, Langer R. Nanomedicine: developing smarter therapeutic and diagnostic modalities. Adv Drug Deliv Rev 2006;58(14):1456-1459.
2. Ferrari M. Cancer nanotechnology: opportunities and challenges. Nat Rev Cancer 2005;5(3):161-171.
3. Peppas NA, Bures P, Leobandung W, Ichikawa H. Hydrogels in pharmaceutical formulations. Eur J Pharm Biopharm 2000;50(1):27-46.
4. Miyata T, Uragami T, Nakamae K. Biomolecule-sensitive hydrogels. Adv Drug Deliv Rev 2002;54(1):79-98.
5. Qiu Y, Park K. Environment-sensitive hydrogels for drug delivery. Adv Drug Deliv Rev 2001;53(3):321-339.
6. Peppas NA, Hilt JZ, Khademhosseini A, Langer R. Hydrogels in biology and medicine: From molecular principles to bionanotechnology. Adv Mater 2006;18(11):1345-1360.
7. Peppas NA, Huang Y, Torres-Lugo M, Ward JH, Zhang J. Physiochemical foundations and structural design of hydrogels in medicine and biology. Annu Rev Biomed Eng 2000;2(1):9-29.
8. Lee KY, Yuk SH. Polymeric protein delivery systems. Prog Polym Sci 2007;32(7):669-697.
9. Kikuchi A, Okano T. Pulsatile drug release control using hydrogels. Adv Drug Deliv Rev 2002;54(1):53-77.

10. Seliktar D, Zisch AH, Lutolf MP, Wrana JL, Hubbell JA. MMP-2 sensitive, VEGF-bearing bioactive hydrogels for promotion of vascular healing. J Biomed Mater Res A 2004;68(4):704-716.

11. Lutolf MP, Weber FE, Schmoekel HG, Schense JC, Kohler T, Muller R, et al. Repair of bone defects using synthetic mimetics of collagenous extracellular matrices. Nat Biotechnol 2003;21(5):513-518.

12. Mann BK, Gobin AS, Tsai AT, Schmedlen RH, West JL. Smooth muscle cell growth in photopolymerized hydrogels with cell adhesive and proteolytically degradable domains: synthetic ECM analogs for tissue engineering. Biomaterials 2001;22(22):3045-3051.

13. Subr V, Strohalm J, Ulbrich K, Duncan R, Hume IC. Polymers containing enzymatically degradable bonds, XII. Effect of spacer structure on the rate of release of daunomycin and adriamycin from poly [N-(2-hydroxypropyl)-methacrylamide] copolymer drug carriers in vitro and antitumour activity measured in vivo. J Control Release 1992;18(2):123-132.

14. Ulbrich K, Subr V, Strohalm J, Plocova D, Jelinkova M, Rihova B. Polymeric drugs based on conjugates of synthetic and natural macromolecules. I. Synthesis and physico-chemical characterisation. J Control Release 2000;64(1-3):63-79.

15. Ulbrich K, Pechar M, Strohalm J, Subr V, Rihova B. Polymeric carriers of drugs for site-specific therapy. Macromol Symp 1997;118:577-585.

16. Ulbrich K, Subr V. Polymeric anticancer drugs with pH-controlled activation. Adv Drug Deliv Rev 2004;56(7):1023-1050.

17. Ulbrich K, Etrych T, Chytil P, Jelinkova M, Rihova B. HPMA copolymers with pH-controlled release of doxorubicin: in vitro cytotoxicity and in vivo antitumor activity. J Control Release 2003;87(1-3):33-47.

18. Kopecek J, Kopeckova P, Minko T, Lu Z. HPMA copolymer-anticancer drug conjugates: design, activity, and mechanism of action. Eur J Pharm Biopharm 2000;50(1):61-81.

19. Minko T, Kopeckova P, Kopecek J. Efficacy of the chemotherapeutic action of HPMA copolymer-bound doxorubicin in a solid tumor model of ovarian carcinoma. Int J Cancer 2000;86(1):108-117.

20. Rejmanova P, Kopecek J, Duncan R, Lloyd JB. Stability in rat plasma and serum of lysosomally degradable oligopeptide sequences in N-(2-hydroxypropyl) methacrylamide copolymers. Biomaterials 1985;6(1):45-48.

21. Duncan R, Cable HC, Lloyd JB, Rejmanova P, Kopecek J. Polymers containing enzymatically degradable bonds. 7: Design of oligopeptide side-chains in poly [N-(2-hydroxypropyl) methacrylamide] copolymers to promote efficient degradation by lysosomal enzymes. Makromol Chem 1983;184(10):1997-2008.

22. Rejmanova P, Kopecek J, Pohl J, Baudy M, Kostka V. Polymers containing enzymatically degradable bonds, 8. Degradation of oligopeptide sequences in N-(2-hydroxypropyl)methacrylamide copolymers by bovine spleen cathepsin B. Makromol Chem 1983;184(10):2009-2020.

23. Putnam D, Kopeček J. Polymer conjugates with anticancer activity. Advances in Polymer Science (Biopolymers II): Springer, 1995. p. 55-123.

24. Putnam DA, Shiah JG, Kopecek J. Intracellularly biorecognizable derivatives of 5-fluorouracil. Implications for site-specific delivery in the human condition. Biochem Pharmacol 1996;52(6):957-962.

25. Duncan R, Cable HC, Lloyd JB, Rejmanova P, Kopecek J. Degradation of side-chains of N-(2-hydroxypropyl)methacrylamide copolymers by lysosomal thiol-proteinases. Biosci Rep 1982;2(12):1041-1046.

26. Subr V, Kopecek J, Pohl J, Baudyo M, Kostka V. Cleavage of oligopeptide side chains in HPMA copolymers by mixtures of lysosomal enzymes. J Control Release 1988;8:133-140.

27. Turk V, Turk B, Turk D. Lysosomal cysteine proteases: facts and opportunities. EMBO J 2001;20(17):4629-4633.

28. Kos J, Lah TT. Cysteine proteinases and their endogenous inhibitors: target proteins for prognosis, diagnosis and therapy in cancer (review). Oncol Rep 1998;5(6):1349-1361.

29. Turk V, Kos J, Turk B. Cysteine cathepsins (proteases)--on the main stage of cancer? Cancer Cell 2004;5(5):409-410.

30. Kopecek J. Controlled biodegradability of polymers--a key to drug delivery systems. Biomaterials 1984;5(1):19-25.

31. Spiess E, Bruning A, Gack S, Ulbricht B, Spring H, Trefz G, et al. Cathepsin B activity in human lung tumor cell lines: ultrastructural localization, pH sensitivity, and inhibitor status at the cellular level. J Histochem Cytochem 1994;42(7):917-929.

32. Heidtmann HH, Salge U, Abrahamson M, Bencina M, Kastelic L, Kopitar-Jerala N, et al. Cathepsin B and cysteine proteinase inhibitors in human lung cancer cell lines. Clin Exp Metastasis 1997;15(4):368-381.

33. Jessup JM. Cathepsin B and other proteases in human colorectal carcinoma. Am J Pathol 1994;145(2):253-262.

34. Campo E, Munoz J, Miquel R, Palacin A, Cardesa A, Sloane BF, et al. Cathepsin B expression in colorectal carcinomas correlates with tumor progression and shortened patient survival. Am J Pathol 1994;145(2):301-309.

35. Higashiyama M, Doi O, Kodama K, Yokouchi H, Tateishi R. Cathepsin B expression in tumour cells and laminin distribution in pulmonary adenocarcinoma. J Clin Pathol 1993;46(1):18-22.

36. Ohta T, Terada T, Nagakawa T, Tajima H, Itoh H, Fonseca L, et al. Pancreatic trypsinogen and cathepsin B in human pancreatic carcinomas and associated metastatic lesions. Br J Cancer 1994;69(1):152-156.

37. Werle B, Ebert W, Klein W, Spiess E. Cathepsin B in tumors, normal tissue and isolated cells from the human lung. Anticancer Res 1994;14(3A):1169-1176.

38. Howie AJ, Burnett D, Crocker J. The distribution of cathespin B in human tissues. J Pathol 1985;145(4):307-314.

39. Werle B, Kraft C, Lah TT, Kos J, Schanzenbacher U, Kayser K, et al. Cathepsin B in infiltrated lymph nodes is of prognostic significance for patients with nonsmall cell lung carcinoma. Cancer 2000;89(11):2282-2291.

40. Krepela E, Prochazka J, Karova B, Cermak J, Roubkova H. Cathepsin B, thiols and cysteine protease inhibitors in squamous-cell lung cancer. Neoplasma 1997;44(4):219-239.

41. Krepela E, Kasafirek E, Novak K, Viklicky J. Increased cathepsin B activity in human lung tumors. Neoplasma 1990;37(1):61-70.

42. Erdel M, Trefz G, Spiess E, Habermaas S, Spring H, Lah T, et al. Localization of cathepsin B in two human lung cancer cell lines. J Histochem Cytochem 1990;38(9):1313-1321.

43. Krepela E, Prochazka J, Mynarikova H, Karova B, Polak J, Cermak J, et al. Multiple forms of cathepsin B in human lung cancer. Int J Cancer 1995;61(1):44-53.

44. Ebert W, Knoch H, Werle B, Trefz G, Muley T, Spiess E. Prognostic value of increased lung tumor tissue cathepsin B. Anticancer Res 1994;14(3A):895-899.

45. Bryant SJ, Anseth KS. Controlling the spatial distribution of ECM components in degradable PEG hydrogels for tissue engineering cartilage. J Biomed Mater Res A 2003;64(1):70-79.

46. Gobin AS, West JL. Effects of epidermal growth factor on fibroblast migration through biomimetic hydrogels. Biotechnol Prog 2003;19(6):1781-1785.

47. Bryant SJ, Bender RJ, Durand KL, Anseth KS. Encapsulating chondrocytes in degrading PEG hydrogels with high modulus: engineering gel structural changes to facilitate cartilaginous tissue production. Biotechnol Bioeng 2004;86(7):747-755.

48. Hern DL, Hubbell JA. Incorporation of adhesion peptides into nonadhesive hydrogels useful for tissue resurfacing. J Biomed Mater Res 1998;39(2):266-276.

49. West JL, Hubbell JA. Polymeric biomaterials with degradation sites for proteases involved in cell migration. Macromolecules 1999;32(1):241-244.

50. Kim S, Healy KE. Synthesis and characterization of injectable poly(N-isopropylacrylamide-co-acrylic acid) hydrogels with proteolytically degradable cross-links. Biomacromolecules 2003;4(5):1214-1223.

51. Etrych T, Jelinkova M, Rihova B, Ulbrich K. New HPMA copolymers containing doxorubicin bound via pH-sensitive linkage: synthesis and preliminary in vitro and in vivo biological properties. J Control Release 2001;73(1):89-102.

52. Tansey W, Ke S, Cao XY, Pasuelo MJ, Wallace S, Li C. Synthesis and characterization of branched poly(L-glutamic acid) as a biodegradable drug carrier. J Control Release 2004;94(1):39-51.

53. Martens PJ, Bryant SJ, Anseth KS. Tailoring the degradation of hydrogels formed from multivinyl poly(ethylene glycol) and poly(vinyl alcohol) macromers for cartilage tissue engineering. Biomacromolecules 2003;4(2):283-292.

54. Merrill EW, Dennison KA, Sung C. Partitioning and diffusion of solutes in hydrogels of poly(ethylene oxide). Biomaterials 1993;14(15):1117-1126.

55. Canal T, Peppas NA. Correlation between mesh size and equilibrium degree of swelling of polymeric networks. J Biomed Mater Res 1989;23(10):1183-1193.

56. Cruise GM, Scharp DS, Hubbell JA. Characterization of permeability and network structure of interfacially photopolymerized poly(ethylene glycol) diacrylate hydrogels. Biomaterials 1998;19(14):1287-1294.

57. Temenoff JS, Athanasiou KA, LeBaron RG, Mikos AG. Effect of poly(ethylene glycol) molecular weight on tensile and swelling properties of oligo(poly(ethylene glycol) fumarate) hydrogels for cartilage tissue engineering. J Biomed Mater Res 2002;59(3):429-437.

58. Marsano E, Gagliardi S, Ghioni F, Bianchi E. Behaviour of gels based on (hydroxypropyl) cellulose methacrylate. Polymer 2000;41(21):7691-7698.

59. Wieland JA, Houchin-Ray TL, Shea LD. Non-viral vector delivery from PEG-hyaluronic acid hydrogels. J Control Release 2007;120(3):233-241.

60. Baier Leach J, Bivens KA, Patrick CW, Schmidt CE. Photocrosslinked hyaluronic acid hydrogels: natural, biodegradable tissue engineering scaffolds. Biotechnol Bioeng 2003;82(5):578-589.

61. Zamyatnin AA. Amino acid, peptide, and protein volume in solution. Annu Rev Biophys Bioeng 1984;13:145-165.

62. Bryant SJ, Anseth KS. Hydrogel properties influence ECM production by chondrocytes photoencapsulated in poly(ethylene glycol) hydrogels. J Biomed Mater Res 2002;59(1):63-72.

63. Stopa B, Rybarska J, Drozd A, Konieczny L, Krol M, Lisowski M, et al. Albumin binds self-assembling dyes as specific polymolecular ligands. Int J Biol Macromol 2006;40(1):1-8.

64. Feng Liu LH. Improving plasmid DNA-mediated liver gene transfer by prolonging its retention in the hepatic vasculature. J Gene Med 2001;3(6):569-576.

65. Raeber GP, Lutolf MP, Hubbell JA. Molecularly engineered PEG hydrogels: a novel model system for proteolytically mediated cell migration. Biophys J 2005;89(2):1374-1388.

66. Mellott MB, Searcy K, Pishko MV. Release of protein from highly cross-linked hydrogels of poly(ethylene glycol) diacrylate fabricated by UV polymerization. Biomaterials 2001;22(9):929-941.

CHAPTER FOUR

Nanoimprint Lithography Techniques for Fabrication of Injectable, Intracellular Drug Delivery Nanoparticles of Specific Size and Shape

4.1 INTRODUCTION

Nanoparticle-based delivery of therapeutics has been extensively studied in a variety of diseases and is considered to be an ideal platform for targeted intravenous and intracellular delivery of bioactive agents. Current concepts in the synthesis of drug nanocarriers primarily involve the use of polymers or lipids to fabricate self-assembled or emulsion-based particles that are mostly spherical, polydisperse, and release drugs through diffusion or hydrolytic degradation. Although significant progress has been made in polymeric or liposomal drug delivery systems, there remain critical limitations in synthesizing nanocarriers with highly controllable architectures that can, at the same time, incorporate multiple functionalities. Our ability to precisely manipulate size, shape, composition, and drug release mechanism of nanoparticles is essential for controlling their in-vivo transport, biodistribution, and therapeutic efficacy [1-3].

Recent reports suggest that particle shape could play a significant role in the in-vivo performance of delivery vehicles [4, 5]. Specifically, shape and shape-related form factors, like aspect ratio or edges, affect particle transport characteristics, influence cell-particle interactions, and alter drug release kinetics [4, 6]. Ferrari and colleagues have shown through theoretical modeling that shape and size of nanovectors and spherical and spheroidal nanoparticles can significantly affect how particles interact with tumor

capillaries during transport [7, 8]. Discher and colleagues demonstrated that self-assembled, filamentous particles with very high aspect ratios (less than 100 nm diameter with several microns in length) have unique long-circulating properties compared to traditional spherical liposomes [5]. Until recently, particle shape has been an unexplored area of research in drug delivery due to our inability to reliably synthesize nano or microparticle carriers with precise and pre-designed geometry.

Several groups have demonstrated the ability to create such shape-specific and monodisperse microparticles using techniques varying from microfluidics, self-assembly, photopolymerization, micromolding and lithography [4, 9-13]; however, there are in fact only a few methods that have been developed to fabricate particles with varying shape and size, especially at the nanoscale. Recently, Mitragotri and colleagues reported a unique solvent-based method to generate polystyrene micro and nanoparticles of various shapes with feature sizes as low as 60 nm [14]. The technique involved stretching particles into a film, heating (120 – 150^{o}C) or placing the film in solvent, and dissolving the film; however, it remains to be studied how these methods are translated to biopolymers.

Currently, the concept of a shape-specific, injectable nanocarrier capable of systemic, intracellular delivery of therapeutics has not fully been explored, especially at the sub-100 nm size. While particles below 500 nm in size can be injected intravenously, only those below 200 nm are efficiently internalized by somatic cells. Reports also suggest that delivery into the lymphatic circulation requires particles that are even smaller in size (< 50 nm) [15]. Significant technological challenges exist in fabricating such

small nanocarriers with a pre-designed geometry and the potential for tunable in-vivo properties; therefore, new nano-scale fabrication techniques are necessary to create such drug delivery devices. Recent advancements in nano-scale fabrication using nanoimprint lithography techniques could provide new approaches for top-down, high-throughput, large scale fabrication of size and shape-specific nanoparticles for drug delivery applications.

DeSimone and colleagues have recently demonstrated top-down nanofabrication to create nanoparticles of specific size and shape, as small as 160 nm using the particle nano-replication (PRINT) method [16-18]. They reported the ability to form nano-size PEG diacrylate (PEGDA) and poly(lactic acid) (PLA) particles using a photocurable perfluoropolyether (PFPE) stamp that is non-wetting to both inorganic and organic materials. Thus formation of particles without a residual film between them was accomplished. To fabricate PLA particles, PLA was in-situ polymerized at 110^{o}C to mold the polymer solution. PEG particles were formed by imprinting and photopolymerization. PEG particles were fabricated in a variety of shapes (trapezoidal, conical, bar and arrow shapes) with sizes ranging from 200 nm to 3 μm. Furthermore, encapsulation of avidin-FITC and doxorubicin in 500 nm PEG particles was demonstrated.

Recently, DeSimone and colleagues demonstrated an improvement in monodispersity when compared to current liposomes [18]. This suggests that top-down fabrication does indeed produce monodisperse nanoparticles using biopolymers. The use of a top-down approach could ensure precise control of particle size and geometry, creating a monodisperse population of particles, therefore yielding better reproducibility

and prediction of properties than current self-assembly and emulsion-based nanoparticle systems. A top-down approach could further allow for incorporation of multiple functionalities, such as targeting, loading multiple agents, and stimuli-responsiveness.

In any fabrication process involving therapeutics or biologics, harvesting of nanoparticles into a usable form is of considerable importance. A major limitation in the PRINT fabrication process is the mechanism of particle harvesting. Currently, the PRINT particles are harvested from the wafer either using physical scraping with surgical blades or by shear force using a glass slide [16-18], both of which could damage the particles and may not be suitable for large scale manufacturing. Although the PRINT fabrication method has demonstrated fabrication of 160 nm conical particles, the process is not immediately scalable and utilizes methods of particle release that could damage the particles. It is evident that successful translation of any top-down nanofabrication technologies to drug delivery applications would require development of techniques that are mild and compatible with a variety of biological molecules. Furthermore, any such technique must allow easy harvesting of nanoparticles and ability to incorporate unique functionalities, such as disease-triggered drug release.

This research provides a more in depth overview of nanoimprint lithography techniques, thermal nanoimprint lithography (ThNIL), and step and flash imprint lithography (SFIL), and discusses the optimization of the process characteristics and materials for imprinting biocompatible polymers and materials. We hypothesized that utilizing semiconductor nanoimprint lithography techniques to pattern biocompatible polymers would enable us to fabricate monodisperse, injectable drug nanocarriers of

precise shape and size suitable for intracellular drug delivery applications. In this research we demonstrate the use of ThNIL and SFIL, coupled with biocompatible polymer and crosslinked networks to imprint monodisperse injectable nanoparticle of pre-designed sizes and geometries as small as 50 nm. Particles of varying shape (square, circular, pentagonal, and triangular), size (50 - 400 nm), and composition (PMMA, PLGA, PEG) were fabricated using these techniques. We have demonstrated full wafer imprinting and successful isolation and release of the particles from the wafer using a mild harvesting method. The SFIL method, with its low temperature and force applications, as well as wafer-scale imprinting capability, was more suitable for large scale fabrication and was chosen for further optimization.

4.1.1 Overview of Step and Flash Imprint Lithography (SFIL) and Thermal Imprint Lithography (ThNIL)

Several recent advancements in nanomanufacturing methods could provide new approaches for top-down, high-throughput, large-scale fabrication of nanocarriers for drug delivery applications. One of the most promising nanoimprinting techniques is the step and flash imprint lithography (SFIL) method invented by Wilson and colleagues at UT Austin. The SFIL process [19-25], shown in **Figure 4.1**, is essentially a nanomolding process in which the topography of a template defines the patterns created on a substrate. In brief, a transparent quartz template is treated with a release agent to facilitate substrate separation. Next, a low viscosity, UV curable, organosilicon monomer is dispensed onto a silicon substrate. The gap between the template and substrate is closed, using low

pressure at room temperature. Following this, the quartz template is irradiated with UV light. The transparency of the quartz allows the UV light to pass through and photopolymerize the monomer beneath the template. When the template is separated from the substrate, the cured monomer on the substrate retains the desired 3D nanotopography. As shown in **Figure 4.2**, this is a step and repeat process. Therefore the wafer is stepped and the process is performed again in the next field. Once the entire wafer has been patterned, further processing with oxygen plasma cleaning removes residual monomer for distinct features.

SFIL has several advantages over conventional lithography and micromolding processes. Unlike conventional lithography, imprint lithography does not use energetic beams, therefore it is not diffraction limited. SFIL is only limited by the resolution of the imprint template created by e-beam lithography. Recent work has demonstrated 20 nm lines using the SFIL process. Traditional micromolding requires high pressures (> 10 MPa) and temperatures (> glass transition temperature of the polymer film), which may distort nanofeatures. SFIL uses a low-viscosity (~ 2-3 cps), photocurable, monomer that allows high resolution features to be imprinted at room temperature with minimal pressure (< 1 psi). Furthermore, the reusable transparent quartz template enables sub-10 nm alignment of nanofeatures, a task very difficult in other processes. Finally, 3D structures can accurately be replicated by the SFIL process, and patterns can be imprinted on top of existing topography by using an appropriate planarization material. The availability of pre-existing equipment (IMPRIO 100) in cleanroom facilities and ease of

high-fidelity replication of features, suggests the potential capability of high-throughput and low cost manufacturing of nanoparticles for drug delivery.

Another nanoimprint method with potential for fabricating nanocarriers is thermal nanoimprint lithography. First proposed in 1995 by SY Chou [26, 27], the process consists of imprinting with a reusable Silicon template and pattern transfer with RIE. However, in contrast to SFIL, thermal nanoimprint lithography requires heating a polymer above its glass transition temperature and applying considerably more pressure. Upon cooling, the polymer hardens into a desired 3D nanotopography. This method has shown the ability to create sub-20 nm features. As with SFIL, this method is advantageous in that its resolution is limited only by the template fabrication process and it is capable of replicating precise 3D features. The SFIL and ThNIL techniques have the potential to create well-defined and characterized drug delivery particles without the limitations of self-assembly, or emulsion techniques.

4.1.1.1 SFIL: IMPRIO 100

The IMPRIO 100, shown in **Figure 4.3A**, is fabricated by Molecular Imprints and is used to perform step and flash imprint lithography. The tool is a precise mechanical system that incorporates a motorized z-head, a fluid dispensing system and a mercury arc lamp, shown in **Figure 4.3C-F**. The IMPRIO has a wafer loading station and template loading station on the front of the tool as seen in **Figure 4.3B**. Within the wafer loading station there is a semi-automated wafer handler that can load wafers (ranging from 2” to 8”) onto a wafer chuck inside the tool (**Figure 4.3D**). The IMPRIO 100 has dual dispense

tips connected to monomer storage vials for the use of two different monomers (**Figure 4.3E-F)**, and has software as well as hardware to create a drop pattern recipe to imprint with these monomers. The fluid dispense system uses a piezo electric ink jet head to dispense droplets smaller than 5 nL (**Figure 4.3E**) [28], with the dispense volume directly proportional to the length of the voltage pulse applied. A typical dispense uses multiple drops of 200 pL.

Figure 4.4 shows a schematic of how the motorized z-head and wafer chuck are situated within the tool. A wafer is loaded onto the wafer chuck, which sits on a vacuum preloaded XY air bearing stage. The template is loaded in the template chuck beneath the z-head and held by vacuum. Following this the template is aligned and leveled to the stage with an upward air gauge; the wafer is subsequently leveled to the stage with a downward air gauge [20]. When the user is ready to imprint the motorized z-head lowers the template towards the wafer, and a flexure ring allows the wafer to match the orientation of the template. Following this a mercury arc lamp provides UV light at 365 nm, which is then collimated by a lens and reflected by a mirror onto the backside onto the template/wafer interface [25]. Throughout the imprinting process Helium gas is supplied around the wafer chuck to displace oxygen so that the monomer can be fully photopolymerized.

4.1.1.2 SFIL: IMPRIO 100 Optimization Parameters

Key factors to obtaining uniform, low residual layer, imprints involve minimization of particles in the environment, flatness of the wafer, a non-wetting release

layer on the template, a suitable fluid for dispensing and an optimized imprinting recipe. The Graphical User Interface (GUI), displayed on the computer screen (**Figure 4.3A**) allows an operator to create recipes, optimize the imprinting and troubleshoot any problems. Within the recipe, the dispensing parameters, imprint force, pre-exposure delay (prior to UV exposure), and UV exposure setting can be set. The imprint force typically used is 2-3 N, but can be varied to optimize the recipe. Changing the pre-exposure delay changes the length of time that the fluid spreads while under the set force, and the UV exposure time dictates the time that the fluid will be exposed to the UV light source. The optimal release force of the substrate from the template is typically ~ 10 N.

Dispensing parameters are optimized by changing the drop box size, drop offset, volume per drop and overall volume per imprint in the Drop Layout Panel, as seen in **Figure 4.5**. The drop box size sets the boundary for where the drops will be placed and the drop offset moves the location of the drops. The volume per drop and location of each drop can be changed as well to provide a more uniform imprint. The overall volume of the liquid, as well as the pattern density of the template, helps determine the residual layer of an imprint.

4.2 MATERIALS AND METHODS

4.2.1 Polymers and Reagents

Chromium was purchased from Williams Advanced Materials. Four inch p-type <100> silicon test wafers single-side polished were ordered from Silicon Quest

International. Four inch p-type <100> silicon test wafers (both single-side polished and double-side polished) were purchased from University Wafers. Four inch p-type <100>, double-side polished, prime silicon wafers with and without an epitaxial layer of silicon on one side were purchased from Montco Silicon Technologies. ZEP 520A and Zedn50 (ZEON Corp.) were provided by the NNIN and MRC at The University of Texas Pickle Research Center. Quartz templates were purchased from the Canadian National Research Center and from the NNIN and MRC at The University of Texas Pickle Research Center. Isopropyl Alcohol (IPA), Acetone, N-Methyl Pyrrolidone (NMP) and other cleanroom processing chemical provided by the NNIN and MRC at The University of Texas Pickle Research Center. Poly(ethylene glycol) diacrylate (PEGDA, MW 3400) was purchased from Nektar Therapeutics. Poly(ethylene glycol) diacrylate (PEGDA, MW 700) was purchased from Sigma Aldrich and poly(ethylene glycol) diacrylate (PEGDA, MW 1000) was purchased from Polysciences. The ultraviolet (UV) photoinitiator, 2-hydroxy-1-[4-(hydroxyethoxy) phenyl]-2-methyl-1 propanone (I2959) was purchased from Ciba Geigy. Polymethyl methacrylate (PMMA, MW 950k and 450k) in Anisole was purchased from MicroChem. Poly(lactide co-glycolide) (PLGA) Resomers 502H (MW 11,000), 503H (MW 25,000) and 502A (MW 12,000) were purchased from Boehringer Ingelheim. A glass viscometer tube (size 100) (viscosity range: 1 – 30 cSt) was ordered from Fisher Scientific. BARC DUV-30J (Brewer Sciences) was supplied by NNIN and the MRC at the University of Texas Pickle Research Center. Tridecafluoro-1,1,2,2-Tetra-Hydrooctyl Dimethylchloro-silane was purchased from Gelest Inc, and toluene was purchased from Sigma. Relmat (Molecular Imprints) was supplied by the NNIN and MRC at the

University of Texas Pickle Research Center. Poly(vinyl alcohol) (PVA, MW 31000) (Fluka) and Dicloromethane (DCM) were purchased from Sigma.

4.2.2 Template Fabrication Process

4.2.2.1 Thermal Imprint Lithography Template

In order to make monodisperse drug delivery particles, patterns were first drawn in L-Edit, a CAD type program, and converted for use with the (JEOL JBX-6000 FS/E) e-beam lithography tool. For the nanoimprint lithography process a reusable nanoimprint template with various shapes and sizes was created using electron beam lithography (EBL) and reactive ion etching (RIE). A schematic of the process is shown in **Figure 4.6**. In brief, four inch p-type <100> silicon test wafers were pre-cleaned with Piranha. The wafers were then pre-baked (180^{o}C, 2 min), spin coated with ZEP520 (3000 rpm for 60 s), and finally post-baked on a hotplate (180^{o}C, 2 min). Next the wafers were patterned using e-beam lithography (JEOL JBX-6000FS/E) with the following process parameters: EOS mode 7, 50 kV, 100 pA, exposure level/dose: 20 to -20. Following this the wafers were developed with ZED n50 (60 s), and rinsed with IPA (30 s).

In order to create patterns of precise size and shape in silicon templates, dose testing was performed with varying e-beam exposure time and developing times to find the optimal parameters for varying shapes and sizes. Different sizes of nanocontainer-shaped features ranging from 100 to 800 nm were exposed at various exposure levels and

developed at various times. Microscopy and SEM were used to determine the parameters that yielded the most distinct features.

After developing the wafer, they were dry etched (3 min 30 s) using a Plasma Therm 790 Series Reactive ion etcher (RIE) at a pressure of 80 mTorr, a power of 200 Watts and the following gases: HBr (49) , Cl_2 (5), He (80) to etch the silicon surface below. In order to make container shaped features, the e-beam and RIE process was performed again, utilizing alignment marks that were fabricated during the first process. Subsequently, the wafers were diced to a size of ~ 1 mm and cleaned with Piranha.

4.2.2.2 Step and Flash Imprint Lithography Template

Figure 4.7 shows the structure and layout of a typical template. Four quartz templates are diced from a larger 6" x 6" substrate. The template contains two primary regions, the active field area and the 15 μm recessed non-active area. The active field is called the mesa. The mesa can be fabricated in a wide variety of sizes ranging and is the area where patterns are created. In order to make monodisperse drug delivery particles, patterns were first drawn in L-Edit, a CAD type program, and converted for use with the (JEOL JBX-6000 FS/E) e-beam lithography tool. To create features in the mesa of the quartz template (see **Figure 4.8**) a 100 Å layer of chromium was evaporated on the surface of a two inch square quartz template with a pre-fabricated mesa, using the CHA Evaporator. Next, the quartz template was spin coated with ZEP 520 (3000 rpm for 60 s), and finally post-baked in an oven (180^{o}C, 10 min). Prior to actual e-beam writing, the true center of the mesa was found by locating the X and Y edges of the mesa, using the

SEM capabilities of the e-beam, and calculating the center point. This center point was then subtracted from the center point of the e-beam, and the offset parameters were input into a recipe.

The quartz template was then patterned using e-beam lithography (JEOL JBX-6000FS/E) with the following process parameters: EOS mode 7, 50 kV, 100 pA, exposure level/dose: 60 to -60. The template was then developed with ZED n50 (2 min), rinsed with IPA (30s). Prior to actual etching of the mesa, dose tests were performed each time to find the optimum parameters for the e-beam dose as well as the development times due to variability of the e-beam. The templates were then etched with two RIE processes: one to etch the chromium and one to etch the quartz. For the template with the 25 x 25 mm mesa, the chromium layer was dry etched using a Plasma Therm Batchtop RIE for 2 minutes. Subsequently the quartz layer was dry etched with an Orange RIE with a power of 150 Watts and the following gases: CHF_3 (60), O_2 (40) for 7 min. The chromium layer was then removed with a wet etch (chromium etchant 1020) at 40^{o}C for several minutes.

For the templates with the 12.5 x 12.5 mm mesa and the 10 x 10 mm mesas, the chromium layer was dry etched using a Trion RIE. First a descum was used to remove any residual ZEP520 at a pressure of 35 mTorr, a power of 20 Watts and the following gases: O_2 (2), He (70) for 90 seconds. Following this, the chromium layer was etched at a pressure of 30 mTorr, a power of 80 Watts and the following gases: O_2 (10), He (70) for 180-200 seconds. Subsequently the quartz layer was dry etched in the same tool at a pressure of 15 mTorr, a power of 130 Watts and the following gases: CF_4 (15) and He

(40) for times ranging from 400 to 1000 seconds. The chromium layer was then removed with a wet etch (chromium etchant 1020) at 40^{o}C for several minutes. The chrome etch time was optimized for chrome removal of 15 nm, and the quartz etch process was specified for an average etch rate of 30 nm/min depending on the feature sizes. For the 12.5 x 12.5 mm mesa the quartz was etched 540 seconds. For the 10 x 10 mm mesa, 400 and 200 nm features were etched for 1000 seconds, and the 100 and 50 nm features etched 400 seconds. After each processing step the template was viewed using microscopy or AFM to see if the etched layer was removed.

4.2.3 Thermal Imprint Lithography Process Development

4.2.3.1 Template Release Layer Preparation

Prior to imprinting, a release layer was placed onto the template to prevent adhesion to the template. Dow Corning (DC 20) was diluted 1:8:1 in isopropanol (IPA) and toluene, respectively. This solution was then diluted 1:200 in xylene and spin-coated onto the stamp at 5000 rpm for 30 seconds, as described by Chen and colleagues [29]. The template was then oven baked (10 min, 180^{o}C).

4.2.3.2 Imprinting PMMA

The setup for the thermal imprinting process included a chromium coated ceramic heater chuck and a micromanipulator with a built in force-sensor connected to power supplies, multimeters, and a thermocouple. Prior to imprinting, the sensor and metal base were cleaned using acetone to remove any particles and double-sided sticky tape was

placed on the base of the device and the sensor. This allowed the substrate to adhere to the base of the device and the template to adhere to the sensor. Prior to imprinting, the imprint template was treated with a self-assembled monolayer (SAM) of Dow-Corning release agent 20 in order to facilitate the separation of the template from the substrate. Small silicon wafers pieces were diced and primer was spin-coated at 4000 rpm for 30s onto the wafer pieces.

Next, 11% (w/v) PMMA (MW 950k) in Anisole was spin-coated onto the wafer pieces for an optimal thickness of 300 nm, based on the manufacturers spinning specifications. Subsequently the substrate was adhered to the base, and the template was adhered to the sensor. The sensor was then aligned to the metal conducting base such that the surfaces would be parallel. The PMMA film was then heated above its glass transition temperature (105^{o}C) using a heater chuck under the wafer (the base was left to heat up to 150 – 200^{o}C). Following this the imprint template was pressed into the PMMA for 10 – 15 minutes using the micromanipulator with a built-in force sensor. A voltage of 3.9 – 3.8 mV was optimized for an imprint depth of about 200 nm. Subsequently, the micromanipulator was raised and the wafer substrate was removed. Finally, residual PMMA was removed with a timed oxygen plasma cleaning using a Plasma Therm 790 Series Reactive ion etcher (RIE) with a pressure of 180 mTorr, a power of 50 Watts and O_2 (80) to etch the silicon surface below. The PMMA particles were removed by sonication in dH_2O.

4.2.3.3 Characterizing PLGA Thickness for Imprinting

In order to determine the thickness of PLGA for spinning onto wafers and for use with thermal imprinting, various poly(lactic-co-glycolic acid) (PLGA) concentrations and solvents were utilized. Resomers 502H, 503H and 502A were dissolved in either acetone or dicloromethane (DCM) to form 3 – 8% (w/v) concentrations and were spin coated at various speeds and times onto primed silicon wafer pieces. Following spin-coating, four or more samples of each variation were analyzed with an M-2000D1 Ellipsometer using a wavelength range of 400 – 1200 nm. Subsequently, the Cauchy characteristics were fitted and the sample thicknesses were determined using the Ellipsometer and a NanoSpec AFT.

4.2.3.4 Imprinting with PLGA

The thermal nanoimprint process was performed on poly(lactic-co-glycolic acid) (PLGA), Resomers 502H, 503H and 502A, and dissolved in either acetone or dicloromethane (DCM) to form 3 – 8% (w/v) concentrations. Prior to imprinting, the imprint template was treated with a self-assembled monolayer (SAM) of Dow-Corning release agent 20 (DC20) in order to facilitate the separation of the template from the polymer layer. Next, wafer pieces were diced and a PLGA layer was spun on the silicon wafer pieces based on the spin-speed curve generated previously. The PLGA was heated slightly above its glass transition temperature (52^{o}C) using a Kapton thin film heating element (Watlow) under the wafer. Subsequently, the imprint template was pressed into the PLGA for 10 minutes using a micromanipulator with a built-in force sensor. The

template was then lifted using the micromanipulator and separated from the wafer after the wafer temperature had reduced to 40^{o}C.

4.2.4 Step and Flash Imprint Lithography Process Development

4.2.4.1 Template Release Layer and Substrate Optimization

In order to imprint whole wafers without the PEGDA solution adhering to the template, two different template coating layers were evaluated: Relmat and a self-assembled monolayer (SAM) of (Tridecafluoro-1,1,2,2-Tetra-Hydrooctyl) Dimethylchloro-silane. Before applying the release layers the quartz template was cleaned using a 30 minute Piranha treatment. If the template was exceptionally dirty, an NMP clean was performed for a minimum of 2 hours, followed by another Piranha treatment. Following this the template was rinsed 5 times in water, post baked in a 90^{o}C oven and then rinsed with IPA to provide a clean hydroxylated surface.

The Relmat was applied using a dropper. Two to three drops of Relmat were placed onto the mesa of the quartz template and subsequently blown dry with Nitrogen. In order to coat the template with the SAM, 100 mL of a 0.5% (v/v) solution of (Tridecafluoro-1,1,2,2-Tetra-Hydrooctyl) Dimethylchloro-silane in toluene was placed in a glass container. The quartz template was then placed in the solution for a minimum of 2 hours. The SAM is formed by reacting the hydroxylated surface of the quartz template with the silane to create a networked siloxane monolayer.

After employing the Relmat and SAM on the quartz template, contact angle measurements were taken using a goniometer (First Ten Angstroms (FTA)) to see the

difference in wettability of the two templates (n=3). The templates were used to imprint various polyethylene glycol (PEG) polymers (PEGDA MW 3400 and MW 700) with and without a peptide-crosslinker, and with a variety of encapsulated proteins as well as DNA.

The initial imprints were performed using a standard Relmat release and a single-side polished test silicon wafer. Following this, imprints were attempted using Relmat and a 100 nm layer of 5% (w/v) PMMA (MW 450k) which was spin-coated on the silicon wafer. Subsequently imprinting was attempted using Relmat and a double-side polished wafer with PMMA. Following this, imprints were performed using a double-side polished wafer and an anti-reflective coating, BARC. Double-side polished wafers were spin-coated with a 60 nm BARC layer (3000 rpm, 60 s). Subsequently, imprinting was performed using the template coated with a SAM of 0.5% (v/v) (Tridecafluoro-1,1,2,2-Tetra-Hydrooctyl) Dimethylchloro-silane in toluene and a wafer with BARC. Finally imprints were performed with the SAM, BARC and a double-side polished silicon wafer with an epitaxial layer of silicon.

4.2.4.2 PEGDA Viscosity Measurements and Dispense Tip Calibration

In order to dispense polymer solution from the dispense tips in the IMPRIO, the viscosity of various concentrations of PEGDA solutions was measured using a viscometer. PEGDA (MW 700) was dissolved in dH_2O to form various weight percentages ranging from 25%, 33%, 50%, 60% and 75% w/v. Five milliliters of pre-polymer solution was placed into the large tube of the viscometer and suctioned into the

measuring area using a large bulb. Once the bulb was removed, the time for the solution to travel from mark A to B was measured. The experiments were performed in triplicate. The kinematic viscosity of the solution was calculated by multiplying the time for the solution to travel from A to B, by an intrinsic constant of the viscometer. The dynamic viscosity was then calculated by multiplying the kinematic viscosity by the bulk density of PEG (1.12 g/mL). Based on the viscosity results, Molecular Imprints calibrated the imprint tip to dispense the polymer solution. Prior to dispensing, the solution was filtered with a maximum 4 nm filter.

4.2.4.3 Imprinting PEGDA

Step and Flash Imprint Lithography was performed using the IMPRIO 100 SFIL system (Molecular Imprints, Austin TX) with various macromers that were drop-cast either manually or through the IMPRIO automated dispenser onto 4 inch silicon wafers. nanoimprinting was evaluated using various polyethylene glycol (PEG) polymers (PEGDA MW 3400 and MW 700) with and without a peptide-crosslinker, with concentrations varying from 25% to100% w/v. Volumes of 0.5 μL (for manual dispensing) to 0.019 μL (for automated dispensing) were evaluated along with an imprinting force of 2-18 N. The pre-polymer solution was prepared in dH_2O and 0.05 to 0.07 wt% of the UV photoinitiator, Irgacure 2959. The UV exposure time was varied from 5 to 30 seconds, and the pre-exposure delay was varied from 120 seconds to 450 seconds.

Figure 4.9 shows a schematic of the process used to create PEGDA nanoparticles of precise size and shape. Prior to imprinting, the template was coated with a SAM of 0.5% (v/v) (Tridecafluoro-1,1,2,2-Tetra-Hydrooctyl) Dimethylchloro-silane in toluene. Subsequently, four inch silicon wafers were spin-coated with a 60 nm BARC layer (3000 rpm, 60 s). To allow for particle release, a second layer (53 nm) of water soluble 2% (w/v) poly(vinyl alcohol) (PVA, MW 31000) was spin-coated on the BARC (3000 rpm, 60 s). The PEG macromer solution was then imprinted at low pressure and with UV light in order to polymerize the solution. In order to isolate the imprinted particles, the residual layer between the nanoparticles was removed by an oxygen or helium plasma etch using a Plasma Therm 790 Series RIE, or with no etching. To release the imprinted nanoparticles, dH_2O was applied to the imprints and gently pipetted up and down to help dissolve the water soluble PVA release layer.

4.2.4.4 Residual Layer Optimization

In order to optimize the residual layer for PEGDA (MW 700) of various macromer concentrations ranging from 75% (w/v) to 25% (w/v) were imprinted with an array of parameters. The dispensing parameters, imprint force, exposure time and pre-exposure delay was optimized. In order to optimize the dispensing parameters, the drop box size, drop location, volume per drop, and overall volume were optimized to provide an even imprint with the lowest possible overall volume of solution and the least number of air bubbles. The dispensing parameters were first optimized using a drop simulation

model, and then through imprinting. The PEGDA residual layer thickness was determined used an SEM, an M-2000D1 Ellipsometer, and a NanoSpec AFT.

4.2.4.5 Optimization of Isolation and Harvesting of Nanoparticles

In order to isolate and release the imprinted nanoparticles from the silicon wafer it is many times necessary to first remove the residual layer in between the particles. This was initially performed by oxygen plasma etching (Plasma Therm 790 Series Reactive Ion Etcher (RIE)). For oxygen etching, the residual layer was etched at a pressure of 180 mTorr, a power of 50 Watts and oxygen: O_2 (18) for 20-60 seconds. Once the residual layer was further optimized, helium etching was also performed at a pressure of 180 mTorr, a power of 50 Watts and helium: He (85) for 20 seconds. To verify that the imprinted particles retain their 3D structure after etching and to measure the feature height, particles were analyzed using atomic force microscopy (AFM). XPS was used to see any change that occurred to the PEGDA surface due to the etching process.

In order to release the nanoparticles, a sacrificial layer of water soluble poly(vinyl alcohol) (PVA) (53 nm) was spin coated (3000 rpm, 60 seconds) on top of a BARC layer (60 nm) prior to macromer dispensing and imprinting. PEGDA solutions of varying concentration were dispensed and imprinted on the BARC and PVA coated wafer. Following residual layer etching, 20 μL of dH_2O was placed on the imprint and rinsed with pipetting. Upon optimization of the residual layer, particles were released without the need for etching. SEM was used to verify particle release of both etched and non-etched released particles.

4.2.4.6 Theoretical Number of Nanoparticles and Drug Loading Capacity

The theoretical number of particles per template and per wafer was calculated based on varying template size, wafer size, and particle size, shape, and spacing. From this, the theoretical loading capacity was calculated assuming a 10 mg/mL solution of model drug in macromer. The actual number of particles for the latest fully patterned 10 x 10 mm mesa was also calculated, as well as the theoretical loading capacity. To get the number of particles per mesa (M), the following equation was used:

$$M = C * A \tag{1}$$

where *C* is the number of features in a chip (dictated by the number drawn in L-edit) and *A* is the number of times the chip is arrayed in the e-beam to pattern a mesa of a given size. To get the number of particles per wafer (*W*) the following equation was used,

$$W = M * F \tag{2}$$

where F is the number of imprintable fields for a given wafer size. The number of imprintable fields (**Table 4.1**) was given by the manufacturer's literature and/or estimated through discussions with technicians. In order to calculate the mass of drug per imprint (D_M), the following equation was used:

$$D_M = M * V * C \tag{3}$$

where V is the volume of the particle shape, and C is the concentration of the drug in the macromer solution. To get the mass of drug per wafer (D_w), the following equation was used:

$$D_W = D_M * F \tag{4}$$

and to calculate the loading level per number of particles, D_w was divided by W.

4.3 RESULTS

4.3.1 Template Process Development

4.3.1.1 Thermal Imprint Lithography Templates

In order to create patterns of precise size and shape in silicon templates, dose testing was performed to find the optimal parameters. **Figure 4.10** reveals a typical dose test that was performed. Using the dose tests, the template fabrication parameters were optimized to an exposure level/dose: 20 to -20, with a development in ZED n50 of 60 s, and a rinse time of 30 sec with IPA. The SEM images in **Figure 4.11** demonstrate the results of the optimized parameters along with reactive ion etching to create nanofeatures in the silicon template. Large-area, dense arrays of nanocontainer features with sizes ranging from 100 to 800 nm were successfully patterned into the silicon (**Figure 4.11A-D**). The smaller features have more noticeably rounded corners due to the resolution limits of the e-beam process, and no longer appear square. **Figure 4.11E-F** shows a profile view of the nanofeatures after reactive ion etching to reveal a depth of approximately 200 nm with anisotropic side walls.

4.3.1.2 Step and Flash Imprint Lithography Templates

In order to create patterns of precise size and shape in quartz templates, dose testing was performed to find the optimal parameters as described for the silicon template. Using the dose tests, the template fabrication parameters were optimized to an exposure level/dose: 60 to -60, with a development in ZED n50 of 2 min, and a rinse time of 30 sec with IPA. **Figure 4.12A-C** shows a schematic of the varying template mesa sizes that were patterned. 25 x 25, 12.5 x 12.5 and 10 x 10 mm mesas were patterned with varying shapes, sizes and spacing ranging. For the 10 x 10 mm mesa with 50 nm features, **Figure 4.12C**, the dose level was optimized to be: 5 to -5. This schematic also shows that two patterned areas were not centered correctly due to the initial process of inputting an offset value for the center of the mesa. **Figure 4.12D** shows a schematic of a fully patterned 10 x 10 mm mesa with 100 nm features and 2:1 spacing, and **Figure 4.12E** shows a fully patterned mesa donated by Molecular Imprints with various spacing and feature sizes ranging from 80 to 100 nm.

SEM images of the patterned mesas, as seen in (**Figure 4.13**), show large-area, dense arrays of features with sizes ranging from 50 to 400 nm. Pentagons, squares, triangles and boxes were successfully patterned with precise size and shape. The smaller features (< 100 nm) have more noticeably rounded corners due to the resolution limits of the e-beam process, and no longer appear square.

4.3.2 Thermal Imprint Lithography Process Development

4.3.2.1 ThNIL Imprinted PMMA Nanocontainers

As demonstrated in **Figure 4.14**, pattern transfer was successfully achieved and three-dimensional PMMA nanocontainers of sizes 100 nm (not shown) up to 800 nm were successfully fabricated using the thermal nanoimprint lithography techniques. The 200 nm nanocontainers, shown in **Figure 4.14**, contained side walls that were 50 nm thick, with a 100 nm open container.

4.3.2.2 PLGA Thickness Measurements

In order to first determine the PLGA thickness the Cauchy characteristic values were determined using the M-2000D1 Ellipsometer (**Figure 4.15A**). The Cauchy characteristics provide a means to calculate the refractive index. The (A) value can be taken to be roughly the refractive index of the material. The refractive index for the PLGA with various formulations ranged from 1.46 to 1.52. Using the refractive index, we were able to determine the thickness using both the M-2000D1 and the NanoSpec AFT. **Figure 4.15B** shows the spin-speed thickness curve for an optimized spin time of 50 seconds. The PLGA 502A and the 502H in acetone had a clear appearance after spinning, while the 503H and 502H in DCM appeared cloudy. The results of the spinning study indicated that for a 200 to 300 nm thick film, the 5% (w/v) 503H, the 3% and 5% (w/v) 502A, and the 5% (w/v) 502H would be the best candidates for imprinting with our template.

4.3.2.3 ThNIL Imprinted PLGA Nanofeatures

Imprinted features were obtained with the PLGA 502H at 5% (w/v) in acetone and DCM with a spin speed of 3500 rpm. **Figure 4.16A** demonstrates imprinted PLGA features using DCM as a solvent, and **Figure 4.16B** demonstrates imprinted PLGA features using acetone. The features appear to be shallow and slightly defined, and the PLGA in acetone appears to have gaps in the film.

4.3.3 Step and Flash Imprint Lithography Process Development

4.3.3.1 Template Release Layer and Substrate Optimization

The contact angle measurements, shown in **Table 4.2**, revealed that the contact angle of the Relmat on the 10 x 10 mm mesa with 100 to 400 nm features was roughly 92.7^{o} over the patterned features and 92^{o} over the smooth quartz surface. Meanwhile, the contact angle of the SAM varied from 109 to 102^{o} over the 400 to 100 nm patterns, respectively. The fully patterned 10 x 10 mm mesa with the SAM had a contact angle of 101.5^{o} over the 100 nm features. The contact angle over the smooth quartz surface with the SAM was roughly 98.2^{o}. Thus the SAM provided a better non-wetting surface.

Using the SAM and a double-side polished wafer, whole wafers of PEGDA, peptide-functionalized PEGDA, and peptide-functionalized PEGDA with encapsulated proteins and DNA were successfully imprinted. **Figure 4.17** shows an initial whole imprinted wafer using various imprinting parameters that had not yet been optimized. For imprinting, the typical release force was 7 to 12 Newtons. Subsequently, a double-side

polished silicon wafer with an epitaxial layer of silicon was used for imprinting and proved to allow for more uniform imprints with thinner residual layers. The optimized wafer and template materials for imprinting included the SAM, the BARC and the double-side polished silicon wafer with the epitaxial layer.

4.3.3.2 PEGDA Viscosity Measurements and Dispense Tip Calibration

In order to dispense polymer solution from the dispense tips in the IMPRIO, the viscosity of various concentrations of PEGDA solutions was measured using a viscometer (assuming a constant density for PEGDA). **Table 4.3** shows the viscosity measurements taken for 75,[2] 60, 50, 33 and 25% (w/v) PEGDA (MW 700). The viscosities range from 40.6 cP down to 2.0 cP. The corresponding equations for dispensing the solution are shown to the right of the viscosity value and were calibrated by Molecular Imprints. The IMPRIO 100 already had a calibration value corresponding to 2-3 cP, the viscosity of the silicon-containing monomer. In order to get thinner residual layers, optimizing was focused on using the 25% and 33% (w/v) PEGDA (MW 700) concentrations using the pre-programmed equation for dispensing.

4.3.3.3 Optimized Residual Layer

In order to optimize the residual layer for PEGDA (MW 700), the dispensing parameters, imprint force, exposure time and pre-exposure delay was optimized. In order to optimize the dispensing parameters, the drop box size, drop location, volume per drop, and overall volume were optimized to provide an even imprint with the lowest possible

[2] Value courtesy Mary C. Moore.

overall volume of solution and the least number of air bubbles. The dispensing parameters were first optimized using a drop simulation model on the IMPRIO, and then through imprinting.

Figure 4.18 through **Figure 4.21** show the different parameters that were compared to optimize the residual layer. All experiments were done with $n > 4$. PEGDA (MW 700) with concentrations of 25% (w/v) and 33% (w/v) were evaluated because these polymers have the lowest viscosities and could yield a lower residual layer. Furthermore the imprinting force values had been narrowed down to 7 to 12 Newtons, the pre-exposure time was narrowed down to 300 to 360 seconds, the exposure time was narrowed down to 5 to 7 seconds and the minimum volume obtained had been 0.025 μL.

Figure 4.18 demonstrates a comparison between the residual layer thickness versus pre-delay time for 25% and 33% (w/v) PEGDA (MW 700) using an overall volume of 0.025 μL, an imprint force of 7 Newtons and a 7 second UV exposure. The data demonstrates that the longer pre-delay time, 360 seconds, successfully lowers the residual layer as expected. For the 25% (w/v) the residual layer is lowered from approximately 20 nm to 15 nm. A t-test was performed for each comparison and each had a p-value < 0.001.

Figure 4.19 demonstrates a comparison between the residual layer thickness versus the imprint force for 25% and 33% (w/v) PEGDA (MW 700) using an overall volume of 0.025 μL, a pre-delay of 300 seconds and a 7 second UV exposure. The data demonstrates that there is no significant decrease in residual layer when using these two forces. For the 25% (w/v) the residual layer remains at approximately 23 nm. A t-test was

performed on both comparisons and they were found to not be statistically significant. Typically, changing forces can change the thickness of the residual layer.

Figure 4.20 demonstrates a comparison between the residual layer thickness versus the UV exposure time for 25% and 33% (w/v) PEGDA (MW 700) using an overall volume of 0.025 μL, a pre-delay of 300 seconds and an imprint force of 7 N. The data demonstrates that there is no significant difference in residual layer between the 7 and 10 seconds exposures. The 5 second exposure shows a slightly larger residual layer. For the 25% (w/v) the residual layer remains at approximately 23 nm. A t-test was performed for both the 25 and 33% (w/v) and only the 33% (w/v) showed a significant difference with $p < 0.05$. The larger thickness may be due to the fact the full polymerization may not have been achieved at this exposure time for the larger PEGDA concentration.

Using a force of 7 Newtons, a pre-delay of 300 seconds and UV exposure time of 7 seconds, the total volume of 33% (w/v) and 25% (w/v) were varied to determine the thickness provided by each volume. **Figure 4.21** demonstrates that as the overall volume decreases, the residual layer decreases as well. The largest volumes of 0.3 μL and 0.174 μl were hand dispensed. A 33% (w/v) solution imprinted with 0.3 μL is approximately 450 nm thick. Using these parameters and further optimizing the drop pattern, a minimum volume of 0.019 μL was achieved. We also see that a larger PEGDA concentration will yield a larger residual layer thickness.

Figure 4.22 shows an optimized drop pattern using a bounding box size of 9.25 mm and a minimum volume per drop of 4.922×10^{-4}. The drop pattern is designed such

that the pre-polymer solution radiates out from the center and has channels to flow out to the edges, thus avoiding gas entrapment. The optimized drop volume was 0.019 μL per imprint, with a force of 7 N, a UV exposure time of 7 seconds and a pre-delay of 300 seconds. As seen in **Table 4.4** using the 0.019 μL over volume, residual layers of 2 nm to 27 nm were achieved over a majority of the imprint for 25% (w/v) and 75% (w/v) PEGDA (MW 700), respectively. However, the center of the imprint remained slightly thicker, in part due to the back pressure of the template. **Figure 4.23** demonstrates SEM images of varying residual layers of PEGDA imprints. **Figure 4.23A** demonstrates the initial hand imprints performed using 75% (w/v) PEGDA (MW 700), showing a large 1.36 μm residual layer that would not be successful in creating and releasing nanoparticles. **Figure 4.23C** shows a 15 nm residual layer with 50% (w/v) PEGDA (MW 700) and **Figure 4.23D** shows a 31 nm residual layer for a 75% (w/v) PEGDA (MW 700), both imprinted with 0.019 μL of pre-polymer solution. The thickness values from the SEM are estimates due to the resolution limits of the SEM. Furthermore, after cutting the wafers, the residual layer would curl over the edge of the wafer, making an actual determination of the thickness difficult.

4.3.3.4 Step and Flash Imprinted PEGDA Nanoparticles

Figure 4.24 demonstrates the variety of shapes and sizes that the SFIL process is capable of imprinting. Dense arrays of three-dimensional nano-sized squares, triangles, containers and pentagons ranging from 50 nm to 800 nm were successfully fabricated with little to no variation. Features sizes larger than 100 nm showed a variation of ± 0.2

nm, while 50 nm features showed a variation of ± 1.5 nm based on SEM measurements. Larger features sizes had more precise and sharp corners, while the smaller features had rounded corners due to the resolution limits of the e-beam lithography process.

The optimized imprinting process involved dispensing 0.019 μL of pre-polymer solution, a pre-delay of 300 seconds and UV exposure for 7 seconds, and a force of 7 N. Dosimeter measurements showed that the UV intensity at the template interface was 2 mW/cm^2. **Figure 4.25** demonstrates the use of varying PEGDA concentration to fabricate 100 nm (rounded) square nanoparticles using a 10 x 10 mm fully patterned mesa. PEGDA concentrations ranging from 75% (w/v) to 25% (w/v) were successfully patterned using the optimized imprinting process and showed no difference in size. All particles had dimension of 97.3 ± 0.2 nm based on SEM measurements. Because no images of the template were taken we can't compare the pattern transfer. **Figure 4.25D** shows a profile view demonstrating anisotropic side-walls of the features.

4.3.3.5 Isolation of Nanoparticles

In order to isolate and release the imprinted nanoparticles from the silicon wafer it is many times necessary to first remove the residual layer in between the particles. This was initially performed by oxygen plasma etching. Once the residual layer was further optimized, helium etching was also performed. Etching was performed on 33% (w/v) PEGDA (MW 700) imprint with 0.025 μL, a pre-exposure delay of 300 seconds, a force of 7 N, and a UV exposure time of 7 seconds. **Table 4.5** shows that after 20 seconds the entire residual layer was removed using an oxygen etch. With the helium etch, 2 nm of

residual layer remained. The AFM images in **Figure 4.26** demonstrate that there is no height difference between particles before and after oxygen etching, and before and after helium etching. **Figure 4.26A-C** demonstrates 50 nm particles before and after oxygen etching. Before etching, the particles were on average 93 ± 2 nm in height. After etching the particles were on average 94 ±2 nm in height. **Figure 4.26D-F** demonstrates 100 nm particles after before and after helium etching. Before etching the particles demonstrated a height of 127 ± 2 nm and after etching the particles demonstrated a height of 129 ± 2 nm. The particles demonstrate little no to change. **Figure 4.26G** demonstrates an etched 200 nm particle with a 413 ± 2 nm, and **Figure 4.2H-I**, demonstrates an etched 400 nm particle with a 626 ± 2 nm.

To further study the effect of the oxygen etching and helium etching on the PEGDA surface, XPS was performed. Initial scans showed a charging effect, therefore scans were charge neutralized. **Figure 4.27** demonstrates high resolution C1s scans of PEGDA samples on BARC and silicon. The thicker sample of 75% (w/v) PEGDA formed by hand imprinting with 0.174 μL shows no difference in the C-O peak (shifted 1.5 eV from the C-C peak) between the non-etched PEGDA and the oxygen etched PEGDA (**Figure 4.27B**); however there is slight increase in the C-C peak. The helium etching shows no change in the C-O peak, but shows an increase in the C-C peak. Both oxygen and helium etching show an increase in the C=O peak. The slight change in the C-C peak with oxygen etching could indicate some slight reactivity, while the C-C peak with helium etching could indicate the deposition of hydrocarbons.

The thinner sample of 75% (w/v) PEGDA formed using 0.025 μL shows the PEGDA with a larger C-C peak (**Figure 4.27B**). Furthermore we see that the C-O peak decreases with oxygen etching and decreases less with helium etching. Once again, both oxygen and helium increase the C-C peak and the C=O peak. With helium etching it is likely that hydrocarbons are depositing, while with oxygen it may indicate reactivity. The growing C-C peak and diminishing C-O peak may be describing the etching of the PEGDA to reveal the surface below.

Upon optimization of the residual layer to a 2 nm thickness etching was no longer required.

4.3.3.6 Harvesting of Nanoparticles

In order to release the nanoparticles, a sacrificial layer of water soluble poly(vinyl alcohol) (PVA) (53 nm) was spin coated (3000 rpm, 60 seconds) on top of a BARC layer (60 nm) prior to dispensing and imprinting the pre-polymer solution. PEGDA solutions of varying concentration were dispensed and imprinted on the BARC and PVA coated wafer. Following residual layer etching, 20 μL of dH_2O was placed on the imprint and rinsed with pipetting. **Figure 4.28** demonstrates successfully released 33% (w/v) PEGDA nanoparticles, ranging from 50 nm to 400 nm, fabricated using 0.025 μL of pre-polymer solution after helium etching. Upon optimization of the residual layer, particles were released without the need for etching. 33% (w/v) PEGDA nanoparticles, imprinted using 0.019 μL, with a 2 nm residual layer were successfully released in water by dropping on 20 μL of dH_2O and gently pipetting, as shown in **Figure 4.29C-D**. The particles were

imaged in the same location they were fabricated instead of pipetting them onto a clean silicon surface, therefore the images appear dirty.

4.3.3.7 Theoretical Number of Nanoparticles and Drug Loading Capacity

The theoretical number of particles per template and per wafer was calculated based on varying template size, wafer size, and particle size, shape, and spacing. From this, the theoretical drug loading capacity was calculated. **Figure 4.30** demonstrates the number of particles that could be generated using different sized templates. We see that overall, the 50 nm particles with 1:1 pitch allows for the production of the most particles. The 25 x 25 mm template shows the greatest number of particles per imprint (**Figure 4.30A)**; however, once an entire 4 inch wafer is imprinted, the 10 x 10 mm template can produce more particles per wafer (**Figure 4.30B**). If an 8 inch wafer is used, the 25 x 25 mm mesa shows the highest production of particles once again (**Figure 4.30C**). As an example, if 100 nm square particles with a 1:1 spacing are created, we could achieve approximately 10^{11} particles per 4 inch wafer and 4 x 10^{11} particles per 8 inch wafer.

Figure 4.31 demonstrates the theoretical loading of particles of various size, shape and spacing, assuming the use of a 10 x 10 mm mesa and an initial loading of a model drug in pre-polymer solution at 10 mg/mL. We can see that 400 nm square particles with a spacing of 1:1 can load the most drugs, followed by the cylindrical particles and then the triangular particles. Using the data from **Figure 4.31**, the loading level for 100 nm square particles with a 1:1 spacing is approximately 1 μg/10^{11} particles for a 4 inch wafer and 4 μg/10^{11} particles for an 8 inch wafer. For a 50 mg/ml

concentration of protein in the pre-polymer solution, the loading level is approximately 5 $\mu g/10^{11}$ particles for a 4"wafer and 10 $\mu g/10^{11}$ particles for an 8" wafer. By doubling the aspect ratio of the particle, creating a 100 x 100 x 200 nm particle, the loading level would be doubled.

Currently, the fully patterned 10 x 10 mesa with 100 nm square particles has a 1:2 spacing and can produce 4.7 x 10^{10} particles per 4 inch wafer (**Table 4.6**). Assuming a 10 mg/mL concentration of drug in pre-polymer solution and a square shape, each imprint has a loading level of 13.5 ng, and an imprinted 4 inch wafer has a loading level of 700 ng. This correlates to a loading level of 150 ng/10^{10} particles per 4 inch wafer. If the particle is more spherical each imprint has a loading level of 10.6 ng, and an imprinted 4 inch wafer has a loading level of 550 ng. This correlates to a loading level of 117.5 ng/10^{10} particles per 4 inch wafer. The 10.5 x 10.5 mm template provided by Molecular Imprints can produce 7.1 x 10^{10} particles per 4 inch wafer (**Table 4.6**). Assuming a 10 mg/mL concentration of drug in pre-polymer solution and a circular shape, each imprint has a loading level of 7.83 ng, and an imprinted 4 inch wafer has a loading level of 410 ng. This correlates to a loading level of 57.6 ng /10^{10} particles per 4 inch wafer.

4.4 DISCUSSION

The overall goal of this research was to optimize nanoimprint lithography techniques to create monodisperse, size and shape-specific, biocompatible, nanoparticles with the potential for injectable and intracellular drug delivery. Because nanoimprint

lithography is a direct pattern transfer process, the creation of the template is one of the most critical aspects of the process. To pattern the template many parallel processing techniques are required to create nanofeatures that have well-defined geometry and that are uniform and reproducible. As can be seen in the SFIL and ThNIL templates (**Figure 4.11** and **4.13**), shape and size specific features were successfully created. As the feature size decreases, the corners of the patterns tend to become more rounded. This is especially apparent in the 50 nm features; however the rounding may be beneficial for drug delivery applications.

The rounding is due to the resolution limit of the e-beam lithography process. The spot size of the beam, the exposure time, the current, the dose, the way in which the e-beam writes the patterns, and the photoresist used, all dictate the resolution of our features. In order to create such high density patterns with small feature sizes the following equation was taken into consideration when designing the e-beam parameters:

$$Q = \frac{I * T}{P^2} \qquad (5)$$

where Q is the sensitivity of the resist (C/cm^2), I is the current (A), T is the shot time (sec) and P is the shot pitch (cm). For a setting of 50 kV in 5^{th} lens, the minimum pixel size is 1.25 nm. For 5^{th} lens and a shot parameter of A,2 this yields a shot every other pixel (2*1.25 nm spacing). The beam diameter is 7 nm, and in order to successfully

pattern the template the minimum pixel*spacing was optimized to be less than the beam diameter. As a note, the patterning of full mesas can take up to two to three days. The e-beam can drift 100 nm every 6 hours, therefore special attention was taken to allow for the drift.

To create precise features in the template, ZEP 520 was used as used a photomask because of its enhanced sensitivity for e-beam lithography and its sensitivity as a mask in reactive ion etching. Because it is a positive resist, the e-beam exposure causes the molecular linear chains to break and increases the solubility of the resist. This allows the developer to remove the exposed area to create a pattern in the resist. To create patterned cavities in the silicon and quartz templates, the selection of etching criteria was important. The etch rate, selectivity, anisotropy, and feature size control are important considerations. Many bulk micromachining techniques utilize wet etching; however this process typically creates isotropic features and is not suitable for creating nanoscale features. Therefore, reactive ion etching was utilized. Reactive ion etching acts to remove material by a combination of physical and chemical bombardment. Plasma is formed by applied RF potentials and consists of gas molecules that have been broken down into fragments and radicals. In the plasma, the fragments are ionized and accelerated toward the sample, thus etching the material.

To create recipes for etching silicon, resist, and organic materials, recipes were modified from standard processes. In each case the selectivity of the gases, the RF power, and the pressure were optimized to provide anisotropic etching. Plasma pressure plays an important role in the development of the etch process and can control the ratio of physical

and/or chemical etching that occurs. At low pressures, ion bombardment is dominant and there is higher ion energy. With a long mean-free path of ions, this can result in an anisotropic etch. Furthermore, lower pressures are less contaminating because reaction by-products show more volatility at lower pressure and can be removed easily from the etch chamber. One drawback is that at low pressure the ion density drops off quickly thus there is lower etch rate.

Higher pressures result in more reactive species, thus chemical etching is enhanced. At higher pressure the ion energy is lower, there is a shorter mean-free path of ions and this can result in an isotropic etch. Increasing the power will increase the etch rate because the remaining ions become more energetic. The use of reactive ion etching allowed for the creation of anisotropic features etched into the templates. As seen in the silicon etching recipe, a low pressure was used, chlorine was used as a reactive gas to chemically assist ion etching to provide anisotropy, and helium was used to stabilize the plasma and assist with anisotropy. Using these parameters allowed for the creation of well-defined anisotropic side-walls in the silicon templates, as seen in **Figure 4.11E-F**.

With the successful creation of a silicon template, thermal imprinting was performed on PMMA and PLGA. With thermal imprinting, the layer thickness that is spin-coated on the wafer is critical with respect to the filling in the feature cavities in the silicon template. The initial layer thickness should be 50 to 100 nm thicker than the height required to fill the feature cavities in the template [30]. Using these guidelines, the PMMA imprints demonstrated precisely patterned nanocontainers with wall thicknesses as low as 50 nm. After oxygen etching the containers were released in water using

sonication; however, sonication would not be desirable for releasing drug-loaded nanoparticles.

With the measurement of the Cauchy characteristics for PLGA, we were able to determine the spinning parameters needed to achieve a desired PLGA thickness of 200 to 300 nm. Although variations in time, pressure applied, and PLGA concentration were studied, the results showed the creation of shallow patterns only in the 5% (w/v) R502H (MW 11,000). Schulz and colleagues have modeled the affect of molecular weight and viscosity of on thermal imprinting of polystyrene and have concluded that polymers with differing molecular weights cannot necessarily be imprinted at the same level above Tg due to differences in the shear rate and mechanical properties [30]. Furthermore they demonstrated that the lower viscosity solutions tended to underfill cavities or fill them irregularly. Potentially the imprints may not have been heated to a high enough temperature and may not have completely filled the cavities. The DCM however, is very viscous and did not show better results. Once again this could be due to the need for a higher temperature.

Although the thermal imprint lithography process does demonstrate the ability to create well defined features in PMMA, the fabrication process may involve temperatures not suitable for encapsulation of biological agents and involves using a high imprinting force. Also, imprinting with different polymers would require optimization each time. Depending on the polymer used, and the molecular weight and viscosity of the polymer, the imprinting temperature would need to be optimized each time. Furthermore, depending on the feature depth in the template, further spinning studies for each polymer

variation would need to be performed and optimized. For these studies, the thermal imprint lithography set-up was only capable of imprinting small wafer pieces using a ~ 1 mm template. In order to have high-throughput capabilities for imprinting nanoparticles for drug delivery, a full-wafer imprinting tool such as the Obducat Soft Press (Obducat) would be required.

Using the Step and Flash Imprint Lithography technique we successfully demonstrated the creation and release of three-dimensional, size and shape-specific PEGDA nanoparticles as small as 50 nm. The first critical aspect of the process was the ability to optimize the substrate and template release layer. An interesting note considering the release layer is that the pre-polymer solution must wet the template well enough to fill in the topography of the template, but it must also release from the template after UV exposure without causing damage to the imprinted nanofeatures. The filling of the template is achieved through capillary action. Colburn and colleagues have modeled the rate that the fluid fills the gap between the substrate and template using the work-adhesion equation [19]:

$$W_{Adh} = \gamma_A + \gamma_B - \gamma_{AB} \tag{6}$$

and the Washburn equation:

$$\frac{dx}{dt} = \frac{(H^2 \gamma_A / R)}{24 \mu x} \tag{7}$$

where W_{adh} is the work of adhesion and is governed by γ_A, the surface tension or surface energy of the pre-polymer solution, dx/dt is the rate of fill of the template feature and μ is the viscosity of the pre-polymer solution. Increasing the surface tension will increase the

work of adhesion but will also maximize the rate of fill of the template feature. The rate of fill is also inversely proportional to the viscosity of the pre-polymer solution. Furthermore, the viscosity is directly proportional to polymer concentration and the rate of cure [19]. Therefore the surface tension must be balanced to create an easy to release template and a pre-polymer solution with a fast filling and curing time. This is a key consideration in designing templates for nanoimprinting with biomolecules, especially since many peptides are adhesive to surfaces [31].

The results of the contact angle study demonstrated that the SAM of 0.5% (v/v) (Tridecafluoro-1,1,2,2-Tetra-Hydrooctyl) Dimethylchloro-silane in toluene coated template proved to have a higher contact angle than the Relmat, and consequently a lower surface energy. Studies of similar release layers and the formation of these self-assembled monolayers have been extensively performed for quartz imprinting templates [32, 33]. The SAM significantly reduced the adhesion to the PEGDA polymer and the peptide-functionalized PEGDA crosslinked networks, as well as the PEGDA polymers incorporating a model drug.

The choice of the correct silicon substrate was also necessary in order to provide the best adhesion of the polymer to the substrate and the lowest residual layer. The flatness of the wafer can dictate the variation of the residual layer. Furthermore, a smooth adhesion layer can help minimize variations in the flatness of the wafer. Using BARC along with the double-side polished wafer with an epitaxial layer of silicon provided uniform imprints with the lowest overall residual layer values. Using the SAM and the optimized substrate allowed for successful imprinting of whole wafers.

In order to dispense the pre-polymer solution from the dispense tips in the IMPRIO, the measurement of the PEGDA viscosity properties and the corresponding volume/voltage equations were invaluable. The viscosity values are only meant to give a close estimate of the viscosity because the bulk density of PEGDA (MW 700) was held constant at 1.12 g/mL. For actual viscosity determination the density value would increase as the polymer concentration increased. A study by Saluja and colleagues demonstrated that PEG 400 behaved as a Newtonian fluid, and for a 40% to 100% (w/v) solution the density changed by only 0.056 g/mL [34]. A key feature of this method is the ability to use a variety of biocompatible polymer solutions of varying concentrations. By determining the viscosities of these solutions they can be successfully imprinted with a corresponding calibrated dispensing equation.

With the ability to dispense a variety of PEGDA pre-polymer solutions, we were successfully able to vary the parameters of the tool in order to create imprints with residual layers as low as 2 nm. Our results from the optimization show that the pre-exposure delay can significantly lower the residual. The results from the small change in imprint force did not equivocally show an improvement in residual layer thickness; however literature has shown that a greater pressure does indeed lower the residual layer [35]. Furthermore, we found that a UV exposure time of 5 seconds showed a larger residual layer than a 7 second UV exposure. This suggests the exposure time may be too small, in particular for PEGDA concentrations larger than 33%. Acrylate polymerization is known to be accompanied by volumetric shrinkage as a result of chemical bond formation [24], thus the polymer may not be fully polymerized. We also saw a strong

dependence in the residual layer versus overall imprint volume as well as polymer concentration.

With the optimized imprinting process we successfully achieved residual layers as low as 2 nm over 80% of the imprint for the 0.019 μL, 25% (w/v) PEGDA (MW 700) pre-polymer solution; however the residual layer height in the center of the template remained slightly thicker. Despite lowering the total volume to the smallest possible value, the center remained thicker for all variations. Because the trend was the same for all the imprints ranging from 25% to 75% w/v we believe that the back-pressure on the template was too low. This can be known to cause a thicker residual layer in the middle with all edges and corners having the same thickness.

Using the optimized imprinting parameters we were also successfully able to create monodisperse, shape-specific particles. The SEM images show little to no variation in size and all patterns showed no defects for incomplete filling of the template feature. Furthermore, we were able to create higher aspect ratio particles, such as the 200 nm particles with 413 nm heights and the 400 nm particles with 626 nm heights. The 100 nm features in the fully patterned quartz template created 97 nm square nanoparticles. The discrepancy may be due to a shrinkage that is known to occur with acrylate polymerization [24] or may be due to the patterned features in the 10 x 10 mm mesa not being fully developed during the e-beam lithography process. The 10 x 10 mm fully patterned mesa was not characterized with SEM and thus the uncertainty exists. However all previous imprints showed direct pattern transfer.

Of key importance to the imprinting of biopolymers and encapsulated biologics is the ability to successfully isolate and release the nanoparticles from the silicon wafer. Through optimization of the residual layer (2 nm) we were successfully able to release the particles with no required etching. However, for higher concentration polymers with thicker residual layers, mild etching may still be required. When isolating the nanoparticles both helium and oxygen plasma etching were used with a low power setting and moderate pressure. The etching process can create dangling bonds and dislocations in the material making it reactive, and can at times cause polymer formation (hydrocarbons) on the surface.

Oxygen ions are highly reactive and known to be selective for etching organic compounds. Etching with oxygen provides more of a chemical etch. Meanwhile, helium is an inert gas wherein the etching is primarily a mechanical/physical bombardment. The XPS data for the thick PEGDA film suggests that the mild etching processes are not chemically modifying the surface. The oxygen etching does however show a slight increase in the C-C peak which may indicate some reactivity, and it appears that the helium etching is causing a deposition of hydrocarbons.

It is interesting to note that the PEGDA peaks seen in the high resolution C1s scan show the thinner PEGDA with a larger C-C peak. XPS is known to analyze the first 50 to 100 Å of a surface, therefore it is likely that we may be seeing the surface below the PEGDA. Desai and colleagues have extensively studied thin PEGDA films on silicon using XPS analysis [36-39]. Their results show that increasing PEG concentrations (see **Figure 4.32**) and increased PEG immobilization times increase the C-O peak in a C1s

scan. However, their data also shows that films of low PEG concentration show both a large C-O and C-C peak. This suggests that we may be seeing the silicon or BARC layer below the PEGDA.

To address the issue of efficient harvesting of intact imprinted particles without physical scraping from the wafers, we have employed a simple release layer-based approach [40]. This allows direct, one-step release of the nanocarriers from the silicon wafer. Since the PVA release layer dissolves in water [40] while the crosslinked nanoparticles do not, this process allows for efficient and mild harvesting of the nanoimprinted particles directly into aqueous buffers suitable for biological studies. This release technique is high-throughput, commercially viable and avoids high temperature or physical force-based removal, both of which could potentially damage the nanoparticles or their content. The process could also be beneficial since it allows for the presence of PVA in the particle suspension. PVA is a well studied polymer/stabilizer used to prevent particle aggregation in colloidal suspensions, especially for drug delivery [41-43].

It is worth noting that the system and polymer choices as described here essentially generate nano-sized hydrogels as drug carriers. A key feature of this method is the ability to vary the crosslink density and composition of the particle matrix using different polymer concentrations, PEGDA to peptide ratio, and peptides of varying degradation kinetics, thus potentially controlling drug release and particle dissolution kinetics. It is important to note that with the SFIL technique, varying concentration or molecular weight of the polymer solution has little effect on the size and shape of the nanoparticle; unlike emulsion or self-assembled particles, SFIL particle formation is not

controlled by phase separation or emulsion stabilization. The molecular weight, in particular the viscosity, of the pre-polymer solution prior to cross-linking does affect the dispensing efficiency of the solution, the filling and the cure rate. The IMPRIO tool is calibrated for specific viscosity ranges to enable reproducible dispensing and imprinting of pre-polymer solutions. The tool can also be re-calibrated when polymers of higher or lower viscosities are used.

Since this is a hydrogel encapsulation process, 100% of the encapsulant is trapped inside the photo polymerized gel. The encapsulation efficiency and loading level is controlled by the pattern density in the template (how close or how far apart the particle patterns are in the quartz template). As demonstrated through the theoretical calculations this method can allow for large scale fabrication of nanoparticles. For a 50 mg/ml solution of protein in pre-polymer solution, the loading level is approximately 5 $\mu g/10^{11}$ particles for a 4 inch wafer and 10 $\mu g/10^{11}$ particles for an 8 inch wafer. By knowing the number of particles and loading levels based on size and shape, we may at some point be able to create a treatment dosing schedule for patients based on particle size and shape. We can also determine the needed number of particles for a dose. Doses for several anticancer drug-GFLG-HPMA conjugates, using doxorubicin and paclitaxel, range from 17 – 320 mg/m^2, as tested in clinical trials [44-46].

By doubling the aspect ratio of the particle to create a 100 x 100 x 200 nm particle the loading level would be doubled; thus a higher dose of drug could be achieved at a target site. This is in agreement with Discher and Ferrari's groups, demonstrating that spheroidal particles can carry more drugs than spherical drugs [5, 7]. Discher and

colleagues demonstrated that filamentous particles with very high aspect ratios (less than 100 nm diameter with several microns in length) showed an increase in dosage of drug to a tumor site [5]. Using the SFIL technique, monodisperse nano-sized rectangles or rods with very large aspect ratios could be created in order to deliver a large dose of drug and to enhance the delivery efficiency of drugs or contrast agents to tumor tissues.

Using the SFIL technique to create size and shape-specific, monodisperse nanoparticles can provide for a reliable study of the effect of shape on in-vivo drug or contrast agent release, and may allow for future tunable in-vivo release and targeting properties. The monodisperse particles could be used to study the affect of shape on particle velocity, diffusion and adhesion to walls in blood vessels [4]. Furthermore, studies could be performed to evaluate the particle's targeting ability, internalization in cells, and ability to target tumor cells. Because UV-crosslinkable polymers can successfully be imprinted, it is conceivable that degradable polymers such as PEG-PLGA-PEG triblock copolymers could be fabricated and studied for shape-specific degradation.

In conclusion, the research presented here provides a novel application of imprint lithography techniques to fabricate biocompatible, easily-harvestable, nanoparticles (as small as 50 nm) of precise sizes, shapes and compositions. We demonstrate that the SFIL technique has the potential to create well-defined and characterized drug delivery particles without the limitations of the PRINT process, emulsion, and micelles formation techniques. We have demonstrated full wafer imprinting and successful isolation and release of the particles from the wafer using a mild harvesting method. The use of a top-

down approach ensures precise control of particle size and geometry, creating a monodisperse population of particles; therefore allowing for better reproducibility and prediction of properties. The top-down technique also avoids high shear and mechanical forces typical for emulsion-based encapsulation, which in turn may improve encapsulation efficiency and drug stability. Furthermore, the SFIL technique can easily fabricate drug delivery devices using a wide variety of currently available biocompatible polymers.

This research provides a significant advance in the creation of monodisperse, injectable nanocarriers of specific geometry and can provide a characterized environment for the study of the effect of size and shape in in-vivo release properties of nanoparticles. It is also conceivable that nano-sized, injectable drug carriers having precise geometry and environmentally-responsive release mechanisms could provide targeted, disease-specific delivery of molecules as well as tunable in-vivo release characteristics.

Figure 4.1 Step and Flash Imprint Lithography. [*1]

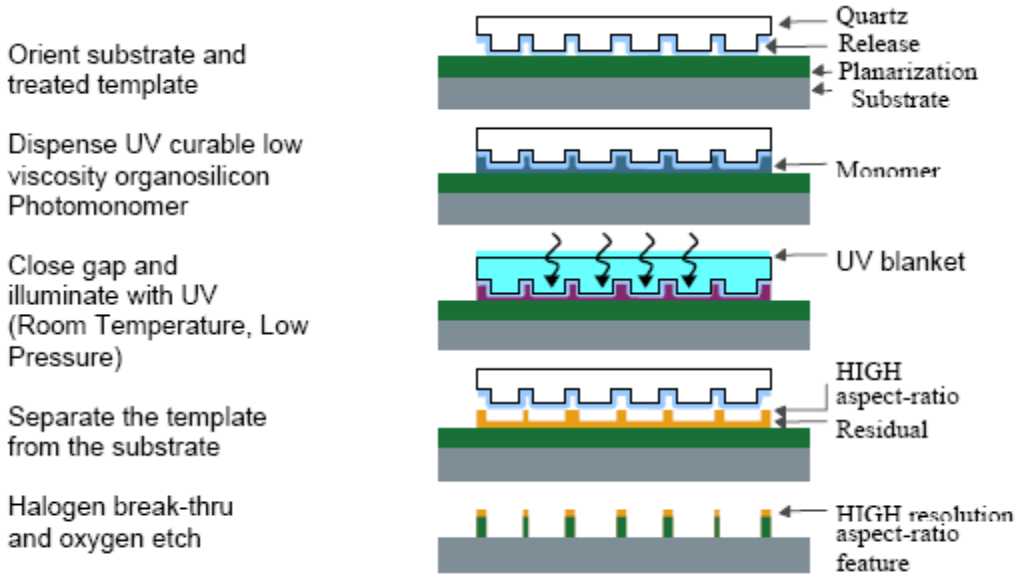

Figure 4.2 Step and Repeat Process. [*1]

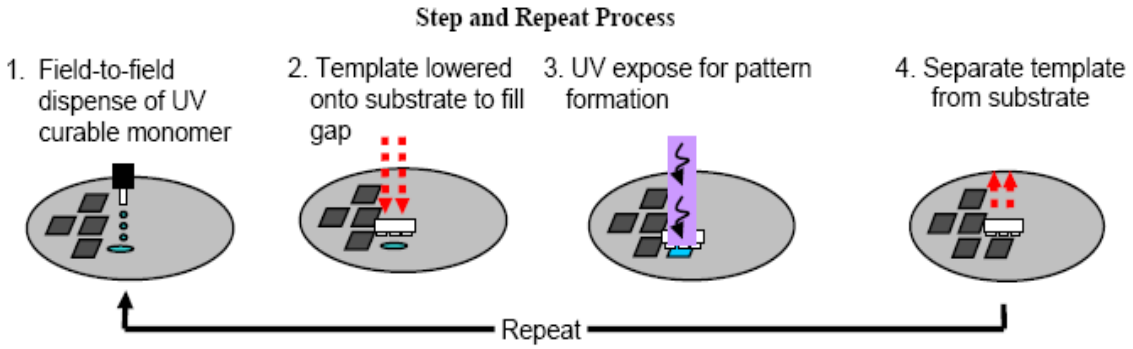

[*1] *Reprinted from I. McMackin, P. Schumaker, D. Babbs, J. Choi, W. Collison, S. V. Sreenivasan, N. Schumaker, M. Watts, and R. Voisin, Design and Performance of a Step and Repeat Imprinting Machine Proc SPIE, Emerging Lithographic Technologies VII, 5037, 2003, with permission from SPIE and S. V. Sreenivasan.*

Figure 4.3 **IMPRIO 100 Process Tool: (A) Tool with computer controller, (B) front sash closed with wafer and template loading stations, (C) front sash opened to show entire system, (D) close up view of the wafer chuck and z-head, (E) close up view of the dispense tips, (F) close up view of the solution holders.**

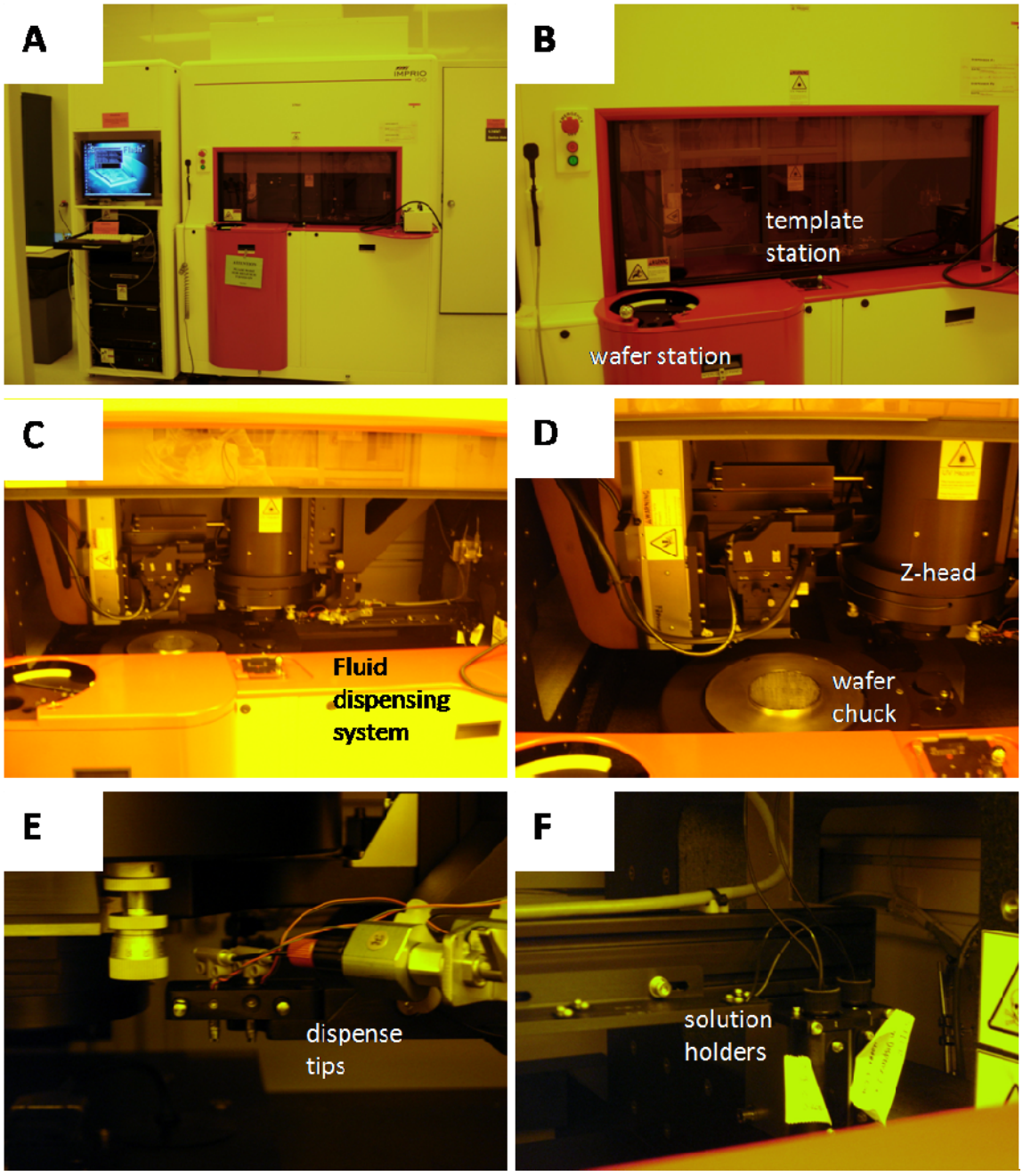

Figure 4.4 Interior View of Z-head, Template location, and Wafer location. The dots represent mechanical degrees of freedom.[*1]

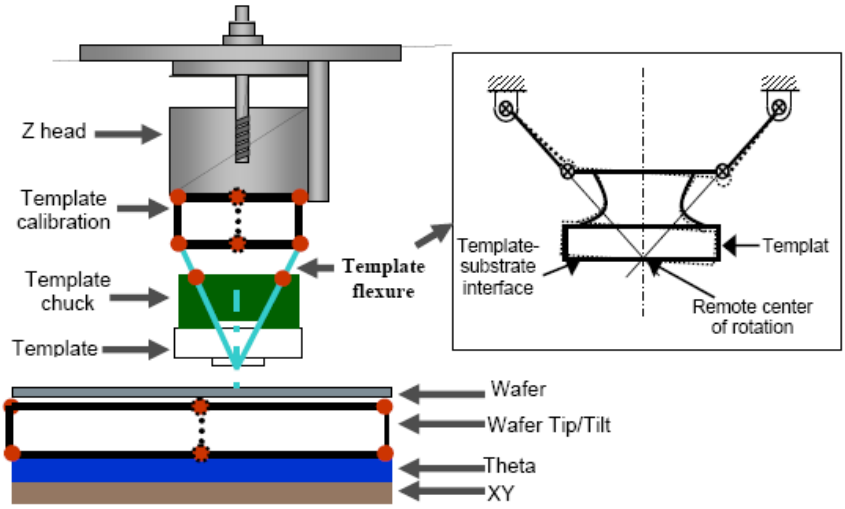

[*1] *Reprinted from I. McMackin, P. Schumaker, D. Babbs, J. Choi, W. Collison, S. V. Sreenivasan, N. Schumaker, M. Watts, and R. Voisin, Design and Performance of a Step and Repeat Imprinting Machine Proc SPIE, Emerging Lithographic Technologies VII, 5037, 2003, with permission from SPIE and S. V. Sreenivasan.*

Figure 4.5 Example of Drop Layout Panel.

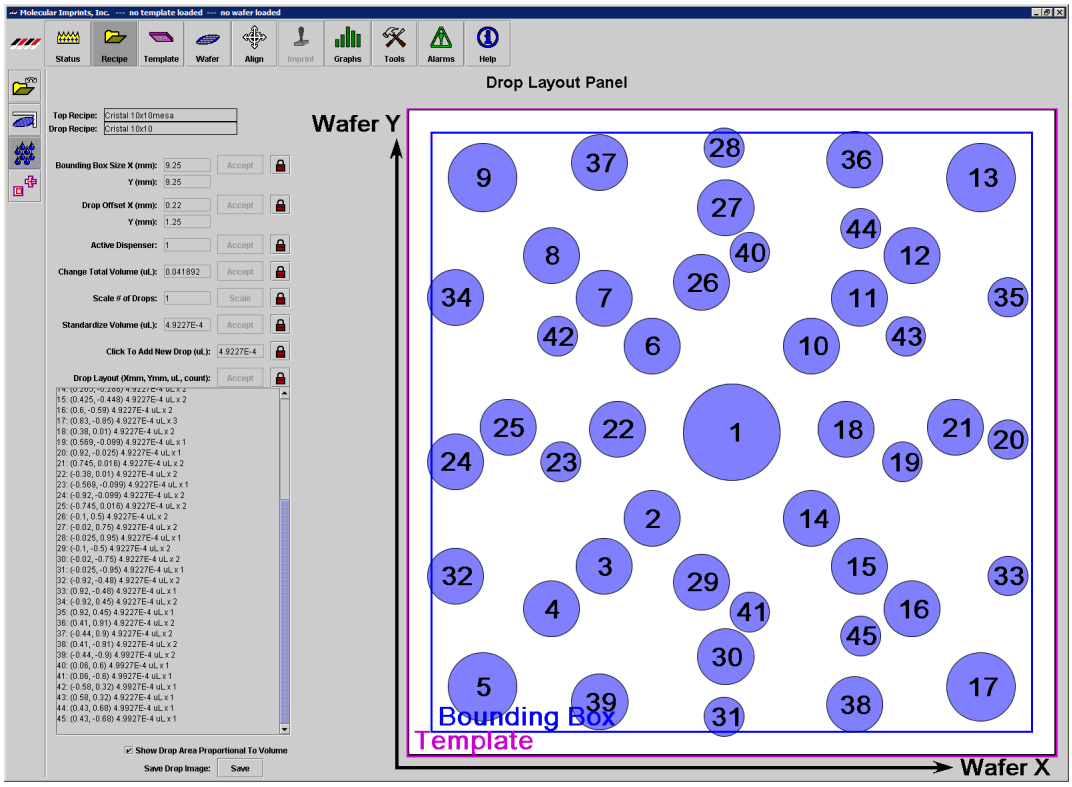

Figure 4.6 **Schematic of a Template Fabrication Process for ThNIL: (A) A wafer is spin-coated with ZEP 520 resist, (B) the resist is exposed to e-beam and patterned, (C) the resist is developed, (D) the exposed silicon is etched with RIE (for single shapes the process ends here), (E) to create nanocontainers a 2nd layer of resist is spin-coated on the wafer, (F) the resist is exposed to e-beam and patterned, (G) the resist is developed, and (H) a second etching is performed, followed by a Piranha clean.**

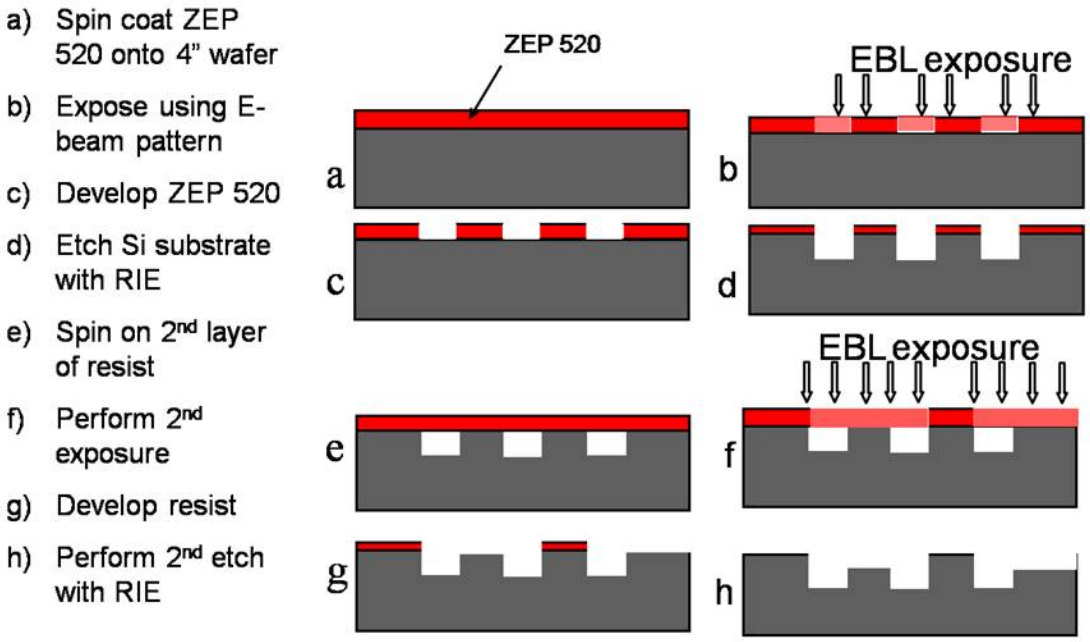

Figure 4.7 Schematic of a Quartz Template. Four quartz templates are diced from a larger 6" x 6" substrate[*1]. Each template has a varying size mesa, which is raised off of the quartz template, and can be patterned.

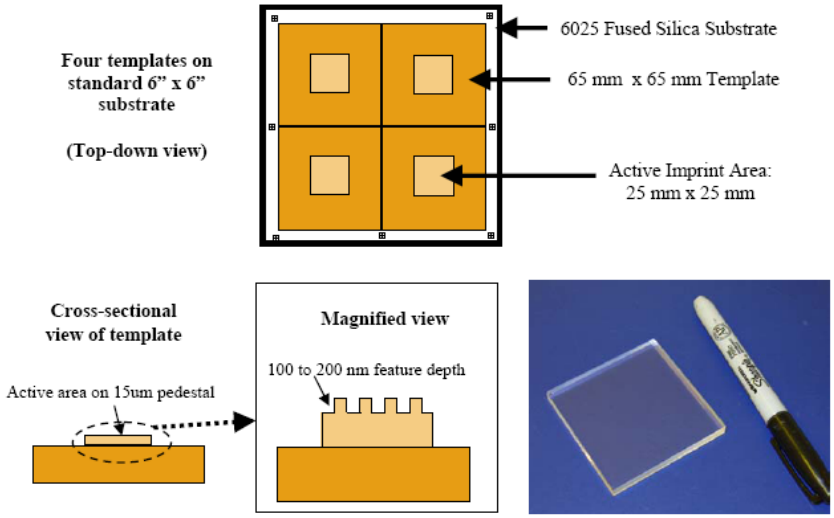

[*1] *Reprinted from I. McMackin, P. Schumaker, D. Babbs, J. Choi, W. Collison, S. V. Sreenivasan, N. Schumaker, M. Watts, and R. Voisin, Design and Performance of a Step and Repeat Imprinting Machine Proc SPIE, Emerging Lithographic Technologies VII, 5037, 2003, with permission from SPIE and S. V. Sreenivasan.*

Figure 4.8 **Template Fabrication Process for SFIL: (A) 15 nm chromium is deposited on a quartz template, (B) the wafer is spin-coated with ZEP 520 resist, (C) the resist is exposed to e-beam, patterned and developed, (D) the chromium layer is etched, (E) the chromium layer is etched, (E) the quartz is etched, (F) the chromium layer is removed with wet etching.**

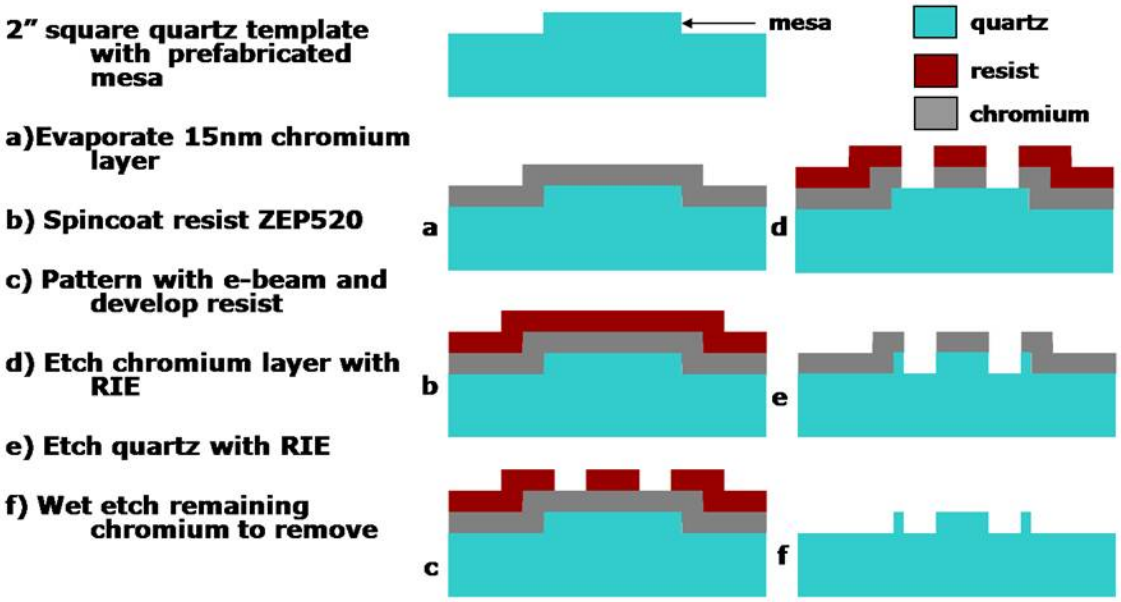

Figure 4.9 **Schematic of PEGDA Nanoparticle Formation using SFIL: (A) Orient the substrate and treat the template with a water soluble layer and adhesive layer, (B) dispense the macromer solution, (C) imprint with low pressure and UV exposure, (D) separate the template and substrate, (E) isolate the nanoparticles, (F) release the nanoparticles in dH_2O.**

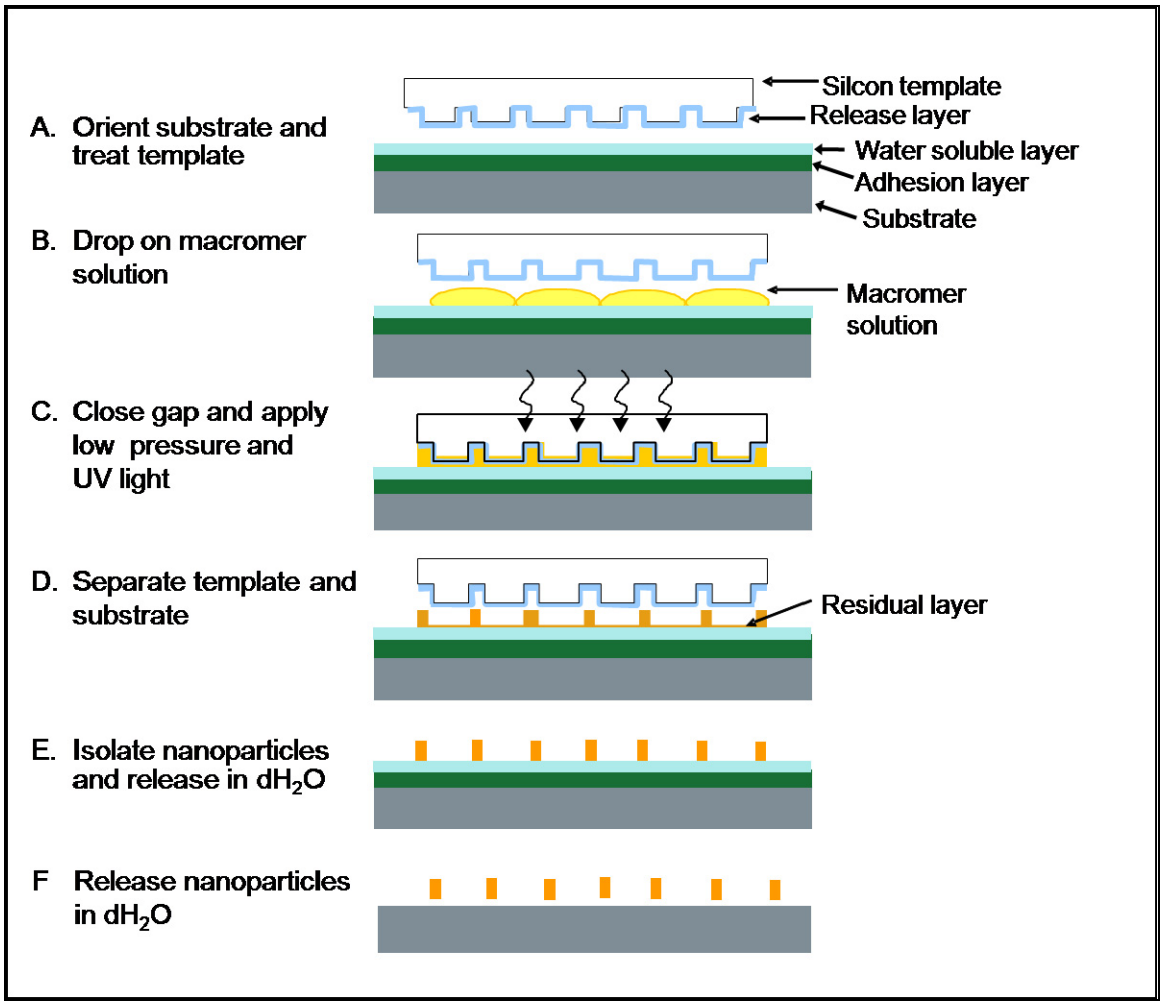

Table 4.1 Imprintable Fields per Wafer (as referenced from the Molecular Imprint's IMPRIO100 Manual and estimated by technicians).

Mesa Size	4 inch	8 inch
10 mm mesa	52	186
12.5mm mesa	32	94
25 mm mesa	6	37

Figure 4.10 Optimization of EBL Parameters Template Fabrication. (A) The schematic indicates a single wafer in which feature size, development time of the e-beam resist ZEP 520A (1, 1.5, 2 and 3 minutes) and the dose level of the e-beam (from -5 to 110) were studied. (B) The SEM image demonstrates a single development time, with the e-beam dose level studied for various shapes and sizes.

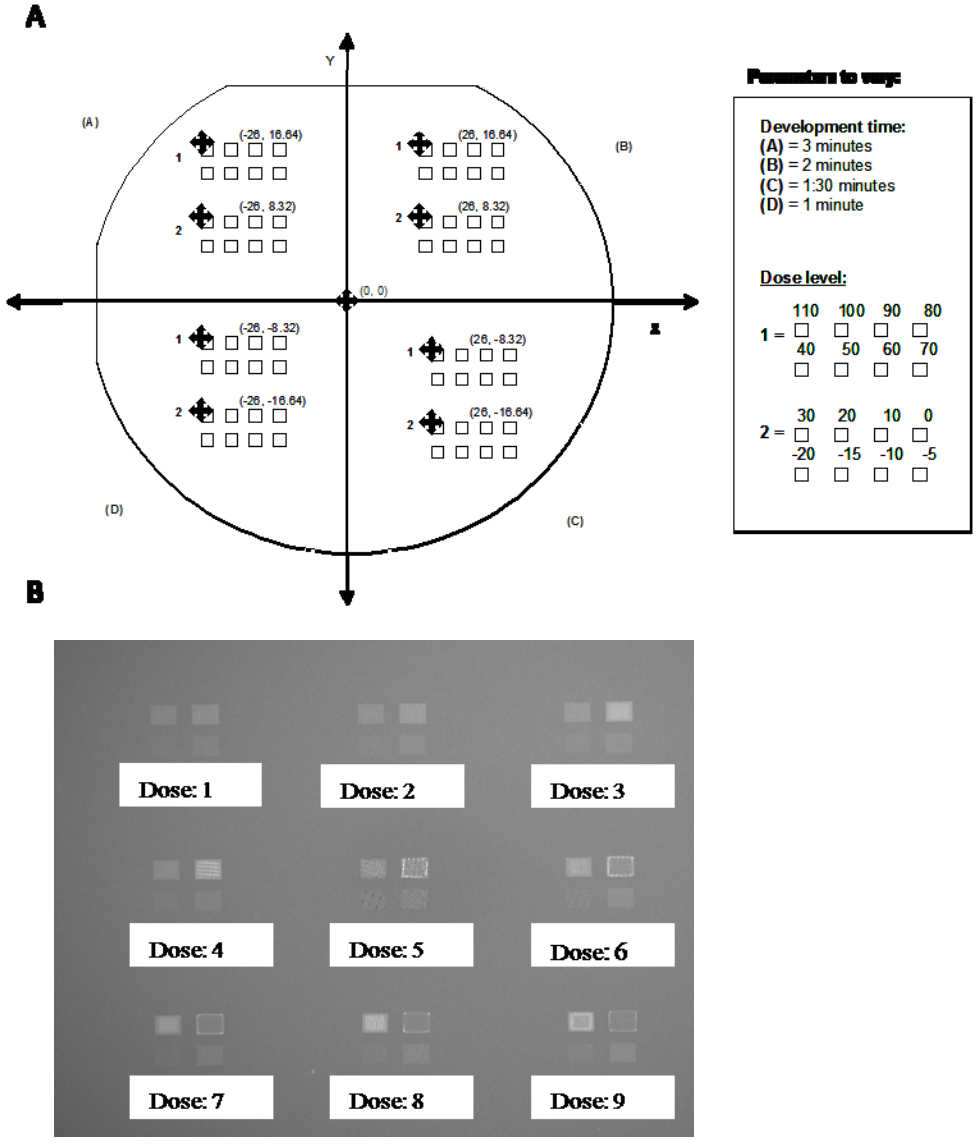

Figure 4.11 SEM images of Patterned Silicon Template using E-beam Lithography and Reactive Ion Etching: (A) 100 nm boxes *(scale bar = 200nm)*, **(B) 200 nm boxes***(scale bar = 200nm)*, **(C) 400 nm boxes***(scale bar = 1μm)*, **(D) 800 nm boxes***(scale bar = 1μm)*, **(E) side profile of 400 nm boxes** *(scale bar = 400nm)*, **and (F) side profile of 800 nm boxes, with etch depth ~ 200 nm** *(scale bar = 1μm)*.

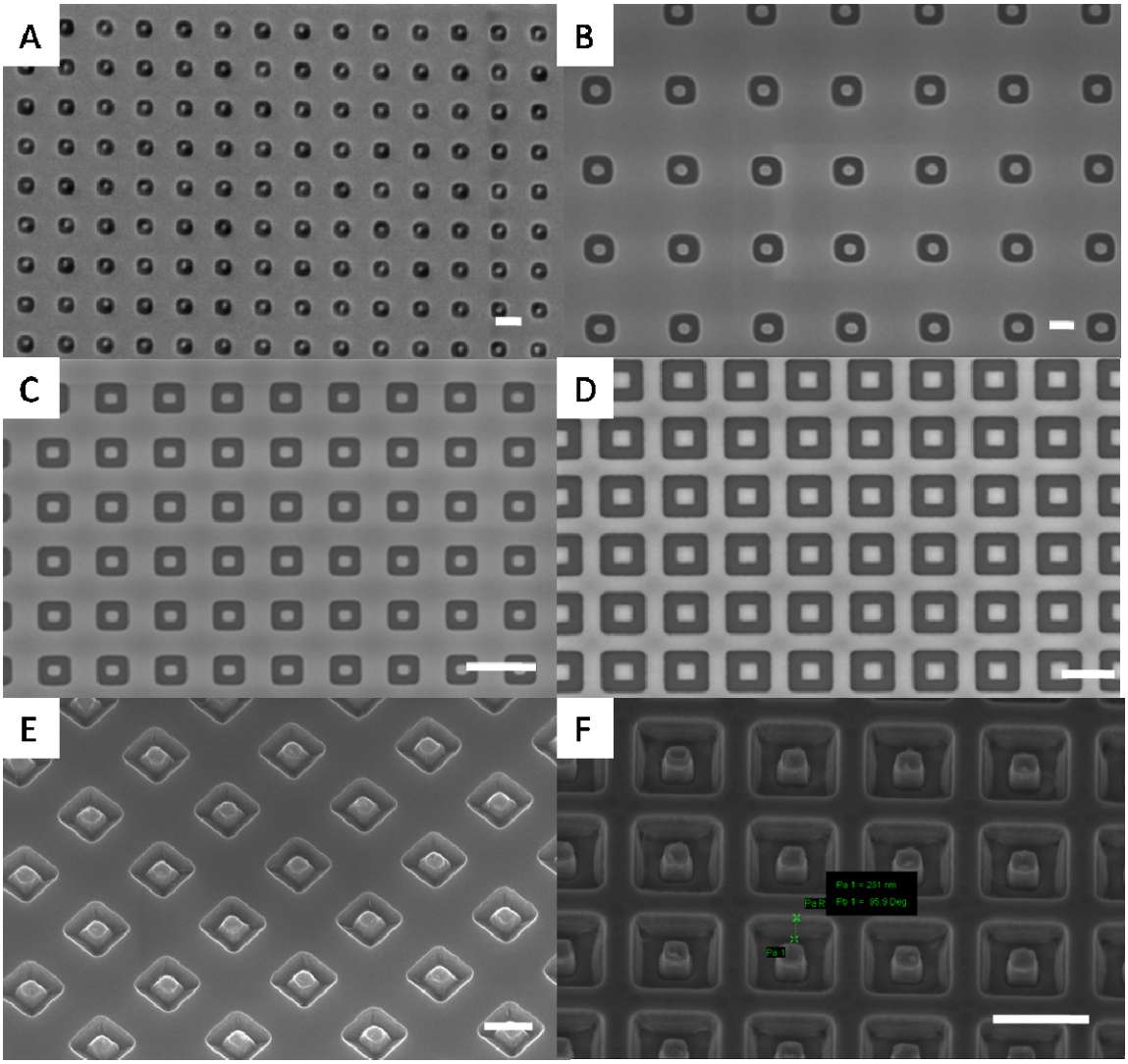

Figure 4.12 Layout of Quartz Template Mesas: (A) 25 x 25 mm mesa with, (B) 12. 5 x 12.5 mm mesa, (C) 10 x 10 mm mesa, (D) fully patterned 10 x 10 mesa with 0.9 billion, 100 nm features, (E) fully patterned 10.5 x 10.5 mm mesa with 1.369 billion, 80 -100 nm features.

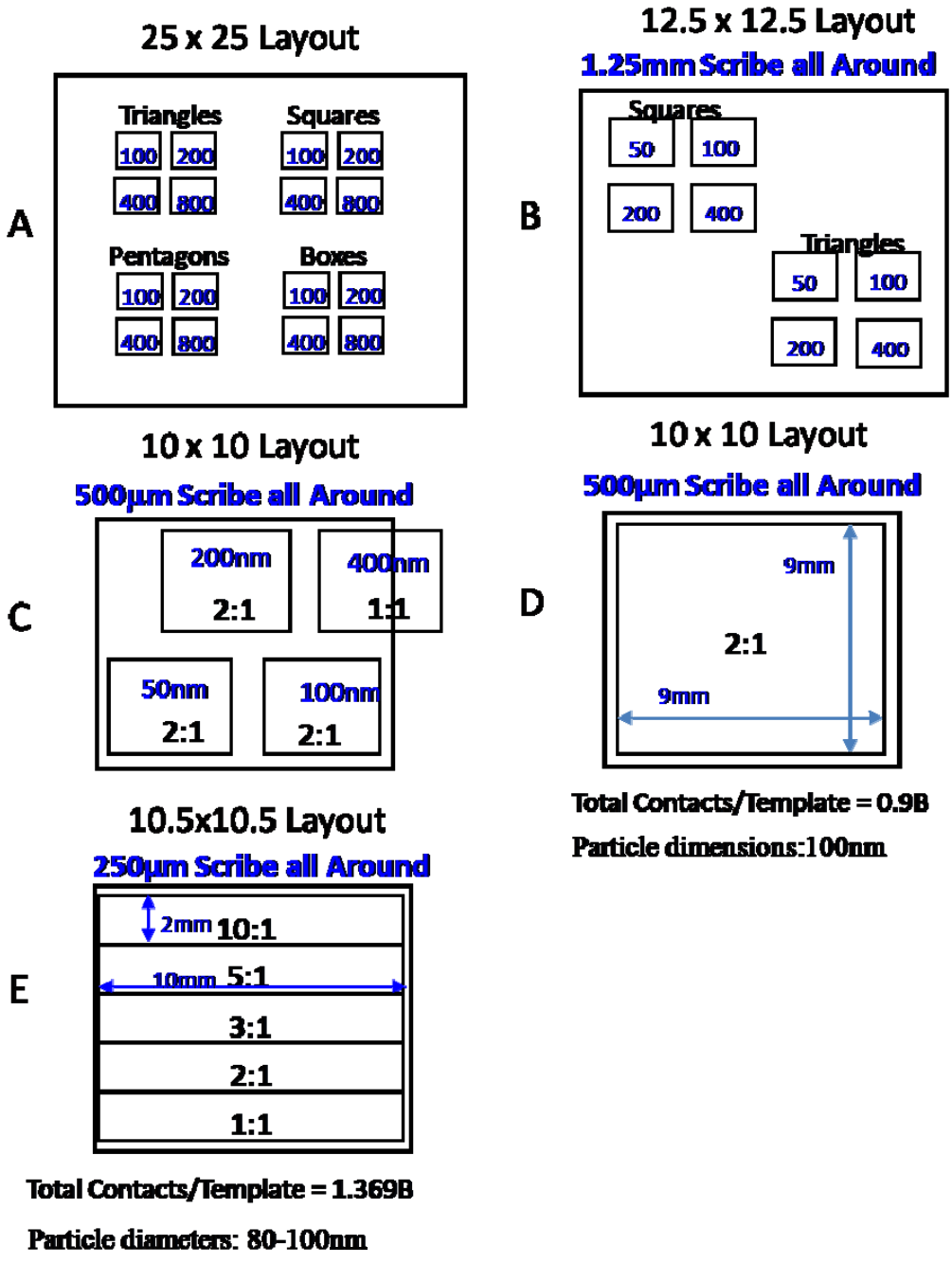

Figure 4.13 SEM Images of Patterned Quartz Template using E-beam Lithography and Reactive Ion Etching: (A) 50 nm squares *(scale bar = 200nm)*, **(B) 100nm squares** *(scale bar = 200nm)*, **(C) 200 nm pentagons** *(scale bar = 200nm)*, **(D) 200 nm triangles** *(scale bar = 200nm)*, **(E) 200 nm squares** *(scale bar = 400nm)*, **and (F) 400 nm nanocontainers** *(scale bar = 400nm)*.

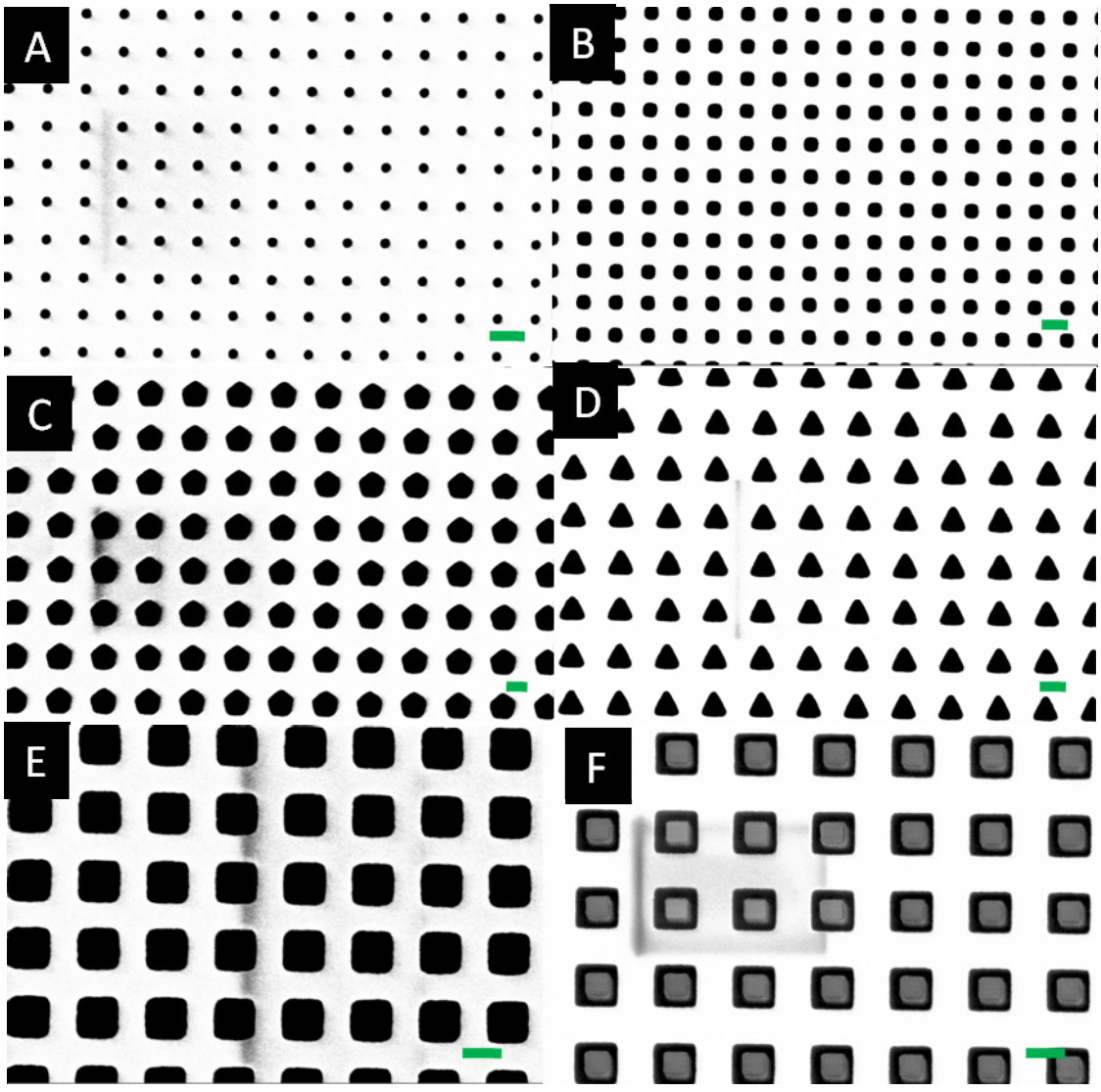

Figure 4.14 Three-dimensional Poly(methyl methacrylate) (PMMA) Nanocontainers Fabricated using ThNIL: (A) 200 nm nanocontainers *(scale bar = 200nm)***, (B) 400 nm nanocontainers** *(scale bar = 200nm)***, (C) 800 nm nanocontainers** *(scale bar = 1μm)***, and (D) a dense array of 400 nm nanocontainers** *(scale bar = 1μm)***.**

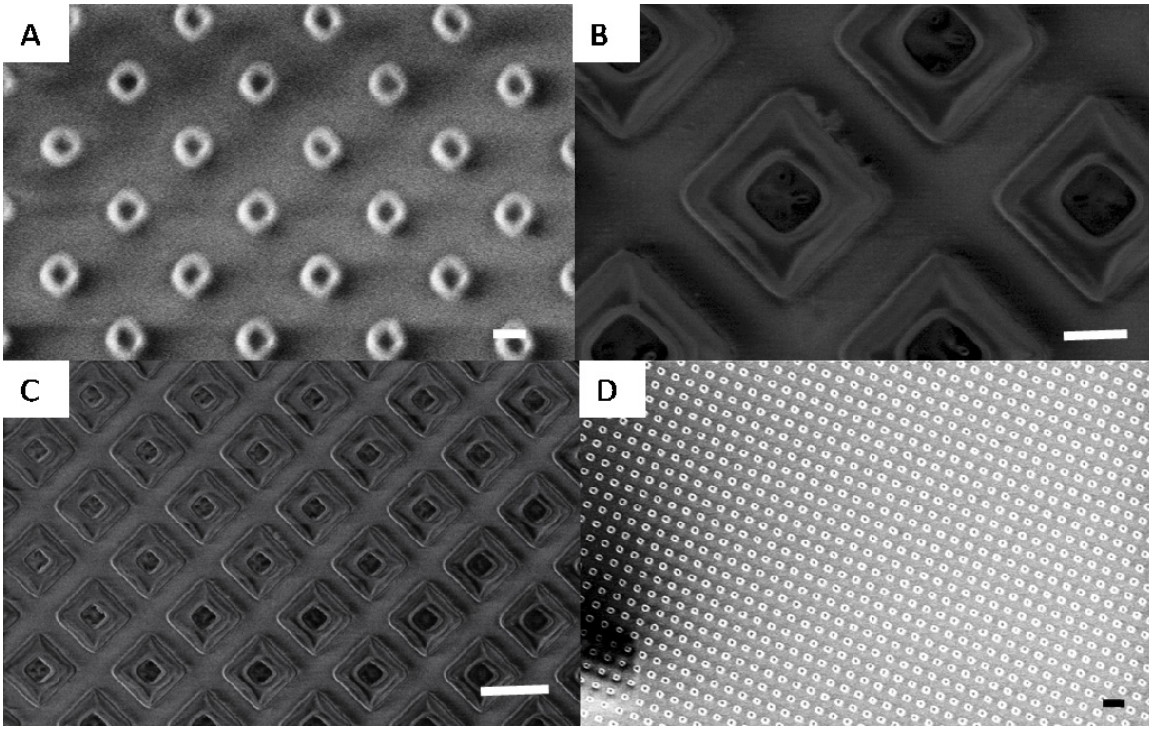

Figure 4.15 PLGA Characterization and Spinning Study Results: (A) Average Cauchy Characteristics needed to determine film thickness, and (B) film thickness of various PLGA concentrations in solvents, acetone and DCM versus spin speed at 50 seconds.

A

		Average Cauchy Characteristics		
		A	B	C
PLGA 502H	5% (w/v) in Acetone	1.522	0.0126	-0.000306
	5% (w/v) in DCM	1.455	0.0123	-0.000302
PLGA 503H	3% (w/v) in Acetone	1.497	0.0034	0.000073
	5% (w/v) in Acetone	1.485	0.0142	-0.000272
	5% (w/v) in DCM	1.538	0.0010	0.000101
PLGA 502A	3% (w/v) in Acetone	1.464	0.0052	-0.000091
	5% (w/v) in Acetone	1.460	0.0041	0.000084
	8% (w/v) in Acetone	1.479	0.0040	0.000072
	8% (w/v) in DCM	1.452	0.0032	0.000115

B

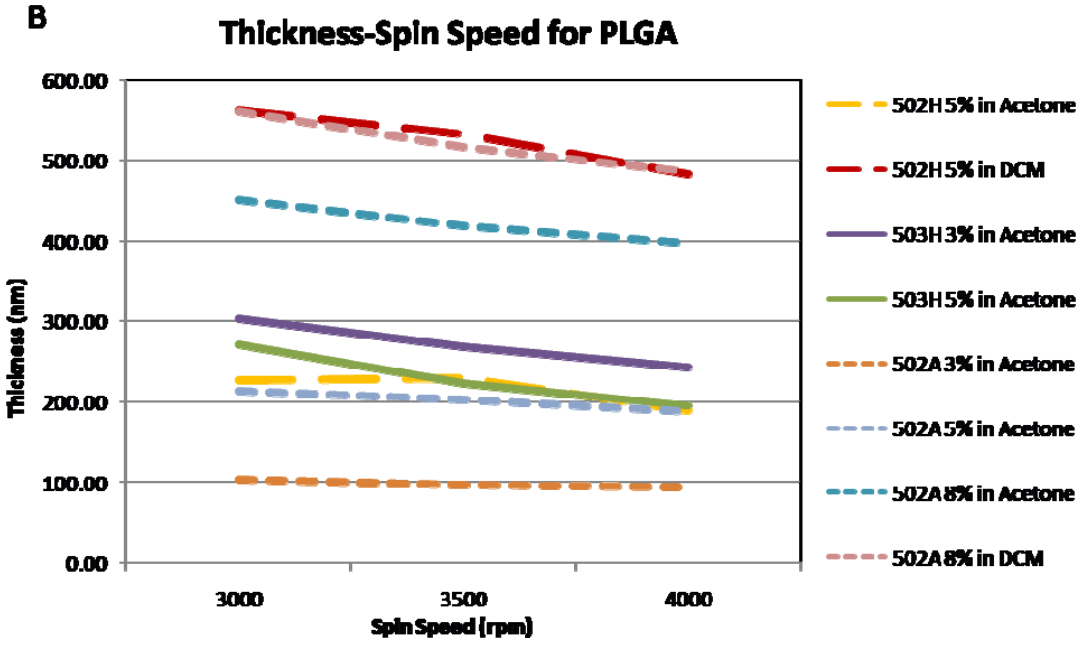

Figure 4.16 PLGA Features Patterned with ThNIL: (A) shallow features in 5% (w/v) PLGA 502H in DCM *scale bar = 4μm)*, **(B) shallow features in 5% (w/v) PLGA 502H in acetone, with surrounding bubbles** *(scale bar = 2μm)*.

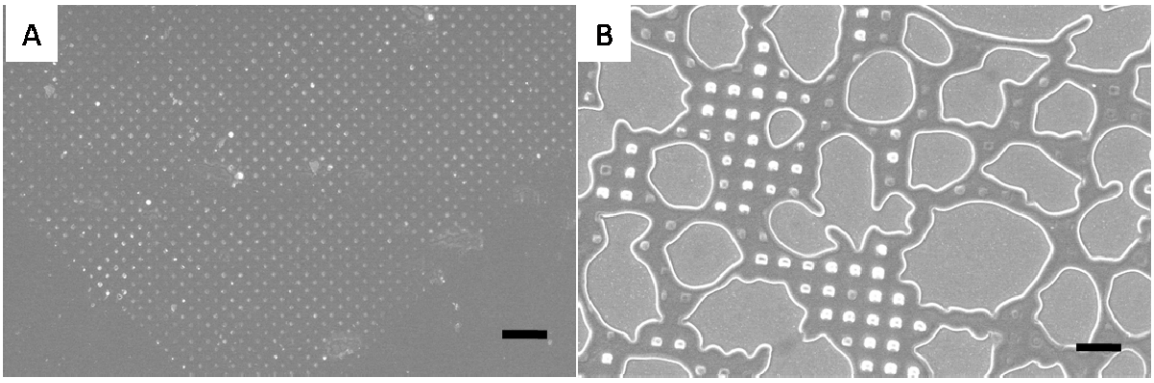

Table 4.2 Contact Angle Measurements for Template Release Layer.

Release Layer	SAM	SAM	Relmat
Template	10 x 10 mm mesa with 400, 200, 100 and 50nm squares	fully patterned 10 x 10 mm mesa with 100nm squares	10 x 10 mm mesa with 400, 200, 100 and 50nm squares
over 400nm squares	109.19	na	93.31
over 200nm squares	108.21	na	93.19
over 100nm squares	107.89	101.5	92.79
over 50nm squares	102.31	na	92.31
over unpatterned quartz surface	98.75	97.8	92.04

Figure 4.17 Initial Whole Imprinted Wafer. As a note, this wafer was used for testing various parameters and is not an optimized wafer imprint.

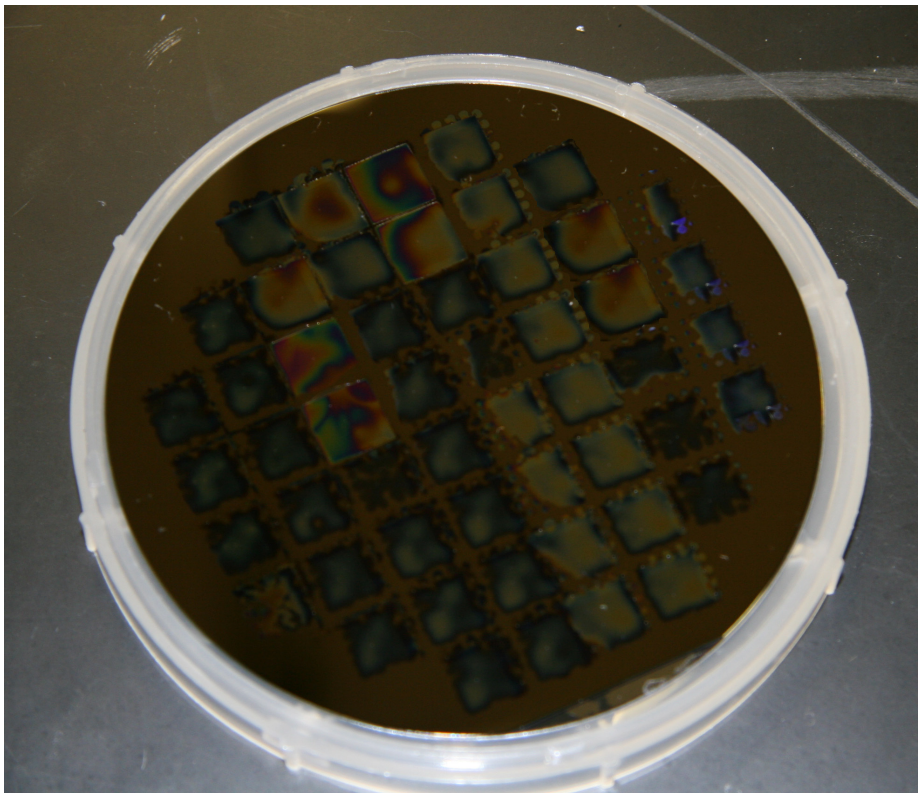

Table 4.3 Viscosity Values for PEGDA (MW 700). The values are based on the bulk density of PEGDA (1.12g/mL) and show the corresponding equation for dispensing of the solution.

PEGDA MW700 (%w/v)	Viscosity (cP)	(SD)	Calibration Equation for Dispensing PEGDA in IMPRIO x = volume (mL), y = voltage (V)
75	40.61*[1]		y = 154862x + 24.596*[2]
60	18.33	0.12	y = 137866x + 25.564*[2]
50	11.10	0.1	
33	4.77	0.05	
25	2.06	0.01	

*[1] Value courtesy Mary C. Moore.

*[2] Calibration equation courtesy Molecular Imprints.

Figure 4.18 Residual Layer Thickness versus Pre-Delay Time. 25% and 33% (w/v) PEGDA (MW 700) using an overall volume of 0.025 μL, an imprint force of 7 N and a 7 second UV exposure.

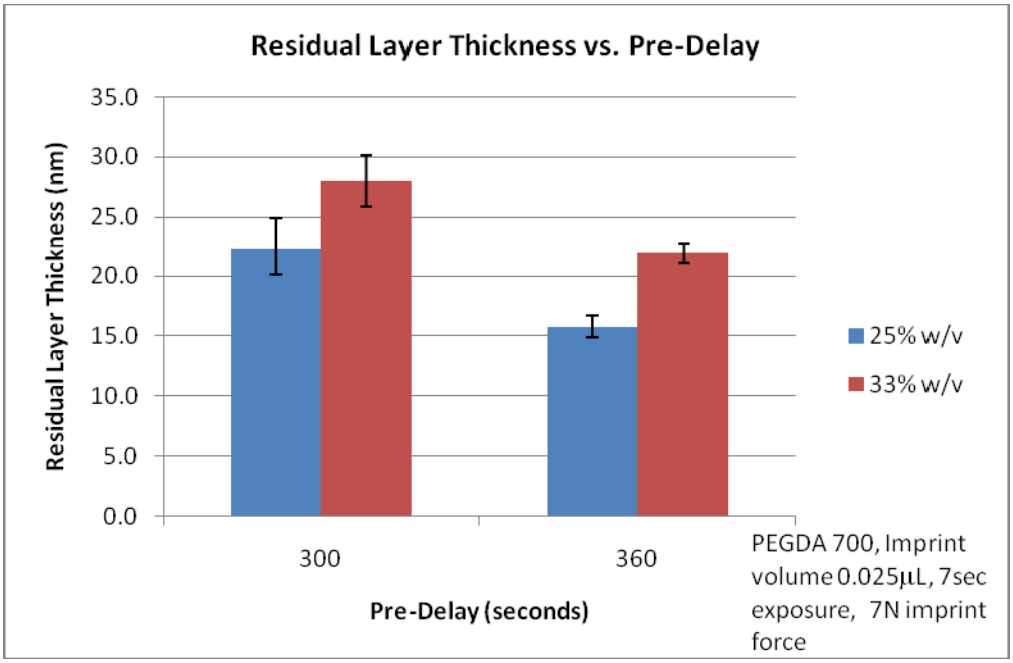

Figure 4.19 Residual Layer Thickness versus Imprint Force. 25% and 33% (w/v) PEGDA (MW 700) using an overall volume of 0.025 μL, a 7 second UV exposure, and a pre-exposure delay of 300 seconds.

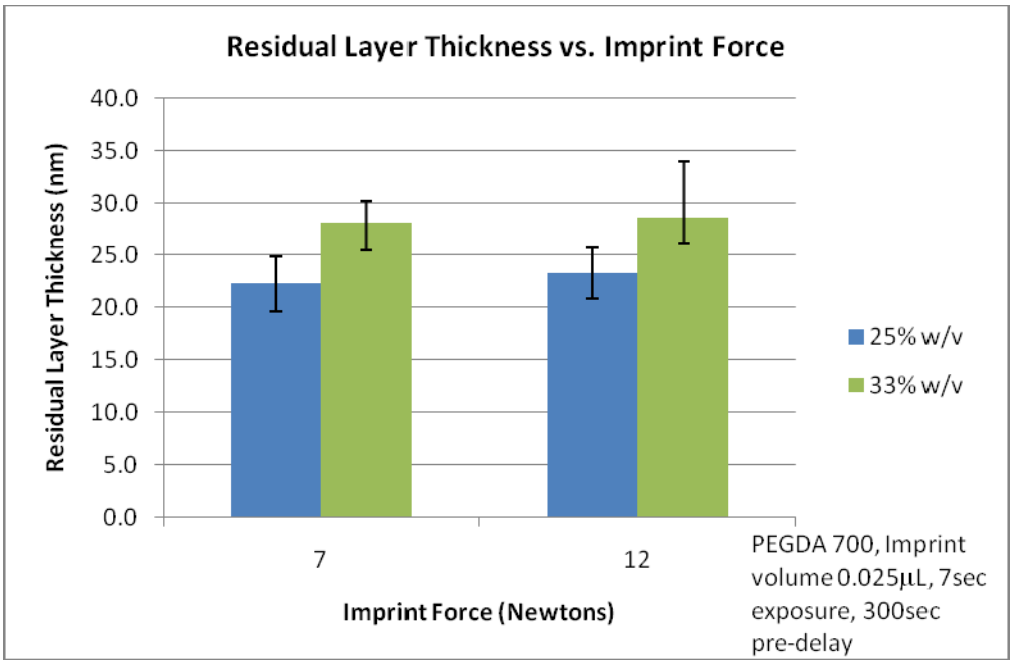

Figure 4.20 Residual Layer Thickness versus UV Exposure Time. 25% and 33% (w/v) PEGDA using an overall volume of 0.025mL, an imprint force of 7N and a 300 second pre-delay.

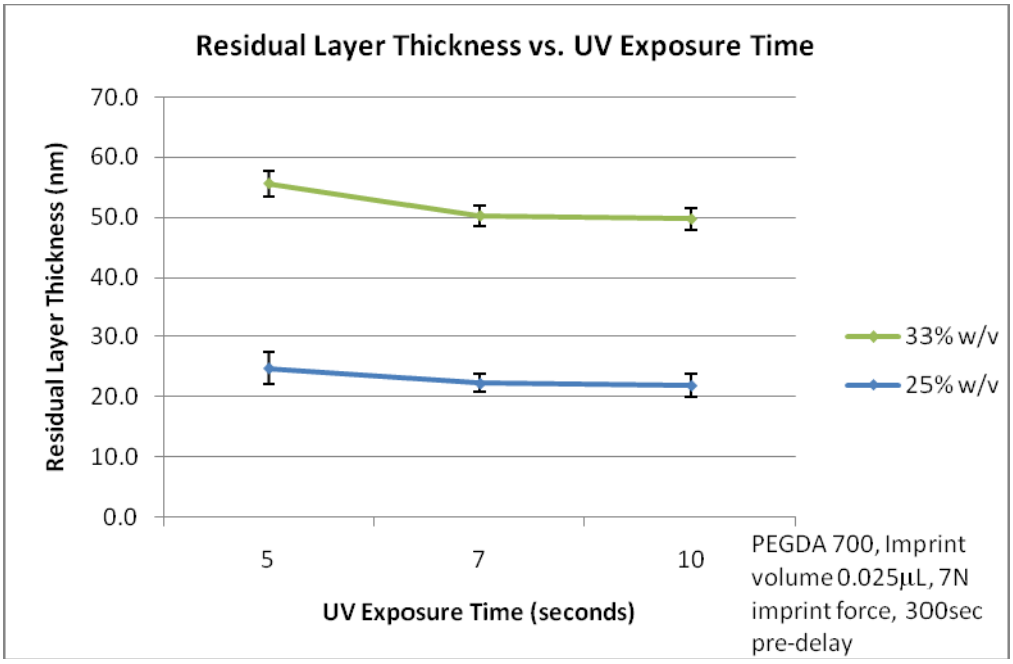

Figure 4.21 Residual Layer Thickness versus Total Imprint Volume. 25% and 33% (w/v) PEGDA using an imprint force of 7 N, a 7 second UV exposure, and a 300 second pre-delay.

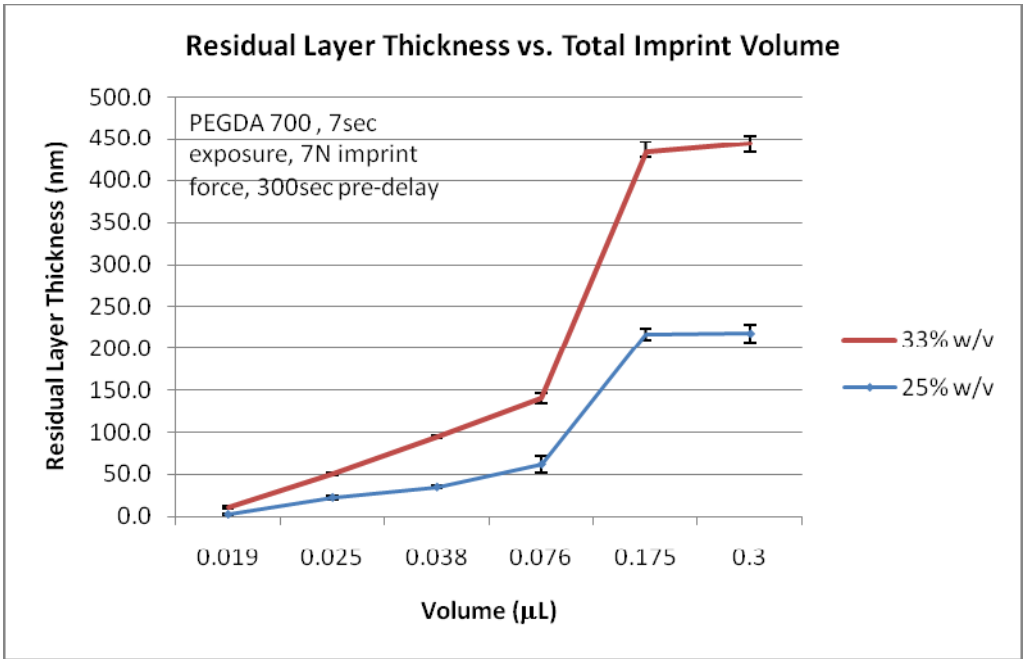

Figure 4.22 Optimized Drop Pattern. The image shows the optimized pattern only. In this image the total drop volume was doubled for imprinting 0.038 µL.

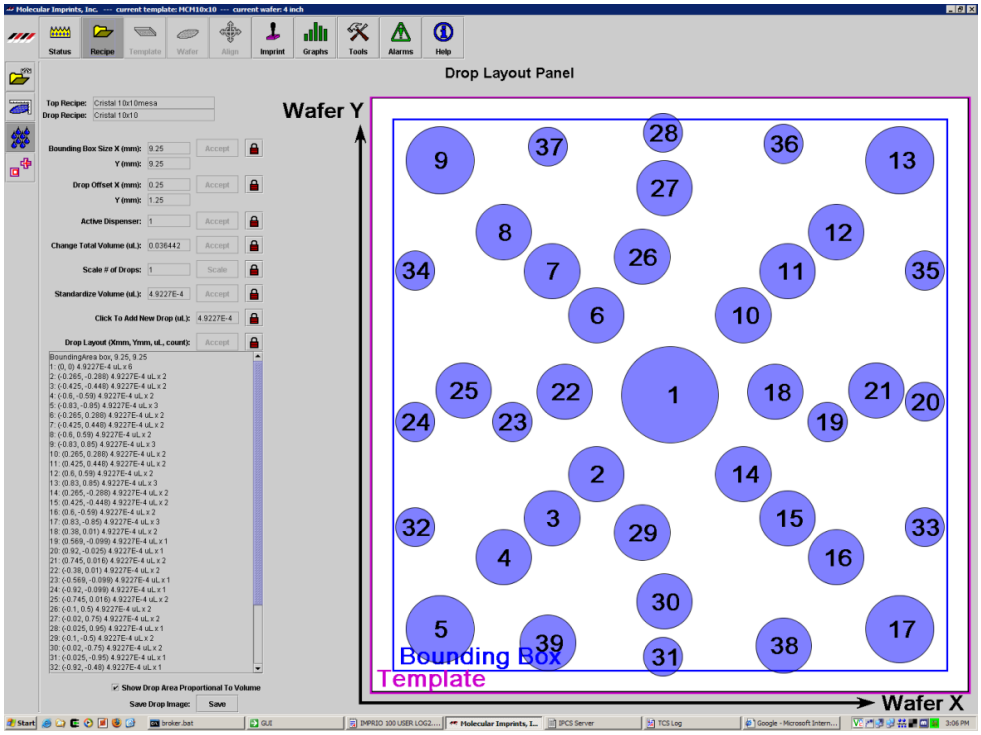

Table 4.4 Residual Layer Thickness versus PEGDA Concentration. Used an optimized setting of 0.019 µL imprint volume, 300 second pre-exposure delay and a 7 second UV exposure.

% (w/v) PEGDA (MW 700)	Residual Layer Thickness in 80% of wafer (nm)	(SD)	Residual Layer Thickness in (20%) of wafer (nm)	(SD)
25	2.1	1.1	9.1	1.3
33	8.7	1.4	15.1	1.2
50	15.6	1.2	22.2	2.1
75	27.0	1.4	30.7	2.6

Figure 4.23 SEM images of PEGDA (MW 700) Residual Layer: (A) manually dispensed macromer with 1.36 μm residual layer *(scale bar = 2μm)*, **(B) 25% (w/v)** *(scale bar = 200nm)*, **(C) 50% (w/v) with 15 nm residual layer** *(scale bar = 300nm)*, **(D) 75% (w/v) with 31 nm residual layer** *(scale bar = 200nm)*.

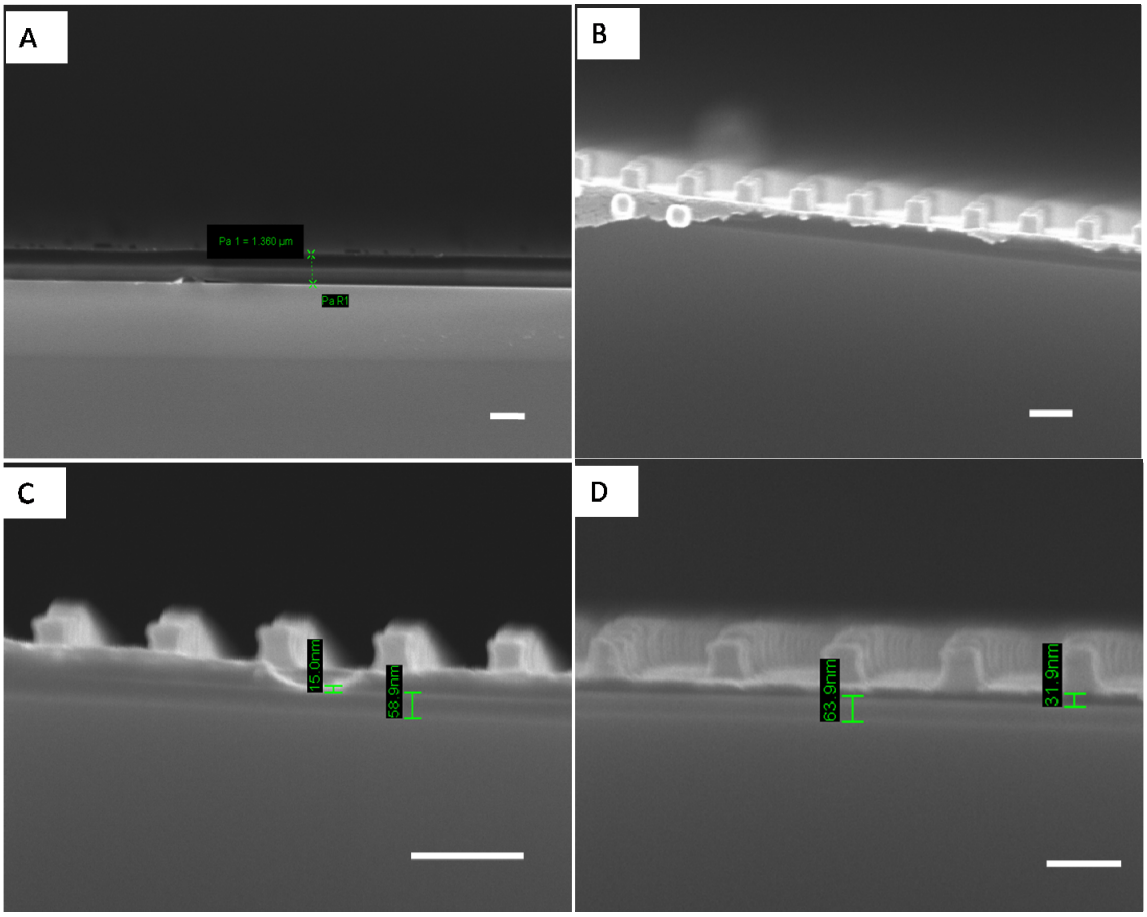

Figure 4.24 SEM images of Three-dimensional PEGDA Nanoparticles: (A) 50 nm squares in 33% (w/v) PEGDA (MW 700) *(scale bar = 200nm)*, **(B) 100 nm squares in 100% (w/v) PEGDA (MW 1000)** *(scale bar = 200nm)*, **(C) 200 nm pentagons in 100% (w/v) PEGDA (MW 1000)** *(scale bar = 200nm)*, **(D) 200 nm triangles in 100% (w/v) PEGDA (MW 1000)** *(scale bar = 200nm)*, **(E) 200 nm squares in 100% (w/v) PEGDA (MW 1000)** *(scale bar = 300nm)*, **and (F) 400 nm pentagons in 100% (w/v) PEGDA (MW 1000)** *(scale bar = 400nm)*, **(G) 400 nm triangles in 100% (w/v) PEGDA (MW 1000)** *(scale bar = 400nm)*, **(H) 400 nm squares in 100% (w/v) PEGDA (MW 1000)** *(scale bar = 400nm)*, **and (I) 400 nm nanocontainers in 100% (w/v) PEGDA (MW 1000)** *(scale bar = 400nm)*.

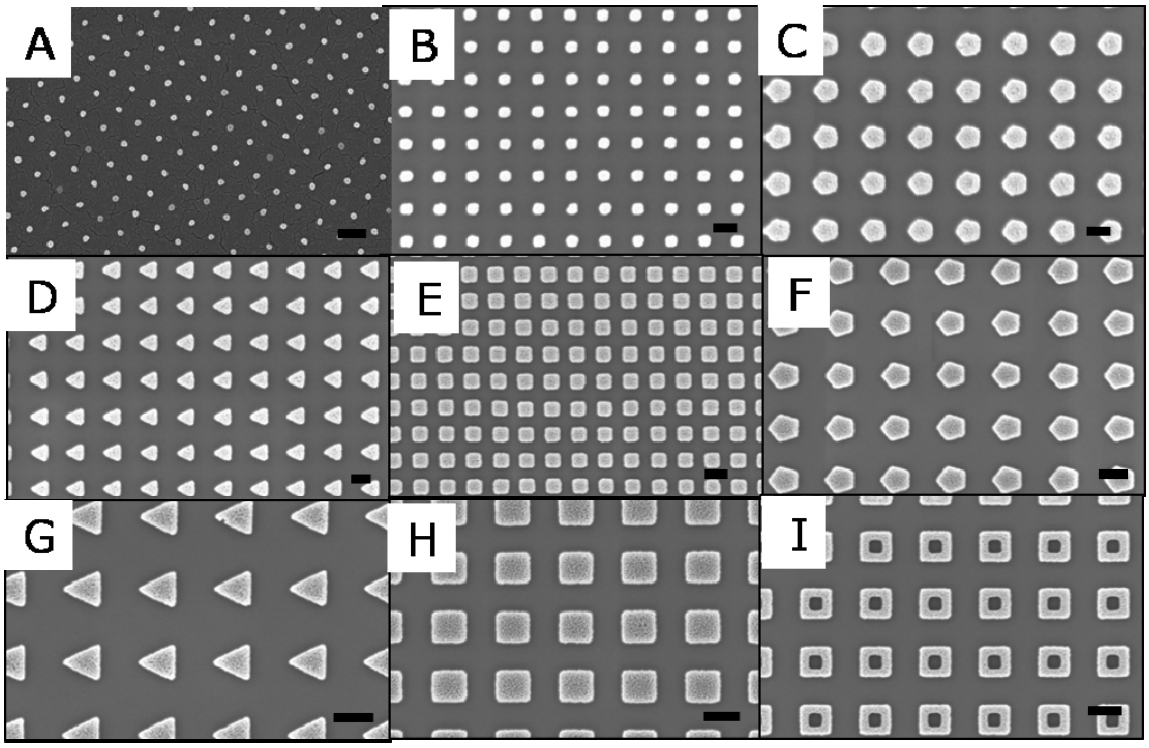

Figure 4.25 SEM images of Monodisperse PEGDA Nanoparticles. 100 nm (97.3 ± 0.2 nm) rounded squares in PEGDA (MW 700) with varying macromer concentrations using 0.019 μL of solution in a 10 x 10 fully patterned mesa: (A) 25% (w/v) *(scale bar = 200nm)***, (B) 33% (w/v)** *(scale bar = 200nm)***, (C) 50% (w/v)** *(scale bar = 200nm)***, (D) profile view of 75% (w/v)** *(scale bar = 200nm)***.**

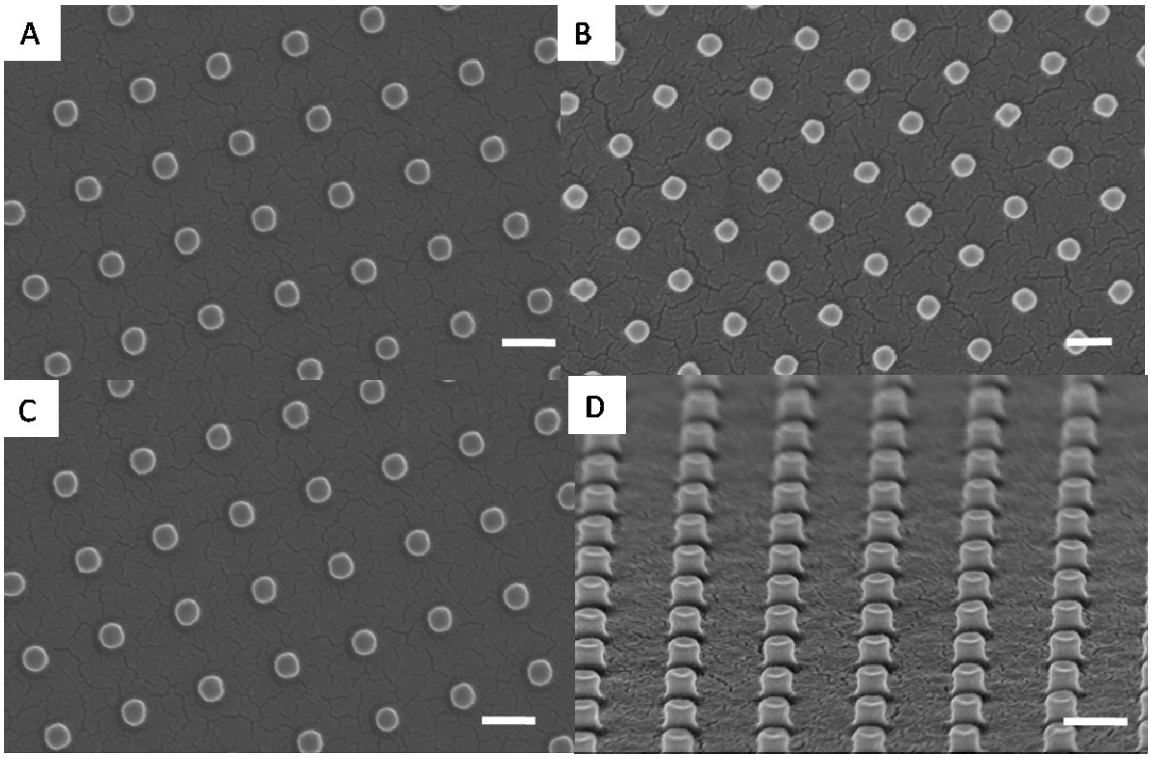

Table 4.5 Residual Layer Thickness of PEGDA Before and After Etching. 33% (w/v) PEGDA (MW 700) imprints were created using a volume of 0.025 μL, an imprint force of 7 N, a pre-exposure delay of 300 seconds and a UV exposure time of 7 seconds.

Etching Process	Residual layer thickness (nm)	(SD)
O2 (20s)	0.10	1.03
He (20s)	2.03	1.52
prior to etch	28.03	2.13

Figure 4.26 AFM Images of Particle Heights Before and After Etching: (A) 50 nm particles before etching, (B) 50 nm particles after etching, (C) top view of 50 nm particles, (D) 100nm particles before etching, (E) 100 nm particles after etching, (F) top view of 100 nm particles, (G) 200 nm particles after etching, (H) 400 nm particles after etching, (I) isometric profile of 400 nm particles.

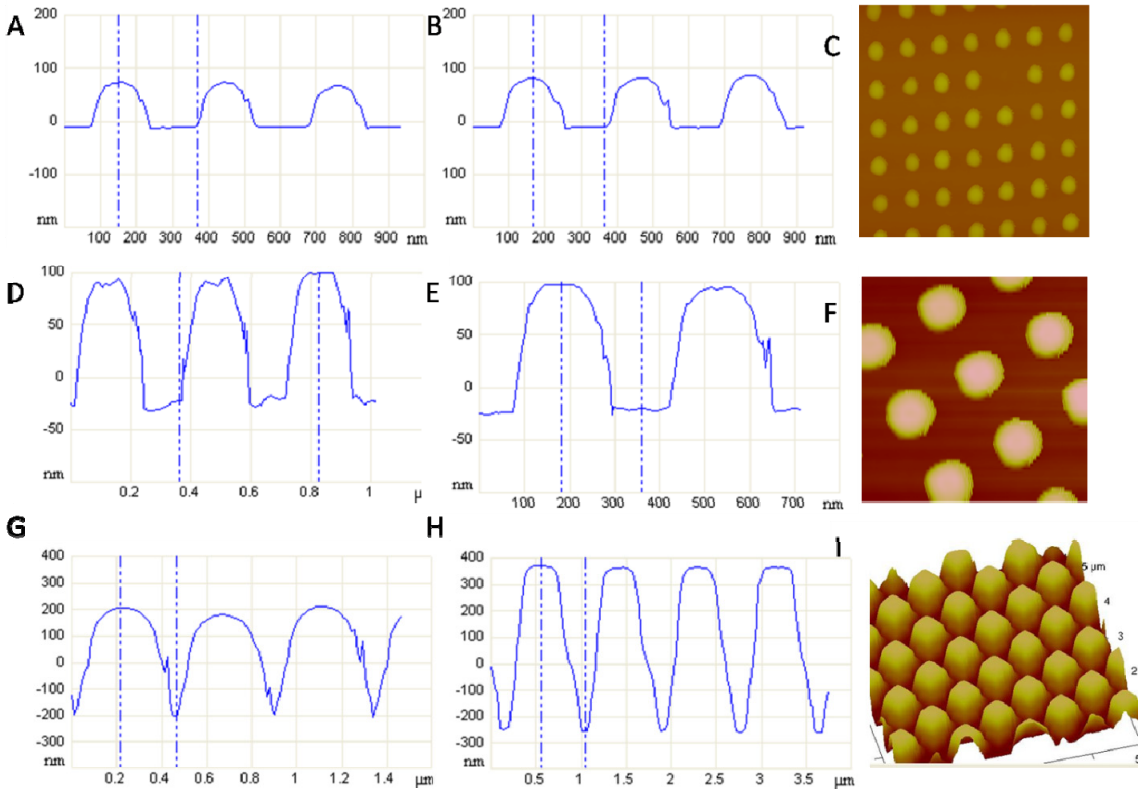

Figure 4.27 C1s Scans of PEGDA Before and After Etching. Comparison of 75% (w/v) PEGDA (MW 700) on BARC and silicon, before and after oxygen and helium etching. (A) 0.174 µL PEGDA sample, and (B) 0.025 µL PEGDA sample. Charge neutralization was utilized and the C-C peak placed at 285 eV.

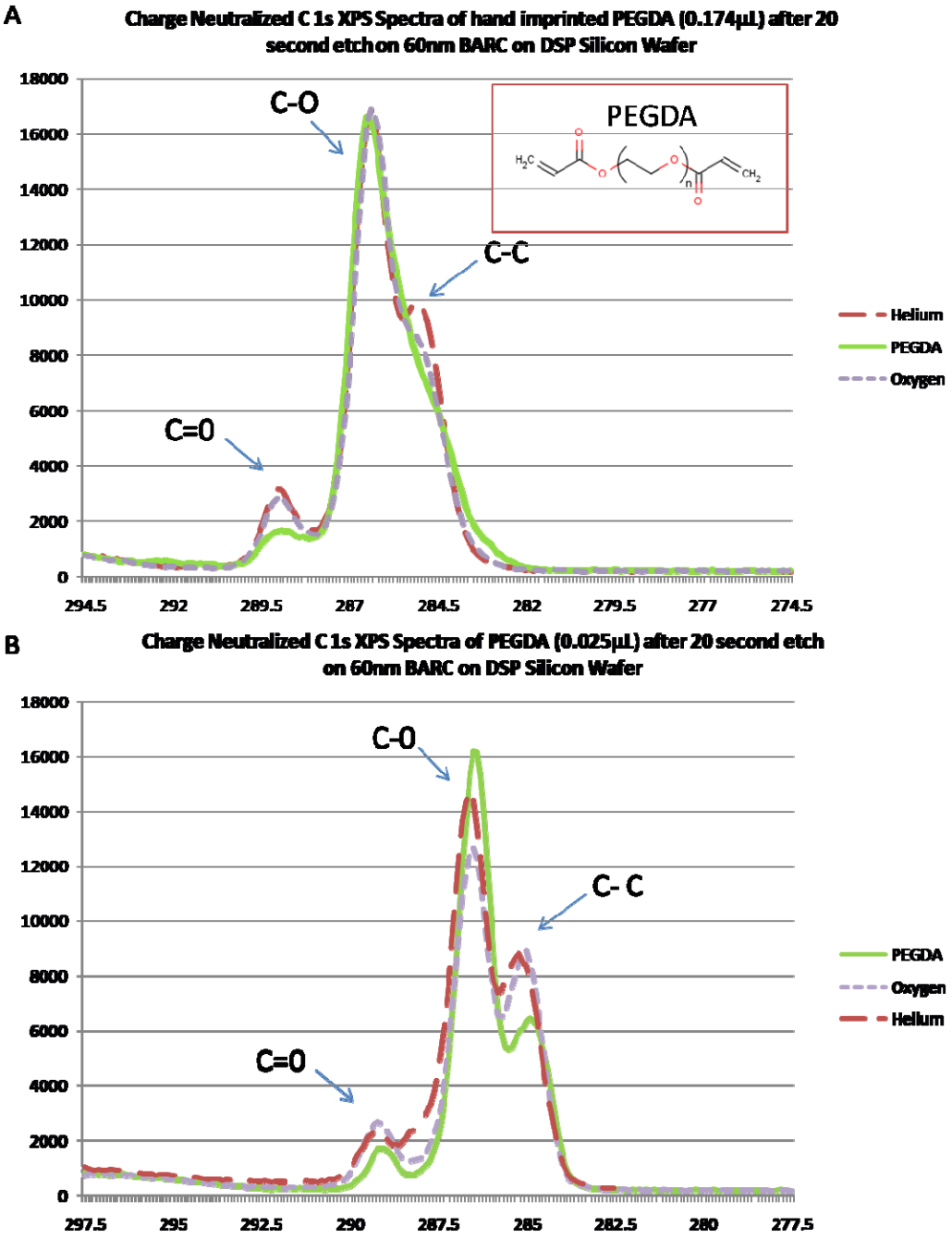

Figure 4.28 Harvested 33% (w/v) PEGDA Nanoparticles After Helium Etching: (A) 400 nm squares *(scale bar = 1μm)*, **(B) 100 nm and 50 nm particles** *(scale bar = 200nm)*, **(C) magnified view of 100 nm square particle** *(scale bar = 200nm)*, **(D) 100 nm square particles** *(scale bar = 200nm)*, **(E) 100 nm squares particle** *(scale bar = 200nm)*, **and (F) 50 nm square particles** *(scale bar = 200nm)*.

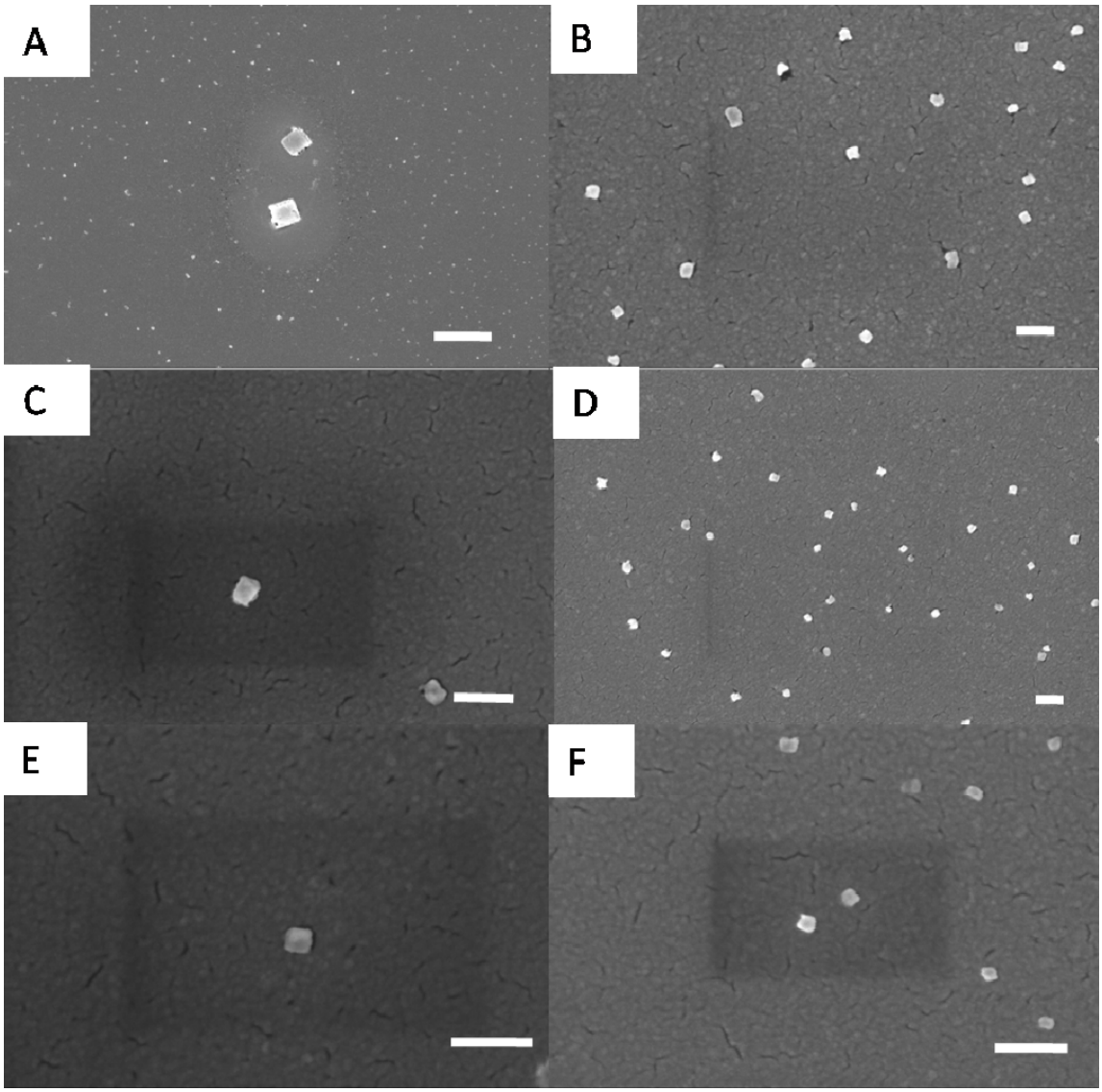

Figure 4.29 Harvested 25% (w/v) PEGDA Nanoparticles Without Etching: (A) 400 nm square particle *(scale bar = 1μm)*, **(B) 400 nm and 200 nm particles** *(scale bar = 2μm)*, **(C) magnified view of 100nm square particle** *(scale bar = 300nm)*, **(D) 200 nm square particles** *(scale bar = 1μm)*, **(E) 400 nm squares particle** *(scale bar = 400nm)*, **and (F) 400 nm square particles** *(scale bar = 1μm)*.

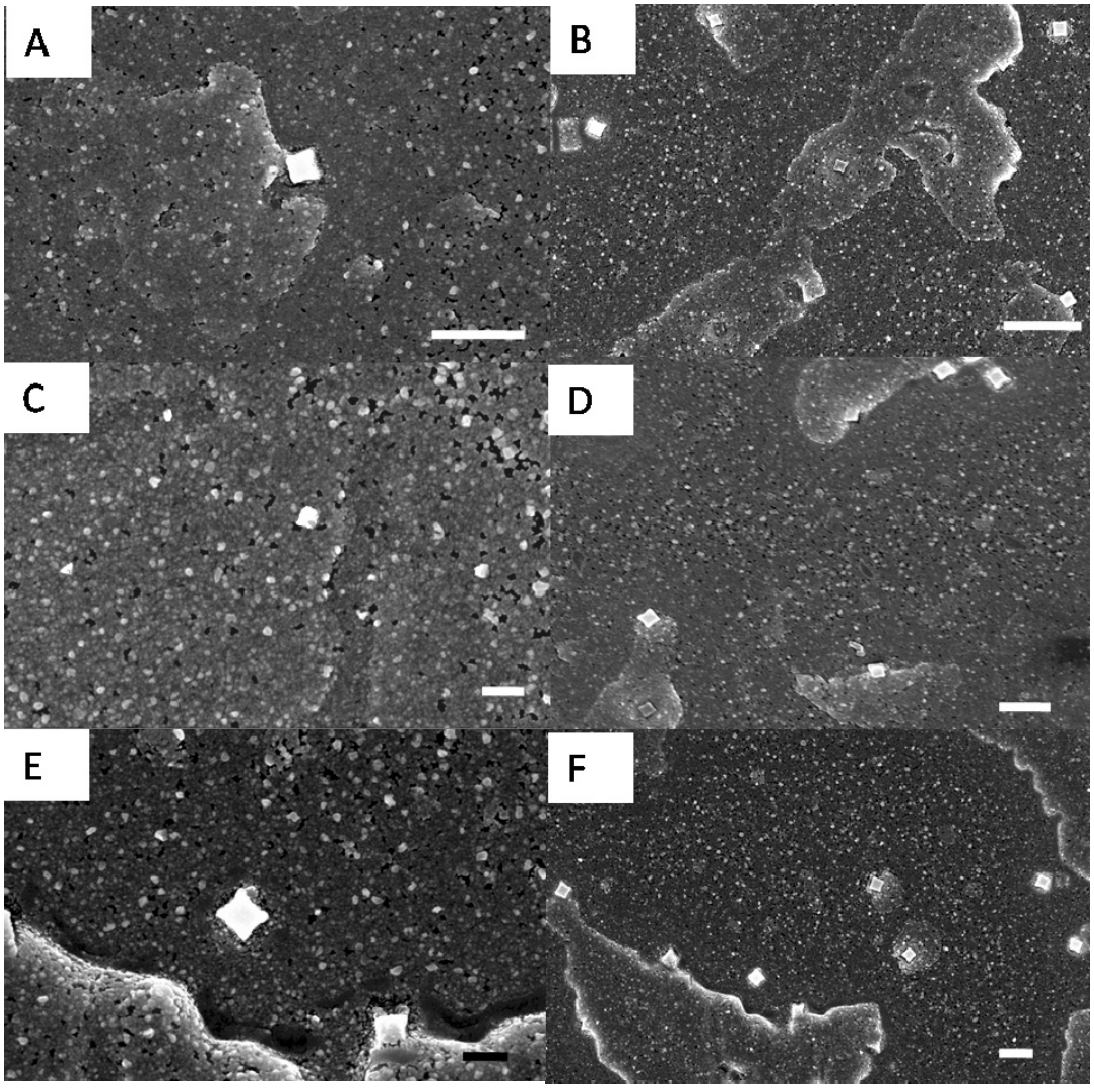

Figure 4.30 Theoretical Number of Particles Generated using SFIL. Particle number based on varying spacing, feature size, and template size: (A) number of particles per template, (B) number of particles per imprinted 4" wafer, and (C) number of particles per imprinted 8" wafer.

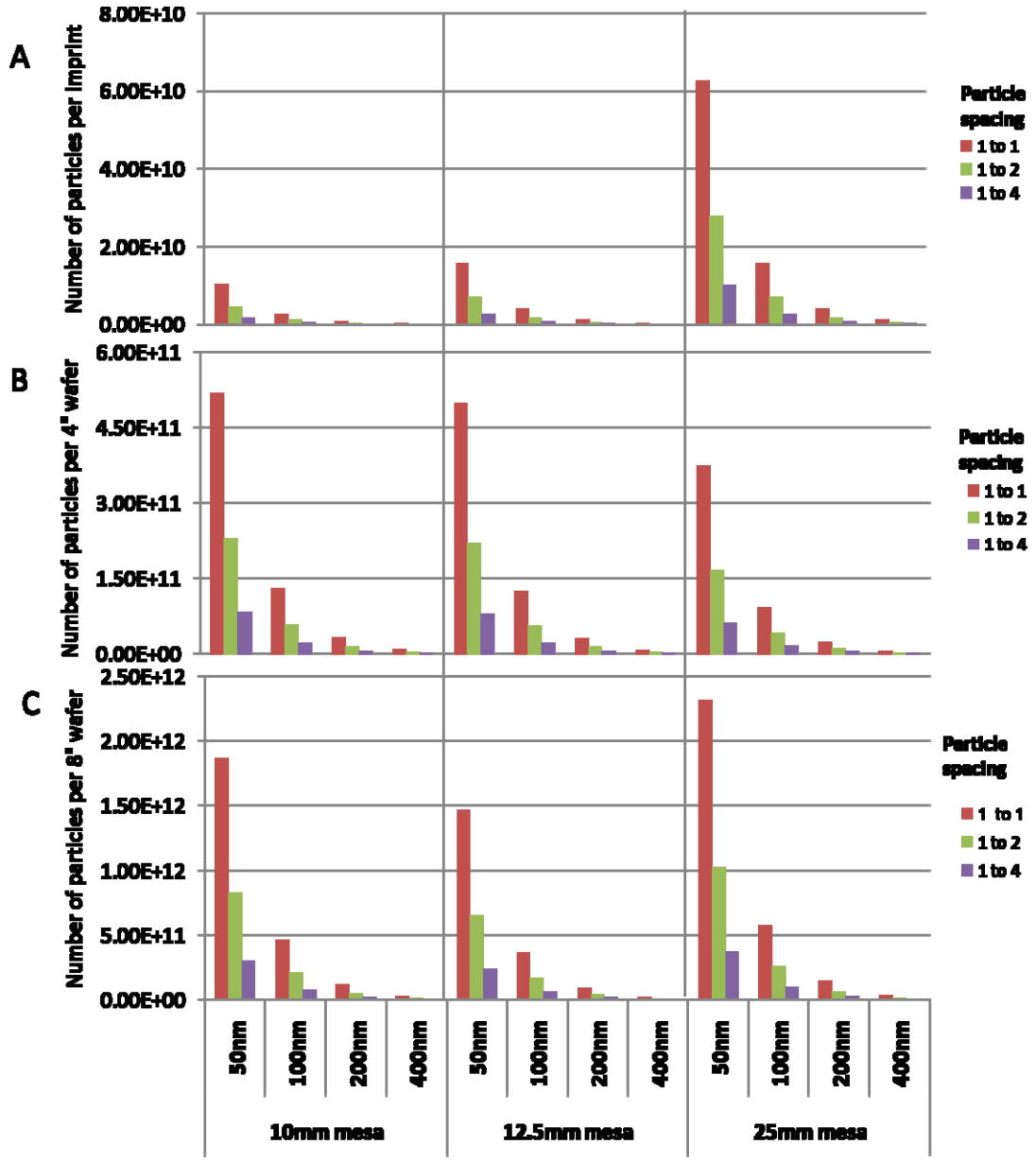

Figure 4.31 Theoretical Loading Level of Particles. For a 10 x 10 mm mesa using a 10 mg/mL solution of model drug in macromer for various particle shapes, sizes and spacing: (A) mass of model drug per imprint, (B) mass of model drug per imprinted 4" wafer, and (C) mass of model drug per imprinted 8" wafer.

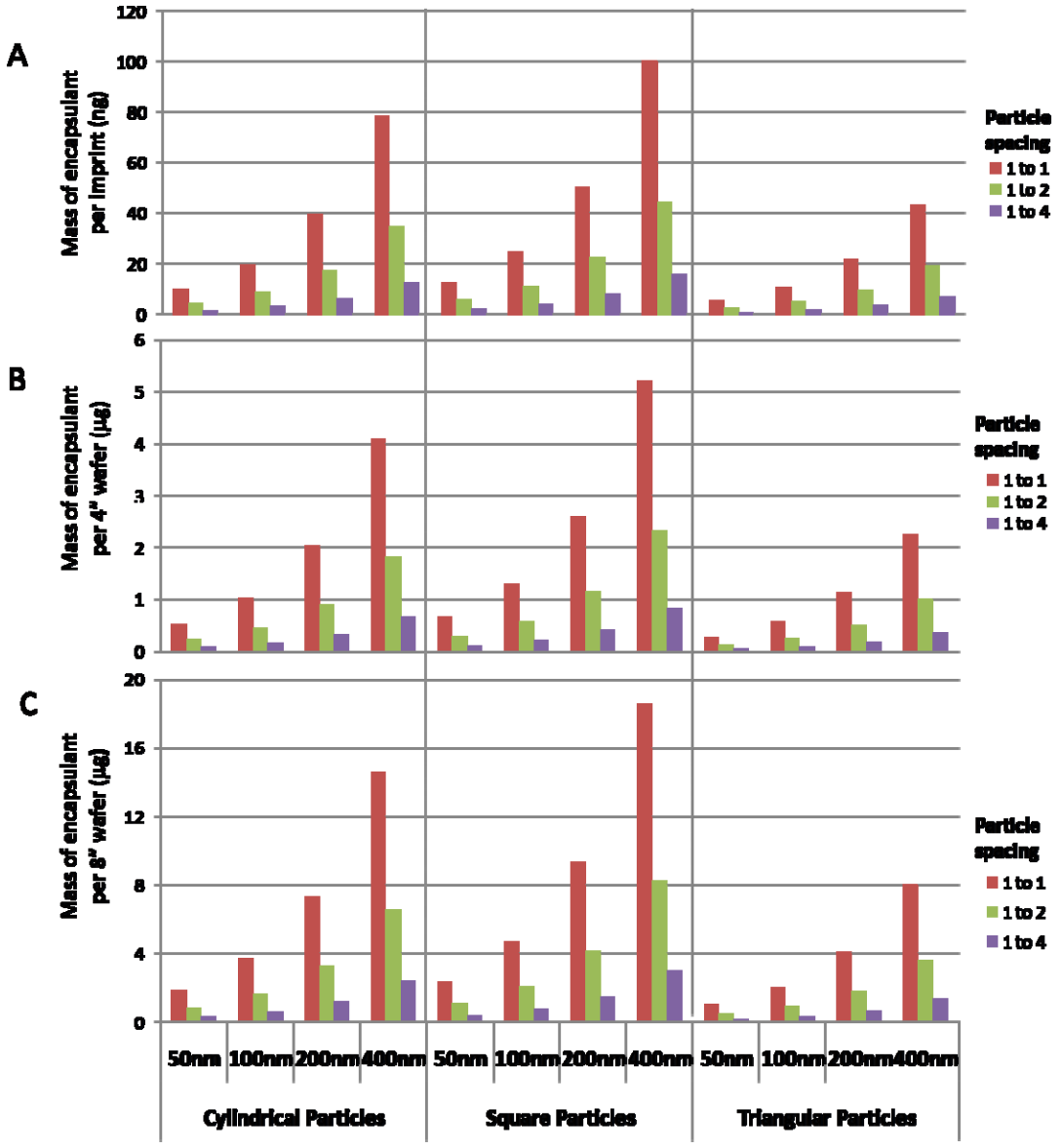

Table 4.6 Actual Number of Particles per 10 x 10 mm Template Mesa, Estimated Number of Particles per Wafer, and Theoretical Loading Level for the 10 x 10 mm fully patterned mesa with 100 nm square features and 1 to 2 spacing and the 10.5 x 10.5 mm fully patterned mesa (assuming initial 10 mg/mL solution of model drug in macromer).

				Cylindrical Features			Square Features		
	Number of particles per imprint (10^8)	Number of particles per 4" wafer (10^{10})	Number of particles per 8" wafer (10^{11})	Total mass encapsulated agent per imprint (ng)	Total mass of agent per 4" wafer (μg)	Total mass of agent per 8" wafer (μg)	Total mass encapsulated agent per imprint (ng)	Total mass of agent per 4" wafer (μg)	Total mass of agent per 8" wafer (μg)
Fully patterned template	9	4.68	1.67	52.99	2.76	9.86	67.50	3.51	12.56
MI's template	13.7	7.12	2.55	39.17	2.04	7.29			

Figure 4.32 C1s Scans of Varying PEGDA Concentrations on Silicon: (A) 5mM, (B) 10mM, (C) 20mM, and (D) 50 mM. *Reprinted from Biosens Bioelectr, 20, S. Sharma, R. W. Johnson, and T. A. Desai, 227-239, 2004, with permission from Elsevier.*

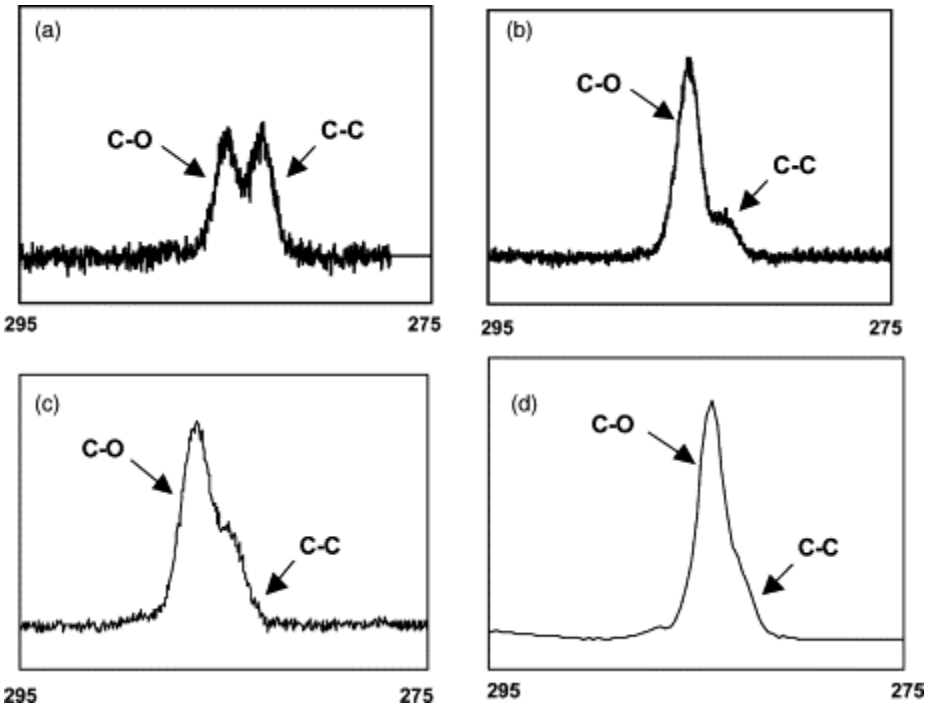

4.5 REFERENCES

1. Wong HL, Bendayan R, Rauth AM, Li Y, Wu XY. Chemotherapy with anticancer drugs encapsulated in solid lipid nanoparticles. Adv Drug Deliv Rev 2007;59(6):491-504.
2. Peer D, Karp JM, Hong S, Farokhzad OC, Margalit R, Langer R. Nanocarriers as an emerging platform for cancer therapy. Nature Nanotech 2007;2(12):751-760.
3. Moghimi SM, Hunter AC, Murray JC. Nanomedicine: current status and future prospects. Faseb J 2005;19(3):311-330.
4. Champion JA, Katare YK, Mitragotri S. Particle shape: a new design parameter for micro- and nanoscale drug delivery carriers. J Control Release 2007;121(1-2):3-9.
5. Geng Y, Dalhaimer P, Cai S, Tsai R, Tewari M, Minko T, et al. Shape effects of filaments versus spherical particles in flow and drug delivery. Nature Nanotech 2007;2(4):249-255.
6. Nishiyama N. Nanomedicine: nanocarriers shape up for long life. Nature Nanotech 2007;2(4):203-204.
7. Decuzzi P, Ferrari M. The adhesive strength of non-spherical particles mediated by specific interactions. Biomaterials 2006;27(30):5307-5314.
8. Decuzzi P, Causa F, Ferrari M, Netti PA. The effective dispersion of nanovectors within the tumor microvasculature. Ann Biomed Eng 2006;34(4):633-641.
9. Velev OD, Lenhoff AM, Kaler EW. A class of microstructured particles through colloidal crystallization. Science 2000;287(5461):2240-2243.

10. Sozzani P, Bracco S, Comotti A, Simonutti R, Valsesia P, Sakamoto Y, et al. Complete shape retention in the transformation of silica to polymer micro-objects. Nat Mater 2006;5(7):545-551.

11. Dendukuri D, Pregibon DC, Collins J, Hatton TA, Doyle PS. Continuous-flow lithography for high-throughput microparticle synthesis. Nat Mater 2006;5(5):365-369.

12. Dendukuri D, Tsoi K, Hatton TA, Doyle PS. Controlled synthesis of nonspherical microparticles using microfluidics. Langmuir 2005;21(6):2113-2116.

13. Xu S, Nie Z, Seo M, Lewis P, Kumacheva E, Stone HA, et al. Generation of monodisperse particles by using microfluidics: control over size, shape, and composition. Angew Chem Int Ed Engl 2005;44(5):724-728.

14. Champion JA, Katare YK, Mitragotri S. Making polymeric micro- and nanoparticles of complex shapes. Proc Natl Acad Sci USA 2007;104(29):11901-11904.

15. Almeida AJ, Souto E. Solid lipid nanoparticles as a drug delivery system for peptides and proteins. Adv Drug Deliver Rev 2007;59(6):478-490.

16. Rolland JP, Maynor BW, Euliss LE, Exner AE, Denison GM, DeSimone JM. Direct fabrication and harvesting of monodisperse, shape-specific nanobiomaterials. J Am Chem Soc 2005;127(28):10096-10100.

17. Euliss LE, Welch CM, Maynor BW, Rolland JP, Denison GM, Gratton SE, et al. Monodisperse nanocarriers: novel fabrication of polymeric nanoparticles for bio-nanotechnology. Proc SPIE 2006;6153:61534A.

18. Gratton SEA, Pohlhaus PD, Lee J, Guo J, Cho MJ, Desimone JM. Nanofabricated particles for engineered drug therapies: a preliminary biodistribution study of PRINT nanoparticles. J Control Release 2007;121(1-2):10-18.

19. Johnson SC, Bailey TC, Dickey MD, Smith BJ, Kim EK, Jamieson AT, et al. Advances in Step and Flash imprint lithography. Proc SPIE 2003;5037:197-202.

20. McMackin I, Schumaker P, Babbs D, Choi J, Collison W, Sreenivasan SV, et al. Design and performance of a step and repeat imprinting machine. Proc SPIE 2003;5037:178-186.

21. Johnson S, Resnick DJ, Mancini D, Nordquist K, Dauksher WJ, Gehoski K, et al. Fabrication of multi-tiered structures on step and flash imprint lithography templates. Microelectron Eng 2003;67-68:221-228.

22. Resnick DJ, Dauksher WJ, Mancini D, Nordquist KJ, Bailey TC, Johnson S, et al. Imprint lithography for integrated circuit fabrication. J Vac Sci Technol B 2003;21(6):2624-2631.

23. Choi BJ, Meissl MJ, Colburn M, Bailey TC, Ruchhoeft P, Sreenivasan SV, et al. Layer-to-layer alignment for step and flash imprint lithography. Proc SPIE 2001;4343:436-442.

24. Resnick DJ, Sreenivasan SV, Willson CG. Step & flash imprint lithography. Mater Today 2005;8(2):34-42.

25. Colburn M, Johnson SC, Stewart MD, Damle S, Bailey TC, Choi B, et al. Step and flash imprint lithography: a new approach to high-resolution patterning. Proc SPIE 1999;3676:379-389.

26. Chou SY, Krauss PR, Renstrom PJ. Imprint lithography with 25-nanometer resolution. Science 1996;272(5258):85-87.

27. Chou SY, Krauss PR. Imprint lithography with sub-10 nmfeature size and high throughput. Microelectron Eng 1997;35(1):237-240.

28. Resnick DJ, Mancini DP, Nordquist KJ, Dauksher WJ, McMackin I, Schumaker P, et al. Initial study of the fabrication of step and flash imprint lithography templates for the printing of contact holes. J Microlith Microfab 2004;3(2):316-321.

29. Chen Y, Macintyre D, Boyd E, Moran D, Thayne I, Thoms S. Fabrication of high electron mobility transistors with T-gates by nanoimprint lithography. J Vac Sci Technol B 2002;20(6):2887-2890.

30. Schulz H, Wissen M, Bogdanski N, Scheer HC, Mattes K, Friedrich C. Impact of molecular weight of polymers and shear rate effects for nanoimprint lithography. Microelectron Eng 2006;83(2):259-280.

31. Willett RL, Baldwin KW, West KW, Pfeiffer LN. Differential adhesion of amino acids to inorganic surfaces. Proc Natl Acad Sci USA 2005;102(22):7817-7822.

32. Resnick DJ, Mancini DP, Sreenivasan SV, Willson CG. Release layers for contact and imprint lithography. Semicond Int 2002;25(6):71-80.

33. Bailey T, Choi BJ, Colburn M, Meissl M, Shaya S, Ekerdt JG, et al. Step and flash imprint lithography: Template surface treatment and defect analysis. J Vac Sci Technol B 2000;18(6):3572-3577.

34. Saluja A, Kalonia DS. Measurement of fluid viscosity at microliter volumes using quartz impedance analysis. AAPS PharmSciTech 2004;5(3):e47.

35. Lee H. Effect of imprinting pressure on residual layer thickness in ultraviolet nanoimprint lithography. J Vac Sci Technol B 2005;23(3):1102-1106.

36. Popat KC, Johnson RW, Desai TA. Characterization of vapor deposited poly (ethylene glycol) films on silicon surfaces for surface modification of microfluidic systems. J Vac Sci Technol B 2003;21(2):645-654.

37. Popat KC, Sharma S, Desai TA. Quantitative XPS analysis of PEG-modified silicon surfaces. J Phys Chem B 2004;108(17):5185-5188.

38. Sharma S, Johnson RW, Desai TA. XPS and AFM analysis of antifouling PEG interfaces for microfabricated silicon biosensors. Biosens Bioelectron 2004;20(2):227-239.

39. Sharma S, Johnson RW, Desai TA. Ultrathin poly(ethylene glycol) films for silicon-based microdevices. Appl Surf Sci 2003;206(1-4):218-229.

40. Guan J, Ferrell N, James Lee L, Hansford DJ. Fabrication of polymeric microparticles for drug delivery by soft lithography. Biomaterials 2006;27(21):4034-4041.

41. Zambaux MF, Bonneaux F, Gref R, Maincent P, Dellacherie E, Alonso MJ, et al. Influence of experimental parameters on the characteristics of poly(lactic acid) nanoparticles prepared by a double emulsion method. J Control Release 1998;50(1-3):31-40.

42. Bezemer JM, Radersma R, Grijpma DW, Dijkstra PJ, van Blitterswijk CA, Feijen J. Microspheres for protein delivery prepared from amphiphilic multiblock copolymers. 1. Influence of preparation techniques on particle characteristics and protein delivery. J Control Release 2000;67(2-3):233-248.

43. Scholes PD, Coombes AGA, Illum L, Davis SS, Vert M, Davies MC. The preparation of sub-200 nm poly (lactide-co-glycolide) microspheres for site-specific drug delivery. J Control Release 1993;25(1-2):145-153.

44. Meerum Terwogt JM, ten Bokkel Huinink WW, Schellens JH, Schot M, Mandjes IA, Zurlo MG, et al. Phase I clinical and pharmacokinetic study of PNU166945, a novel water-soluble polymer-conjugated pro-drug of paclitaxel. Anticancer Drugs 2001;12(4):315-323.

45. Seymour LW, Ferry DR, Anderson D, Hesslewood S, Julyan PJ, Poyner R, et al. Hepatic Drug Targeting: Phase I Evaluation of Polymer-Bound Doxorubicin. 2002;20(6):1668.

46. Vasey PA, Kaye SB, Morrison R, Twelves C, Wilson P, Duncan R, et al. Phase I clinical and pharmacokinetic study of PK1 [N-(2-hydroxypropyl)methacrylamide copolymer doxorubicin]: first member of a new class of chemotherapeutic agents-drug-polymer conjugates. Cancer Research Campaign Phase I/II Committee. Clin Cancer Res 1999;5(1):83-94.

CHAPTER FIVE

Stimuli-Responsive Nanoimprinted Nanocarriers: Swelling, Enzymatic Degradation and In-vitro Release Studies

5.1 INTRODUCTION

A major milestone in creating nanoscale, intravenously injectable delivery systems is the incorporation of multiple functions such as: shape-specificity, targeting, loading of multiple agents, and incorporating stimuli-sensitive properties. Current polymeric and liposomal-based nanocarriers have been well studied and optimized in preclinical and clinical settings, and surface modification of these carriers has led to advances in stability, half-life, biodistribution, targeting, and in-vivo efficiency [1-5]. The synthesis of these drug nanocarriers primarily involves self-assembled or emulsion-based spherical particles that release drugs through diffusion or hydrolytic degradation. Although significant progress has been made in polymeric or liposomal drug delivery systems, there remain critical limitations in synthesizing nanocarriers with highly controllable architecture and drug release properties. Our ability to precisely manipulate size, shape, composition, and drug release mechanism of nanoparticles is essential for controlling their in-vivo transport, biodistribution, and therapeutic efficacy [6-8].

Disease-responsive release is a key issue in 'intelligent' nanocarrier design. Intravenously injectable nanocarriers, that can efficiently deliver drugs or contrast agents to target tissues only in response to cellular or disease-specific signals, could significantly improve therapeutic and diagnostic care of complex diseases [6, 9]. Despite current

efforts to target drug nanoparticles and liposomal drug carriers to diseased cells in-vivo, significant amounts of toxic drugs diffuse to normal tissues during transport [10-13]. If the encapsulated cargo can be released preferentially at a particular diseased tissue or cell or inside a specific cellular compartment, it could provide significant improvement in patient compliance, especially for highly toxic chemotherapeutic drugs or for molecules with short half-life.

Although stimuli-responsive release mechanisms are well established for macroscale devices and hydrogels [14-16], reports on nanocarriers incorporating environmental- or disease-triggered release of drugs are limited to only pH-responsive systems [17, 18]. Polymer-based pro-drugs combine multiple functionalities [19, 20]; however, they do not allow for simultaneous delivery of multiple agents (drugs, contrast agents etc.). The design of carriers at the nanometer length scale that incorporate such triggered-release mechanisms has remained elusive because of the lack of flexible fabrication methods that can incorporate responsive bio-molecules within a nanoparticle matrix. Recent advances in nanoscale fabrication methods could provide unique solutions to manufacture stimuli-sensitive nanocarriers for drug delivery in a high-throughput manner.

Using Step and Flash Imprint Lithography (SFIL), discussed in *Chapter Four*, we have already demonstrated the ability to imprint on a wafer scale and ensure precise control of particle size, shape, and geometry [21]. DeSimone and colleagues have also reported the ability to form nano-size poly(ethylene glycol) (PEG) and poly(lactide) (PLA) particles using a top-down particle nano-replication (PRINT) method, which is

similar to nanoimprint lithography [22-24]. Although nanoparticle synthesis was demonstrated using the PRINT method, stimuli-responsive nanoparticle fabrication has not been demonstrated. Top-down nanofabrication methods to generate particles with precise size and shape that also incorporate environmentally-triggered drug release have yet to be reported.

In this research we discuss the fabrication of particles with precise size and shape that also incorporate environmentally-triggered drug release, with features as small as 100 nm, using SFIL. We hypothesized that after imprinting of the PEGDA-GFLGK-DA stimuli-responsive hydrogel material, developed in *Chapter Three*, the crosslinked network would degrade in the presence of the tumor-specific enzyme Cathepsin B and display stimuli-responsive release. In this research we demonstrate enzymatic degradation of the imprinted PEGDA-GFLGK-DA nanofeatures. We further demonstrate that biological agents can be successfully incorporated within stimuli-responsive nanoparticles during the imprinting process by simply mixing the agents with the macromer solution prior to polymerization. In order to show release of both a nucleic acid and a protein, plasmid DNA and a fluorescently-labeled IgG were each encapsulated in PEGDA-GLFLG-DA and imprinted. The release studies performed demonstrate successful retention of the model drug in the absence of tumor-specific enzymes (with an initial leakage) and an enzyme-triggered release of model drug upon the addition of Cathepsin B. Swelling studies had been performed on macroscale PEGDA hydrogels in *Chapter Three*, and we further characterize the change in PEGDA nanoparticle

morphology utilizing scanning electron microscopy (SEM) and atomic force microscopy (AFM) before and after swelling of the particles.

5.2 MATERIALS AND METHODS

5.2.1 Polymers and Reagents

The peptide sequence Gly-Phe-Leu-Gly-Lys (GFLGK) (MW 527) was purchased from Bachem and acrylated in dH_20 as described in *Chapter Three*. Poly(ethylene glycol) diacrylate (PEGDA, MW 700) was purchased from Sigma Aldrich. Phosphate buffered saline (PBS, pH 7.4) was purchased from Sigma Aldrich. The ultraviolet (UV) photoinitiator, 2-hydroxy-1-[4-(hydroxyethoxy) phenyl]-2-methyl-1 propanone (I2959) was purchased from Ciba Geigy. Plasmid DNA, pgWiz β-galactosidase (8500 bps), was purchased from Aldevron. The Picogreen assay was purchased from Invitrogen. Fluorescently-labeled antibody, Alexa Fluor 594 labeled goat anti–mouse IgG, was purchased from Invitrogen. Cathepsin B from bovine spleen was purchased from Sigma Aldrich. BARC DUV-30J (Brewer Sciences) was supplied by NNIN and the MRC at the University of Texas Pickle Research Center. Tridecafluoro-1,1,2,2-Tetra-Hydrooctyl Dimethylchloro-silane was purchased from Gelest Inc, and toluene was purchased from Sigma. Four inch p-type <100>, double-sided polished, prime silicon wafers with an epi-layer of silicon on one side were purchased from Montco Silicon Technologies.

5.2.2 Cathepsin B Mediated Degradation of PEGDA-GFLGK-DA

A 1:1 molar ratio of 100% (w/v) PEGDA (MW 700) and diacrylated GFLGK was prepared, and 0.07 wt% I2959 was added to generate free radicals to induce chain polymerization. Prior to imprinting the polymer solution, the template and the wafer were prepared. A self-assembled monolayer (SAM) of 0.5% (v/v) (Tridecafluoro-1,1,2,2-Tetra-Hydrooctyl) Dimethylchloro-silane in toluene was applied to the quartz template, as described in *Chapter Four*, the day prior to imprinting. Subsequently, a four inch silicon wafer was spin-coated with BARC (3000 rpm, 60 s). Nanoimprinting was performed using the IMPRIO 100 SFIL system (Molecular Imprints). The automated dispensing system was inactivated and 0.2 μL of polymer was dispensed onto the wafer prior to each imprint. The solution was then imprinted with an imprint force of 12 N, a UV exposure of 7 seconds and a pre-delay of 300 seconds.

After imprinting, the nanoimprinted polymer membranes (containing 100 nm square shaped particles) were subsequently exposed to 25 U/mL Cathepsin B (Sigma-Aldrich) in PBS pH 5 for varying time periods. SEM images were taken of individual imprints after 30 min, 2 hrs, 4 hrs, 8 hrs, 12 hrs and 48 hours of enzyme exposure. A control sample that was not exposed to Cathepsin B was left in dH_2O for the duration of the 48 hrs to evaluate if any degradation occurs in the absence of the enzyme. The experiment was performed in triplicate and scanning electron microscopy (SEM) was used to verify degradation of the nanoparticles.

5.2.3 Enzyme-Triggered Release of Biologics

5.2.3.1 Stimuli-Responsive Release of DNA

The enzyme-triggered release kinetics of encapsulated plasmid DNA, pgWiz β-galactosidase (8500 bps), from PEGDA-GFLGK-DA imprints with square-shaped nanoparticles were evaluated in vitro. A 1:1 molar ratio of 75% (w/v) PEGDA (MW 700) and diacrylated GFLGK was prepared with 0.16 % plasmid DNA (w/w of polymer) and 0.07 wt% I2959. The experiment was performed in triplicate in 0.01 *M* PBS solution (pH 7.4). 0.174 μL of the macromer-DNA mixture was dispensed onto a double-sided polished 4" silicon wafer with an epi-layer and BARC. The solution was then imprinted with the IMPRIO 100 (Molecular Imprints) using an imprint force of 18 N, a UV exposure of 7 seconds and a pre-delay of 300 seconds.

Subsequently the imprints (without etching) were rinsed in PBS for 30 minutes, placed in 500 μL PBS and incubated at 37^{o}C. At various time intervals (4 hrs, 8 hrs, 12 hrs, 24 hrs), buffer samples were collected and replaced with fresh solution. At 24 hrs, the entire buffer was removed and a 500 μL solution of Cathepsin B (20 U/mL in PBS pH 5) was added to each sample, except the control samples which continued to be incubated in PBS. Samples were returned to the incubator and at various intervals (4 hrs, 8 hrs, 12 hrs, 24 hrs, and 48 hrs), buffer was collected. Each time 100 μL of enzyme solution was removed, and 100 μL of fresh enzyme solution was replaced. The amount of plasmid DNA released into the buffer was measured using a Picogreen Assay, an ultra-

sensitive fluorescent nucleic acid stain used for quantification of double stranded DNA, and a fluorescence plate reader (DTX 880, Beckman Coulter).

5.2.3.2 Stimuli-Responsive Release of Fluorescently-labeled Antibody

The stimuli-responsive release of encapsulated antibodies (Alexa Fluor 594 labeled goat anti–mouse IgG, Invitrogen) from PEGDA-GFLGK-DA imprints with square-shaped nanoparticles was evaluated in-vitro. A 1:1 molar ratio of 100% (w/v) PEGDA (MW 700) and diacrylated GFLGK was prepared with 0.075% (w/w of polymer) antibody and 0.07 wt% I2959. The experiment was performed in triplicate in 0.01M PBS solution (pH 7.4). 0.174 μL of the macromer-Antibody mixture was dispensed onto a double-sided polished 4" silicon wafer with an epi-layer and BARC. The solution was then imprinted with the IMPRIO 100 (Molecular Imprints) using an imprint force of 18 N, a UV exposure of 7 seconds and a pre-delay of 300 seconds.

Subsequently the imprints (without etching) were rinsed in PBS for 30 minutes, placed in 500 μL PBS and incubated at 37^{o}C. At various time intervals (4 hrs, 8 hrs, 12 hrs, 24 hrs), buffer samples were collected and replaced with fresh solution. At 24 hrs, the entire buffer was removed and a 500 μL solution of Cathepsin B (20 U/mL in PBS pH 5) was added to each sample, except the control samples which continued to be incubated in PBS. Samples were returned to the incubator and at various intervals (4 hrs, 8 hrs, 12 hrs, 24 hrs, and 48 hrs), buffer was collected. Each time 100 μL of enzyme solution was removed, and 100 μL of fresh enzyme solution was replaced. The amt of

fluorescently labeled antibody released into buffer was measured for each time point using a fluorescence plate reader (DTX 880, Beckman Coulter).

5.2.4 Imprinted PEGDA Swelling Morphology

PEGDA (MW 700) was dissolved in dH_20 to form various concentrations ranging from 25%, 33%, 50%, and 75% (w/v), and 0.05 wt% I2959 was added to initiate chain polymerization. 0.019 μL of the PEGDA solution was dispensed through the automated dispensing system onto a double-sided polished 4" silicon wafer with an epi-layer and BARC. The PEGDA solutions were then imprinted with the IMPRIO 100 (Molecular Imprints) using an imprint force of 7 N, a UV exposure of 7 seconds, and a pre-delay of 300 seconds. The 25%, 50% and 75% (w/v) imprints (containing 100 nm square-shaped particles) were placed in 3 mL dH_2O and incubated at 37°C for 48 hours. The 33% (w/v) imprints were placed in 3 mL of 0.01 *M* PBS solution (pH 7.4) and incubated at 37°C for 48 hrs. The particles were then imaged using scanning electron microscopy (SEM) (LEO 1530 scanning electron microscope) and atomic force microscopy (AFM). SEM images of 33% w/v particle widths were taken before and after swelling using air-dried and critical point dried samples to see any critical change in dimension. AFM images of 25%, 50%, and 75% were taken in order to see any change in particle height. AFM images before swelling were taken using a Digital Instruments AFM in tapping mode. AFM images after swelling were taken with an Asylum Research MFP-3D AFM in solution in contact mode using a Veeco NanoProbe with a low spring constant meant for imaging biological specimens.

5.3 RESULTS

5.3.1 Cathepsin B Mediated Degradation of PEGDA-GFLGK-DA

In order to demonstrate disease-responsive release, we fabricated nanoparticles using an equimolar mixture of PEGDA (75% w/v, MW 700) and GFLGK-DA. This creates a particle matrix crosslinked by the degradable peptide. We have evaluated enzyme-triggered degradation kinetics of imprinted PEGDA-GFLGK-DA with square nanoparticles using SEM at various time points following addition of Cathepsin B. As shown in **Figure 5.1A-F**, the nanoparticles begin to degrade within 30 minutes and between 24 and 48 hours all particles were fully degraded. Looking closely at **Figure 5.1E- F**, we can see that although the particles have degraded, the remaining residual layer beneath the particles has not completely degraded. Meanwhile, particles that are exposed to dH_20 without Cathepsin remain intact during this period (**Figure 5.1A**).

5.3.2 Enzyme-Triggered Release of Biologics

We have further studied how such enzyme-mediated degradation provides triggered release of encapsulated model drugs. Fluorescently labeled antibodies and plasmid DNA, encoding for beta galactosidase, were successfully incorporated during SFIL into PEGDA-GFLGK-DA nanoparticles. Antibody and DNA release from the imprinted nanoparticles, prior to and following addition of Cathepsin B, were monitored over time (see methods). As shown in **Figure 5.2A-B**, efficient enzyme-triggered release was achieved. A minimal amount of antibody (~ 1%) and some amount of DNA (~ 11%) was released prior to Cathepsin addition indicating some baseline DNA leakage from the

matrix. This is likely due to the highly hydrophilic nature of DNA compared to the antibody. However, most of the encapsulated cargo was released only after exposure to the enzyme.

5.3.3 Imprinted PEGDA Swelling Morphology

In order to characterize the change in morphology of the PEGDA-GFLGK-DA nanoparticles, AFM and SEM were utilized. **Figure 5.3A-C** demonstrates AFM images of 25% (w/v), 50% (w/v) and 75% (w/v) PEGDA particles in solution, respectively. The images show a top-down view of the particle, as well as the height profile, and a three-dimensional view. The particle heights were on average of 175 ± 4 nm after 48 hours of swelling. Non-swollen 100 nm particles (obtained using tapping mode) had a height of approximately 129 nm. Therefore we see a 48 nm increase in height. The three-dimensional view in **Figure 5.3A** shows the large deformation in particle shape that occurs with the 25% (w/v) PEGDA particle due to the contact force of the AFM tip.

Figure 5.4A-B demonstrates 33% (w/v) particles with a pre-swollen width of 97 ± 0.1 nm for both air-dried and critical point dried particles. The two different drying methods showed no change in dimension. **Figure 5.4C** demonstrates post 48 hour-swollen particles with a width of 108 ± 0.2 nm for critical point dried particles. Thus we see an 11.3% increase in width for the swollen particles after 48 hours.

5.4 DISCUSSION

The overall goal of these experiments was to demonstrate fabrication of nanoparticles with precise size and shape that also incorporate environmentally-triggered drug release, using the SFIL technique. We fabricated nanoparticles using an equimolar mixture of PEGDA (MW 700) and a diacrylated, enzymatically degradable peptide GFLGK-DA, to create a particle matrix crosslinked by the degradable peptide. GFLG is known to be readily degraded by Cathepsin B, an enzyme that is sequestered intracellularly in lysosomes of normal cells, but is highly up-regulated, secreted and present in the lysosomes and extracellular tissue in certain tumors [25-30].

An important consideration in imprinting with drugs or biological molecules is the orifice size of the dispense tip used to dispense the solution. Our current tip orifice for all experiments is 80 μm and the manufacturer suggests filtering all solutions for this tip with a filter of 4 nm. Therefore, depending on the size of the therapeutics to be encapsulated in a stimulus-responsive polymer, a dispenser tip with a larger orifice may be required. For studies using large therapeutics, such as DNA and IgG, a larger orifice would likely be required for ease of flow and to prevent clogging of the tip. Due to the small quantity of PEGDA-GFLGK-DA available and the large size of the DNA and antibody, we manually dispensed the solution to maximize the amount of solution for further studies and prevent clogging of the dispenser tip. Using manually dispensed solution, we successfully demonstrated enzyme-triggered degradation of the imprinted PEGDA-GFLGK-DA nanoparticles after exposure to Cathepsin B for 48 hours. Because

we manually dispensed the polymer solution, the residual layer was still quite large and not completely degraded.

We have also demonstrated that biological agents can be successfully incorporated within these imprints during the nanoimprinting process by simply mixing the agents with the macromer solution prior to polymerization, and we have demonstrated successful retention of model drug (DNA and antibody) in the absence of tumor-specific enzymes and an enzyme-triggered release of model drug upon the addition of Cathepsin B. Although we see an initial release for DNA, most of the encapsulated cargo was released only after exposure to the enzyme indicating a possible means to achieve highly controlled, disease-responsive or intracellular release of drugs and contrast agents.

With the successful enzymatic release of the DNA and antibody, we believe the PEGDA-GFLGK-DA design should allow the nanoimprinted particles to degrade in the presence of Cathepsin B and release the encapsulated drug preferentially inside particular cellular compartments (lysosomes) or inside tumor tissues. The combination of shape-specific and stimuli-responsiveness could also provide a secondary means of targeting and controlled release in addition to traditional surface-ligand based targeting concepts. It is also easily conceivable that incorporation of different peptide sequences, specific for particular tissue targets or pathophysiological conditions, should allow for other disease or tissue-specific carrier designs. For example, Cathepsin D is highly over-expressed in breast cancer and has been related to its prognosis [31], and matrix metalloproteinase (MMP) over-expression has been correlated with tumor metastasis [32] and a host of inflammatory and vascular diseases [33, 34]. Incorporation of peptides specific for these

enzymes within the particle matrix, as described here, could provide highly specific, disease-triggered drug nanocarriers. Similar enzymatically degradable macroscale matrices have been reported for controlled release and tissue engineering applications [35, 36]. However, to our knowledge this is the first demonstration of nanoimprinting and nanocarrier synthesis using such biologically responsive macromolecules.

It is worth noting that the system and material choices as described here essentially generate nano-sized hydrogels as drug carriers. The particle composition designed here essentially generates nano-sized hydrogels as drug carriers. The pore size (ξ) and molecular weight between crosslinks (Mc) of these nanoparticles would dictate whether a certain drug can be entrapped without significant diffusive leaching prior to an environmental trigger. Pore size measurements for bulk PEGDA (MW 3400) hydrogels of various concentrations have been previously reported by Bryant et al. [37] and we calculated the mesh size for bulk PEGDA (MW 700) hydrogels, **Table 5.1**. Thus it is possible to a priori model which particular therapeutic or diagnostic agents are suitable for stimuli-responsive, triggered release from particles of a specific composition. Depending on the concentration of the PEGDA (MW 700), we hypothesize that protein and nucleic acid-based drugs with hydrodynamic radii larger than two nanometers should be successfully retained and slowly released from such particles, even with a 25% (w/v) concentration. Thus protein, peptide and nucleic acid-based drugs, hydrophobic drug particles as well as nanoparticle-based contrast agents could be successfully retained within such imprinted nanocarriers and released primarily upon environmentally-triggered matrix degradation.

An interesting aspect for future research would be to compare the change in swelling dimensions of the nanoparticles to the estimated swelling properties calculated from the swelling studies discussed in *Chapter One*. We have started an initial study, using AFM and SEM. The AFM images in this study were performed in solution in order to see the actual morphology of the particles in solution; however, AFM was used in contact mode. Even though a low spring constant tip that is meant for analyzing biological samples was used, the AFM tip was dragging along the surface and deforming the nanoparticles, as can been seen in the three-dimensional AFM views, **Figure 5.3A-C**. The 25% (w/v) particles seemed to deform more, as would be expected. In each case, the top of the particle was flat and we assumed a swollen height based on these measurements; however this height is not an accurate measurement. The most accurate way to measure the height, however, would be to use force-volume measurements, and the next method, with less accuracy, would be to use tapping mode in solution.

The SEM images of the 33% (w/v) particles demonstrated an 11% increase in width; this can be corresponded to the mesh size, crosslink density and volumetric swelling ratios seen in **Table 5.1A** for the 33% (w/v) PEGDA. Although critical point drying was used to obtain these measurements, the critical point drying process still does not prevent shrinkage of the polymer structure in the vacuum chamber of the SEM. The most accurate way to perform all of these measurements would be to use a Field Emission Gun Environmental Scanning Electron Microscope (FEG-ESEM). With this SEM, samples can be imaged from 0 to 100% humidity.

In conclusion, we have shown the first demonstration to our knowledge of nanoimprinting and nanocarrier synthesis using biologically responsive macromolecules. The SFIL process has demonstrated the versatility for creating well-defined nanoparticles and stimuli-responsive nanoparticles, and has the potential to scale up to industrial production, as demonstrated in *Chapter Four*. Furthermore, biological agents can easily be incorporated into nanoparticle drug delivery systems using this method and the macromer concentration can be varied to encapsulate a wide variety of therapeutics and contrast agents. The creation of nanoscale, drug or contrast agent delivery systems with stimuli-responsive and environmentally-degradable features is a significant milestone in creating "intelligent" multi-functional nanocarriers. If the encapsulated therapeutic or diagnostic agent can be released only at a particular diseased tissue or cell or only inside a specific cellular component, it could provide significant improvement in patient compliance, especially for highly toxic chemotherapeutic drugs or for molecules with a short half-life. The nanoimprinted drug-loaded polymer nanoparticles have the potential to allow for unique control of over particle transport, biodistribution and tissue or disease-specific release properties.

Future studies for optimization would require in depth characterization of the degradation and release kinetics. For solutions that are manually dispensed and for thicker residual layers, the etching process required to isolate the nanoparticles etches the residual layer away as well as the therapeutics located within the residual layer; thus the overall release kinetics cannot be determined until the loading efficiency of the particles is determined. Our lab has already begun work on this process. In order to automatically

dispense drug-polymer solutions it would also be necessary to use an appropriate dispenser tip for the radius of the therapeutic being encapsulated. With the use of automated dispensing, the volume of the solution dispensed could be set such that there would be little residual layer and little to no etching required, and could allow for large-scale fabrication enzyme-responsive-nanocarriers.

Figure 5.1 SEM Images of Imprinted Enzymatic Degradation. SFIL imprinted 75% (w/v) PEGDA-GFLGK-DA polymer membrane with 400 nm square particles, showing enzymatic degradation by Cathepsin B at various time points: (A) at t=48 hrs after dH_20 addition *(scale bar = 1μm)*, **(B) at t=30 min. after Cathepsin addition** *(scale bar = 4μm)*, **(C) at t=12 hrs after Cathepsin addition** *(scale bar = 10μm)*, **(D) at t=12 hrs after Cathepsin addition** *(scale bar = 40μm)*, **(E) at t=48 hrs after Cathepsin addition** *(scale bar = 600nm)*, **(F) at t=48 hrs after Cathepsin addition** *(scale bar = 600nm).*

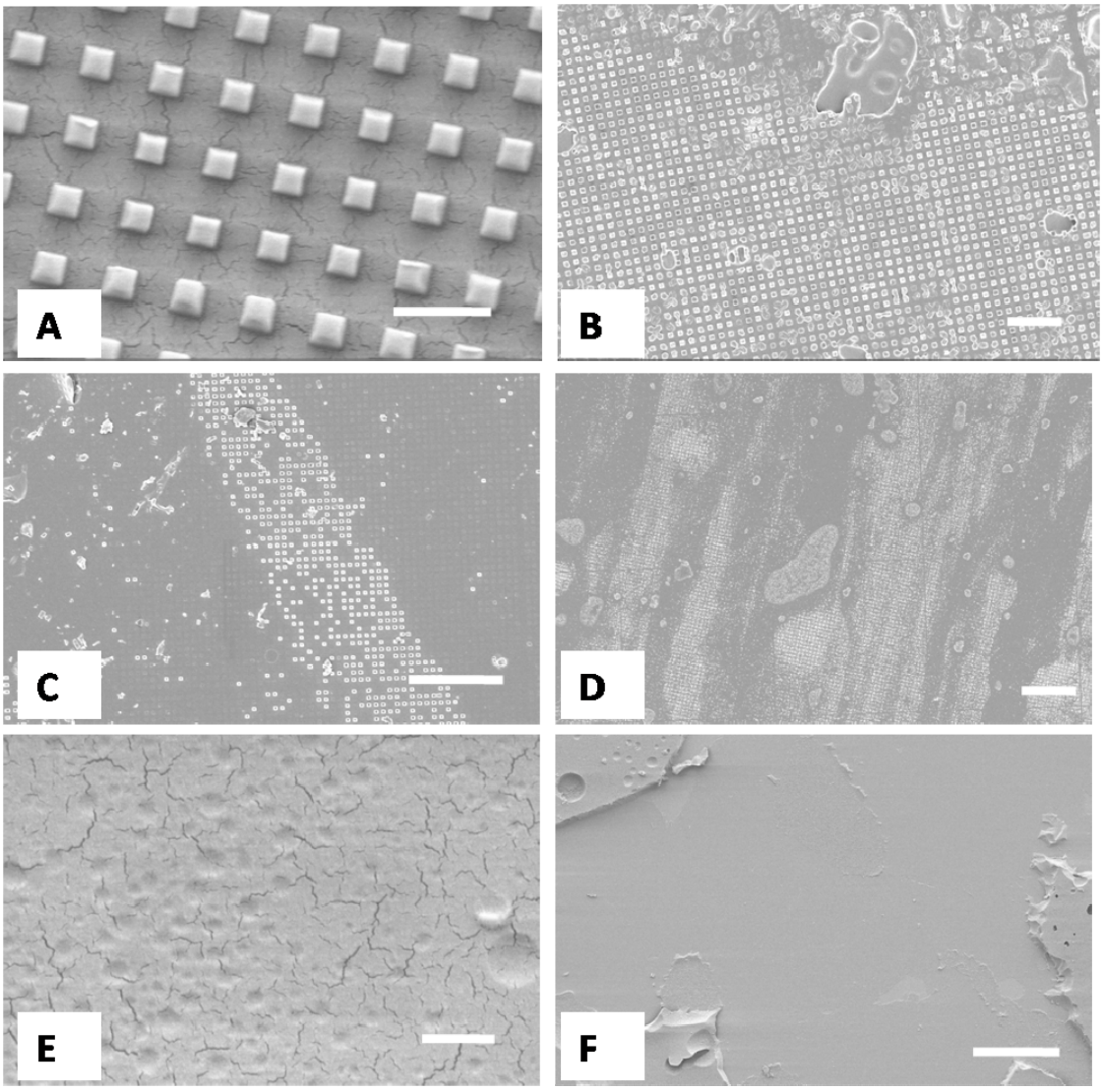

Figure 5.2 **Imprinted Stimuli-Responsive DNA Release: (A) DNA released from nanoimprinted 75% (w/v) PEGDA-GFLGK-DA and (B) Antibody release from nanoimprinted 100% (w/v) PEGDA-GFLGK-DA hydrogel (PEGDA MW 1000), both showing enzyme-triggered release of DNA upon addition of Cathepsin B . The figures demonstrate the first known imprinting of shape-specific, stimuli-responsive nanoimprinted particles.**

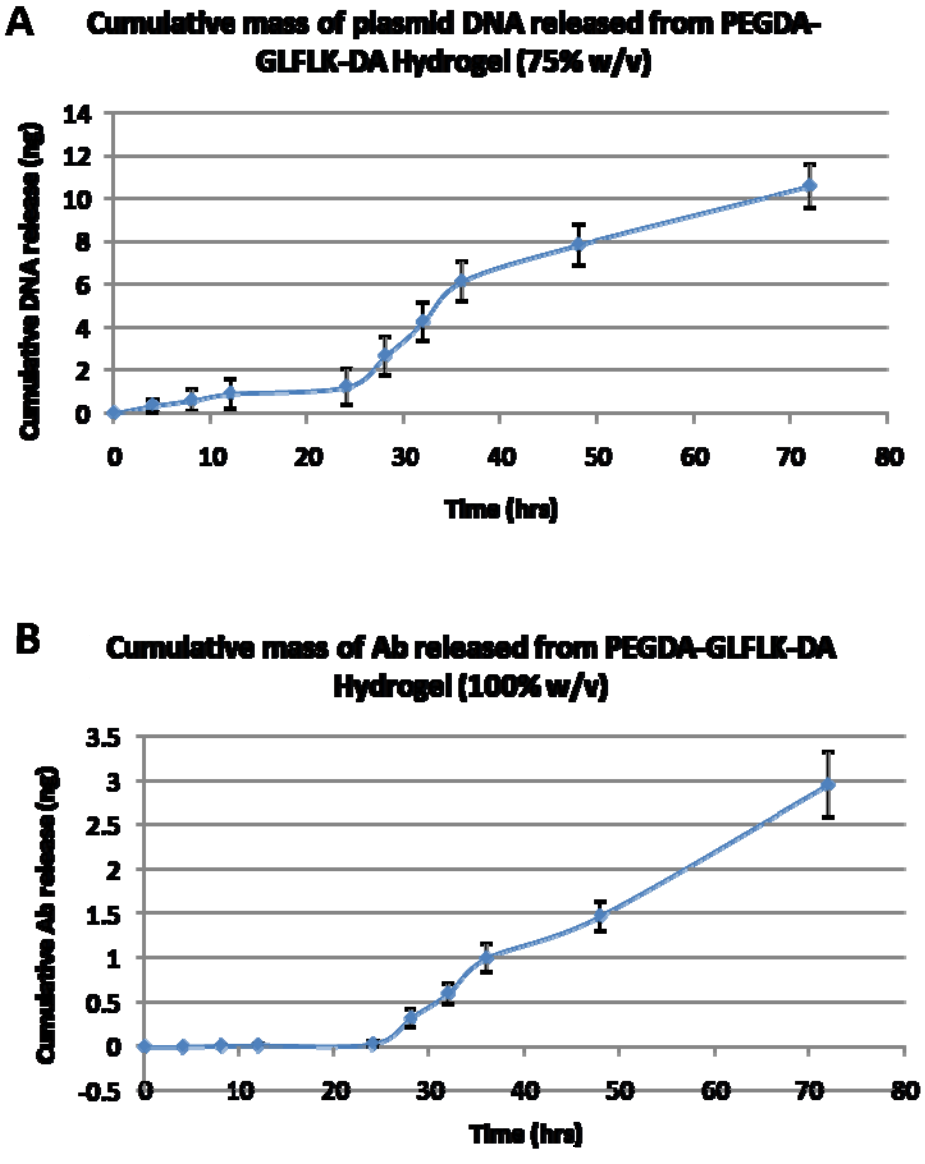

Figure 5.3 AFM Images of 48 Hour Swollen 100 nm PEGDA Nanoparticles. Imprinted with 0.019 μL, showing the top view, side profile, and isometric profile: (A) 25% (w/v) particles, (B) 50% (w/v) particles, and (C) 75% (w/v) particles.

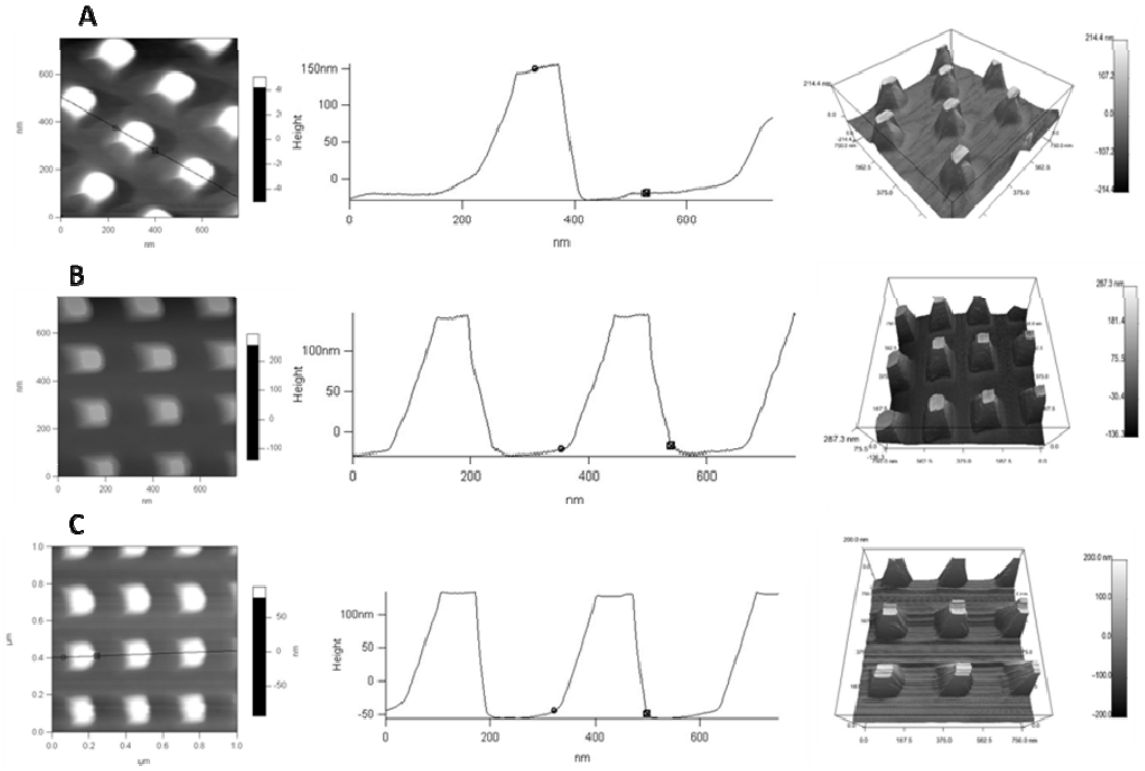

Figure 5.4 SEM Images of 48 Hour Swollen 100 nm PEGDA Nanoparticles. Squares imprinted with 33% (w/v) PEGDA using 0.019 μL of solution per imprint: (A) particles air dried before swelling, (B) particles dried using critical point drying before swelling, (C) particles dried using critical point drying after swelling. *All scale bars = 200nm.*

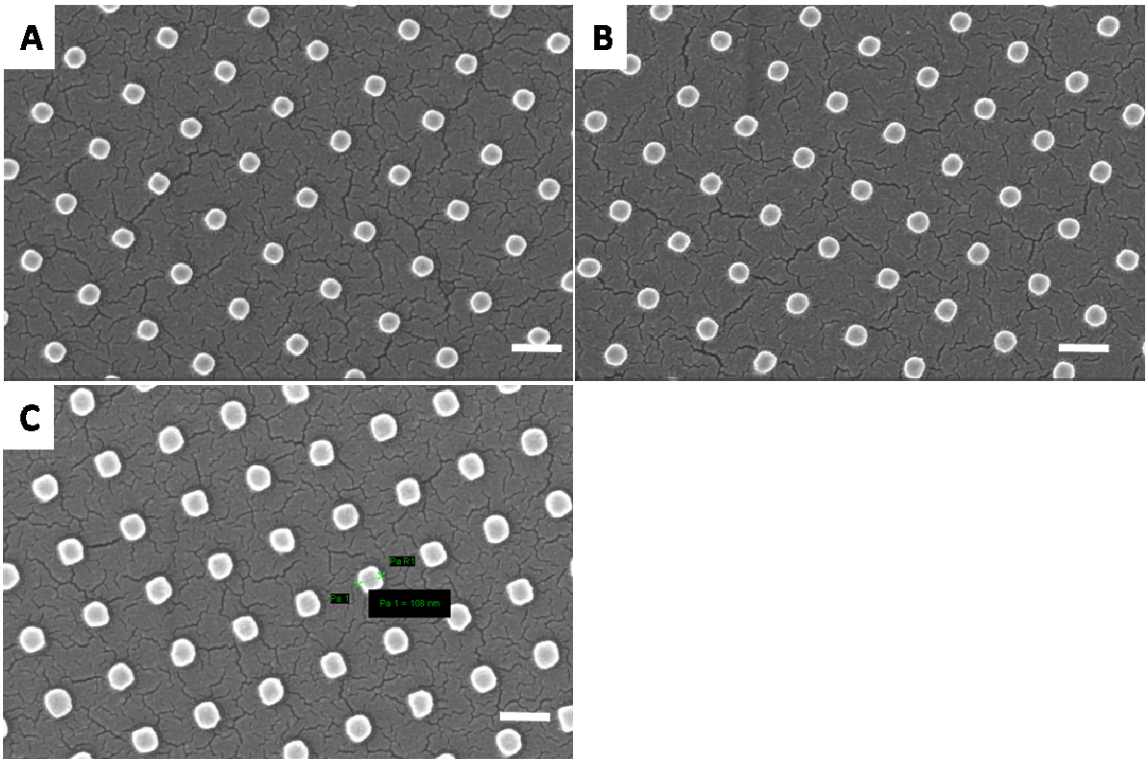

Table 5.1 Swelling Properties of PEGDA and PEGDA-GLFGK-DA: (A) PEGDA (MW 700) with concentrations varying from 75% to 25% (w/v) (n=8), and (B) mass swelling ratio of PEGDA-GFLGK-DA (60% w/v) (n=2).

A

% (w/v) PEGDA MW700	ζ (Angstrom)	(SD)	Mc	(SD)	v_{2s}	(SD)	Qv	(SD)
75	2.86	0.30	18.09	1.59	0.86	0.05	1.16	0.05
60	3.15	0.48	21.47	2.69	0.84	0.07	1.19	0.07
50	5.07	0.55	47.23	3.90	0.65	0.05	1.53	0.05
33	8.75	1.36	106.42	11.30	0.43	0.05	2.34	0.05
25	12.92	1.56	179.10	13.53	0.29	0.03	3.44	0.03

B

%(w/v) PEGDA-GFLGKDA (MW700)	Qm	(SD)	Qv	(SD)
60	3.59	0.59	3.36	0.56

5.5 REFERENCES

1. Torchilin VP, Lukyanov AN, Gao Z, Papahadjopoulos-Sternberg B. Immunomicelles: targeted pharmaceutical carriers for poorly soluble drugs. Proc Natl Acad Sci USA 2003;100(10):6039-6044.
2. Torchilin VP. Multifunctional nanocarriers. Adv Drug Deliv Rev 2006;58(14):1532-1555.
3. Alonso MJ. Nanomedicines for overcoming biological barriers. Biomed Pharmacother 2004;58(3):168-172.
4. Portney NG, Ozkan M. Nano-oncology: drug delivery, imaging, and sensing. Anal Bioanal Chem 2006;384(3):620-630.
5. Torchilin VP. Recent advances with liposomes as pharmaceutical carriers. Nat Rev Drug Discov 2005;4(2):145-160.
6. Ferrari M. Cancer nanotechnology: opportunities and challenges. Nat Rev Cancer 2005;5(3):161-171.
7. Nishiyama N. Nanomedicine: Nanocarriers shape up for long life. Nature Nanotech 2007;2(4):203-204.
8. Champion JA, Katare YK, Mitragotri S. Particle shape: a new design parameter for micro- and nanoscale drug delivery carriers. J Control Release 2007;121(1-2):3-9.
9. Farokhzad OC, Langer R. Nanomedicine: developing smarter therapeutic and diagnostic modalities. Adv Drug Deliv Rev 2006;58(14):1456-1459.

10. Noble CO, Kirpotin DB, Hayes ME, Mamot C, Hong K, Park JW, et al. Development of ligand-targeted liposomes for cancer therapy. Expert Opin Ther Targets 2004;8(4):335-353.

11. Park JW, Benz CC, Martin FJ. Future directions of liposome-and immunoliposome-based cancer therapeutics. Semin Oncol 2004;31(6):196-205.

12. Park JW, Hong K, Kirpotin DB, Papahadjopoulos D, Benz CC. Immunoliposomes for cancer treatment. Adv Pharmacol 1997;40:399-435.

13. Kreuter J. Influence of the surface properties on nanoparticle-mediated transport of drugs to the brain. J Nanosci Nanotechnol 2004;4(5):484-488.

14. Miyata T, Uragami T, Nakamae K. Biomolecule-sensitive hydrogels. Adv Drug Deliv Rev 2002;54(1):79-98.

15. Qiu Y, Park K. Environment-sensitive hydrogels for drug delivery. Adv Drug Deliv Rev 2001;53(3):321-339.

16. Peppas NA, Bures P, Leobandung W, Ichikawa H. Hydrogels in pharmaceutical formulations. Eur J Pharm Biopharm 2000;50(1):27-46.

17. Shenoy D, Little S, Langer R, Amiji M. Poly(ethylene oxide)-modified poly(beta-amino ester) nanoparticles as a pH-sensitive system for tumor-targeted delivery of hydrophobic drugs: part 2. In vivo distribution and tumor localization studies. Pharm Res 2005;22(12):2107-2114.

18. Na K, Bae YH. Self-assembled hydrogel nanoparticles responsive to tumor extracellular pH from pullulan derivative/sulfonamide conjugate: characterization, aggregation, and adriamycin release in vitro. Pharm Res 2002;19(5):681-688.

19. Lu ZR, Shiah JG, Sakuma S, Kopeckova P, Kopecek J. Design of novel bioconjugates for targeted drug delivery. J Control Release 2002;78(1-3):165-173.

20. Ulbrich K, Subr V, Strohalm J, Plocova D, Jelinkova M, Rihova B. Polymeric drugs based on conjugates of synthetic and natural macromolecules. I. Synthesis and physico-chemical characterisation. J Control Release 2000;64(1-3):63-79.

21. Glangchai LC, Caldorera-Moore M, Shi L, Roy K. Nanoimprint lithography based fabrication of shape-specific, enzymatically-triggered smart nanoparticles. J Control Release 2008;125(3):263-272.

22. Rolland JP, Maynor BW, Euliss LE, Exner AE, Denison GM, DeSimone JM. Direct fabrication and harvesting of monodisperse, shape-specific nanobiomaterials. J Am Chem Soc 2005;127(28):10096-10100.

23. Euliss LE, Welch CM, Maynor BW, Rolland JP, Denison GM, Gratton SE, et al. Monodisperse nanocarriers: novel fabrication of polymeric nanoparticles for bio-nanotechnology. Proc SPIE 2006;6153:61534A.

24. Gratton SEA, Pohlhaus PD, Lee J, Guo J, Cho MJ, Desimone JM. Nanofabricated particles for engineered drug therapies: a preliminary biodistribution study of PRINT nanoparticles. J Control Release 2007;121(1-2):10-18.

25. Werle B, Ebert W, Klein W, Spiess E. Cathepsin B in tumors, normal tissue and isolated cells from the human lung. Anticancer Res 1994;14(3A):1169-1176.

26. Werle B, Kraft C, Lah TT, Kos J, Schanzenbacher U, Kayser K, et al. Cathepsin B in infiltrated lymph nodes is of prognostic significance for patients with nonsmall cell lung carcinoma. Cancer 2000;89(11):2282-2291.

27. Heidtmann HH, Salge U, Abrahamson M, Bencina M, Kastelic L, Kopitar-Jerala N, et al. Cathepsin B and cysteine proteinase inhibitors in human lung cancer cell lines. Clin Exp Metastasis 1997;15(4):368-381.

28. Higashiyama M, Doi O, Kodama K, Yokouchi H, Tateishi R. Cathepsin B expression in tumour cells and laminin distribution in pulmonary adenocarcinoma. J Clin Pathol 1993;46(1):18-22.

29. Howie AJ, Burnett D, Crocker J. The distribution of cathespin B in human tissues. J Pathol 1985;145(4):307-314.

30. Spiess E, Bruning A, Gack S, Ulbricht B, Spring H, Trefz G, et al. Cathepsin B activity in human lung tumor cell lines: ultrastructural localization, pH sensitivity, and inhibitor status at the cellular level. J Histochem Cytochem 1994;42(7):917-929.

31. Liaudet-Coopman E, Beaujouin M, Derocq D, Garcia M, Glondu-Lassis M, Laurent-Matha V, et al. Cathepsin D: newly discovered functions of a long-standing aspartic protease in cancer and apoptosis. Cancer Lett 2006;237(2):167-179.

32. Deryugina EI, Quigley JP. Matrix metalloproteinases and tumor metastasis. Cancer Metastasis Rev 2006;25(1):9-34.

33. Hu J, Van den Steen PE, Sang Q-XA, Opdenakker G. Matrix metalloproteinase inhibitors as therapy for inflammatory and vascular diseases. Nat Rev Drug Discov 2007;6(6):480-498.

34. Belvisi MG, Bottomley KM. The role of matrix metalloproteinases (MMPs) in the pathophysiology of chronic obstructive pulmonary disease (COPD): a therapeutic role for inhibitors of MMPs? Inflamm Res 2003;52(3):95-100.

35. Lutolf MP, Weber FE, Schmoekel HG, Schense JC, Kohler T, Muller R, et al. Repair of bone defects using synthetic mimetics of collagenous extracellular matrices. Nat Biotechnol 2003;21(5):513-518.

36. Mann BK, Gobin AS, Tsai AT, Schmedlen RH, West JL. Smooth muscle cell growth in photopolymerized hydrogels with cell adhesive and proteolytically degradable domains: synthetic ECM analogs for tissue engineering. Biomaterials 2001;22(22):3045-3051.

37. Bryant SJ, Anseth KS. Hydrogel properties influence ECM production by chondrocytes photoencapsulated in poly(ethylene glycol) hydrogels. J Biomed Mater Res 2002;59(1):63-72.

CHAPTER SIX

Bioactivity of Biologics Encapsulated in Nanoimprinted PEGDA Nanocarriers

6.1 INTRODUCTION

A critical aspect in fabricating nanoparticles capable of intracellular drug delivery is the maintenance of the stability and bioactivity of the encapsulated drug. The Step and Flash Imprint Lithography process has shown to be unlike any other fabrication technique in its ability to fabricate monodisperse, shape-specific, and stimuli-responsive biomaterials as small as 50 nm. Because the process utilizes low pressure, and standard UV illumination, and provides a gentle harvesting method for releasing the particles, we hypothesized that encapsulated model drugs such as proteins and nucleic acids would remain bioactive after undergoing the imprinting process. DeSimone and colleagues have demonstrated the bioactivity of PRINT imprinted PEG particles by encapsulating avidin within the particle matrix and subsequently exposing the particles to a solution of fluorescein-labeled biotin. Through the use of confocal microscopy they observed fluorescence only in particles with the encapsulated avidin [1].

This research discusses bioactivity studies performed through encapsulation of proteins and nucleic acids within imprinted poly(ethylene glycol) diacrylate (PEGDA) or stimuli-responsive, peptide-functionalized PEGDA-GFLGK-DA. Similar crosslinking chemistries have been shown to be compatible with retaining the bioactivity of biomolecules and cells within macroscale hydrogel matrices. Various groups have

encapsulated cells, growth factors, ECM proteins, peptides, small molecules and nucleic acids within such photo polymerized hydrogels and have shown their release characteristics and bioactivity [2-12]. Nucleic acids are generally more susceptible to UV photopolymerization. The Anseth group, in addition to cell studies, has performed studies evaluating the effects of UV and photoinitiator on DNA stability [6, 7]. UV exposure was found to have no denaturing effect on the DNA; however free radicals generated by the photoinitiator were found to affect the DNA stability. DNA inside UV polymerized hydrogels retained ~ 50% integrity and this increased significantly in the presence of free radical scavengers, such as ascorbic acids. The hydrogel extracted DNA was shown to be bioactive using transfection assays.

Through this research we demonstrate both a qualitative and quantitative measure of bioactivity. A streptavidin-biocytin binding study demonstrates successfully binding of the proteins after imprinting, indicating protein stability. Furthermore, the luciferase and trypsin bioactivity studies show limited quantitative bioactivity. However we hypothesize that this limited bioactivity is due to an inability to accurately measure the concentration of the proteins on a pico- and nano-molar concentration, as well as due to the very small pore size of the PEGDA nanogels. The DNA transfection studies themselves have proven unsuccessful due to a limitation in the ability to concentrate and measure the DNA. Although qualitative and quantitative bioactivity has been demonstrated, we suggest ways to further demonstrate the bioactivity of proteins and nucleic acids.

6.2 MATERIALS AND METHODS

6.2.1 Polymers and Reagents

The peptide sequence Gly-Phe-Leu-Gly-Lys (GFLGK) (MW 527) was purchased from Bachem and acrylated in dH_20 as described in *Chapter Three*. Poly(ethylene glycol) diacrylate (PEGDA, MW 700) was purchased from Sigma Aldrich. Phosphate buffered saline and phosphate buffered saline without Mg and Ca (PBS, pH 7.4) were purchased from Sigma Aldrich. HEPES buffer and DMSO was purchased from Sigma. The ultraviolet (UV) photoinitiator, 2-hydroxy-1-[4-(hydroxyethoxy) phenyl]-2-methyl-1 propanone (I2959) was purchased from Ciba Geigy. The UV photoinitiator, dimethoxy-2-phenyl-acetophenone (DMPA), was purchased from Sigma. The Picogreen assay and the NanoOrange assay were purchased from Invitrogen. Cathepsin B from bovine spleen was purchased from Sigma Aldrich. The Bright Glo Luciferase assay, including Luciferase assay reagent (containing Luciferin), Glo-Lysis buffer, and QuantiLum® Recombinant Luciferase, were purchased from Promega. Plasmid DNA, pgWizLuciferase (6732 bps), was purchased from Aldevron. Alexa Fluor 488 Bioctyin was purchased from Invitrogen. Streptavidin-CY5 was purchased from Southern Biotech. Trypsin from bovine pancreas was purchased from Sigma. The fluorogenic proteinase substrate, Rhodamine 110, bis-(CBZ-L-alanyl-L-arginine amide), dihydrochloride, was ordered from Invitrogen. BARC DUV-30J (Brewer Sciences) was supplied by NNIN and the MRC at the University of Texas Pickle Research Center. Tridecafluoro-1,1,2,2-Tetra-Hydrooctyl Dimethylchloro-silane was purchased from Gelest Inc, and toluene was purchased from Sigma. Four inch

p-type <100>, double-sided polished, prime silicon wafers with and without an epi-layer of silicon on one side were purchased from Montco Silicon Technologies. Amicon Ultra Centrifugal Filter Unit 50K and 100K were purchased from Cole-Parmer.

6.2.2 Streptavidin-Biotin Bioactivity Studies

Streptavidin-CY5 (Southern Biotech) was encapsulated within nanoimprinted PEGDA particles. PEGDA (75% w/v, MW 700) was prepared with 0.01% (v/v) streptavidin-CY5 and 0.07 wt% I2959. Prior to imprinting the polymer solution, the template and the wafer were prepared. A self-assembled monolayer (SAM) of 0.5% (v/v) (Tridecafluoro-1,1,2,2-Tetra-Hydrooctyl) Dimethylchloro-silane in toluene was applied to the quartz template with a fully patterned 10 x 10 mm mesa, the day prior to imprinting. Subsequently, a four inch silicon wafer was spin-coated with BARC (3000 rpm, 60 s).

0.019 μL of the macromer-protein solution was then dispensed from the IMPRIO 100 (Molecular Imprints) and imprinted with a force of 7 N with a 300 s pre-exposure delay and a 10 second UV exposure. Next the nanoimprinted samples were oxygen plasma etched for 20 s at a power setting of 50 W, using the Plasma Therm 790 Series RIE to remove any residual layer. Control samples remained unetched. Following this, the imprints were incubated in 100 μL of 0.427 μ*M* Alexa Fluor 488 biocytin for 30 minutes. Subsequently the imprints were rinsed thoroughly 5 times with dH_2O and dried with Nitrogen. Following this the imprints were prepared on slides and imaged using a

using a fluorescence microscope at 160X (Zeiss Axiovert 100M) in order to determine whether the encapsulated streptavidin retained its biotin binding property.

6.2.3 Luciferase and Bioactivity Studies

6.2.3.1 Luciferase Study with PEGDA-GFLGK-DA

To demonstrate luciferase bioactivity, luciferase was encapsulated, imprinted, etched, and then incubated in Cathepsin B in PBS (pH 5.5) buffer for 48 hours at 37^{o}C (n=3). To prepare the luciferase encapsulated PEGDA-GFLGK solution, a 1:1 molar ratio of PEGDA (75% w/v, MW 700) was prepared in dH_2O with 0.5 mg luciferase and 0.05 wt% I2959. 0.4 μL of the macromer-protein solution was then manually dispensed and imprinted with the IMPRIO 100 (Molecular Imprints) with a force of 7 N with a 300 sec pre-exposure delay and a 7 sec UV exposure. Next the nanoimprinted samples were oxygen plasma etched for 40 sec at a power setting of 50 W, using the Plasma Therm 790 Series RIE to remove residual layer. Control samples remained unetched. Following this, the imprints were incubated in 500 μL of Cathepsin B (25 U/mL) in PBS (pH 5.5) for 48 hours at 37^{o}C. Furthermore, to determine if temperature could play a factor in the results, an equivalent luciferase concentration was incubated in dH_2O (at room temperature and 37^{o}C) in 500 μL of solution for 48 hours. For each sample 50 μL of solution was placed in a 96-well plate and luminescence measurements were taken with the luciferase assay reagent.

6.2.3.2 Luciferase Study with PEGDA

Further studies were performed to find the optimum temperature, and buffer for luciferase. To show luciferase bioactivity using PEGDA, luciferase was encapsulated and imprinted, etched, and then immediately placed in Glo-Lysis buffer in a 96-well plate (n=25 for samples, n=6 for controls). To prepare the luciferase encapsulated PEGDA solution, PEGDA (25% w/v, MW 700) was prepared in dH_2O with 0.5 mg trypsin and 0.05 wt% I2959. 0.2 μL of the macromer-protein solution was then manually dispensed and imprinted with the IMPRIO 100 (Molecular Imprints) with a force of 7 N with a 300 s pre-exposure delay and a 7 sec UV exposure. Next the nanoimprinted samples were oxygen plasma etched for 40 sec at a power setting of 50 W, using the Plasma Therm 790 Series RIE to remove residual layer. Control samples remained unetched. Following this, each imprint was cut into $1/8^{th}$ pieces and each piece was fit into the wells of a 96-well plate with 50 μL of Glo-Lysis buffer. Samples sat in the 96-well plate for 30 minutes during preparatory set up and the luminescence measurements were then taken with the luciferase assay reagent.

6.2.4 Trypsin Bioactivity Studies

6.2.4.1 Trypsin Study with Oxygen Etching

To show bioactivity of trypsin, trypsin was encapsulated and imprinted, etched, and then released in both 10 m*M* HEPES buffer pH 7.55 and/or PBS (w/o Mg^{2+} or Ca^{2+}) buffer for 24 hours. Subsequently the imprinted trypsin sample was exposed to

Rhodamine 110 proteinase substrate to ensure bioactivity. The experiment was performed in triplicate with imprinted trypsin samples before O2 etching, trypsin samples after oxygen etching and plain PEG imprints as controls.

To prepare the trypsin encapsulated PEGDA solution, a stock solution of trypsin (50 mg/mL in 1 m*M* HCl) was diluted to 10 mg/mL in 10 m*M* HEPES and/or 0.01 *M* PBS (w/o Mg^{2+} or Ca^{2+}). PEGDA (25% w/v, MW 700) was prepared in dH_2O with 2.5% trypsin (w/w of polymer) and 0.05 wt% I2959. 0.08 μL of the macromer-protein solution was then dispensed from the IMPRIO 100 (Molecular Imprints) and imprinted with a force of 7 N with a 300 sec pre-exposure delay and a 7 sec UV exposure. Next the nanoimprinted samples were either oxygen plasma etched for 40 sec at a power setting of 50 W, using the Plasma Therm 790 Series RIE to remove any residual layer. Control samples remained unetched. Following this, the imprints were incubated in 500 μL of 10 m*M* HEPES buffer pH 7.55 and/or PBS for 24 hours at room temperature.

To prepare the fluorescence assay Rhodamine 110 proteinase substrate was dissolved in DMSO to a 10 m*M* concentration. It was then diluted into 10 m*M* HEPES buffer, pH 7.55 to 2.5 m*M* concentration (5 m*M* is reported in literature). 25 μL of trypsin supernatant was mixed with 25 μL Rhodamine 110 proteinase substrate in a black 96-well plate. The solution was then allowed to react for 5 minutes and then fluorescence measurements were taken with the excitation and emission wavelengths of 498 nm and 521 nm respectively.

In order to create a standard curve, a range of known trypsin concentrations was created in PBS. 25 μL of trypsin supernatant was mixed with 25 μL Rhodamine 110

proteinase substrate in a black 96-well plate. The solution was then allowed to react for 5 minutes and then fluorescence measurements were taken with excitation and emission wavelengths of 498 nm and 521 nm respectively. Using this standard curve, a fresh trypsin solution with the values indicated in the standard curve was created and its bioactivity measured as a positive control.

6.2.4.2 Rhodamine 110 Fluorogenic Proteinase Sensitivity Optimization

In order to characterize the assay and provide better sensitivity, the fluorescence values of known trypsin concentrations (n=2) in PBS were measured at different reaction times with the Rhodamine 110 fluorogenic substrate. 50 μL of trypsin solution and 25 μL of Rhodamine 110 substrate at 4.5 m*M* concentration were stored at 2-8^{o}C for the duration of the study. Subsequently, fluorescence measurements were taken with the excitation and emission wavelengths of 498 nm and 521 nm respectively.

6.2.4.3 Optimized Trypsin Study with Oxygen Etching

To show bioactivity of trypsin, trypsin was encapsulated and imprinted, etched, and then released in PBS (w/o Mg^{2+} or Ca^{2+}) buffer for 24 hours. Subsequently the imprinted trypsin sample was exposed to Rhodamine 110 proteinase substrate to ensure bioactivity. The experiment was performed in triplicate with imprinted trypsin samples before O_2 etching, trypsin samples after O_2 etching and plain PEG imprints as controls.

To prepare the trypsin encapsulated PEGDA solution, a stock solution of trypsin (50 mg/mL in 1 m*M* HCl) was diluted to 10 mg/mL in 0.01 *M* PBS (w/o Mg^{2+} or Ca^{2+}).

PEGDA (25% w/v, MW 700) was prepared in dH_2O with 2.5% trypsin (w/w of polymer) and 0.05 wt% I2959. 0.08 μL of the macromer-protein solution (theoretically 0.5 μg of trypsin) was then dispensed from the IMPRIO 100 (Molecular Imprints) and imprinted with a force of 7 N with a 300 sec pre-exposure delay and a 7 sec UV exposure. Next the nanoimprinted samples were either oxygen plasma etched for 40 sec at a power setting of 50 W, using the Plasma Therm 790 Series RIE to remove any residual layer. Control samples remained unetched. Following this, the imprints were incubated in 500 μL of 10 mM HEPES buffer pH 7.55 and/or PBS for 24 hours at room temperature.

To prepare the fluorescence assay Rhodamine 110 proteinase substrate was dissolved in DMSO to a 10 m*M* concentration. It was then diluted into 10 m*M* HEPES buffer, pH 7.55 to 4.5 m*M* concentration (5m*M* is reported in literature). 50 μL of trypsin supernatant was mixed with 25 μL Rhodamine 110 proteinase substrate in a black 96-well plate. The samples were then allowed to react at 2-8^{o}C and fluorescent measurements were taken at 20, 30 and 90 minutes with an excitation and emission wavelengths of 498 nm and 521 nm respectively.

6.2.4.4 Assays to Determine Trypsin Concentration

In order to have a positive control to compare the bioactivity studies with, the concentration of the trypsin released was needed. To determine the concentration of trypsin being released from the nanoparticles, the NanoOrange Assay was used. Reagents were prepared as described in the manufacturer's protocol. Standard samples were created using the manufacturer's protocol as well as using a serial dilution. Following

reagent preparation, samples with volumes of 250 μL were placed into 1 mL centrifuge tubes and heated in a water bath at 90°C - 96°C for 10 minutes. The samples were allowed to cool to room temperature for 1 hour, protected from light, and then the tubes were centrifuged in order to make sure that any solution that had accumulated at the top of the tube was accounted for. Subsequently, 200 μL from each tube was placed into a 96-well black plate and the fluorescence intensity was measured with a fluorescence plate reader (Beckman Coulter) at an excitation and emission of 485 nm and 595 nm respectively.

6.2.5 DNA Bioactivity Studies

6.2.5.1 Initial DNA Bioactivity Study

A 1:1 molar ratio of PEGDA (MW 700) to GFLGK was added to dH_2O to create a 75% (w/v) PEGDA-GFLGK solution with 0.35 mg encapsulated pLuc DNA and 0.07 wt% I2959. 0.4 μL of macromer solution was hand dispensed and imprinted using the IMPRIO 100 SFIL system (Molecular Imprints). The imprints were then etched for 40 seconds with oxygen plasma using a Plasma Therm II. After etching, samples (n=4) were placed in 250 μL of 25 U/mL Cathepsin B solution for 48 hours. For controls, 700 ng pLuc DNA was placed in 250 μL of both 25 U/mL Cathepsin B and dH_20 for 48 hours. The etched samples were then concentrated, and the samples, along with the DNA control in Cathepsin B, and the DNA in dH_2O were transfected using HEK293T cells,

with PEI being the positive control. After transfection, the samples were analyzed using the Luciferase Assay and the luminescence was measured.[3]

6.2.5.2 DNA Bioactivity Study Optimization

In order to determine if the temperature, Cathepsin B, or pH affected the DNA concentration readings, DNA was placed in varying conditions for 24 hours, then measured with the NanoDrop. To see if temperature had a large effect, samples were placed in the refrigerator, at room temperature and in the incubator at 37^{o}C. Samples were also placed in 25 U/mL of Cathepsin B in the refrigerator, at room temperature and in the incubator at 37^{o}C. For controls a fresh sample of DNA and a fresh sample of DNA in Cathepsin B at 25 U/mL were made.

In order to create a large enough sample size for transfection, 25% w/v PEG-GFLGK polymer with encapsulated DNA was imprinted using a sample size of n=12 for the following conditions: before etching, after oxygen etching, and after helium etching. The 12 imprints for each condition were placed in 3 mL of 16 U/mL Cathepsin B (pH 5.5) for 48 hours in the refrigerator. Aliquots were taken from each sample, and subsequently the remainder of the samples was concentrated. A 40 μm cell strainer was used to separate out the wafers and polymer material from the solution. The strainer was rinsed cell strainer 3 times with PBS pH 5.5 Next, the remaining solution was concentrated with an Amicon Centrifugal Device (100 kDa MWCO) to filter out the Cathepsin and retain the DNA. The centrifugal device was rinsed 3 times with PBS pH

[3] Transfection performed courtesy Bilal Ghosn.

5.5 and brought up to a final volume of 100 μL. DNA standards were created in both TE buffer and PBS pH 5.5, and the Picogreen assay was performed.

6.3 RESULTS

6.3.1 Streptavidin-Biotin Bioactivity Studies

Figure 6.1 demonstrates that the encapsulated streptavidin successfully retained its ability to bind to Alexa Fluor 488 biocytin after imprinting and etching. Both the before and after etching imprints showed a strong fluorescence with no difference in fluorescence intensity. The control PEGDA imprint (**Figure 6.1C**) with no streptavidin shows no background fluorescence. Although this is not a quantitative study, it qualitatively provides evidence of protein stability. Interestingly, **Figure 6.1D** shows a Helium etched sample in which the particles appear to be detaching from the wafer surface.

6.3.2 Luciferase Bioactivity Studies

6.3.2.1 Luciferase Study: PEGDA-GFLGK-DA

Because luciferase is a large 60 kDa protein, it should not be able to release from imprinted nanocarriers. In order to release the luciferase, it was encapsulated in the PEGDA-GFLGK-DA stimuli-responsive nanoparticles. As seen in **Figure 6.2**, the luciferase in Cathepsin solution showed no difference from the control in Cathepsin 25

U/mL. The results suggest either that there is no bioactivity or that the Cathepsin in the sample solution may be affecting the luciferase. The graph further demonstrates that the control DNA has a higher bioactivity at room temperature than at 37^{o}C, which is the temperature used for the experiment. Thus there are many factors in the assay affecting the bioactivity. Further optimization was performed to determine how Cathepsin and varying buffers affected the luciferase. It was determined that pH and temperature both cause a decrease in luciferase bioactivity, and that the optimal buffer was the Glo-Lysis buffer from the Luciferase assay kit.

6.3.2.2 Luciferase Study: PEGDA

Because pH affects the bioactivity and Cathepsin is most active at pH 5, luciferase was encapsulated in plain PEGDA without the use of Cathepsin. Although the pore size is too small to allow luciferase to diffuse out, the luciferin in the luciferase reagent is a 318 Da molecule that can penetrate the nanoparticles. The results are illustrated in **Figure 6.3**. The samples with luciferase before etching seemed to show less bioactivity than the samples with luciferase after etching. However, a t-test revealed that there was no significant difference between the two. Furthermore, there was a significant difference in the samples with the luciferase when compared to the PEGDA control with no luciferase. This suggests that the luciferase is bioactive. However, when compared to the total amount of luciferase encapsulated, there is a large difference in bioactivity. The results demonstrate bioactivity but the exact concentration of luciferin reacting with luciferase cannot be determined, thus there is no positive control.

6.3.3 Trypsin Bioactivity Studies

Trypsin was initially encapsulated in PEGDA nanoparticles and allowed to release in HEPES and PBS buffer. As seen in **Figure 6.3A**, the PBS buffer allows for better sensitivity of the results than the PBS buffer. Using the PBS buffer, the before and after etched samples showed no significant difference in bioactivity level, as verified by a t-test. Furthermore, a t-test was used to compare the before etched sample to the control PEG sample. The results demonstrate a p-value of 0.05; thus the results cannot statistically be determined, but may show a slight significance. **Figure 6.3B** demonstrates a standard curve that was created for the trypsin in PBS. It demonstrates the bioactivity values for given trypsin concentrations. As can be seen, it shows very little sensitivity at lower concentration levels.

Using known standards of trypsin, the incubation time in the Rhodamine 110 substrate was varied in order to determine the incubation time that would yield the best sensitivity. As shown in **Figure 6.4B** the shape of the standard curves remains consistent from 5 minutes to 90 minutes incubation time. The graph shows that the greatest sensitivity occurs at longer incubation times, and that the optimal lower detection limit appears to be a concentration of 100 ng/mL. The 48 hour incubation time shows greater sensitivity to lower trypsin concentration, but the shape of the curve is not as consistent with the initial curves. Using longer incubation times, the bioactivity of the trypsin released from the nanoparticles was measured for 20 minutes, 30 minutes and 90 minutes. **Figure 6.4A** demonstrates that, for each incubation time, there was no significant difference between the etched and non-etched samples. Furthermore, the non-

etched samples when compared to the control PEGDA samples with no trypsin showed a significant difference with $p < 0.05$. Thus the results suggest that the trypsin is still active.

In order to verify that the standard curves at the various incubation times (20, 30 and 90 min.) were not showing different concentration values, the standard curves were used to estimate the trypsin concentration for each sample. The concentration of trypsin in the solutions was measured for each incubation time, using the respective incubation standard curve. The results in **Table 4.1** demonstrate that the concentrations for the 20 and 30 minute incubation are consistent with an average value of 0.976 ng/mL. The concentration values for the 90 minute incubation time show a concentration of on average 1.138 ng/mL. Overall there is little variation in concentration reading. The 90 minute incubation time does show a larger variation in results as can be seen by the larger standard deviations.

6.3.3.1 NanoOrange Assay to Determine Trypsin Concentration

In order to have a positive control to compare for the bioactivity studies, the NanoOrange assay was used for each experiment to try to determine the trypsin concentration. The NanoOrange assay is, in theory, able to detect concentrations as low as 10 ng/mL, using cuvettes and a fluorometer, and 100 ng/mL using a fluorescence plate reader. Despite encapsulating up to 0.5 μg of trypsin per imprint, the NanoOrange assay was never able to supply a usable standard curve as demonstrated in the manufacturer's protocol. A new kit was ordered to verify that there was nothing wrong with the assay kit;

however the new kit was not able to provide accurate results. The only other kit found for measuring nanomolar concentration was the CBQCA assay; however, this assay requires a minimum of 100 ng in the aliquoted sample for measurement. Thus the trypsin concentration of released trypsin from the PEGDA nanoparticles was not able to be calculated for use as a positive control.

6.3.4 DNA Bioactivity Studies

The results from the initial DNA transfection and bioactivity study revealed no difference between the native cells, the experimental samples, and the control DNA in Cathepsin B (**Figure 6.5**). Because the DNA control in Cathepsin solution also showed no difference in bioactivity, this suggests that the Cathepsin may be affecting the study and that it is not the imprinting process. Further studies revealed that the optimal conditions for maintaining the DNA integrity were keeping the samples in dH_2O or PBS at 2 - 8^{o}C.

Because the DNA was hand imprinted on PVA, it was necessary to separate the DNA from any unetched polymer remnants; this was achieved by filtering the solution. To concentrate the DNA, the solution was placed in concentrating centrifuges. As seen in **Table 6.2**, after the filtering and concentrating, most of the DNA was lost. At minimum, 200 ng in 100 μL of solution is required per 96-well plate for the transfection. Thus we were not getting a high enough concentration of DNA for the transfection studies.

6.4 DISCUSSION

The overall goal of this research was to demonstrate that model drugs would remain active after undergoing the Step and Flash Imprint Lithography process. All process parameters for the experiments involved minimum pressure, a short exposure 7 to 10 second exposure time, and a mild UV exposure at a wavelength of 365 nm. The dosimeter reading panel of the IMPRIO showed a dose of 2 mW/cm^2 at the template-substrate interface. These exposure parameters have been previously reported to be DNA and cell compatible [7, 8].

We were successfully able to demonstrate that model biological drugs could be incorporated within the macromer and solution and imprinted using IMPRIO 100 dispensing system, and we successfully demonstrated qualitative evidence of streptavidin bioactivity. The streptavidin bioactivity study demonstrated that the streptavidin binding sites remain active and are not damaged by the imprinting process. Both the luciferase and trypsin bioactivity studies showed limited quantitative bioactivity; however we were not able to compare to a positive control. We hypothesize that this limited bioactivity is due to an inability to accurately measure the concentration of the proteins on a pico and nanomolar concentration, as well as due to the very small pore size of the PEGDA.

From the luciferase studies we modified an assay that was typically used with firefly luciferase DNA, to detect the expression of luciferase. For our studies we directly encapsulated the luciferase. Through the experiment, we learned that the temperature, pH and buffer played a large role in affecting the bioactivity. Based on the manufacturer's literature, the luciferase assay is optimal at a pH of 7.8, and once the pH reaches 5.5 or

lower there is no longer an emission at 562 because the oxyluciferin (ie. - the reaction product which emits light) becomes protonated. The Cathepsin B used for our initial experiment has optimum activity around pH 5 to 5.5. Furthermore, the enzymes become degraded at temperatures above 30^{o}C and are only stable at room temperature in Glo-Lysis buffer for two days. The initial luciferase assay utilized a low pH and with a 48 hour incubation at 37^{o}C, thus the luciferase enzyme had been degraded. The second luciferase assay accounted for these factors and demonstrated limited quantitative bioactivity. Unfortunately, the luciferase was too large to leach out from the nanoparticles. Therefore we could not determine the quantity of the luciferase reacting with the luciferin inside the nanoparticles. Furthermore, because the luciferin was entering the particles and creating luminescence, the luminescence values may have been dampened by the polymer.

Because trypsin is a smaller protein (MW 23.8 kDa, 18 Å radius of gyration), we hypothesized that it would successfully leach out from the PEGDA nanoparticles. After optimizing the assay parameters we have shown limited bioactivity of the trypsin when compared to the negative control of PEGDA alone. The difficulties with this study are with measuring the concentration of trypsin that has been released from the imprints. Because the molecular weight of trypsin is 23.8 kDa, the measured concentration values of ~ 1 ng/mL correspond to a 0.042 n*M* protein concentration; this is a picomolar concentration. Currently we have been unable to find an assay to measure such small concentrations.

Using the standard curves created with the Rhodamine-110 protease substrate showed fluorescence on the level of a 1 ng/mL concentration of trypsin. This is interesting considering that the theoretically calculated maximum amount of encapsulated trypsin per imprint was 0.5 μg of trypsin. This discrepancy could suggest that the trypsin is not easily leaching from the PEGDA nanoparticles. From *Chapter Three* we determined the pore size of a 25% (w/v) PEGDA hydrogel to be 12.92 ± 1.56 Å. Thus it is plausible that the trypsin is not successfully able to leave the hydrogel. This would account for the small measured concentration values as well as some of the inability to measure the concentration with standard protein assays. Another factor to consider could be that the protein may be adhering to the tubing of the dispense system. This could also affect the amount of trypsin we see in the imprints. This factor could quickly be resolved by coating the tubing with Sigmacoat or by purchasing low adhesion tubing. The DNA transfection studies themselves have proven unsuccessful in proving bioactivity, due to an inability to concentrate and measure the DNA, as well Cathepsin interaction.

In conclusion, we have demonstrated qualitative proof that the Step and Flash Imprint Lithography can successfully imprint encapsulated biologics that remain bioactive. We have also shown limited quantitative proof that the proteins trypsin and luciferase retain their bioactivity. The SFIL process uses low pressure and already established UV wavelengths and exposure energies. It should be noted that UV photo polymerization need not be a necessary step in generating nanoparticles using SFIL. It is easily conceivable that any other cross linking chemistry, such as Michael's addition

nucleophilic-electrophilic crosslinks, can also be used with templates followed by etching.

The limiting factor in demonstrating decisive quantitative bioactivity has been due to the limitations of the experiments themselves. The fact that the model biologics are too large to leach out from the PEGDA nanoparticles has lead to an inability to measure such small concentrations. For future studies we suggest encapsulating smaller molecular weight molecules such as fibroblast growth factor-2 (FGF-2) which is an 18 kDa molecule with a 14.5 Å radius of gyration [13, 14], or human growth hormone releasing factor (hGRF) which is a 3400 Da molecule [15]. These factors could be released and bioactivity could be determined using an ELISA assay. Furthermore, doxorubicin could be encapsulated and analyzed with HPLC, and siRNA could also easily be encapsulated and analyzed. For future studies with DNA transfection, separating the DNA from the Cathepsin is critical as well as concentrating enough for the transfection. We would suggest using an ion exchange column to separate the DNA and Cathepsin B, and then collecting the DNA fraction. This could then be concentrated in a dialysis membrane using a concentration solution.

Figure 6.1 Fluorescence Micrographs Demonstrating Streptavidin Bioactivity. Encapsulated streptavidin in 400 nm imprinted features, after soaking in biocytin Alexa Fluor for 30 minutes using a 75% (w/v) PEGDA (MW 700) and a 0.019 μL volume. (A) Before etching, (B), after oxygen etching, (C), control PEGDA imprint with 400 nm features, and (D) imprinting with helium, see particle release. *(All scale bars = 5μm)*

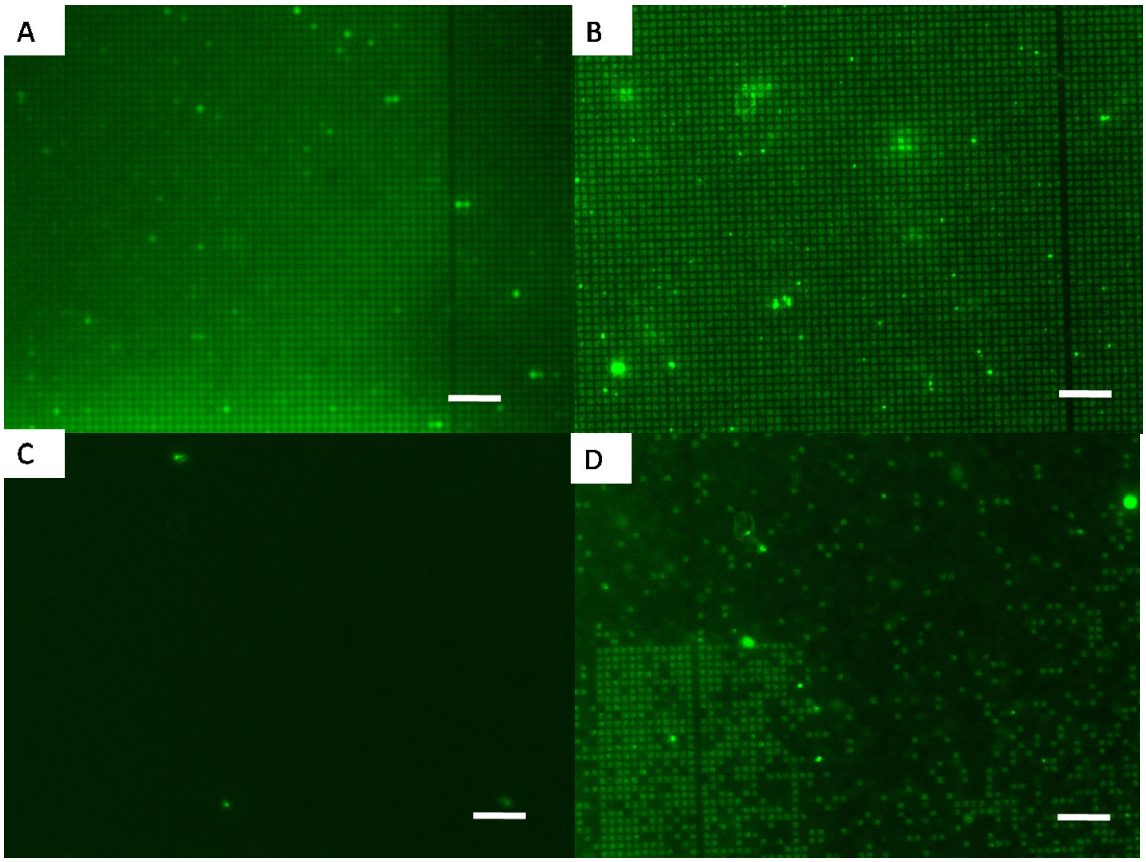

Figure 6.2 Bioactivity of Luciferase. Graphs demonstrating bioactivity levels of luciferase encapsulated in (A) PEGDA-GFLGK-DA and (B) PEGDA.

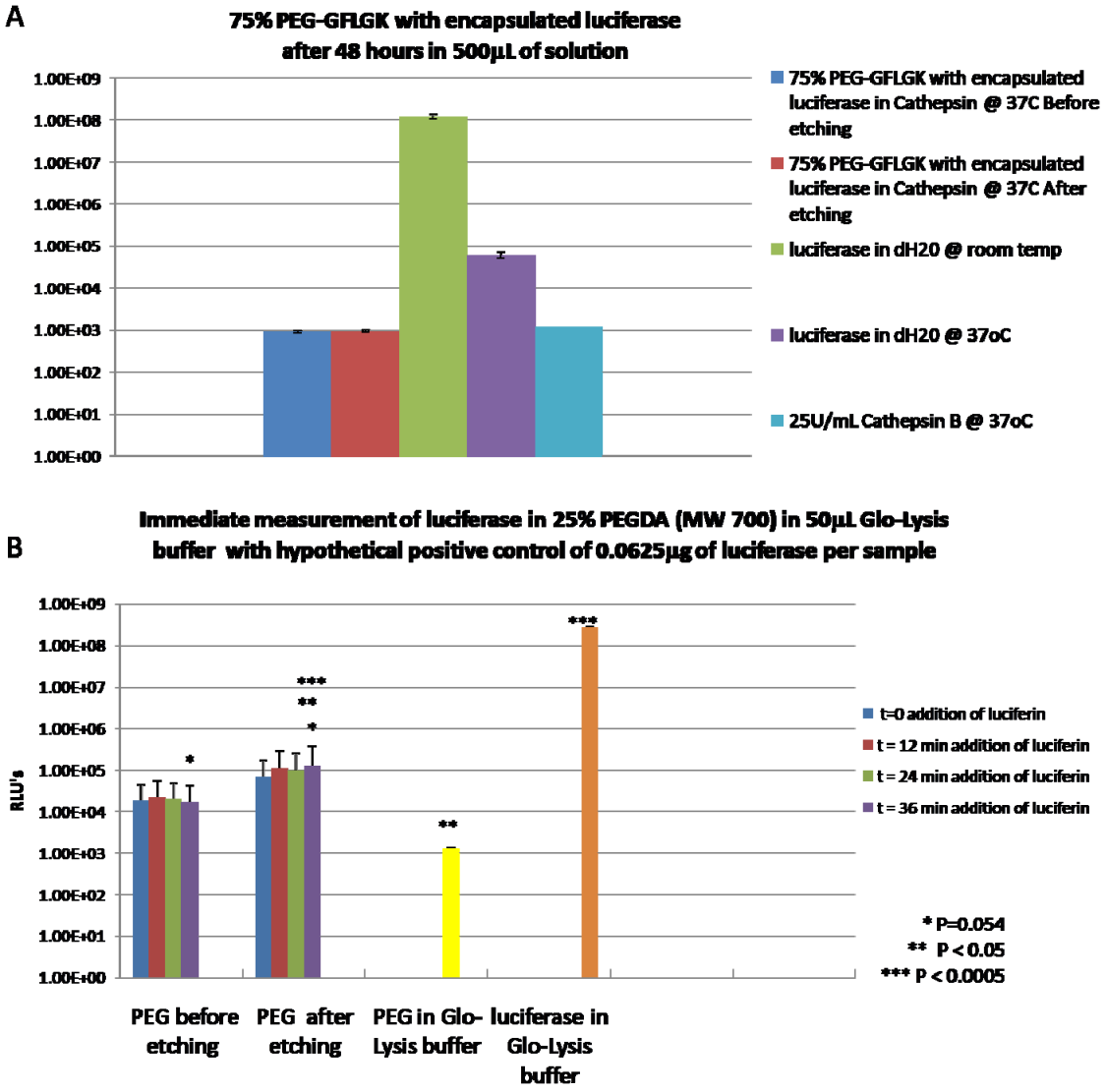

Figure 6.3 **Trypsin Bioactivity Optimization. Graphs demonstrating trypsin bioactivity optimization using various buffers: (A) trypsin in PBS and HEPES buffers, and (B) standard curve using PBS buffer.**

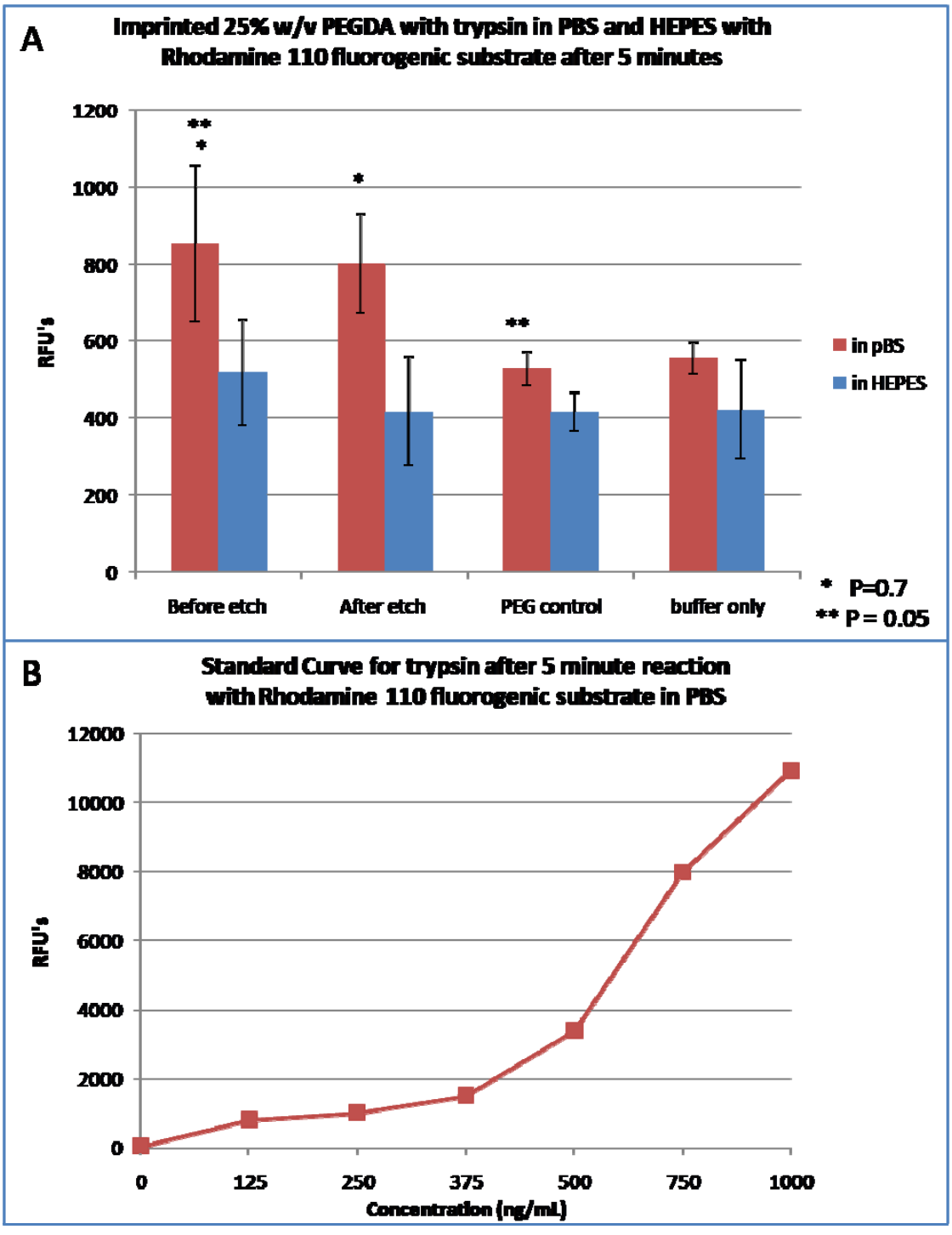

Figure 6.4 **Trypsin Bioactivity Measured with Varying Incubation Times in Rhodamine 110: (A) trypsin incubated in PBS buffer with substrate incubation times of 20 to 90 minutes, and (B) standard curve using PBS buffer with varying incubation times from 5 minutes to 48 hours.**

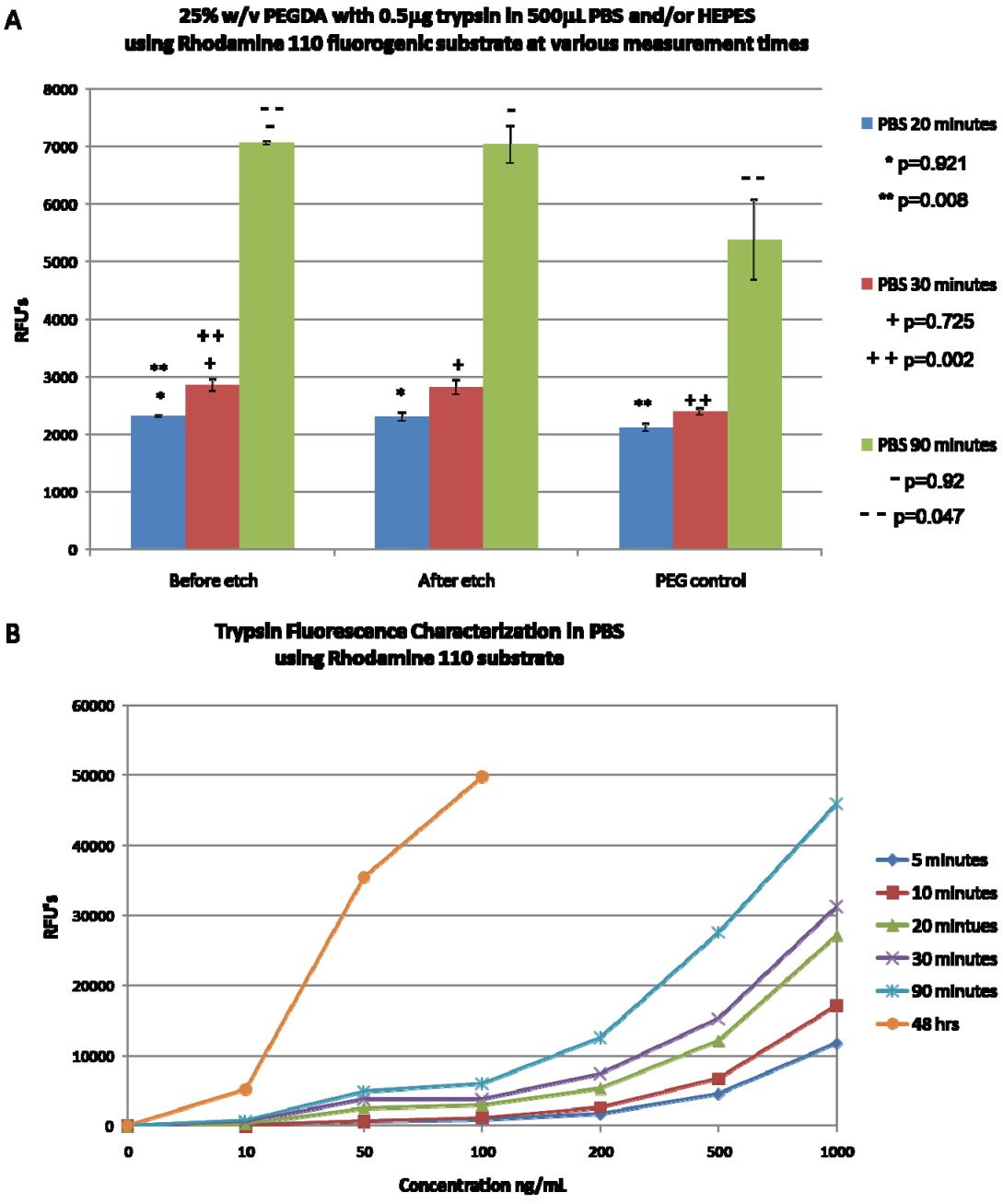

Table 6.1 Concentration of Trypsin Released from PEGDA. Concentrations of etched and non-etched PEGDA based on the standard curves created for various incubation times.

	concentration (ng/mL)					
	20 min	(SD)	30 min	(SD)	90 min	(SD)
PEGDA before etch	0.980	0.007	0.979	0.031	1.142	0.008
PEGDA after etch	0.977	0.036	0.968	0.038	1.135	0.080

Figure 6.5 Luciferase DNA Transfection. The experiment was performed with HEK293T cells and shows no difference between native cells, the experimental DNA samples, and the control DNA in Cathepsin solution.

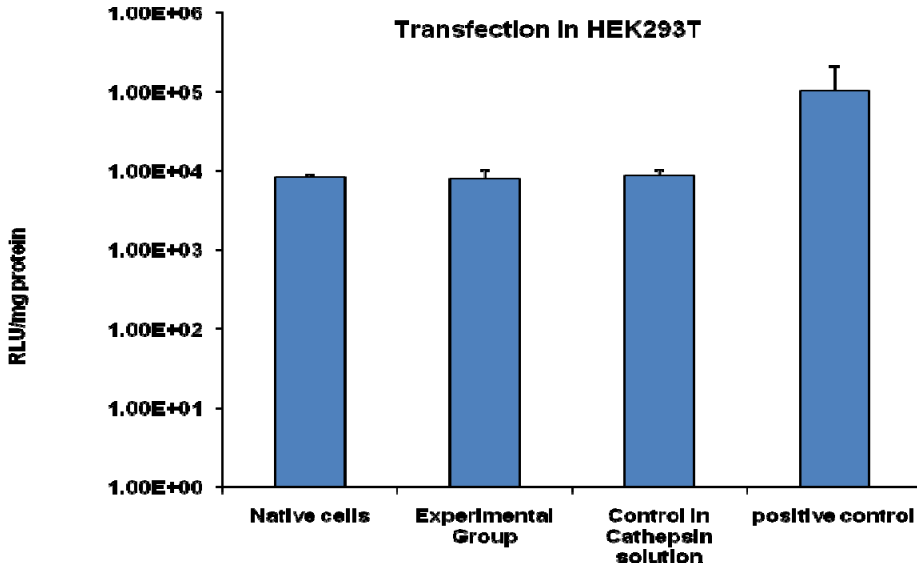

Table 6.2 Average DNA Concentration Before and After Concentrating and Filtering.

		After concentrating (ng/mL)	Before concentrating (ng/mL)
PBS buffer	Before etch	2.62	294.74
	After O2 etch	2.68	315.16
	After He etch	3.48	372.88
TE buffer	Before etch	2.75	273.22
	After O2 etch	2.63	266.22
	After He etch	3.62	342.88

6.5 REFERENCES

1. Rolland JP, Maynor BW, Euliss LE, Exner AE, Denison GM, DeSimone JM. Direct fabrication and harvesting of monodisperse, shape-specific nanobiomaterials. J Am Chem Soc 2005;127(28):10096-10100.
2. Leach JB, Schmidt CE. Characterization of protein release from photocrosslinkable hyaluronic acid-polyethylene glycol hydrogel tissue engineering scaffolds. Biomaterials 2005;26(2):125-135.
3. Ishihara M, Obara K, Ishizuka T, Fujita M, Sato M, Masuoka K, et al. Controlled release of fibroblast growth factors and heparin from photocrosslinked chitosan hydrogels and subsequent effect on in vivo vascularization. J Biomed Mater Res A 2003;64(3):551-559.
4. DeLong SA, Moon JJ, West JL. Covalently immobilized gradients of bFGF on hydrogel scaffolds for directed cell migration. Biomaterials 2005;26(16):3227-3234.
5. Burdick JA, Mason MN, Hinman AD, Thorne K, Anseth KS. Delivery of osteoinductive growth factors from degradable PEG hydrogels influences osteoblast differentiation and mineralization. J Control Release 2002;83(1):53-63.
6. Quick DJ, Anseth KS. DNA delivery from photocrosslinked PEG hydrogels: encapsulation efficiency, release profiles, and DNA quality. J Control Release 2004;96(2):341-351.

7. Quick DJ, Anseth KS. Gene delivery in tissue engineering: a photopolymer platform to coencapsulate cells and plasmid DNA. Pharm Res 2003;20(11):1730-1737.

8. Bryant SJ, Anseth KS. Hydrogel properties influence ECM production by chondrocytes photoencapsulated in poly(ethylene glycol) hydrogels. J Biomed Mater Res 2002;59(1):63-72.

9. Kasper FK, Kushibiki T, Kimura Y, Mikos AG, Tabata Y. In vivo release of plasmid DNA from composites of oligo(poly(ethylene glycol)fumarate) and cationized gelatin microspheres. J Control Release 2005;107(3):547-561.

10. Mapili G, Lu Y, Chen S, Roy K. Laser-layered microfabrication of spatially patterned functionalized tissue-engineering scaffolds. J Biomed Mater Res B 2005;75(2):414-424.

11. Bourke SL, Al-Khalili M, Briggs T, Michniak BB, Kohn J, Poole-Warren LA. A photo-crosslinked poly(vinyl alcohol) hydrogel growth factor release vehicle for wound healing applications. AAPS PharmSci 2003;5(4):E33.

12. Mellott MB, Searcy K, Pishko MV. Release of protein from highly cross-linked hydrogels of poly(ethylene glycol) diacrylate fabricated by UV polymerization. Biomaterials 2001;22(9):929-941.

13. Seghezzi G, Patel S, Ren CJ, Gualandris A, Pintucci G, Robbins ES, et al. Fibroblast growth factor-2 (FGF-2) induces vascular endothelial growth factor (VEGF) expression in the endothelial cells of forming capillaries: an autocrine mechanism contributing to angiogenesis. J Cell Biol 1998;141(7):1659-1673.

14. Filion RJ, Popel AS. Intracoronary administration of FGF-2: a computational model of myocardial deposition and retention. Am J Physiol Heart Circ Physiol 2005;288(1):H263-279.

15. Peticlerc D, Pelletier G, Lapierre H, Gaudreau P, Couture Y, Dubreuil P, et al. Dose response of two synthetic human growth hormone-releasing factors on growth hormone release in heifers and pigs. J Anim Sci 1987;65(4):996-1005.

CHAPTER SEVEN

Conclusions and Future Directions

7.1 SUMMARY

In summary, we have developed a peptide-functionalized, enzyme-responsive poly(ethylene glycol) hydrogel capable for use with nanoimprint lithography. We have also developed a unique method for creating nanocarriers of precise sizes and shapes for drug and contrast agent delivery, utilizing Step and Flash Imprint Lithography. We have achieved 50 nm particle size and demonstrated efficient stimuli-responsive release of encapsulated drugs. The particles can be directly harvested into aqueous buffers using a simple, biocompatible process. In addition, the method does not require high temperature, high shear, organic solvents or long UV light exposure, which allows for direct encapsulation of biological agents. This process uses commercially available instruments and thus has the potential to be a translatable, high-throughput technique. A single 4 inch wafer could generate 1 x 10^{11} 100 nm particles and an 8 inch wafer could generate 4 x 10^{11} 100 nm particles using a 10 x 10 mm mesa. Since the latest generation SFIL systems have the capability to imprint whole wafers at a time, imprint on top of existing nanofeatures, generate sub-50 nm structures and allow sub-10 nm alignment accuracy (manufacturer's specifications), we envision that the process could fabricate, at a larger scale, smaller nanoparticles as well as multi-layered particles with varying composition and release mechanisms between layers.

The material chemistry used here is well established and also conducive to easily attaching specific ligands to the particle surface thus providing opportunities of cell targeted, disease-triggered delivery of drugs and imaging agents. The development of this technique for fabricating injectable nanoparticles for drug delivery, has also provided a path to enhance the field of study on the effects of shape and size on in-vivo properties. We have successfully demonstrated that model drugs can easily be incorporated into the imprinting system and retain biological activity. Thus, the use of SFIL along with gentle nanoparticle harvesting techniques can allow for the creation of multifunctional nanocarriers, with potential for targeting, stimuli-responsive release and the ability to incorporate drug and imaging agent. This ties into the long-term goal of the research to achieve site-specific, controlled, on-demand drug delivery leading to lower side-effects, increased bio-availability and improved therapeutic effectiveness and at the same time be able to effectively monitor the biodistribution of therapeutics using conventional imaging techniques.

7.2 Conclusions and Future Directions with Photo-crosslinked, PEG-peptide Material Systems for use as Nanoimprinted, Enzyme-Responsive Nanocarriers

Chapter Three discussed the synthesis and characterization of photo-crosslinked, PEG-peptide hydrogels suitable for use as nanoimprinted, enzyme-responsive material systems. The overall goal of the research was to create a stimuli-responsive, peptide-

functionalized, PEG-based system that demonstrated: (a) minimal diffusion of the drug through it in the absence of enzyme-triggered degradation, and (b) the ability to be nanoimprinted. We successfully synthesized two photo-crosslinkable configurations: PEG-GFGLK-PEG and PEGDA-GFLGK-DA. Both configurations create a matrix crosslinked with a degradable peptide spacer, GFLGK, designed for degradation by Cathepsin B.

We demonstrated successful synthesis, imprintability, and enzyme-responsive release. Based on mesh size analysis we believe protein, peptide and nucleic acid-based drugs, hydrophobic drug particles as well as nanoparticle-based contrast agents could be successfully retained within such hydrogels and released primarily upon environmentally-triggered matrix degradation. The key relevance of these studies is the possibility that these polymer designs, as well as other similar peptide-functionalized, enzyme-degradable hydrogels could be nanoimprinted, and used to control drug release from nanoimprinted carriers. Future studies would be required in order to characterize the degradation and release kinetics of the two polymer configurations.

7.3 Conclusions and Future Directions with Nanoimprint Lithography Techniques for Fabrication of Injectable, Intracellular Drug Delivery Nanoparticles of Specific Size and Shape

Chapter Four discussed nanoimprint lithography techniques for fabrication of injectable, intracellular drug delivery nanoparticles of specific size and shape. Thermal

Nanoimprint Lithography (ThNIL) and Step and Flash Imprint Lithography (SFIL) were evaluated, and the optimization of the SFIL process for biopolymer imprinting was discussed. We demonstrated the use of ThNIL and SFIL, coupled with biocompatible material systems to imprint and develop monodisperse injectable nanoparticles of pre-designed sizes and geometries as small as 50 nm. Particles of varying shape (square, circular, pentagonal, and triangular), size (50 - 400 nm), and composition (PMMA, PLGA, PEG) were fabricated using these techniques with little to no variation in geometry.

We demonstrated that the SFIL technique has the potential to create well-defined and characterized drug delivery particles without the limitations of thermal imprint lithography, the PRINT process, or self-assembly formation techniques. Furthermore, we have demonstrated full wafer imprinting and successful isolation and release of the nanoparticles from the wafer using a mild harvesting method. The SFIL method, with its low temperature and force applications, as well as wafer-scale imprinting capability, was shown to be suitable for large scale fabrication of injectable drug delivery particles. Further optimization of the parameters will still be required to reach a true zero residual layer.

This research provides a significant advance in the creation of monodisperse, injectable nanocarriers of specific geometry and can provide a characterized environment for the study of the effect of size and shape in in-vivo release properties of nanoparticles. With the development of such a method, we believe there is broad applicability to aid in further study of how nanoparticle shape and size affect delivery of drugs to tissues and

cells within the body. Future studies could be performed to evaluate the effect of shape on in-vivo drug or contrast agent release, and may allow for future tunable in-vivo release and targeting properties.

7.4 Conclusions and Future Directions with Stimuli-Responsive Nanoimprinted Nanocarriers: Enzymatic Degradation and In-vitro Release Studies

Chapter Five demonstrated in-vitro drug release of DNA and proteins after nanoimprinting the enzyme-responsive material system developed in *Chapter Three*, and demonstrated enzyme-mediated degradation. We successfully fabricated nanoparticles using an equimolar mixture of PEGDA (MW 700) and a diacrylated, enzymatically degradable peptide GFLGK-DA, to create a particle matrix crosslinked by the degradable peptide. We demonstrated that biological agents can be successfully incorporated within these imprints during the nanoimprinting process by simply mixing the agents with the macromer solution prior to polymerization, and we have demonstrated successful retention of model drug (DNA and antibody) in the absence of tumor-specific enzymes (with an initial leakage of DNA) and successful enzyme-triggered release of model drug upon the addition of Cathepsin B. To our knowledge this is the first demonstration of nanoimprinting and nanocarrier synthesis using biologically responsive macromolecules. The creation of nanoscale, drug or contrast agent delivery systems with stimuli-

responsive and environmentally-degradable features is a significant milestone in creating "intelligent" multi-functional nanocarriers.

The SFIL process has demonstrated the versatility for creating well-defined nanoparticles and stimuli-responsive nanoparticles. Furthermore, biological agents can easily be incorporated into nanoparticle drug delivery systems using this method and the macromer concentration can be varied to encapsulate a wide variety of therapeutics and contrast agent. Future studies to compare the macroscale swelling properties of the PEGDA and PEGDA-GFLGK-DA to the nanoscale gels would provide an interesting insight into the nano-gel properties, and in the understanding of what agents could be encapsulated.

Future studies for optimization would require in depth characterization of the degradation and release kinetics. For solutions that are manually dispensed and for thicker residual layers, the etching process required to isolate the nanoparticles etches the residual layer away as well as the therapeutics located within the residual layer; thus the overall release kinetics cannot be determined until the loading efficiency of the particles is determined. In order to automatically dispense the drug - polymer solution for the creation of stimuli-responsive nanoparticles it would also be necessary to use an appropriate dispenser tip for the radius of the therapeutic being encapsulated. With the use of automated dispensing, the volume of the solution dispensed could be set such that there would be little residual layer and little to no etching required, and could allow for large-scale fabrication enzyme-responsive-nanocarriers.

7.5 Conclusions and Future Directions with Bioactivity of Biologics Encapsulated in Nanoimprinted Nanocarriers

Chapter Six described in-vitro bioactivity studies of DNA and proteins encapsulated in nanoimprinted PEGDA and peptide-functionalized PEGDA. The protein bioactivity assays demonstrate qualitative and quantitative evidence of bioactivity. We demonstrated qualitative proof that the Step and Flash Imprint Lithography can successfully imprint encapsulated biologics, such as streptavidin, and allow the biologic to remain bioactive. We have also shown limited quantitative proof that the proteins trypsin and luciferase retain their bioactivity. The SFIL process uses low pressure and already established UV wavelengths and exposure energies.

The limiting factor in demonstrating decisive quantitative bioactivity has been due to the limitations of the experiments themselves. The fact that the model biologics are too large to leach out from the PEGDA nanoparticles has lead to an inability to measure such small concentrations. For future studies we suggest encapsulating smaller molecular weight molecules such as fibroblast growth factor-2 (FGF-2) which is an 18 kDa molecule with a 14.5 Å radius of gyration, or human growth hormone releasing factor (hGRF) which is a 3400 Da molecule. These factors could be released and bioactivity could be determined using an ELISA assay. Furthermore, doxorubicin could be encapsulated and analyzed with HPLC, and small interfering RNA (siRNA) could be encapsulated and analyzed. For future studies with DNA transfection, separating the DNA from the Cathepsin is critical as well as concentrating enough for the transfection. We would suggest using an ion exchange column to separate the DNA and Cathepsin B,

and then collecting the DNA fraction. This could then be concentrated in a dialysis membrane using a concentration solution.

Another factor leading to such small concentrations could be that the proteins are sticking to the tubing of the dispense system. This can be solved by coating the inside of the tubing with Sigmacoat, or by purchasing low adhesion tubing. It should also be noted that other than UV photo-crosslinking, Michael's addition polymerization could also be conceivably used with templates followed by etching.

Glossary of Acronyms

ACRL	Acrylate
AFM	Atomic Force Microscopy
CF_4	Carbon Tetrafluoride
CHF_3	Fluoroform
Cl_2	Chlorine
Da	Dalton
DCM	Dicloromethane
dH_2O	Deionized Water
DMAc	Dimethylacetamide
D_2O	Deuterium Oxide
EBL	Electron Beam Lithography
EPR	Enhanced permeability and retention
FGF-2	Fibroblast growth factor-2
GFLGK	Gly-Phe-Leu-Gly-Lys
GFLGK-DA	acrylate-Gly-Phe-Leu-Gly-Lys-acrylate
HBr	Hydrogen-bromide
He	Helium
hGRF	Human growth hormone releasing factor
I2959	2-hydroxy-1-[4-(hydroxyethoxy) phenyl]-2-methyl-1 propanone
IPA	Isopropyl Alcohol
MALDI-TOF	Matrix-Assisted Laser Desorption/Ionization Time of Flight
MMP	Matrix metalloproteinase
MPS	Mononuclear phagocytic system
MW	Molecular Weight
N	Newtons
NHS-PEG-ACRL	Acrylate-PEG-N-Hydroxy-succinamide
NMP	N-Methyl Pyrrolidone

NMR	Nuclear Magnetic Resonance
O_2	Oxygen
PBS	Phosphate buffered saline
PEG	Poly(ethylene glycol)
PEGDA	Poly(ethylene glycol) diacrylate
PLA	Poly(lactide)
PLGA	Poly(lactide-co-glycolide)
PMMA	Poly(methyl methacrylate)
PVA	Poly(vinyl alcohol)
RES	Reticuloendothelial system
rhBMP	Recombinant human bone morphogenetic protein
RIE	Reactive Ion Etching
SAM	Self-assembled Monolayer
SEM	Scanning Electron Microscopy
SFIL	Step and Flash Imprint Lithography
siRNA	Small interfering RNA
ThNIL	Thermal Imprint Lithography

Bibliography

Ahmed A, Bonner C, Desai TA. Bioadhesive microdevices with multiple reservoirs: a new platform for oral drug delivery. J Control Release 2002;81(3):291-306.

Almeida AJ, Souto E. Solid lipid nanoparticles as a drug delivery system for peptides and proteins. Adv Drug Deliv Rev 2007;59(6):478-490.

Alonso MJ. Nanomedicines for overcoming biological barriers. Biomed Pharmacother 2004;58(3):168-172.

Asokan A, Cho MJ. Exploitation of intracellular pH gradients in the cellular delivery of macromolecules. J Pharm Sci 2002;91(4):903-913.

Awasthi VD, Garcia D, Goins BA, Phillips WT. Circulation and biodistribution profiles of long-circulating PEG-liposomes of various sizes in rabbits. Int J Pharm 2003;253(1-2):121-132.

Baier Leach J, Bivens KA, Patrick CW, Schmidt CE. Photocrosslinked hyaluronic acid hydrogels: natural, biodegradable tissue engineering scaffolds. Biotechnol Bioeng 2003;82(5):578-589.

Bailey T, Choi BJ, Colburn M, Meissl M, Shaya S, Ekerdt JG, et al. Step and flash imprint lithography: Template surface treatment and defect analysis. J Vac Sci Technol B 2000;18(6):3572-3577.

Bell CL, Peppas NA. Water, solute and protein diffusion in physiologically responsive hydrogels of poly(methacrylic acid-g-ethylene glycol). Biomaterials 1996;17(12):1203-1218.

Belvisi MG, Bottomley KM. The role of matrix metalloproteinases (MMPs) in the pathophysiology of chronic obstructive pulmonary disease (COPD): a therapeutic role for inhibitors of MMPs? Inflamm Res 2003;52(3):95-100.

Berger J, Reist M, Mayer JM, Felt O, Peppas NA, Gurny R. Structure and interactions in covalently and ionically crosslinked chitosan hydrogels for biomedical applications. Eur J Pharm Biopharm 2004;57(1):19-34.

Besheer A, Wood KM, Peppas NA, Mader K. Loading and mobility of spin-labeled insulin in physiologically responsive complexation hydrogels intended for oral administration. J Control Release 2006;111(1-2):73-80.

Betancourt T, Brannon-Peppas L. Micro-and nanofabrication methods in nanotechnological medical and pharmaceutical devices. Int J Nanomedicine 2006;1(4):483-495.

Bezemer JM, Radersma R, Grijpma DW, Dijkstra PJ, van Blitterswijk CA, Feijen J. Microspheres for protein delivery prepared from amphiphilic multiblock copolymers. 1. Influence of preparation techniques on particle characteristics and protein delivery. J Control Release 2000;67(2-3):233-248.

Blanchette J, Peppas NA. Oral chemotherapeutic delivery: design and cellular response. Ann Biomed Eng 2005;33(2):142-149.

Blanchette J, Peppas NA. Cellular evaluation of oral chemotherapy carriers. J Biomed Mater Res A 2005;72A(4):381-388.

Bourke SL, Al-Khalili M, Briggs T, Michniak BB, Kohn J, Poole-Warren LA. A photo-crosslinked poly(vinyl alcohol) hydrogel growth factor release vehicle for wound healing applications. AAPS PharmSci 2003;5(4):E33.

Brannon-Peppas L, Blanchette JO. Nanoparticle and targeted systems for cancer therapy. Adv Drug Deliv Rev 2004;56(11):1649-1659.

Brannon-Peppas L, Peppas NA. Dynamic and equilibrium swelling behaviour of pH-sensitive hydrogels containing 2-hydroxyethyl methacrylate. Biomaterials 1990;11(9):635-644.

Brigger I, Dubernet C, Couvreur P. Nanoparticles in cancer therapy and diagnosis. Adv Drug Deliv Rev 2002;54(5):631-651.

Bryant SJ, Anseth KS. Hydrogel properties influence ECM production by chondrocytes photoencapsulated in poly(ethylene glycol) hydrogels. J Biomed Mater Res 2002;59(1):63-72.

Bryant SJ, Anseth KS. Controlling the spatial distribution of ECM components in degradable PEG hydrogels for tissue engineering cartilage. J Biomed Mater Res A 2003;64(1):70-79.

Bryant SJ, Bender RJ, Durand KL, Anseth KS. Encapsulating chondrocytes in degrading PEG hydrogels with high modulus: engineering gel structural changes to facilitate cartilaginous tissue production. Biotechnol Bioeng 2004;86(7):747-755.

Burdick JA, Mason MN, Hinman AD, Thorne K, Anseth KS. Delivery of osteoinductive growth factors from degradable PEG hydrogels influences osteoblast differentiation and mineralization. J Control Release 2002;83(1):53-63.

Byrne ME, Hilt JZ, Peppas NA. Recognitive biomimetic networks with moiety imprinting for intelligent drug delivery. J Biomed Mater Res A 2008;84A(1):137-147.

Byrne ME, Park K, Peppas NA. Molecular imprinting within hydrogels. Adv Drug Deliv Rev 2002;54(1):149-161.

Campo E, Munoz J, Miquel R, Palacin A, Cardesa A, Sloane BF, et al. Cathepsin B expression in colorectal carcinomas correlates with tumor progression and shortened patient survival. Am J Pathol 1994;145(2):301-309.

Canal T, Peppas NA. Correlation between mesh size and equilibrium degree of swelling of polymeric networks. J Biomed Mater Res 1989;23(10):1183-1193.

Champion JA, Katare YK, Mitragotri S. Particle shape: a new design parameter for micro- and nanoscale drug delivery carriers. J Control Release 2007;121(1-2):3-9.

Champion JA, Katare YK, Mitragotri S. Making polymeric micro- and nanoparticles of complex shapes. Proc Natl Acad Sci USA 2007;104(29):11901-11904.

Chen Y, Macintyre D, Boyd E, Moran D, Thayne I, Thoms S. Fabrication of high electron mobility transistors with T-gates by nanoimprint lithography. J Vac Sci Technol B 2002;20(6):2887-2890.

Choi BJ, Meissl MJ, Colburn M, Bailey TC, Ruchhoeft P, Sreenivasan SV, et al. Layer-to-layer alignment for step and flash imprint lithography. Proc SPIE 2001;4343:436-442.

Chou SY, Krauss PR. Imprint lithography with sub-10 nmfeature size and high throughput. Microelectron Eng 1997;35(1):237-240.

Chou SY, Krauss PR, Renstrom PJ. Imprint lithography with 25-nanometer resolution. Science 1996;272(5258):85-87.

Colburn M, Johnson SC, Stewart MD, Damle S, Bailey TC, Choi B, et al. Step and flash imprint lithography: a new approach to high-resolution patterning. Proc SPIE 1999;3676:379-389.

Couvreur P, Vauthier C. Nanotechnology: intelligent design to treat complex disease. Pharm Res 2006;23(7):1417-1450.

Cruise GM, Scharp DS, Hubbell JA. Characterization of permeability and network structure of interfacially photopolymerized poly(ethylene glycol) diacrylate hydrogels. Biomaterials 1998;19(14):1287-1294.

Decuzzi P, Causa F, Ferrari M, Netti PA. The effective dispersion of nanovectors within the tumor microvasculature. Ann Biomed Eng 2006;34(4):633-641.

Decuzzi P, Ferrari M. The adhesive strength of non-spherical particles mediated by specific interactions. Biomaterials 2006;27(30):5307-5314.

DeLong SA, Moon JJ, West JL. Covalently immobilized gradients of bFGF on hydrogel scaffolds for directed cell migration. Biomaterials 2005;26(16):3227-3234.

Dendukuri D, Pregibon DC, Collins J, Hatton TA, Doyle PS. Continuous-flow lithography for high-throughput microparticle synthesis. Nat Mater 2006;5(5):365-369.

Dendukuri D, Tsoi K, Hatton TA, Doyle PS. Controlled synthesis of nonspherical microparticles using microfluidics. Langmuir 2005;21(6):2113-2116.

Deryugina EI, Quigley JP. Matrix metalloproteinases and tumor metastasis. Cancer Metastasis Rev 2006;25(1):9-34.

Doan KT, Olson RJ, Mamalis N. Survey of intraocular lens material and design. Curr Opin Ophthalmol 2002;13(1):24-29.

Duncan R, Cable HC, Lloyd JB, Rejmanova P, Kopecek J. Degradation of side-chains of N-(2-hydroxypropyl)methacrylamide copolymers by lysosomal thiol-proteinases. Biosci Rep 1982;2(12):1041-1046.

Duncan R, Cable HC, Lloyd JB, Rejmanova P, Kopecek J. Polymers containing enzymatically degradable bonds. 7: Design of oligopeptide side-chains in poly [N-(2-hydroxypropyl) methacrylamide] copolymers to promote efficient degradation by lysosomal enzymes. Makromol Chem 1983;184(10):1997-2008.

Ebert W, Knoch H, Werle B, Trefz G, Muley T, Spiess E. Prognostic value of increased lung tumor tissue cathepsin B. Anticancer Res 1994;14(3A):895-899.

Ebru O, Peppas NA. Hydrophilic molecularly imprinted poly(hydroxyethyl-methacrylate) polymers. J Biomed Mater Res A 2006;78A(1):205-210.

Erdel M, Trefz G, Spiess E, Habermaas S, Spring H, Lah T, et al. Localization of cathepsin B in two human lung cancer cell lines. J Histochem Cytochem 1990;38(9):1313-1321.

Etrych T, Jelinkova M, Rihova B, Ulbrich K. New HPMA copolymers containing doxorubicin bound via pH-sensitive linkage: synthesis and preliminary in vitro and in vivo biological properties. J Control Release 2001;73(1):89-102.

Euliss LE, Welch CM, Maynor BW, Rolland JP, Denison GM, Gratton SE, et al. Monodisperse nanocarriers: novel fabrication of polymeric nanoparticles for bio-nanotechnology. Proc SPIE 2006;6153:61534A.

Farokhzad OC, Langer R. Nanomedicine: developing smarter therapeutic and diagnostic modalities. Adv Drug Deliv Rev 2006;58(14):1456-1459.

Feng Liu LH. Improving plasmid DNA-mediated liver gene transfer by prolonging its retention in the hepatic vasculature. J Gene Med 2001;3(6):569-576.

Ferrari M. Cancer nanotechnology: opportunities and challenges. Nat Rev Cancer 2005;5(3):161-171.

Filion RJ, Popel AS. Intracoronary administration of FGF-2: a computational model of myocardial deposition and retention. Am J Physiol Heart Circ Physiol 2005;288(1):H263-279.

Foss AC, Goto T, Morishita M, Peppas NA. Development of acrylic-based copolymers for oral insulin delivery. Eur J Pharm Biopharm 2004;57(2):163-169.

Gaubert HE, Frey W. Highly parallel fabrication of nanopatterned surfaces with nanoscale orthogonal biofunctionalization imprint lithography. Nanotechnology 2007;18(13):135101.

Geng Y, Dalhaimer P, Cai S, Tsai R, Tewari M, Minko T, et al. Shape effects of filaments versus spherical particles in flow and drug delivery. Nature Nanotech 2007;2(4):249-255.

Glangchai LC, Caldorera-Moore M, Shi L, Roy K. Nanoimprint lithography based fabrication of shape-specific, enzymatically-triggered smart nanoparticles. J Control Release 2008;125(3):263-272.

Gobin AS, West JL. Effects of epidermal growth factor on fibroblast migration through biomimetic hydrogels. Biotechnol Prog 2003;19(6):1781-1785.

Gratton SEA, Pohlhaus PD, Lee J, Guo J, Cho MJ, Desimone JM. Nanofabricated particles for engineered drug therapies: a preliminary biodistribution study of PRINT nanoparticles. J Control Release 2007;121(1-2):10-18.

Gref R, Luck M, Quellec P, Marchand M, Dellacherie E, Harnisch S, et al. 'Stealth' corona-core nanoparticles surface modified by polyethylene glycol (PEG): influences of the corona (PEG chain length and surface density) and of the core composition on phagocytic uptake and plasma protein adsorption. Colloid Surf B 2000;18(3-4):301-313.

Guan J, Ferrell N, James Lee L, Hansford DJ. Fabrication of polymeric microparticles for drug delivery by soft lithography. Biomaterials 2006;27(21):4034-4041.

Heidtmann HH, Salge U, Abrahamson M, Bencina M, Kastelic L, Kopitar-Jerala N, et al. Cathepsin B and cysteine proteinase inhibitors in human lung cancer cell lines. Clin Exp Metastasis 1997;15(4):368-381.

Hern DL, Hubbell JA. Incorporation of adhesion peptides into nonadhesive hydrogels useful for tissue resurfacing. J Biomed Mater Res 1998;39(2):266-276.

Higashiyama M, Doi O, Kodama K, Yokouchi H, Tateishi R. Cathepsin B expression in tumour cells and laminin distribution in pulmonary adenocarcinoma. J Clin Pathol 1993;46(1):18-22.

Hilt JZ, Peppas NA. Microfabricated drug delivery devices. Int J Pharm 2005;306(1-2):15-23.

Hobbs SK, Monsky WL, Yuan F, Roberts WG, Griffith L, Torchilin VP, et al. Regulation of transport pathways in tumor vessels: role of tumor type and microenvironment. Proc Natl Acad Sci USA 1998;95(8):4607-4612.

Hoffman AS, Stayton PS, Press O, Murthy N, Lackey CA, Cheung C, et al. Design of 'smart' polymers that can direct intracellular drug delivery. Polym Adv Technol 2002;13(10-12):992-999.

Howie AJ, Burnett D, Crocker J. The distribution of cathespin B in human tissues. J Pathol 1985;145(4):307-314.

Hu J, Van den Steen PE, Sang Q-XA, Opdenakker G. Matrix metalloproteinase inhibitors as therapy for inflammatory and vascular diseases. Nat Rev Drug Discov 2007;6(6):480-498.

Ishihara M, Obara K, Ishizuka T, Fujita M, Sato M, Masuoka K, et al. Controlled release of fibroblast growth factors and heparin from photocrosslinked chitosan hydrogels and subsequent effect on in vivo vascularization. J Biomed Mater Res A 2003;64(3):551-559.

Jessup JM. Cathepsin B and other proteases in human colorectal carcinoma. Am J Pathol 1994;145(2):253-262.

Johnson S, Resnick DJ, Mancini D, Nordquist K, Dauksher WJ, Gehoski K, et al. Fabrication of multi-tiered structures on step and flash imprint lithography templates. Microelectron Eng 2003;67-68:221-228.

Johnson SC, Bailey TC, Dickey MD, Smith BJ, Kim EK, Jamieson AT, et al. Advances in Step and Flash imprint lithography. Proc SPIE 2003;5037:197-202.

Johnston RC. Acrylic bone cement: clinical development and current status in North America. Orthop Clin North Am 2005;36(1):75-84.

Kamath KR, Park K. Biodegradable hydrogels in drug delivery. Adv Drug Deliv Rev 1993;11(1-2):59-84.

Kasper FK, Kushibiki T, Kimura Y, Mikos AG, Tabata Y. In vivo release of plasmid DNA from composites of oligo(poly(ethylene glycol)fumarate) and cationized gelatin microspheres. J Control Release 2005;107(3):547-561.

Khare AR, Peppas NA. Release behavior of bioactive agents from pH-sensitive hydrogels. J Biomat Sci-Polym E 1993;4(3):275-289.

Kikuchi A, Okano T. Pulsatile drug release control using hydrogels. Adv Drug Deliv Rev 2002;54(1):53-77.

Kim B, Peppas NA. Synthesis and characterization of pH-sensitive glycopolymers for oral drug delivery systems. J Biomat Sci-Polym E 2002;13:1271-1281.

Kim B, Peppas NA. In vitro release behavior and stability of insulin in complexation hydrogels as oral drug delivery carriers. Int J Pharm 2003;266(1-2):29-37.

Kim S, Healy KE. Synthesis and characterization of injectable poly(N-isopropylacrylamide-co-acrylic acid) hydrogels with proteolytically degradable cross-links. Biomacromolecules 2003;4(5):1214-1223.

Kishida A, Mishima K, Corretge E, Konishi H, Ikada Y. Interactions of poly(ethylene glycol)-grafted cellulose membranes with proteins and platelets. Biomaterials 1992;13(2):113-118.

Kopecek J. Controlled biodegradability of polymers--a key to drug delivery systems. Biomaterials 1984;5(1):19-25.

Kopecek J, Kopeckova P, Minko T, Lu Z. HPMA copolymer-anticancer drug conjugates: design, activity, and mechanism of action. Eur J Pharm Biopharm 2000;50(1):61-81.

Kos J, Lah TT. Cysteine proteinases and their endogenous inhibitors: target proteins for prognosis, diagnosis and therapy in cancer (review). Oncol Rep 1998;5(6):1349-1361.

Kovar M, Kovar L, Subr V, Etrych T, Ulbrich K, Mrkvan T, et al. HPMA copolymers containing doxorubicin bound by a proteolytically or hydrolytically cleavable bond: comparison of biological properties in vitro. J Control Release 2004;99(2):301-314.

Krepela E, Kasafirek E, Novak K, Viklicky J. Increased cathepsin B activity in human lung tumors. Neoplasma 1990;37(1):61-70.

Krepela E, Prochazka J, Karova B, Cermak J, Roubkova H. Cathepsin B, thiols and cysteine protease inhibitors in squamous-cell lung cancer. Neoplasma 1997;44(4):219-239.

Krepela E, Prochazka J, Mynarikova H, Karova B, Polak J, Cermak J, et al. Multiple forms of cathepsin B in human lung cancer. Int J Cancer 1995;61(1):44-53.

Kreuter J. Influence of the surface properties on nanoparticle-mediated transport of drugs to the brain. J Nanosci Nanotechnol 2004;4(5):484-488.

LaVan DA, McGuire T, Langer R. Small-scale systems for in vivo drug delivery. Nat Biotechnol 2003;21(10):1184-1191.

Leach JB, Schmidt CE. Characterization of protein release from photocrosslinkable hyaluronic acid-polyethylene glycol hydrogel tissue engineering scaffolds. Biomaterials 2005;26(2):125-135.

Lee H. Effect of imprinting pressure on residual layer thickness in ultraviolet nanoimprint lithography. J Vac Sci Technol B 2005;23(3):1102-1106.

Lee KY, Yuk SH. Polymeric protein delivery systems. Prog Polym Sci 2007;32(7):669-697.

Lian T, Ho RJ. Trends and developments in liposome drug delivery systems. J Pharm Sci 2001;90(6):667-680.

Liaudet-Coopman E, Beaujouin M, Derocq D, Garcia M, Glondu-Lassis M, Laurent-Matha V, et al. Cathepsin D: newly discovered functions of a long-standing aspartic protease in cancer and apoptosis. Cancer Lett 2006;237(2):167-179.

Lode J, Fichtner I, Kreuter J, Berndt A, Diederichs JE, Reszka R. Influence of surface-modifying surfactants on the pharmacokinetic behavior of 14C-poly (methylmethacrylate) nanoparticles in experimental tumor models. Pharm Res 2001;18(11):1613-1619.

Losi E, Bettini R, Santi P, Sonvico F, Colombo G, Lofthus K, et al. Assemblage of novel release modules for the development of adaptable drug delivery systems. J Control Release 2006;111(1-2):212-218.

Lowman AM, Morishita M, Kajita M, Nagai T, Peppas NA. Oral delivery of insulin using pH-responsive complexation gels. J Pharm Sci 1999;88(9):933-937.

Lowman AM, Peppas NA. Solute transport analysis in pH-responsive, complexing hydrogels of poly(methacrylic acid-g-ethylene glycol). J Biomat Sci-Polym E 1999;10:999-1009.

Lu Y, Aguilar CA, Chen S. Shaping biodegradable polymers as nanostructures: Fabrication and applications. Drug Discov Today 2005;2(1):97-102.

Lu Y, Chen SC. Micro and nano-fabrication of biodegradable polymers for drug delivery. Adv Drug Deliv Rev 2004;56(11):1621-1633.

Lu ZR, Shiah JG, Sakuma S, Kopeckova P, Kopecek J. Design of novel bioconjugates for targeted drug delivery. J Control Release 2002;78(1-3):165-173.

Lutolf MP, Weber FE, Schmoekel HG, Schense JC, Kohler T, Muller R, et al. Repair of bone defects using synthetic mimetics of collagenous extracellular matrices. Nat Biotechnol 2003;21(5):513-518.

Maeda H, Sawa T, Konno T. Mechanism of tumor-targeted delivery of macromolecular drugs, including the EPR effect in solid tumor and clinical overview of the prototype polymeric drug SMANCS. J Control Release 2001;74(1-3):47-61.

Maeda H, Wu J, Sawa T, Matsumura Y, Hori K. Tumor vascular permeability and the EPR effect in macromolecular therapeutics: a review. J Control Release 2000;65(1-2):271-284.

Mann BK, Gobin AS, Tsai AT, Schmedlen RH, West JL. Smooth muscle cell growth in photopolymerized hydrogels with cell adhesive and proteolytically degradable domains: synthetic ECM analogs for tissue engineering. Biomaterials 2001;22(22):3045-3051.

Mapili G, Lu Y, Chen S, Roy K. Laser-layered microfabrication of spatially patterned functionalized tissue-engineering scaffolds. J Biomed Mater Res B 2005;75(2):414-424.

Marsano E, Gagliardi S, Ghioni F, Bianchi E. Behaviour of gels based on (hydroxypropyl) cellulose methacrylate. Polymer 2000;41(21):7691-7698.

Martens PJ, Bryant SJ, Anseth KS. Tailoring the degradation of hydrogels formed from multivinyl poly(ethylene glycol) and poly(vinyl alcohol) macromers for cartilage tissue engineering. Biomacromolecules 2003;4(2):283-292.

McMackin I, Schumaker P, Babbs D, Choi J, Collison W, Sreenivasan SV, et al. Design and performance of a step and repeat imprinting machine. Proc SPIE 2003;5037:178-186.

Meerum Terwogt JM, ten Bokkel Huinink WW, Schellens JH, Schot M, Mandjes IA, Zurlo MG, et al. Phase I clinical and pharmacokinetic study of PNU166945, a novel water-soluble polymer-conjugated pro-drug of paclitaxel. Anticancer Drugs 2001;12(4):315-323.

Mellott MB, Searcy K, Pishko MV. Release of protein from highly cross-linked hydrogels of poly(ethylene glycol) diacrylate fabricated by UV polymerization. Biomaterials 2001;22(9):929-941.

Merrill EW, Dennison KA, Sung C. Partitioning and diffusion of solutes in hydrogels of poly(ethylene oxide). Biomaterials 1993;14(15):1117-1126.

Merrill EW, Salzman EW. Polyethylene oxide as a biomaterial. ASAIO J 1983;6(2):60-64.

Minko T, Kopeckova P, Kopecek J. Efficacy of the chemotherapeutic action of HPMA copolymer-bound doxorubicin in a solid tumor model of ovarian carcinoma. Int J Cancer 2000;86(1):108-117.

Miyata T, Uragami T, Nakamae K. Biomolecule-sensitive hydrogels. Adv Drug Deliv Rev 2002;54(1):79-98.

Moghimi SM, Hunter AC, Murray JC. Nanomedicine: current status and future prospects. Faseb J 2005;19(3):311-330.

Murthy N, Campbell J, Fausto N, Hoffman AS, Stayton PS. Bioinspired pH-responsive polymers for the intracellular delivery of biomolecular drugs. Bioconjug Chem 2003;14(2):412-419.

Na K, Bae YH. Self-assembled hydrogel nanoparticles responsive to tumor extracellular pH from pullulan derivative/sulfonamide conjugate: characterization, aggregation, and adriamycin release in vitro. Pharm Res 2002;19(5):681-688.

Nakamura K, Maitani Y, Lowman AM, Takayama K, Peppas NA, Nagai T. Uptake and release of budesonide from mucoadhesive, pH-sensitive copolymers and their application to nasal delivery. J Control Release 1999;61(3):329-335.

Nakamura K, Murray RJ, Joseph JI, Peppas NA, Morishita M, Lowman AM. Oral insulin delivery using P(MAA-g-EG) hydrogels: effects of network morphology on insulin delivery characteristics. J Control Release 2004;95(3):589-599.

Nishiyama N. Nanomedicine: nanocarriers shape up for long life. Nature Nanotech 2007;2(4):203-204.

Noble CO, Kirpotin DB, Hayes ME, Mamot C, Hong K, Park JW, et al. Development of ligand-targeted liposomes for cancer therapy. Expert Opin Ther Targets 2004;8(4):335-353.

Ohta T, Terada T, Nagakawa T, Tajima H, Itoh H, Fonseca L, et al. Pancreatic trypsinogen and cathepsin B in human pancreatic carcinomas and associated metastatic lesions. Br J Cancer 1994;69(1):152-156.

Oral E, Peppas NA. Responsive and recognitive hydrogels using star polymers. J Biomed Mater Res A 2004;68A(3):439-447.

Owens Iii DE, Peppas NA. Opsonization, biodistribution, and pharmacokinetics of polymeric nanoparticles. Int J Pharm 2006;307(1):93-102.

Page M, editor. Tumor targeting in cancer therapy. Totowa, NJ: Humana Press Inc., 2002.

Park JW, Benz CC, Martin FJ. Future directions of liposome-and immunoliposome-based cancer therapeutics. Semin Oncol 2004;31(6):196-205.

Park JW, Hong K, Kirpotin DB, Papahadjopoulos D, Benz CC. Immunoliposomes for cancer treatment. Adv Pharmacol 1997;40:399-435.

Peer D, Karp JM, Hong S, Farokhzad OC, Margalit R, Langer R. Nanocarriers as an emerging platform for cancer therapy. Nature Nanotech 2007;2(12):751-760.

Peppas NA. Devices based on intelligent biopolymers for oral protein delivery. Int J Pharm 2004;277(1-2):11-17.

Peppas NA, Bures P, Leobandung W, Ichikawa H. Hydrogels in pharmaceutical formulations. Eur J Pharm Biopharm 2000;50(1):27-46.

Peppas NA, Hilt JZ, Khademhosseini A, Langer R. Hydrogels in biology and medicine: From molecular principles to bionanotechnology. Adv Mater 2006;18(11):1345-1360.

Peppas NA, Huang Y. Polymers and Gels as Molecular Recognition Agents. Pharm Res 2002;19(5):578-587.

Peppas NA, Huang Y. Nanoscale technology of mucoadhesive interactions. Adv Drug Deliv Rev 2004;56(11):1675-1687.

Peppas NA, Huang Y, Torres-Lugo M, Ward JH, Zhang J. Physiochemical foundations and structural design of hydrogels in medicine and biology. Annu Rev Biomed Eng 2000;2(1):9-29.

Peppas NA, Kavimandan NJ. Nanoscale analysis of protein and peptide absorption: Insulin absorption using complexation and pH-sensitive hydrogels as delivery vehicles. European J Pharm Sci 2006;29(3-4):183-197.

Peppas NA, Ward JH. Biomimetic materials and micropatterned structures using iniferters. Adv Drug Deliv Rev 2004;56(11):1587-1597.

Peterson CM, Shiah JG, Sun Y, Kopeckova P, Minko T, Straight RC, et al. HPMA copolymer delivery of chemotherapy and photodynamic therapy in ovarian cancer. Adv Exp Med Biol 2003;519:101-123.

Peticlerc D, Pelletier G, Lapierre H, Gaudreau P, Couture Y, Dubreuil P, et al. Dose response of two synthetic human growth hormone-releasing factors on growth hormone release in heifers and pigs. J Anim Sci 1987;65(4):996-1005.

Podual K, Doyle FJ, Peppas NA. Glucose-sensitivity of glucose oxidase-containing cationic copolymer hydrogels having poly(ethylene glycol) grafts. J Control Release 2000;67(1):9-17.

Podual K, Doyle Iii FJ, Peppas NA. Dynamic behavior of glucose oxidase-containing microparticles of poly(ethylene glycol)-grafted cationic hydrogels in an environment of changing pH. Biomaterials 2000;21(14):1439-1450.

Popat KC, Johnson RW, Desai TA. Characterization of vapor deposited poly (ethylene glycol) films on silicon surfaces for surface modification of microfluidic systems. J Vac Sci Technol B 2003;21(2):645-654.

Popat KC, Sharma S, Desai TA. Quantitative XPS analysis of PEG-modified silicon surfaces. J Phys Chem B 2004;108(17):5185-5188.

Portney NG, Ozkan M. Nano-oncology: drug delivery, imaging, and sensing. Anal Bioanal Chem 2006;384(3):620-630.

Putnam D, Kopeček J. Polymer conjugates with anticancer activity. Advances in Polymer Science (Biopolymers II): Springer, 1995. p. 55-123.

Putnam DA, Shiah JG, Kopecek J. Intracellularly biorecognizable derivatives of 5-fluorouracil. Implications for site-specific delivery in the human condition. Biochem Pharmacol 1996;52(6):957-962.

Qiu Y, Park K. Environment-sensitive hydrogels for drug delivery. Adv Drug Deliv Rev 2001;53(3):321-339.

Quick DJ, Anseth KS. Gene delivery in tissue engineering: a photopolymer platform to coencapsulate cells and plasmid DNA. Pharm Res 2003;20(11):1730-1737.

Quick DJ, Anseth KS. DNA delivery from photocrosslinked PEG hydrogels: encapsulation efficiency, release profiles, and DNA quality. J Control Release 2004;96(2):341-351.

Raeber GP, Lutolf MP, Hubbell JA. Molecularly engineered PEG hydrogels: a novel model system for proteolytically mediated cell migration. Biophys J 2005;89(2):1374-1388.

Reddy ST, Rehor A, Schmoekel HG, Hubbell JA, Swartz MA. In vivo targeting of dendritic cells in lymph nodes with poly(propylene sulfide) nanoparticles. J Control Release 2006;112(1):26-34.

Rejmanova P, Kopecek J, Duncan R, Lloyd JB. Stability in rat plasma and serum of lysosomally degradable oligopeptide sequences in N-(2-hydroxypropyl) methacrylamide copolymers. Biomaterials 1985;6(1):45-48.

Rejmanova P, Kopecek J, Pohl J, Baudy M, Kostka V. Polymers containing enzymatically degradable bonds, 8. Degradation of oligopeptide sequences in N-(2-hydroxypropyl)methacrylamide copolymers by bovine spleen cathepsin B. Makromol Chem 1983;184(10):2009-2020.

Resnick DJ, Dauksher WJ, Mancini D, Nordquist KJ, Bailey TC, Johnson S, et al. Imprint lithography for integrated circuit fabrication. J Vac Sci Technol B 2003;21(6):2624-2631.

Resnick DJ, Mancini DP, Nordquist KJ, Dauksher WJ, McMackin I, Schumaker P, et al. Initial study of the fabrication of step and flash imprint lithography templates for the printing of contact holes. J Microlith Microfab 2004;3(2):316-321.

Resnick DJ, Mancini DP, Sreenivasan SV, Willson CG. Release layers for contact and imprint lithography. Semicond Int 2002;25(6):71-80.

Resnick DJ, Sreenivasan SV, Willson CG. Step & flash imprint lithography. Mater Today 2005;8(2):34-42.

Rihova B, Jelinkova M, Strohalm J, Subr V, Plocova D, Hovorka O, et al. Polymeric drugs based on conjugates of synthetic and natural macromolecules. II. Anti-cancer activity of antibody or (Fab')(2)-targeted conjugates and combined therapy with immunomodulators. J Control Release 2000;64(1-3):241-261.

Rolland JP, Maynor BW, Euliss LE, Exner AE, Denison GM, DeSimone JM. Direct fabrication and harvesting of monodisperse, shape-specific nanobiomaterials. J Am Chem Soc 2005;127(28):10096-10100.

Saluja A, Kalonia DS. Measurement of fluid viscosity at microliter volumes using quartz impedance analysis. AAPS PharmSciTech 2004;5(3):e47.

Scholes PD, Coombes AGA, Illum L, Davis SS, Vert M, Davies MC. The preparation of sub-200 nm poly (lactide-co-glycolide) microspheres for site-specific drug delivery. J Control Release 1993;25(1-2):145-153.

Schulz H, Wissen M, Bogdanski N, Scheer HC, Mattes K, Friedrich C. Impact of molecular weight of polymers and shear rate effects for nanoimprint lithography. Microelectron Eng 2006;83(2):259-280.

Seghezzi G, Patel S, Ren CJ, Gualandris A, Pintucci G, Robbins ES, et al. Fibroblast growth factor-2 (FGF-2) induces vascular endothelial growth factor (VEGF) expression in the endothelial cells of forming capillaries: an autocrine mechanism contributing to angiogenesis. J Cell Biol 1998;141(7):1659-1673.

Seliktar D, Zisch AH, Lutolf MP, Wrana JL, Hubbell JA. MMP-2 sensitive, VEGF-bearing bioactive hydrogels for promotion of vascular healing. J Biomed Mater Res A 2004;68(4):704-716.

Serra L, Domenech J, Peppas NA. Drug transport mechanisms and release kinetics from molecularly designed poly(acrylic acid-g-ethylene glycol) hydrogels. Biomaterials 2006;27(31):5440-5451.

Seymour LW, Ferry DR, Anderson D, Hesslewood S, Julyan PJ, Poyner R, et al. Hepatic Drug Targeting: Phase I Evaluation of Polymer-Bound Doxorubicin. J Clin Oncol 2002;20(6):1668.

Sharma S, Desai TA. Nanostructured antifouling poly(ethylene glycol) films for silicon-based microsystems. J Nanosci Nanotechnol 2005;5(2):235-243.

Sharma S, Johnson RW, Desai TA. Ultrathin poly(ethylene glycol) films for silicon-based microdevices. Appl Surf Sci 2003;206(1-4):218-229.

Sharma S, Johnson RW, Desai TA. XPS and AFM analysis of antifouling PEG interfaces for microfabricated silicon biosensors. Biosens Bioelectron 2004;20(2):227-239.

Sharma S, Johnson RW, Desai TA. Evaluation of the stability of nonfouling ultrathin poly(ethylene glycol) films for silicon-based microdevices. Langmuir 2004;20(2):348-356.

Shenoy D, Little S, Langer R, Amiji M. Poly(ethylene oxide)-modified poly(beta-amino ester) nanoparticles as a pH-sensitive system for tumor-targeted delivery of hydrophobic drugs: part 2. In vivo distribution and tumor localization studies. Pharm Res 2005;22(12):2107-2114.

Sozzani P, Bracco S, Comotti A, Simonutti R, Valsesia P, Sakamoto Y, et al. Complete shape retention in the transformation of silica to polymer micro-objects. Nat Mater 2006;5(7):545-551.

Spiess E, Bruning A, Gack S, Ulbricht B, Spring H, Trefz G, et al. Cathepsin B activity in human lung tumor cell lines: ultrastructural localization, pH sensitivity, and inhibitor status at the cellular level. J Histochem Cytochem 1994;42(7):917-929.

Stopa B, Rybarska J, Drozd A, Konieczny L, Krol M, Lisowski M, et al. Albumin binds self-assembling dyes as specific polymolecular ligands. Int J Biol Macromol 2006;40(1):1-8.

Subr V, Kopecek J, Pohl J, Baudyo M, Kostka V. Cleavage of oligopeptide side chains in HPMA copolymers by mixtures of lysosomal enzymes. J Control Release 1988;8:133-140.

Subr V, Strohalm J, Ulbrich K, Duncan R, Hume IC. Polymers containing enzymatically degradable bonds, XII. Effect of spacer structure on the rate of release of daunomycin and adriamycin from poly [N-(2-hydroxypropyl)-methacrylamide] copolymer drug carriers in vitro and antitumour activity measured in vivo. J Control Release 1992;18(2):123-132.

Tansey W, Ke S, Cao XY, Pasuelo MJ, Wallace S, Li C. Synthesis and characterization of branched poly(L-glutamic acid) as a biodegradable drug carrier. J Control Release 2004;94(1):39-51.

Tao SL, Desai TA. Microfabrication of multilayer, asymmetric, polymeric devices for drug delivery. Adv Mater 2005;17(13):1625-1630.

Tao SL, Lubeley MW, Desai TA. Bioadhesive poly(methyl methacrylate) microdevices for controlled drug delivery. J Control Release 2003;88(2):215-228.

Tao SL, Lubeley MW, Desai TA. Synthesis of cytoadhesive poly(methylmethacrylate) for applications in targeted drug delivery. J Biomed Mater Res A 2003;67(2):369-375.

Temenoff JS, Athanasiou KA, LeBaron RG, Mikos AG. Effect of poly(ethylene glycol) molecular weight on tensile and swelling properties of oligo(poly(ethylene glycol) fumarate) hydrogels for cartilage tissue engineering. J Biomed Mater Res 2002;59(3):429-437.

Torchilin VP. Recent advances with liposomes as pharmaceutical carriers. Nat Rev Drug Discov 2005;4(2):145-160.

Torchilin VP. Multifunctional nanocarriers. Adv Drug Deliv Rev 2006;58(14):1532-1555.

Torchilin VP, Lukyanov AN, Gao Z, Papahadjopoulos-Sternberg B. Immunomicelles: targeted pharmaceutical carriers for poorly soluble drugs. Proc Natl Acad Sci USA 2003;100(10):6039-6044.

Torres-Lugo M, Garcia M, Record R, Peppas NA. pH-Sensitive hydrogels as gastrointestinal tract absorption enhancers: transport mechanisms of salmon calcitonin and other model molecules using the Caco-2 cell model. Biotechnol Prog 2002;18(3):612-616.

Turk V, Kos J, Turk B. Cysteine cathepsins (proteases)--on the main stage of cancer? Cancer Cell 2004;5(5):409-410.

Turk V, Turk B, Turk D. Lysosomal cysteine proteases: facts and opportunities. EMBO J 2001;20(17):4629-4633.

Ulbrich K, Etrych T, Chytil P, Jelinkova M, Rihova B. HPMA copolymers with pH-controlled release of doxorubicin: in vitro cytotoxicity and in vivo antitumor activity. J Control Release 2003;87(1-3):33-47.

Ulbrich K, Pechar M, Strohalm J, Subr V, Rihova B. Polymeric carriers of drugs for site-specific therapy. Macromol Symp 1997;118:577-585.

Ulbrich K, Subr V. Polymeric anticancer drugs with pH-controlled activation. Adv Drug Deliv Rev 2004;56(7):1023-1050.

Ulbrich K, Subr V, Strohalm J, Plocova D, Jelinkova M, Rihova B. Polymeric drugs based on conjugates of synthetic and natural macromolecules. I. Synthesis and physico-chemical characterisation. J Control Release 2000;64(1-3):63-79.

Vakkalanka SK, Brazel CS, Peppas NA. Temperature- and pH-sensitive terpolymers for modulated delivery of streptokinase. J Biomat Sci-Polym E 1997;8:119-129.

Vasey PA, Kaye SB, Morrison R, Twelves C, Wilson P, Duncan R, et al. Phase I clinical and pharmacokinetic study of PK1 [N-(2-hydroxypropyl)methacrylamide copolymer doxorubicin]: first member of a new class of chemotherapeutic agents-drug-polymer conjugates. Cancer Research Campaign Phase I/II Committee. Clin Cancer Res 1999;5(1):83-94.

Vasir JK, Reddy MK, Labhasetwar VD. Nanosystems in drug targeting: opportunities and challenges. Curr Nanosci 2005;1:47-64.

Velev OD, Lenhoff AM, Kaler EW. A class of microstructured particles through colloidal crystallization. Science 2000;287(5461):2240-2243.

Vonarbourg A, Passirani C, Saulnier P, Benoit JP. Parameters influencing the stealthiness of colloidal drug delivery systems. Biomaterials 2006;27(24):4356-4373.

Ward JH, Bashir R, Peppas NA. Micropatterning of biomedical polymer surfaces by novel UV polymerization techniques. J Biomed Mater Res 2001;56(3):351-360.

Werle B, Ebert W, Klein W, Spiess E. Cathepsin B in tumors, normal tissue and isolated cells from the human lung. Anticancer Res 1994;14(3A):1169-1176.

Werle B, Kraft C, Lah TT, Kos J, Schanzenbacher U, Kayser K, et al. Cathepsin B in infiltrated lymph nodes is of prognostic significance for patients with nonsmall cell lung carcinoma. Cancer 2000;89(11):2282-2291.

West JL, Hubbell JA. Polymeric biomaterials with degradation sites for proteases involved in cell migration. Macromolecules 1999;32(1):241-244.

Wieland JA, Houchin-Ray TL, Shea LD. Non-viral vector delivery from PEG-hyaluronic acid hydrogels. J Control Release 2007;120(3):233-241.

Willett RL, Baldwin KW, West KW, Pfeiffer LN. Differential adhesion of amino acids to inorganic surfaces. Proc Natl Acad Sci USA 2005;102(22):7817-7822.

Wong HL, Bendayan R, Rauth AM, Li Y, Wu XY. Chemotherapy with anticancer drugs encapsulated in solid lipid nanoparticles. Adv Drug Deliv Rev 2007;59(6):491-504.

Xu S, Nie Z, Seo M, Lewis P, Kumacheva E, Stone HA, et al. Generation of monodisperse particles by using microfluidics: control over size, shape, and composition. Angew Chem Int Ed Engl 2005;44(5):724-728.

Yuan F, Dellian M, Fukumura D, Leunig M, Berk DA, Torchilin VP, et al. Vascular permeability in a human tumor xenograft: molecular size dependence and cutoff size. Cancer Res 1995;55(17):3752-3756.

Zambaux MF, Bonneaux F, Gref R, Maincent P, Dellacherie E, Alonso MJ, et al. Influence of experimental parameters on the characteristics of poly(lactic acid) nanoparticles prepared by a double emulsion method. J Control Release 1998;50(1-3):31-40.

Zamyatnin AA. Amino acid, peptide, and protein volume in solution. Annu Rev Biophys Bioeng 1984;13:145-165.

Vita

Luz Cristal Sanchez Glangchai was born in Austin, TX on November 20, 1977 to Elaine and Adolfo Sanchez. After graduating from Austin High School in 1996, she attended the University of Texas at Austin where she obtained a Bachelor of Science degree in Mechanical Engineering and a Bachelor of Arts degree in the Plan II Honors Program. Upon graduating in December 2000, she married Saranyoo Golf Glangchai and began working at 3M, in Austin, TX. She worked as a product development engineer, designing copper connectors for automated test equipment until 2003 when her interests turned towards biomedical engineering.

Cristal began her PhD studies in August 2003 and received her Master of Science degree in 2005. Her research efforts focused on the merging of semiconductor techniques with drug delivery applications. Cristal received a National Science Foundation Integrative Graduate Education and Research Traineeship (IGERT) Fellowship in 2004. She presented her work at several leading biomedical and mechanical engineering based conferences, and published one first author paper in a peer reviewed journal. She placed in several idea and business plan competitions with an application of her research. These included the Idea-to-Product Competition (1st place), the Texas MootCorp Competition (2nd place), the RICE Business Plan Competition (7th place), and the Oak Ridge National Labs NANO I2P competition (1st place) where she won $25,000.

During the course of her studies she gave birth to her first child, Javier Silar Glangchai on May 30, 2006. Cristal, her husband Golf, and their son Javier, currently reside in Austin, TX.

Permanent address: 13421 Wyoming Valley Dr. Austin, TX 78727

This dissertation was typed by Luz Cristal Sanchez Glangchai.